

**Application of the Fuller-Thompson equation in sinter
blend design to increase sinter plant productivity**

by

Alex James Purnell

Thesis submitted to Cardiff University
for a degree of Engineering Doctorate

School of Engineering
Cardiff University

June 2017

Summary

TATA Steel Europe are the second largest steel producers in Europe (2015) with operations focused in the UK and Netherlands. The sintering process is an upstream process in the iron and steelmaking chain to create part of the blast furnace burden. A blend of raw materials composing of iron ore, flux, coke breeze and revert materials are sintered on a moving strand to produce an iron rich, strong and porous agglomerate known as sinter. Before sintering, the blend is processed through a mixer and granulator to create granules, which enhances sinter bed permeability. Sinter bed permeability is the driving factor behind sinter strand productivity.

Differing compositions of sinter blends are known to impact the sintering process. More specifically concerned in this study is blend particle size distribution (PSD). A new application of the Fuller-Thompson (FT) equation is proposed, which was originally developed for designing the aggregates in concrete and shown to improve properties like strength. The FT equation determines the PSD to create the maximum particle packing density. The FT equation is applied to sinter blend design through the granulation process. During granulation, finer particles are layered around coarser nuclei particles to produce granules. Designing the finer or layering proportion of sinter blends to the FT equation is proposed to create granules with denser and stronger layers. Thus, enabling greater bed permeability during the process and increased sinter strand productivity.

The first phase of the Author's study determined the parameters of the FT equation that gave the optimum granule beds in terms of 'cold' bed permeability and efficiency in maintaining 'cold' permeability under an applied motion. These were established to be a maximum layering particle size (D) of 0.5mm and a FT exponent (Ψ) of 0.5.

Bimodal sinter blends were used to study the impact of layering PSD spread (n), which is a relative measure for the uniformity of sizes in the distribution on bed permeability and sintering time. Widening the spread of layering particle sizes increased 'cold' bed permeability due to the narrowing in granule size distribution spread and increasing mean granule diameter. With the blends investigated the layering PSD spread of the FT blend gave the greatest 'hot' permeability and shortest sintering times, as it maintained more permeability than expected based on the trend with mean granule diameter.

Industrial base blends were compared with blends designed to the FT equation. At equal layering particle proportions the FT blends increased 'cold' permeability by up to 20% and reduced sintering times by up to 9.5%. The FT blends could also incorporate 4wt% more layering particles and still exhibit the same 'cold' permeability and sintering times as the base blends. No changes in sinter quality were observed.

Full-scale plant trials with FT blend design at Tata Steel Europe showed positive impacts on ignition permeability, flame front speed and net production rate compared to typically used blends. No changes in sinter quality were identified. The methodology is currently being implemented into sinter blend design practice at Tata Steel Europe.

Declaration

This work has not been submitted in substance for any other degree or award at this or any other university or place of learning, nor is being submitted concurrently in candidature for any degree or other award.

Signed  (candidate) Date 27/06/2017

Statement 1

This thesis is being submitted in partial fulfilment of the requirements for the degree of EngD.

Signed  (candidate) Date 27/06/2017

Statement 2

This thesis is the result of my own independent work/investigation, except where otherwise stated, and the thesis has not been edited by a third party beyond what is permitted by Cardiff University's Policy on the Use of Third Party Editors by Research Degree Students. Other sources are acknowledged by explicit references. The views expressed are my own.

Signed  (candidate) Date 27/06/2017

Statement 3

I hereby give consent for my thesis, if accepted, to be available online in the University's Open Access repository and for inter-library loan, and for the title and summary to be made available to outside organisations.

Signed  (candidate) Date 27/06/2017

Acknowledgements

I would firstly like to thank Cardiff University School of Engineering for the opportunity to conduct an Engineering Doctorate degree. I am very grateful to my supervisor's Dr Devin Sapsford and Professor Sam Evans for their endeavours throughout the project.

Without the support of Tata Steel Europe this project would have never materialised. Access to state-of-the-art RD&T facilities and conducting full-scale plant trials allowed a new research idea to develop into a method that's currently being incorporated into sinter blend design practice. Some of the key enablers were; Chris Kooij (Principal Researcher), Willemijn Husslage-van Kaam (Agglomeration Manager) and Jaap Rengersen (General Manager Ironmaking).

A special mention must go to Philippe Wauters my Industrial Supervisor at Tata Steel Europe for his guidance and assistance during the project and particularly in the early stages.

Contents

Contents	v
Figures	ix
Tables	xiii
Chapter 1 – Introduction	1
1.1 Aims and objectives	3
Chapter 2 – Background	4
2.1 Fuller-Thompson equation	4
2.1.1 Fuller-Thompson equation in concrete design	5
2.1.2 Other Fuller-Thompson applications.....	7
2.1.3 Summary.....	8
2.2 The sintering process	9
2.2.1 Sintering process procedure	10
2.2.2 Sinter bed permeability	12
2.2.3 Sinter bed ‘strength’	14
2.2.4 Sintering mechanisms	15
2.2.5 Sinter mineralogy	16
2.2.6 Sinter properties	17
2.2.7 Summary.....	19
2.3 Sinter blend raw materials	20
2.3.1 Iron ores.....	20
Iron ores in sinter blends	21
Global iron ore market.....	23
2.3.2 Coke breeze	24
2.3.3 Flux	24
2.3.4 Plant reverts.....	25
2.3.5 Return sinter fines	26
2.3.6 Summary.....	27
2.4 Granulation process	28
2.4.1 Key early granulation studies	29
2.4.2 Granulation in the sintering process	31
2.4.3 Summary.....	32
2.5 Parameters influencing granulation in sintering	34
2.5.1 Particle size distribution	34
2.5.2 Particle surface properties.....	38
2.5.3 Moisture content	39
2.5.4 Summary.....	43
Chapter 3 – Materials and Methods	45

3.1 Materials	45
3.2 Methods	46
3.2.1 Iron ore characterisation	46
Particle size distribution	46
Rosin-Rammler distribution	47
Qualitative description of particle shape	49
Chemical composition	50
Mineralogy	50
Density	50
Wettability	51
3.2.2 Sinter blend design	52
Determining Fuller-Thompson equation parameters	52
Maximum particle size (D)	52
Fuller-Thompson exponent (Ψ)	53
Blends designed to study the influence of layering PSD spread (n)	54
Industrial application of Fuller-Thompson blend design	55
Industrial base blends	56
Fuller-Thompson blends	57
Summary of blends for analysis	60
Blend composition sheet	61
3.2.3 Mixing and granulation	62
Moisture content	64
3.2.4 Granule size distribution	65
3.2.5 Granule microscopic analysis	66
3.2.6 ‘Cold’ permeability and efficiency	68
Ergun equation permeability measurement	71
3.2.7 Sintering	73
‘Hot’ permeability and efficiency	75
Production rate	76
3.2.8 Sinter cold strength	77
3.2.9 Sinter chemical composition	77
3.2.10 Sinter mineralogy	78
Chapter 4 – Pilot Plant Testing	79
4.1 Iron ore characterisation	79
4.1.1 Particle size distribution	79
4.1.2 Qualitative description of particle shape	80
4.1.3 Chemical composition	82
4.1.4 Mineralogy	83
4.1.5 Density	84
4.1.6 Wettability	84
4.2 Determining the Fuller-Thompson equation parameters	86
4.2.1 Maximum layering particle size (D)	86
4.2.2 Fuller-Thompson exponent (Ψ)	87

‘Cold’ Permeability	87
‘Cold’ permeability efficiency.....	90
Optimum moisture	92
4.2.3 Fuller-Thompson exponent (Ψ) conclusion.....	93
4.3 Influence of layering particle spread (n) in bimodal blends	96
4.3.1 ‘Cold’ permeability	96
4.3.2 ‘Hot’ permeability, efficiency and production rate.....	101
4.4 Industrial application of Fuller-Thompson blend design.....	104
4.4.1 ‘Cold’ permeability	104
4.4.2 ‘Hot’ permeability, efficiency and production rate.....	108
4.4.3 Sinter cold strength	110
4.4.4 Sinter chemical composition.....	112
4.4.5 Sinter mineralogy	114
Chapter 5 – TATA Steel Europe Trials	116
5.1 Introduction.....	116
5.2 FT trial design	116
5.3 Ignition permeability	118
5.3.1 FT trial 1	118
5.3.2 FT trial 2 and 3	121
5.3.3 FT trial 4 and 5	122
5.3.4 Ignition permeability results summary.....	123
5.4 Flame front speed	124
5.4.1 FT trial 1	126
5.4.2 FT trial 2 and 3	126
5.4.3 FT trial 4 and 5	127
5.4.4 FFS results summary.....	127
5.5 Production rate.....	128
5.5.1 FT trial 1	128
5.5.2 FT trial 2 and 3	130
5.5.3 FT trial 4 and 5	130
5.5.4 FT trial production rate summary	131
5.6 Quality	132
5.6.1 Cold strength	133
5.6.2 Reduction-disintegration index (RDI)	133
5.6.3 Dust production rate	134
5.7 FT trial summary	135
Chapter 6 – Conclusions	138
Chapter 7 – Recommendations	140
7.1 Sinter blend particle size distribution	140

7.2 TATA Steel Europe implementation	140
7.2.1 Development of FT blend design tool	140
7.2.2 Continued R&D	141
7.2.3 Plant trials 2	141
Chapter 8 – References	142
Chapter 9 – Appendices	148
9.1 Summary of methods	148
9.2 Pending publications	148

Figures

FIGURE 2.1 – 2D IMAGE OF FULLER-THOMPSON CONCEPT.....	4
FIGURE 2.2 – 3D IMAGE OF FULLER-THOMPSON CONCEPT (FAVRE AND KOOIJ 2013).....	4
FIGURE 2.3 – FULLER-THOMPSON PSD FOR MAXIMUM PARTICLE SIZE (D) OF 10MM AND EXPONENT (Ψ) OF 0.5.....	5
FIGURE 2.4 – PSDS OF THE FT EQUATION WITH EXPONENTS 0.45 TO 0.7 AND D=10MM	6
FIGURE 2.5 – IMPACT OF RMSD ON HOT COMPRESSIVE STRENGTH (SEN ET AL. 2010)	7
FIGURE 2.6 – 2D ILLUSTRATION OF THE CONCEPT OF APPLYING THE FT EQUATION TO SINTER BLEND DESIGN	8
FIGURE 2.7 – SCHEMATIC DIAGRAM OF SINTERING PROCESS AT TATA STEEL UK (ALLERDICE 2007)	10
FIGURE 2.8 – CROSS-SECTIONAL PROFILE THROUGH SINTER BED (ALLERDICE 2007)	11
FIGURE 2.9 – BED PERMEABILITY AS FUNCTION OF MIX MOISTURE FOR DIFFERENT BLENDS (ELLIS ET AL. 2007)	13
FIGURE 2.10 – SEGMENTAL ANALYSIS OF PERMEABILITY-MOISTURE CURVE (ELLIS ET AL. 2007)	13
FIGURE 2.11 – RELATIONSHIP BETWEEN BED ‘STRENGTH’ AND MOISTURE FOR DIFFERENT ORES (ELLIS ET AL. 2007)	14
FIGURE 2.12 – IMAGE OF SINTER	15
FIGURE 2.13 – PHASE COMPOSITION OF SINTERS (GEERDES ET AL. 2009)	17
FIGURE 2.14 – GLOBAL IRON ORE PRODUCTION 2009 (U.S GEOLOGICAL SURVEY 2017)	20
FIGURE 2.15 – GLOBAL IRON ORE PRICES FOR 2012 TO 2014 (MARSDEN 2014)	23
FIGURE 2.16 – DIAGRAM OF GRANULATION PROCESS (FLUID AIR 2013)	28
FIGURE 2.17 – GRANULATION GROWTH MODELS PROPOSED BY IVESON AND LITSTER (1998)	30
FIGURE 2.18 – CONTINUOUS DRUM MIXER AND GRANULATOR (LITSTER AND ENNIS 2004)	31
FIGURE 2.19 – IRON ORE SINTER BLEND GRANULATION MECHANISM PRESENTED BY LITSTER AND WATERS (1988).....	32
FIGURE 2.20 – 2D ILLUSTRATION OF THE CREATION OF GRANULES BY THE LAYERING OF FINER PARTICLES AROUND A NUCLEUS WITH MOISTURE	32
FIGURE 2.21 – LITSTER AND WATERS (1988) PARTITION COEFFICIENT (α_1) WITH PARTICLE SIZE.....	35
FIGURE 2.22 – THE EFFECT OF THE PROPORTION OF LAYERING PARTICLES ON $X_{0.5}$ (LITSTER AND WATERS 1988)	35
FIGURE 2.23 – EFFECT OF CHANGING THE MASS MEAN SIZE OF LAYERING PARTICLES ON $X_{0.5}$ (LITSTER AND WATERS 1988).....	36
FIGURE 2.24 – CHANGE IN OPTIMUM BLEND BED RESISTANCE WITH PARTICLE SIZES (KHOSA AND MANUEL 2015)	37
FIGURE 2.25 – SCHEMATIC DIAGRAM OF IMPACT OF LAYERING PARTICLE COMPOSITION (WU ET AL. 2015)	38
FIGURE 2.26 – SCHEMATIC DIAGRAM OF IMPACT OF NUCLEI PARTICLE COMPOSITION (WU ET AL. 2015) .	38
FIGURE 2.27 – $X_{0.5}$ AGAINST TOTAL MOISTURE (W_T) FOR DIFFERENT NUCLEI TYPES	41
(LITSTER AND WATERS 1988)	41
FIGURE 2.28 – $X_{0.5}$ AGAINST AVAILABLE MOISTURE (W_e) FOR DIFFERENT NUCLEI TYPES (LITSTER AND WATERS 1988).....	41
FIGURE 2.29 – RELATIONSHIP BETWEEN MOISTURE CONTENT AND BED PERMEABILITY FOR DIFFERENT ORES (MATSUMURA ET AL. 2009)	41

FIGURE 2.30 – RELATIONSHIP BETWEEN OPTIMUM MOISTURE AND INCREASING >5MM ORE PARTICLES (MATSUMURA ET AL. 2009)	42
FIGURE 3.1 – HAVER AND BOECKER DIGITAL PLUS SIEVE SHAKERS	46
FIGURE 3.2 – SIEVE SERIES FOR DRY SIZE ANALYSIS.....	46
FIGURE 3.3 – EXAMPLE CUMULATIVE PSD MEASUREMENTS	48
FIGURE 3.4 – ROSIN-RAMMLER DISTRIBUTION FIT TO EXAMPLE CUMULATIVE PSD MEASUREMENTS.....	49
FIGURE 3.5 – PARTICLE SHAPE ANALYSIS CRITERIA (UNIVERSITY SASKATCHEWAN 2002).....	49
FIGURE 3.6 – CUMULATIVE PSD OF BLENDS WITH DIFFERING FT EXPONENTS	54
FIGURE 3.7 – MASS RETAINED (%) FOR A FULLER-THOMPSON (FT) AND ARBITRARY (ARB) BLEND	57
FIGURE 3.8 – MICROSOFT EXCEL™ SOLVER PARAMETERS WITH OBJECTIVES AND CONSTRAINTS TO DESIGN FULLER-THOMPSON BLENDS	58
FIGURE 3.9 – MASS RETAINED PSD OF FULLER-THOMPSON OPTIMISED (FTOPT) BLEND AND FULLER- THOMPSON (FT) EQUATION	59
FIGURE 3.10 – EIRICH MIXER (TATA STEEL EUROPE RD&T)	62
FIGURE 3.11 – FLOWS IN GRANULATION DRUM (HAGE 2015).....	63
FIGURE 3.12 – FLOWS IN GRANULATION DRUM AS FUNCTION OF FROUDE NUMBER (N_{FR}) AND FILLING DEGREE (HAGE 2015)	63
FIGURE 3.13 – VIBRATING FEEDER AND LIQUID NITROGEN POT	65
FIGURE 3.14 – FROZEN SIEVE ANALYSIS SIEVE SERIES.....	65
FIGURE 3.15 – CROSS-SECTION OF GRANULES SET IN EPOXY RESIN	66
FIGURE 3.16 – EXAMPLE MICROSCOPIC IMAGE OF GRANULES IN CROSS-SECTION.....	67
FIGURE 3.17 – EXAMPLE MICROSCOPIC IMAGE OF GRANULES IN CROSS-SECTION WITH NUCLEI AND LAYERS OUTLINED.....	67
FIGURE 3.18 – NUCLEI PARTICLE BINARY IMAGE PRODUCED BY AXIOVISION IMAGE ANALYSIS SOFTWARE ..	68
FIGURE 3.19 – LAYERING PARTICLE BINARY IMAGE PRODUCED BY AXIOVISION IMAGE ANALYSIS SOFTWARE	68
FIGURE 3.20 – ‘NON-LAYERED’ PARTICLE BINARY IMAGE PRODUCED BY AXIOVISION IMAGE ANALYSIS SOFTWARE.....	68
FIGURE 3.21 – ‘COLD’ PERMEABILITY AND EFFICIENCY TEST EQUIPMENT (TATA STEEL EUROPE RD&T) ...	70
FIGURE 3.22 – DIAGRAM OF SINTER BED AND MEASUREMENT DEVICES FOR ‘COLD’ PERMEABILITY	70
FIGURE 3.23 – EXAMPLE ‘COLD’ PERMEABILITY MEASUREMENTS BEFORE AND AFTER MOVEMENT (FAVRE AND KOOIJ 2013).....	70
FIGURE 3.24 – EXAMPLE OF THE METHOD TO CALCULATE SINTER BED ‘COLD’ PERMEABILITY FROM THE ERGUN EQUATION	72
FIGURE 3.25 – GRAPH SHOWING TEST FLOW RATE AND PRESSURE DROP DATA (ΔP -NORM) FITTED TO THE ERGUN EQUATION (ΔP -FIT).....	72
FIGURE 3.26 – IMAGE OF SINTERING EQUIPMENT (TATA STEEL EUROPE RD&T)	74
FIGURE 3.27 – EXAMPLE RESULTS ON SINTER EQUIPMENT INTERFACE.....	75
FIGURE 3.28 – SINTER COLD STRENGTH DRUM (TATA STEEL EUROPE RD&T).....	77
FIGURE 4.1 – CUMULATIVE PARTICLE SIZE DISTRIBUTION OF IRON ORES FITTED WITH THE ROSIN-RAMMLER EQUATION	79
FIGURE 4.2 – MICROSCOPIC IMAGE OF ORE A	81
FIGURE 4.3 – MICROSCOPIC IMAGE OF ORE B	81
FIGURE 4.4 – MICROSCOPIC IMAGE OF ORE C	81
FIGURE 4.5 – MICROSCOPIC IMAGE OF ORE D	81

FIGURE 4.6 – MICROSCOPIC IMAGE OF GRANULE FROM THE BASE (BB) BLEND	86
FIGURE 4.7 – ‘COLD’ PERMEABILITY OF BLENDS WITH DIFFERING FT EXPONENTS (Ψ).....	88
FIGURE 4.8 – RELATIONSHIP BETWEEN ‘COLD’ PERMEABILITY AND GRANULE SIZE DISTRIBUTION SPREAD (N) FOR BLENDS WITH DIFFERING FT EXPONENTS (Ψ).....	88
FIGURE 4.9 – MASS OF PARTICLES <1MM AND MEAN GRANULE DIAMETER (D_M) FOR DIFFERING FT EXPONENTS (Ψ) AT OPTIMUM ‘COLD’ PERMEABILITY.....	89
FIGURE 4.10 – RELATIONSHIP BETWEEN LAYERING PARTICLE SIZE DISTRIBUTION SPREAD (N) AND MEAN GRANULE DIAMETER (D_M) FOR THE FT EXPONENTS (Ψ) AT OPTIMUM ‘COLD’ PERMEABILITY.....	89
FIGURE 4.11 – ‘COLD’ PERMEABILITY EFFICIENCY OF BLENDS WITH DIFFERING FT EXPONENTS (Ψ)	91
FIGURE 4.12 – RELATIONSHIP BETWEEN OPTIMUM ‘COLD’ PERMEABILITY EFFICIENCY AND MEAN GRANULE DIAMETER (D_M)	91
FIGURE 4.13 – ‘COLD’ PERMEABILITY BEFORE AND AFTER COMPACTION (FAVRE AND KOOIJ 2013).....	91
FIGURE 4.14 – FT EXPONENT (Ψ) OPTIMUM MOISTURE FOR ‘COLD’ PERMEABILITY	93
FIGURE 4.15 – FT EXPONENT (Ψ) OPTIMUM MOISTURE FOR ‘COLD’ PERMEABILITY EFFICIENCY	93
FIGURE 4.16 – ‘COLD’ PERMEABILITY OF BLENDS WITH FT EXPONENT (Ψ) OF 0.4 AND 0.5 IN COMPLETE SINTER BLENDS	95
FIGURE 4.17 – ‘COLD’ PERMEABILITY EFFICIENCY OF BLENDS WITH FT EXPONENT (Ψ) OF 0.4 AND 0.5 IN COMPLETE SINTER BLENDS	95
FIGURE 4.18 – ‘COLD’ PERMEABILITY AS A FUNCTION OF GSD SPREAD (N)	97
FIGURE 4.19 – RELATIONSHIP BETWEEN LAYER PSD SPREAD (N) AND GSD SPREAD (N) AND MASS PASSING 1MM SIEVE FOR ALL BLENDS	98
FIGURE 4.20 – RELATIONSHIP BETWEEN MEAN GRANULE DIAMETER (D_M) AND LAYER PSD AND GSD SPREAD (N) FOR ALL BLENDS.....	98
FIGURE 4.21 – MICROSCOPIC IMAGE OF LAYERS IN NON-FT0.....	99
FIGURE 4.22 – MICROSCOPIC IMAGE OF LAYERS IN FT	99
FIGURE 4.23 – MICROSCOPIC IMAGE OF LAYERS IN NON-FT1.....	100
FIGURE 4.24 – MICROSCOPIC IMAGE OF LAYERS IN NON-FT2.....	100
FIGURE 4.25 – MICROSCOPIC IMAGE OF ‘NON-LAYERED’ PARTICLES IN NON-FT0.....	100
FIGURE 4.26 – MICROSCOPIC IMAGE OF ‘NON-LAYERED’ PARTICLES IN FT	100
FIGURE 4.27 – MICROSCOPIC IMAGE OF ‘NON-LAYERED’ PARTICLES IN NON-FT1	100
FIGURE 4.28 – MICROSCOPIC IMAGE OF ‘NON-LAYERED’ PARTICLES IN NON-FT2	100
FIGURE 4.29 – 2D ILLUSTRATION OF THE IMPACT OF LAYERING PSD SPREAD (N) ON GRANULE AND SINTER BED FORMATION A) WIDER SPREAD B) NARROWER SPREAD.....	101
FIGURE 4.30 – RELATIONSHIP BETWEEN ‘HOT’ PERMEABILITY AND SINTERING TIME	102
FIGURE 4.31 – RELATIONSHIP BETWEEN ‘HOT’ PERMEABILITY EFFICIENCY AND MEAN GRANULE DIAMETER (D_M).....	102
FIGURE 4.32 – ‘COLD’ PERMEABILITY AND GSD SPREAD (N) FOR BASE (BB) AND FULLER-THOMPSON (FT) BLENDS	104
FIGURE 4.33 – INCREASE IN ‘COLD’ PERMEABILITY WITH FULLER-THOMPSON (FT) BLENDS COMPARED TO BASE (BB) BLENDS	105
FIGURE 4.34 – MICROSCOPIC IMAGE OF LAYERS IN BB1	106
FIGURE 4.35 – MICROSCOPIC IMAGE OF LAYERS IN FT1	106
FIGURE 4.36 – MICROSCOPIC IMAGE OF LAYERS IN BB3	107
FIGURE 4.37 – MICROSCOPIC IMAGE OF LAYERS IN FT3	107

FIGURE 4.38 – MICROSCOPIC IMAGE OF 'NON-LAYERED' PARTICLES IN BB1	107
FIGURE 4.39 – MICROSCOPIC IMAGE OF 'NON-LAYERED' PARTICLES IN FT1	107
FIGURE 4.40 – MICROSCOPIC IMAGE OF 'NON-LAYERED' PARTICLES IN BB3	107
FIGURE 4.41 – MICROSCOPIC IMAGE OF 'NON-LAYERED' PARTICLES IN FT3	107
FIGURE 4.42 – 'HOT' PERMEABILITY AND SINTERING TIME FOR BASE (BB) AND FULLER-THOMPSON (FT) BLENDS AT EQUAL LAYERING PARTICLE PROPORTIONS	108
FIGURE 4.43 – DECREASE IN SINTERING TIME WITH FULLER-THOMPSON (FT) AGAINST BASE (BB) BLENDS AT EQUAL LAYERING PARTICLE PROPORTIONS	109
FIGURE 4.44 – 'HOT' PERMEABILITY EFFICIENCY OF BASE (BB) AND FULLER-THOMPSON (FT) BLENDS ...	109
FIGURE 4.45 – MEDIAN SINTER DIAMETER (D ₅₀) AFTER COLD STRENGTH TESTING FOR BASE (BB) AND FULLER-THOMPSON (FT) BLENDS	110
FIGURE 4.46 – MASS PASSING 5MM SIEVE AFTER COLD STRENGTH TESTING FOR BASE (BB) AND FULLER- THOMPSON (FT) BLENDS	111
FIGURE 4.47 – MEDIAN SINTER DIAMETER (D ₅₀) AFTER COLD STRENGTH TESTING FOR COKE BREEZE SERIES	112
FIGURE 4.48 – CHEMICAL COMPOSITION OF BASE (BB) AND FULLER-THOMPSON (FT) BLENDS AT 46WT% LAYERING PARTICLE PROPORTION.....	113
FIGURE 4.49 – SINTER MINERALOGY OF BASE (BB) AND FULLER-THOMPSON (FT) BLENDS AT 46WT% LAYERING PARTICLE PROPORTION.....	115
FIGURE 5.1 – MASS RETAINED LAYERING PSD OF TS1, TS2, TS3	117
FIGURE 5.2 – MASS RETAINED LAYERING PSD OF FT1	117
FIGURE 5.3 – SINTER MACHINE IGNITION PERMEABILITY (RELATIVE UNITS) FOR FT TRIALS	119
FIGURE 5.4 – GSD FITTED WITH THE ROSIN-RAMMLER EQUATION FOR BLENDS IN TS2, FT1 AND TS3 ..	121
FIGURE 5.5 – MEAN GRANULE DIAMETER (D _m) FOR TS2, FT1 AND TS3.....	121
FIGURE 5.6 – GSD SPREAD (N) FOR TS2, FT1 AND TS3	121
FIGURE 5.7 – INCREASES IN AVERAGE SINTER MACHINE (SMAV) IGNITION PERMEABILITY COMPARED TO THE BEST PLANNED BLEND FOR FT TRIALS	124
FIGURE 5.8 – RELATIONSHIP BETWEEN TOTAL FINE ORE PROPORTION AND AVERAGE SINTER MACHINE (SMAV) IGNITION PERMEABILITY (RELATIVE UNITS)	124
FIGURE 5.9 – FLAME FRONT SPEED (FFS) FOR FT TRIALS	125
FIGURE 5.10 – AVERAGE SINTER MACHINE (SMAV) IGNITION PERMEABILITY (RELATIVE UNITS) AND FLAME FRONT SPEED (FFS) FOR FT TRIALS.....	128
FIGURE 5.11 – CHANGE IN SPECIFIC NET PRODUCTION RATE FOR FT TRIALS	129
FIGURE 5.12 – RELATIONSHIP BETWEEN AVERAGE SINTER MACHINE (SMAV) FLAME FRONT SPEED (FFS) AND SPECIFIC NET PRODUCTION RATE (RELATIVE UNITS).....	131
FIGURE 5.13 – INCREASES IN AVERAGE SINTER MACHINE (SMAV) SPECIFIC NET PRODUCTION RATE COMPARED TO THE BEST PLANNED BLEND FOR FT TRIALS	131
FIGURE 5.14 – JAPANESE TUMBLE TEST RESULTS FOR FT TRIALS	134
FIGURE 5.15 – REDUCTION-DISINTEGRATION (RDI) RESULTS FOR FT TRIALS	134
FIGURE 5.16 – DUST PRODUCTION FOR FT TRIALS.....	135
FIGURE 5.17 – RELATIONSHIP BETWEEN AVERAGE SINTER MACHINE (SMAV) IGNITION PERMEABILITY (RELATIVE UNITS) AND DUST PRODUCTION FOR FT TRIALS.....	135

Tables

TABLE 2.1 – COMPOSITION OF A TYPICAL SINTER BLEND AND SINTER (ALLERDICE 2007)	9
TABLE 2.2 – SUMMARY OF SINTER PROPERTIES	18
TABLE 2.3 – CHEMICAL COMPOSITION OF SINTER BLEND FLUX (TATA STEEL EUROPE 2016A)	25
TABLE 2.4 – TATA STEEL UK REVERT PLANT MATERIALS (TATA STEEL 2016B)	26
TABLE 2.5 – SUMMARY OF KEY EARLY GRANULATION STUDIES	30
TABLE 3.1 – SINTER BLEND RAW MATERIALS	45
TABLE 3.2 – CHEMICAL COMPOSITION OF SINTER BLEND ADDITIVES	45
TABLE 3.3 – BLEND LAYER COMPOSITIONS OF FT EXPONENTS (Ψ)	54
TABLE 3.4 – LAYER COMPOSITION OF BLENDS TO STUDY THE INFLUENCE OF LAYERING PSD SPREAD (N)	55
TABLE 3.5 – BASE (BB) BLEND COMPOSITIONS AT DIFFERENT TOTAL LAYERING PARTICLE PROPORTIONS ..	56
TABLE 3.6 – FULLER-THOMPSON (FT) BLEND COMPOSITIONS AT DIFFERENT TOTAL LAYERING PARTICLE PROPORTIONS	59
TABLE 3.7 – SUMMARY OF BLENDS FOR ANALYSIS	60
TABLE 3.8 – COMPLETE SINTER BLEND COMPOSITION	60
TABLE 3.9 – SINTER BLEND COMPOSITION SHEET	61
TABLE 4.1 – IRON ORE PSD PROPERTIES	80
TABLE 4.2 – IRON ORE PSD PROPERTIES OF LAYERING PARTICLES	80
TABLE 4.3 – CHEMICAL COMPOSITION OF IRON ORES	82
TABLE 4.4 – DENSITY OF IRON ORES	84
TABLE 4.5 – LAYERING PSD PROPERTIES FOR FT EXPONENTS (Ψ)	89
TABLE 4.6 – LAYERING PSD SPREAD (N) OF BLENDS TO STUDY THE INFLUENCE OF LAYERING PSD SPREAD (N)	96
TABLE 4.7 – GSD MEASUREMENTS FOR BLENDS DESIGNED TO STUDY THE INFLUENCE OF LAYERING PSD SPREAD (N)	97
TABLE 4.8 – GRANULE IMAGE ANALYSIS MEASUREMENTS OF BLENDS TO STUDY THE INFLUENCE OF LAYERING PSD SPREAD (N)	99
TABLE 4.9 – GSD MEASUREMENTS OF BASE (BB) AND FULLER-THOMPSON (FT) BLENDS	105
TABLE 4.10 – LAYERING PSD SPREAD (N) OF BASE (BB) AND FULLER-THOMPSON (FT) BLENDS	106
TABLE 4.11 – GRANULE IMAGE ANALYSIS MEASUREMENTS FOR BASE (BB) AND FULLER-THOMPSON (FT) BLENDS	106
TABLE 4.12 – XRF RESULTS OF BASE (BB) AND FULLER-THOMPSON (FT) BLENDS AT 46WT% LAYERING PARTICLE PROPORTION	113
TABLE 4.13 – XRD RESULTS FOR BASE (BB) AND FULLER-THOMPSON (FT) BLENDS AT 46WT% LAYERING PARTICLE PROPORTION	115
TABLE 5.1 – BLEND COMPOSITIONS FOR FT TRIALS	118

Chapter 1 – Introduction

TATA Steel Europe are the second largest steel producers in Europe (2015). Operations are focused in The Netherlands and UK which produce a wide variety of strip steel products. The key ingredient in producing steel is liquid iron, which is created within a blast furnace. The blast furnace burden consists of a ferrous component (sinter and pellets) along with coke and injection coals. Hot air is blown in the bottom of the furnace to create the temperatures and reducing atmosphere required to produce liquid hot metal. The sintering process is a further upstream process in the iron and steelmaking chain to create part of the blast furnace burden. A blend of raw materials composing of iron ore, flux, coke breeze and revert materials are sintered on a moving strand at temperatures of around 1300°C. The sinter product contains approximately 55% iron and is chemically tailored, which primarily concerns maintenance of correct basicity ($\frac{\text{CaO}+\text{MgO}}{\text{SiO}_2}$) for the blast furnace process. Sinter is an iron-rich reducible material and provides an energy efficient means to adjust blast furnace chemistry. The sintering process also enables a variety of iron ores and plant waste materials to be converted into an effective blast furnace burden. Sinter has become increasingly utilised as a blast furnace burden due to its reducibility and chemical composition, thus the need for greater production grows.

An essential phase in the sintering process is the mixing and granulation of the sinter blend materials. Located prior to the sintering strand, the mixing and granulation process converts the blend into a product that can be sintered, known as granules. Preliminary mixing followed by water addition in a continuous rotating drum causes the layering of finer particles around coarser nuclei particles. The granulating mechanism narrows the spread of particle sizes in the distribution, which enhances the bed permeability on the strand. Sinter bed permeability is the driving parameter behind strand productivity, as it limits the rate at which the combustion gases and flame front can pass through the bed. Sinter blend composition has an impact on important process parameters like permeability. This research focuses on the iron ore proportion of the blend and how its particle size distribution (PSD) can be optimised to create granules that can increase bed permeability and thus strand productivity.

Fuller and Thompson's studies concerning the optimisation of PSDs to achieve maximum material packing density is acknowledged across several fields to improve certain performance properties. Improvements have included increases in strength and durability. A new application of the Fuller-Thompson (FT) equation with the design of sinter blends is proposed. More specifically, in designing the finer or layering proportion of the blend. During granulation, finer particles layer around coarser nuclei particles. Designing the layering part of the blend to the FT equation is hypothesised to create granules that can provide greater resistance to permeability losses during the sintering process. It is further hypothesised that blends designed to the FT equation create increased bed permeability and strand productivity when compared to typically used blends by TATA Steel Europe.

The format of this study initially evaluates the key aspects and investigations surrounding the Fuller-Thompson (FT) equation, sintering and mixing and granulation processes (Chapter 2 – Background). Chapter 3 introduces the materials and methods required to assess the aims and objectives of this study. Pilot sinter plant testing (Chapter 4) is split into two sections. Primarily, manipulated sinter blends are used to study the impact of the layering PSD on key granule and sintering process measurements. More specifically, focusing on the spread of layering particle sizes (n), which is a relative measure for the uniformity of particle sizes in the distribution. The next phase involves the comparison of the key granule and sintering process measurements of blends designed to the FT equation and blends simulating those typically used in TATA Steel Europe's operations. This is to assess whether FT blends at pilot scale can provide enhanced performance.

The full-scale plant trials at TATA Steel Europe are assessed in Chapter 5. Blends designed to the FT equation are fitted alongside blends that were in the current plan. The performance of the FT blends was evaluated against the planned blends to determine if there are bed permeability and strand productivity increases to be obtained from utilising this concept in blend design at full-plant scale in the future.

Chapter 6 concludes the previous chapters from the study. Chapters 7 and 8 provides recommendations and future work based on the results and conclusions.

1.1 Aims and objectives

The aims and objectives of this study are:

1. To apply a Fuller-Thompson based design method to sinter blend design. Initially, determining the Fuller-Thompson equation parameters that create granules with optimum properties.
2. To investigate the impact of the layering PSD on sinter bed permeability and productivity. Focusing specifically on the spread of layering particle sizes (n), which is a relative measure for the uniformity of sizes in the distribution.
3. To ascertain at pilot scale if blends designed to the Fuller-Thompson equation provide enhanced sinter bed permeability and productivity when compared to those that simulate typically used blends by TATA Steel Europe.
4. To investigate the influence of increasing the proportion of layering particles in sinter blends on sinter bed permeability and productivity.
5. To establish if there is the capability with blends designed to the FT equation to incorporate an increased proportion of layering particles in sinter blends without jeopardising bed permeability and productivity.
6. Apply the findings from this study to full-scale plant trials at TATA Steel Europe.

Chapter 2 – Background

2.1 Fuller-Thompson equation

Fuller and Thompson (1907) developed an equation to produce the particle size distribution (PSD) with maximum particle packing density for aggregates used in concrete. They identified the PSD where the particles arrange themselves to minimise the void spaces or maximise the packing density (Figure 2.1 and 2.2). This would create more contact points between the particles and increase key properties such as strength, durability and workability (Yu and Brouwers 2012; Glavind and Pedersen 1999; Fennis and Walraven 2012). The Fuller-Thompson (FT) equation (Equation 1) has been applied across several industries including concrete, pavement and briquette design (Miranda 2012; Fwa 2005; Mong and Adelman 1958; Sen et al. 2010). The distribution developed by the FT equation is on a volume basis with the assumption of spherical particles.

$$P = \left(\frac{d}{D}\right)^{\Psi} \times 100 \tag{1}$$

where: P = volume percentage mass less than d (%)

d = particle size (mm)

D = maximum particle size (mm)

Ψ = exponent

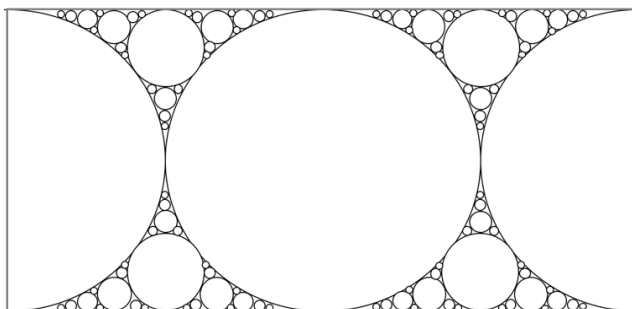


Figure 2.1 – 2D image of Fuller-Thompson concept

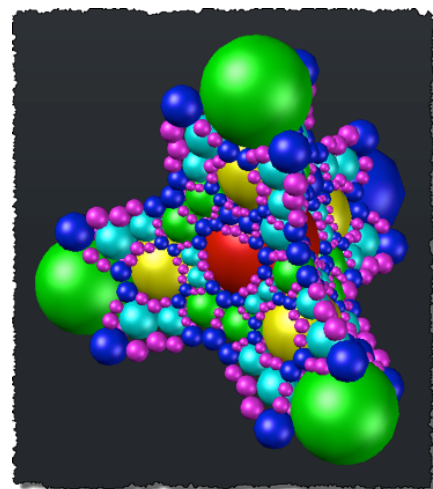


Figure 2.2 – 3D image of Fuller-Thompson concept (Favre and Kooij 2013)

2.1.1 Fuller-Thompson equation in concrete design

Primary testing by Fuller and Thompson (1907) evaluated the factors that influence the density and strength of concrete. They concluded that there was an aggregate PSD that provided greater strength. Utilising a wide-range of materials including crushed stone, screenings and sand it was found that the optimum PSD would have a curve shape for the finer particles in the distribution and a tangent line to the curve that passes through the maximum particle size (D) at 100vol% (Weeks 1965). This is presented in Figure 2.3 for the maximum particle size (D) of 10mm and exponent (Ψ) of 0.5.

It was determined that PSD plays a significant role in the determining the properties of concrete. A mix that followed the PSD determined by the Fuller-Thompson (FT) equation yielded higher stability when compared to mixtures that did not, which was attributed to there being increased surface contact between the particles as a direct result of the denser distribution (Quiroga and Fowler 2003). The key properties of aggregates that affect the performance of concrete are their shape, texture but also PSD (Polat et al. 2013). The increased packing or density of the aggregate mixture has also been reported to improve concrete characteristics including; strength, stiffness and shrinkage (Richardson 2005; Sobolev and Amirjanov 2007; Vazquez et al. 2010).

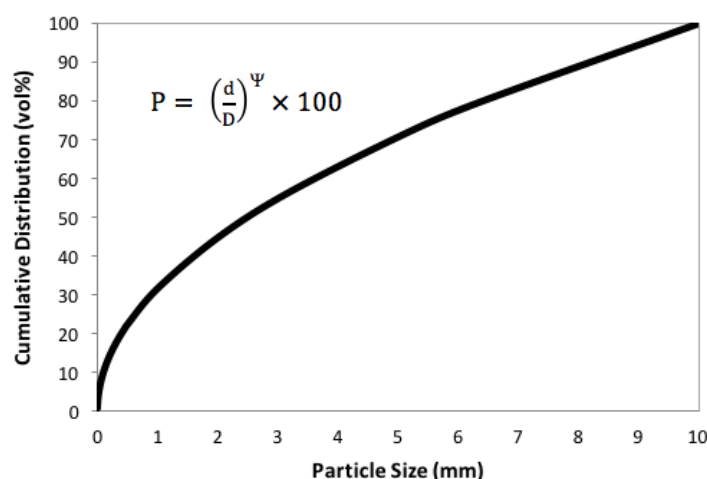


Figure 2.3 – Fuller-Thompson PSD for maximum particle size (D) of 10mm and exponent (Ψ) of 0.5

Fuller and Thompson (1907) progressed to develop the industry standards of aggregate PSD curves. The equation they presented was the same as that detailed in Equation 1. The relative simplicity to achieve the PSD determined by the FT equation with

minimum deviation paved the way to it being successfully applied in practice. Fuller and Thompson suggested for aggregates used in concrete the FT exponent (Ψ) should be between 0.45 and 0.7. The different FT exponent values accounted for allowing a constant proportion of aggregates but adapting the PSD to suit differing types of materials, as displayed in Figure 2.4. Andreasen and Anderson found that the density of the concrete increased with smaller exponent values than that of Fuller and Thompson (Zheng et al. 1990). The exponent values for densest packing in their studies were between 0.33 and 0.5. Further, Wig et al. suggested that Fuller and Thompson's conclusions could not be applied to aggregates unlike the ones used in their studies, as the FT exponents did not always give the best strength nor density (Richardson 2005). This added further to the debate on the exponent of the FT equation that best suited designing aggregates in concrete.

PSD is a material property that can be controlled in the design of the mix. Through utilising the FT equation in the design of aggregate mixtures a profound impact on several important concrete properties was proven and is the reason for the continuous application of this method. However, inconsistencies on the conclusions on a universal FT exponent (Ψ) suggests that the most accurate means to obtain the PSD for maximum particle packing density in a specific material is through experimental testing. The mixtures with PSDs created by the differing FT exponents can be assessed and the optimum performing FT exponent used in further design.

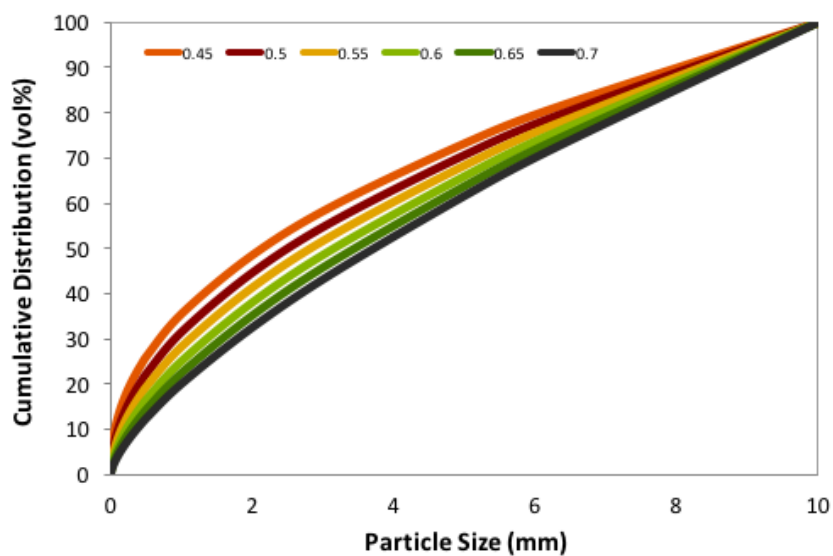


Figure 2.4 – PSDs of the FT equation with exponents 0.45 to 0.7 and D=10mm

2.1.2 Other Fuller-Thompson applications

Other applications of the FT equation have been reported since, namely in the briquetting of chrome ore fines for the smelting process (Sen et al. 2010). Briquette strength is a key property. Briquettes were created with PSDs designed at certain increments away from the FT PSD with exponent (Ψ) of 0.5. Root mean square deviation (RMSD) was used as a measure for the closeness to the FT PSD with lower RMSD values representing closer proximity. Figure 2.5 shows that as the RMSD reduced (moving closer to the FT PSD) there was an increase in hot compressive strength of the briquette. This was similarly observed for the briquette's shatter strength. The reason for improved briquette strength related back to Fuller and Thompson's concept on mixtures with the FT PSD creating the denser packing of particles and thus more particle contact points and greater strength.

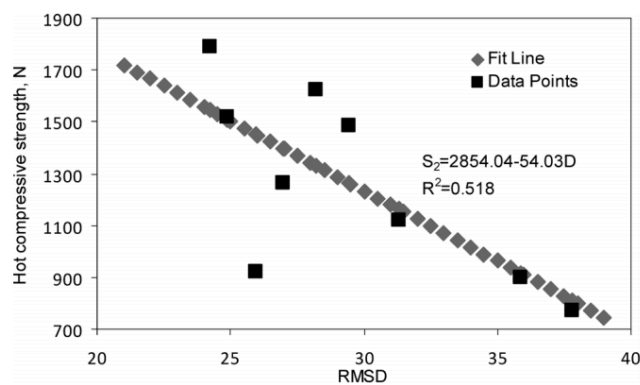


Figure 2.5 – Impact of RMSD on hot compressive strength (Sen et al. 2010)

The FT equation has also been applied to the design of bentonite and rock seals for nuclear waste repositories (Ouyang and Daemen 1991). Bentonite content and rock PSD were the factors investigated and the sealing performance in terms of mixture permeability evaluated. Two of the mixtures were designed to the FT equation with differing maximum particle sizes (D). With a 'standard' mixture an increase in the amount of bentonite from 25% to 35% enhanced the sealing performance, which was stated to be similar to the increase in performance when designing the mixture to the FT equation with an FT exponent (Ψ) of 0.5. Again, the FT equation enabled increases in material particle packing density to produce the required sealing performance which in this case had the benefit of not requiring additional bentonite binder in the mixture.

2.1.3 Summary

The original concept by Fuller and Thompson to design the PSD of materials to obtain maximum particle packing density was founded in the concrete industry. It has been applied successfully in number of studies with differing concrete types and also other industries to give improvements in material properties. Some of the enhancements have concerned strength and stability. One common factor highlighted throughout this section was developing the FT exponent (Ψ), which best suited the systems under investigation. Much focus was attributed to this area; however, it can be concluded that there was no agreement behind a universal FT exponent to create the PSD of maximum particle packing density for all materials. In most studies, PSDs were designed with differing FT exponents, similar to that shown in Figure 2.4, their performance evaluated and the optimum performing exponent used in further design.

Designing sinter blends to the FT equation is a new application of this method. As will become clearer, the granulation phase of the sintering process involves the mechanism of layering finer particles around coarser nuclei particles with the addition of water to create granules (Figure 2.6). The finer or layering part of the blend is to be designed to the FT equation. Designing the layering PSD to the FT equation will increase the density of particle packing of the layering material. It is hypothesised that this will translate to increases in sintering process productivity due to a more permeable granule bed on the sintering strand. The non-agreement of a universal FT exponent (Ψ) and new application of the FT equation means that the equation parameters (D and Ψ) that create granules with the optimum performing properties are to be determined in the first part of the study. These parameters can then be utilised in blend design in the further investigations with the comparison of blends simulating those used at Tata Steel Europe with FT blends.

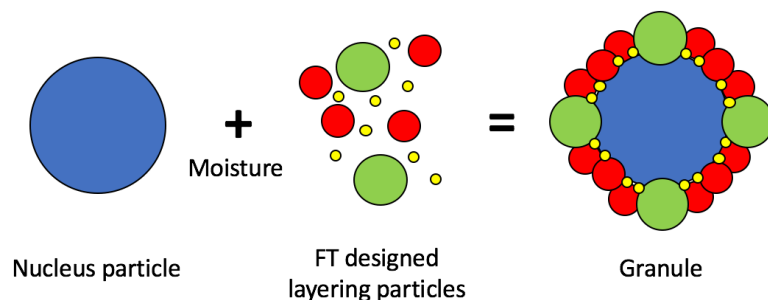


Figure 2.6 – 2D Illustration of the concept of applying the FT equation to sinter blend design

2.2 The sintering process

The sintering process is employed within iron-making to create a burden for the blast furnace from many different raw materials. It involves raising the temperature of a granule bed to around 1250-1350°C to obtain softening and partial melting (Cores et al. 2013). On cooling the material crystallises into various mineral phases and bonds the structure together to form a type of agglomerate known as sinter. The key mineral phases present include hematite, magnetite and silica-ferrites of calcium and aluminium (SFCAs) (Wang et al. 2014). The raw materials used in sinter blends include: iron ores, flux, coke breeze and recycled plant materials and are processed through a continuous mixing and granulation drum to produce granules suitable for sintering. An example of a typical sinter blend and sinter composition is shown in Table 2.1.

Table 2.1 – Composition of a typical sinter blend and sinter (Allerdice 2007)

Sinter Blend	(wt%)	Sinter	(wt%)
		Fe	55.8
Iron ore	63.8	FeO	6.5
Fluxes	13.3	SiO ₂	6.0
Coke breeze	5.2	Al ₂ O ₃	1.3
Return & revert fines	17.7	CaO	9.5
		MgO	1.9

The first continuous sinter plant was developed by Dwight and Lloyd between 1903 and 1906, which was initially for the continuous sintering of copper ore but the same principles were applied later to iron ore sintering (Ghosh and Chatterjee 2008). A complete schematic diagram of the sintering process is shown in Figure 2.7. Through recent improvements in sinter quality it has become the main blast furnace burden for iron and steelmakers across Europe and Asia (Geerdes et al. 2009).

Sinter is widely produced as it:

1. Allows the use of iron ore fines from many sources with different chemical compositions, physical properties and prices.

2. Allows the recycling of waste materials generated on-site e.g. return sinter fines and plant revert materials.
3. Has a high rate of reduction in the blast furnace.
4. Allows prior tailoring of blast furnace chemistry. Flux additions such as limestone can occur in the sintering process rather than the blast furnace to save on energy consumption.

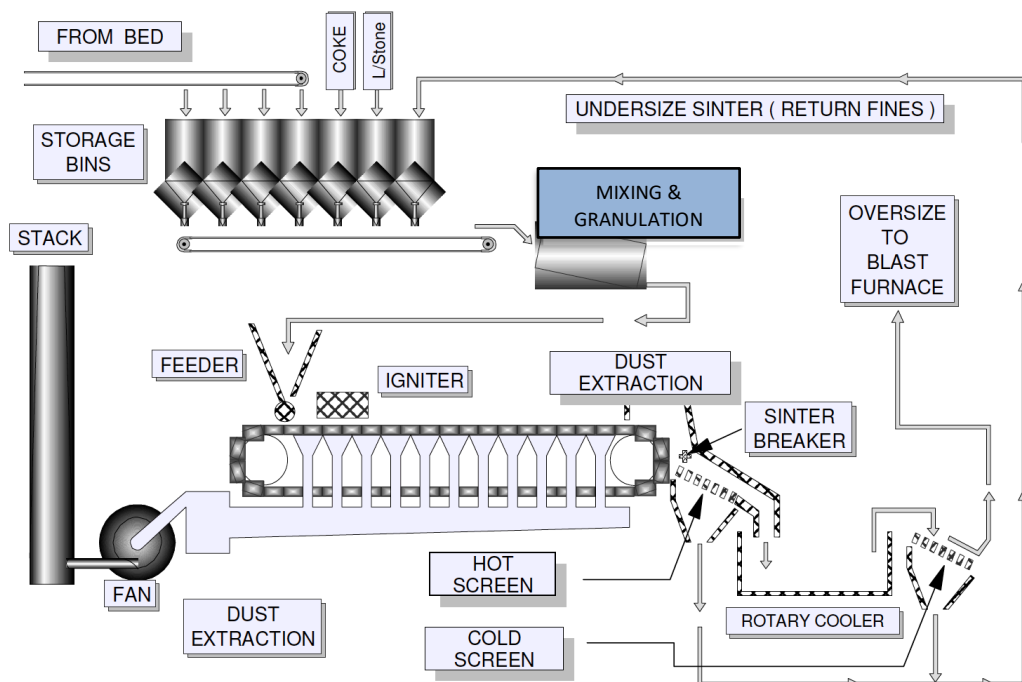


Figure 2.7 – Schematic diagram of sintering process at TATA Steel UK (Allerdice 2007)

2.2.1 Sintering process procedure

The process procedure employed to produce sinter follows the schematic diagram in Figure 2.7:

1. The iron ores, flux and revert materials are transferred from the blending bed to the sinter plant through conveyors. Coke breeze, further flux and return sinter fines are then added in plant by the dosing bunkers.

2. The blend is fed into a continuous mixing and granulation drum where they are mixed before water is added to allow granulation of the blend particles into granules.
3. The granules are charged on to the sinter strand before ignition of the top of the bed to around 1000°C by the burning of a combination of gases in the ignition hood.
4. Fans suck the heated combustion gas down through the sinter bed and the fuels (coke breeze) generate enough heat to create a flame front, which partially melts the granules together.
5. As the strand moves the flame front passes through the sinter bed. A simplified cross-sectional profile is shown in Figure 2.8. The flame front proceeds downwards through the bed until sintered.
6. Once the cooling molten sinter has travelled to the end of the strand it falls into a sinter breaker to be crushed.
7. The material is hot screened before being allowed to cool further in a rotary cooler.
8. The final porous solid sinter material is then cold screened with the oversized material going through to the blast furnace (>5mm) and the undersized material (<5mm) transferred to dosing bins for recycling through the process as return sinter fines.

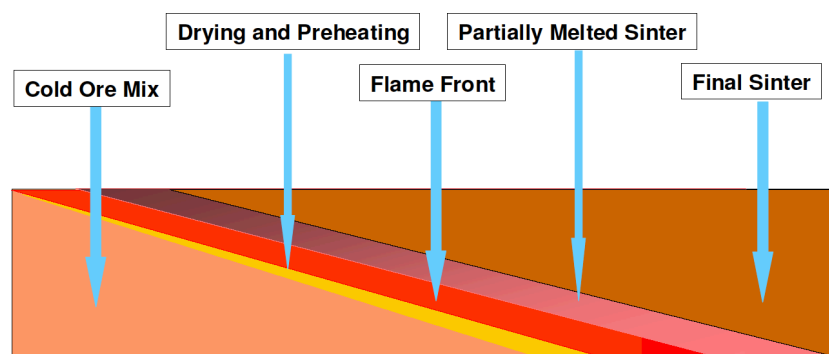


Figure 2.8 – Cross-sectional profile through sinter bed (Allerdice 2007)

2.2.2 Sinter bed permeability

Sinter beds must provide certain properties to obtain sufficient productivity from the strand. During the sintering process, heat transfer drives the flame front through the sinter bed. As the applied pressure by the fans is constant, the amount of combustion gas able to pass through the bed is a result of its permeability. Oxygen availability during the sintering process is the limiting factor behind process productivity and is directly influenced by sinter bed permeability (Umadevi et al. 2011).

The Ergun equation expresses the relationship between pressure drop and flow through packed beds (Equation 2) (Ergun 1952). This equation is dependent on several key factors including bed voidage and mean particle diameter. It has been applied in previous studies to obtain a measure for sinter bed permeability (Gan et al. 2015; Favre and Kooij 2013). Bed permeability can be calculated by determining the gas flow velocity (U) at a specific pressure drop (ΔP).

$$\frac{\Delta P}{L} = 150 \frac{\mu(1-\varepsilon)^2}{\phi^2 d_p^2 \varepsilon^3} U + 1.75 \frac{\rho(1-\varepsilon)}{\phi d_p \varepsilon^3} U^2 \quad (2)$$

where: ΔP = pressure drop (Pa) ρ = gas density (kg/m^3)
 ε = bed voidage ϕ = shape factor
 L = height of bed (m) d_p = mean particle diameter (m)
 μ = gas viscosity (Pa.s) U = gas flow velocity (m/s)

The Ergun equation shows that gas flow velocity (U) is sensitive to changes in the bed voidage (ε). If the bed voidage decreases, then this leads to a reduction in gas flow velocity and permeability for the same pressure drop. Sinter beds require sufficient bed voidage, as the combustion gas flow through the bed is limited by permeability and thus limits the speed of the process. The two forms of permeability related to sinter beds are termed 'cold' and 'hot' permeability. The 'cold' permeability relates to the bed permeability before sintering has started, thus is the permeability of the granule bed. The 'hot' permeability has received lesser focus in previous studies and is classed as the permeability of the bed during sintering. Due to numerous reactions taking place

simultaneously in the bed during sintering pressure drop regions develop and thus ‘hot’ permeability will never be greater than ‘cold’ permeability.

Ellis et al. (2007) conducted comprehensive research on the impact of iron ore properties on the ‘cold’ permeability of sinter beds. Their studies focused on PSD, moisture content and porosity. Using Japanese Permeability Units (JPU) as a replacement to the permeability determined by the Ergun equation, they developed permeability curves for several blends (B, N, Y and M). Figure 2.9 shows the quadratic trend of an initial increase in ‘cold’ permeability with increasing moisture, passing through an optimum ‘cold’ permeability before decreasing at higher moisture contents. Ellis et al. translated these findings into a permeability segment analysis curve (Figure 2.10).

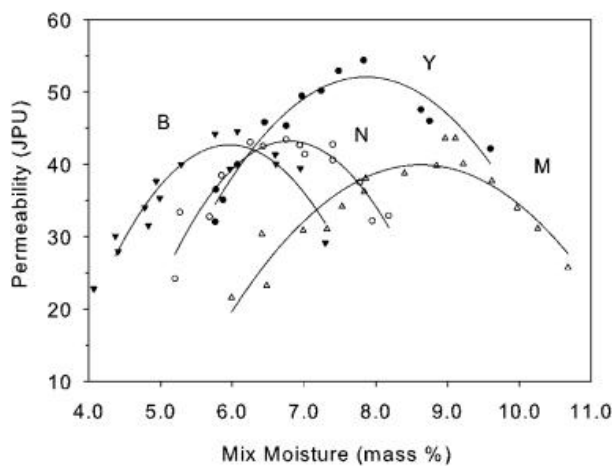


Figure 2.9 – Bed permeability as function of mix moisture for different blends (Ellis et al. 2007)

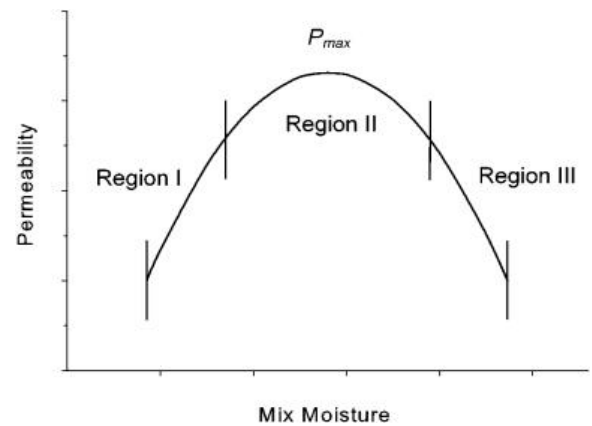


Figure 2.10 – Segmental analysis of permeability-moisture curve (Ellis et al. 2007)

In Figure 2.10 Region I shows a steady increase in ‘cold’ permeability with moisture, which was defined to be because of the narrowing in the spread of granule sizes in the distribution and increasing mean granule diameter. This continued into Region II before a maximum ‘cold’ permeability (P_{max}) was reached. A region between Region II and III at higher moistures was described where there was a decrease in ‘cold’ permeability due to bed deformation on charging. It was evident that there was differing behaviour between blends (Figure 2.9) with factors such as ore PSD and porosity having influence. This relates to the difficulty of optimising ‘cold’ permeability in practice by showing the influence of several blend properties, thus proving the requirement to monitor and control ‘cold’ permeability to maximise process capacity.

2.2.3 Sinter bed 'strength'

The ability of the granule bed to provide sufficient resistance or 'strength' to maintain permeability once on the strand is another essential property. Few studies have confronted this bed property, however, Ellis et al. (2007) linked bed 'strength' in their study on 'cold' permeability. It was stated by Ellis et al. that the layers created by the layering of finer particles around coarser nuclei particles were relatively weak and deformable. Even though moisture promoted the layering of particles it led to a weaker more deformable granule bed. Emphasising that permeability optimisation as a balance between the layering of finer particles for 'cold' permeability and bed 'strength' to maintain 'cold' permeability on the strand.

Ellis et al. (2007) studies showed that bed 'strength' showed similar behaviour to that of the 'cold' permeability curves in Figure 2.9 and 2.10. Following a quadratic trend there was a decrease in bed 'strength' (greater k_2) with increasing moisture followed by a minimum and subsequent increase at higher moistures (Figure 2.11). Again, showing that different blends exhibited differing bed 'strength' behaviour with moisture. The decrease in bed 'strength' was the same as described with the development of weaker layers at higher moistures. The increase in bed 'strength' at higher moistures was stated to be related to how the granules were charged into the equipment. It was postulated at higher moisture that the motion of charging granules caused the layers to deform upon impact and compact to fill the void spaces. Thus, during the compression test the bed began to resist deformation when lower strain values were applied which represented a less compliant bed (smaller k_2).

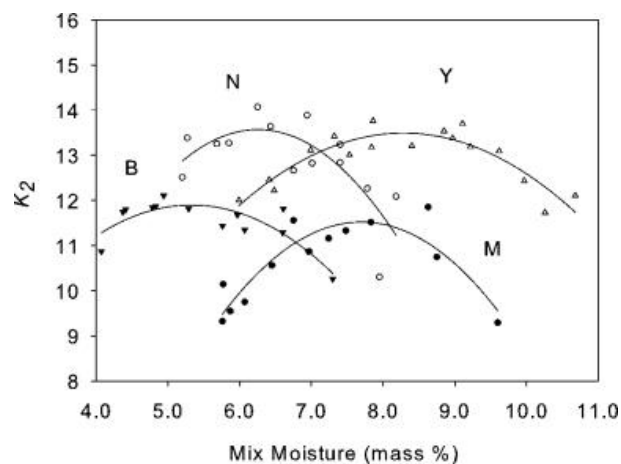


Figure 2.11 – Relationship between bed 'strength' and moisture for different ores (Ellis et al. 2007)

2.2.4 Sintering mechanisms

The agglomeration of particles by sintering is achieved by the application of heat and converts the granule bed into larger, hard, porous lumps of material (Figure 2.12). The formation of sinter is a result of the combination of the following mechanisms (Suresh et al. 2015):

- **Fusion bonding:** can also be known as slag bonding and is the partial or complete embedding of crystalline constituents in a matrix of a glassy melt (Bhagat 2007).
- **Diffusion bonding:** the recrystallization and crystal growth of mineral phases of mainly hematite and magnetite (Bhagat 2007).

The heat required for the mechanisms is generated through the combustion of coke breeze, which can enable the bed to attain temperatures of 1250-1350°C (Cores et al. 2013). The combustion of the coke breeze in the top layer is initiated through the ignition hood by the burning of combustion gases, which creates a flame front that is maintained by suction through the bed. The cross-sectional profile at a given point, as presented previously in Figure 2.8 shows several chemical and physical changes including evaporation and melting. The heat available for these reactions is dependent on the gaseous heat transfer, coke consumption and the exothermic and endothermic reactions taking place (Dawson 1992). The maximum temperature able to be achieved



Figure 2.12 – Image of sinter

in the bed therefore is mainly dependent on the quantity, location and combustibility of the fuel (Geerdes et al. 2009).

2.2.5 Sinter mineralogy

Sinter is a heterogeneous material with various mineral phases present. The most prominent of which are (Geerdes et al. 2009):

- **Primary and secondary magnetite (Fe_3O_4):** where secondary magnetite is formed in the high temperature, reducing areas of the bed.
- **Primary and secondary hematite (Fe_2O_3):** where secondary hematite is formed in the cooling regions of the bed in the presence of oxygen.
- **Silica ferrites of calcium and alumina (SFCAs):** produced from the flux and iron oxide constituents.

Figure 2.13 identifies the various mineral phases that are present in sinter. The increase in basicity of the sinter ($\frac{\text{CaO}+\text{MgO}}{\text{SiO}_2}$) increases the amount of calcium ferrites contained. This impacts the sintering process through the temperatures at which the first melt is produced. Less basic sinters have a higher melt temperature than higher basicity sinters, which is due to calcium ferrite structures having a melt temperature as low as 1200°C (Geerdes et al. 2009). Sintering is complete at lower temperatures for more basic sinter blends when compared to less basic sinter blends. The lower temperatures in sintering with higher basicity sinters can mean large ore particles in the mix remain partially unreacted in the product. For this reason, less basic sinters are generally coarser and have a higher cold strength than basic sinters (Geerdes et al. 2009). This implies that a compromise must be obtained in plant operations between the required basicity of the sinter for the blast furnace but also the sinter's cold strength. Cold strength, which is introduced in Section 2.2.6 concerns the degradation of sinter on handling to produce return fines which must be recycled through the process reducing net process productivity.

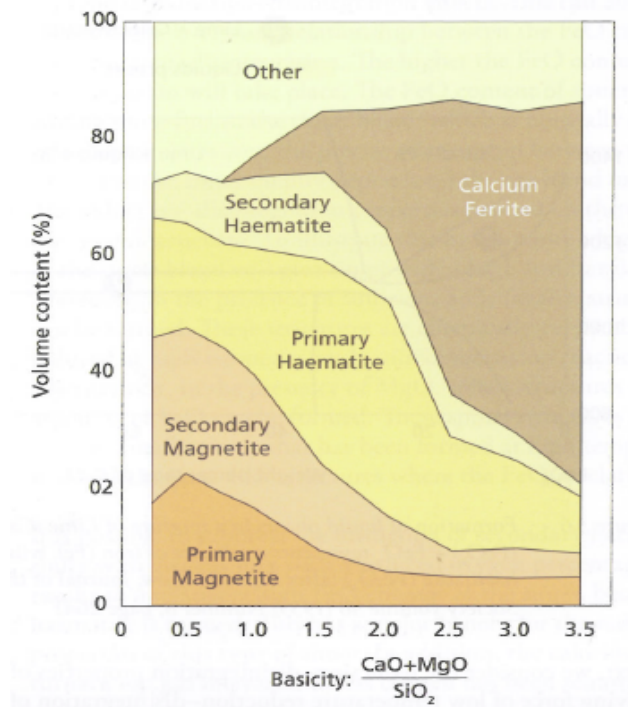


Figure 2.13 – Phase composition of sinters (Geerdes et al. 2009)

2.2.6 Sinter properties

There are certain properties that sinter must possess to be an effective blast furnace burden. Table 2.2 summarises the properties but the most important are as follows:

1. **Size distribution:** Usable sinter as a blast furnace burden is between 5-40mm and is screened at the sinter plant (Harsha Nistala et al. 2015). However, on transportation sinter can degrade (cold strength) so is rescreened at the blast furnace to remove any further undersized material (<5mm). The undersized material is returned to the sinter plant as return sinter fines.
2. **Cold strength:** characterises sinter degradation during transport and handling to the blast furnace. The cold strength of sinter has an influence on process productivity, as sinter with a low cold strength results in a high return fines rate and a reduction in net productivity.
3. **Reduction-disintegration index (RDI):** The reduction from hematite to magnetite in the blast furnace generates internal stresses in the sinter (Geerdes

et al. 2009). This causes sinter to break-up and produce finer material in the furnace, which can impact gas flow. Stronger sinters with higher RDI values have greater resistance to these stresses.

4. **Chemical properties:** Sinter incorporates a wide range of chemicals, however the foremost to consider are iron and the chemicals that contribute towards basicity. Sinter must possess a high total iron content (approximately Fe=50-60%) (Allerdice 2007). Basicity is the ratio of basic to acidic components and can be narrowed down to $\frac{\text{CaO}+\text{MgO}}{\text{SiO}_2}$. The basicity of the sinter is tailored to suit the required chemistry in the blast furnace. Limits are also set for the amount of gangue materials in the sinter such as phosphorous (P) and zinc (Zn), as these can cause issues further down the iron and steelmaking chain.

5. **Reducibility:** Reducibility is the ease that oxygen is removed from the sinter. The importance of the sinter reducibility is its effect on the fuel required in the blast furnace (Giorgio et al. 2011). Less reducible sinters require more heat and reducing gas (CO) and increases the amount of fuel (coke and injection coal) necessary to be inputted into the furnace.

Table 2.2 – Summary of sinter properties

Sinter property	Details
Size distribution	5-40mm size range. Fines below this size are recycled as return sinter fines.
Cold strength	Must possess certain cold strength during handling to minimise the return fines rate.
Reduction-disintegration index (RDI)	Cannot produce too many fines on reduction, as this impacts gas flow in blast furnace.
Chemical composition	Iron content and required basicity. Limits set to amount of gangue materials e.g. P and Zn.
Reducibility	Must possess certain reducibility to minimise blast furnace fuel rates.

2.2.7 Summary

The sintering process is an intricate process that converts a wide-range of materials into a suitable blast furnace burden with several key properties. Sinter blend materials are mixed and granulated to create granules, which are charged onto the sintering strand and sintered. The mixing and granulation phase is the main phase of focus in this study, which is employed to narrow the particle size distribution (PSD) spread of the raw materials in the blend through the addition of water to create a more permeable granule bed on the strand. This is achieved by utilising a continuous rotating drum. Sinter bed permeability was emphasised as a key property. Increased permeability allows increased sinter productivity, as the combustion gases and flame front can pass through the bed faster. Closely connected was sinter bed 'strength', which is the ability of the bed to resist deformation. Beds must maintain their integrity once on the strand so as not to collapse and reduce permeability. It has been stressed that the bed must therefore also provide 'strength' or resistance to permeability losses once on the strand, which is often a neglected bed parameter.

The chemical and mineralogical composition of the sinter blend constituents in combination with the reaction mechanisms results in sinter having distinct characteristics. Sinter must possess several certain qualities to be able to be used as an effective blast furnace burden. The chemical composition of sinter is designed on the desired blast furnace chemistry. The iron content and basicity ($\frac{\text{CaO}+\text{MgO}}{\text{SiO}_2}$) of sinter are the most important components. Sinter must have sufficient reducing properties in the blast furnace, as this directly impacts fuel rates. Sinter must be strong enough to resist break-up due to the stresses encountered through reduction (RDI) so as to not to affect gas flow in the furnace. Required volumes of sinter must be produced of a certain size distribution (5-40mm) and the return fines rate (cold strength) minimised to maximise net process productivity.

2.3 Sinter blend raw materials

Sinter, pellets, lump ore, coal and coke are used as a blast furnace burden with sinter, which can be up to 70% of the total burden (Ghosh and Chatterjee 2008) comprising of iron ores, coke breeze, flux, revert materials and return sinter fines. The raw materials used in sinter blends are evaluated individually in this section.

2.3.1 Iron ores

Iron is one of the most abundant metallic elements worldwide. Its oxides, or ores, compose about 5% of the earth's crust (World Steel Association 2017). The average iron content for ores is between 60-70%, which varies with differing ore mineralogy (Australian Government 2015). Worldwide iron ore resources are estimated to exceed 800 billion tonnes, containing 230 billion tonnes of iron (U.S Geological Survey 2003). Iron ore is mined in around 50 countries worldwide with the largest operations conducted in Brazil, Australia and China (Minerals Council of Australia 2015). Figure 2.14 gives a graphical representation of global iron ore production in 2009, which hasn't changed significantly to this date. It can be observed that the world iron ore production is dominated by only a small number of countries.

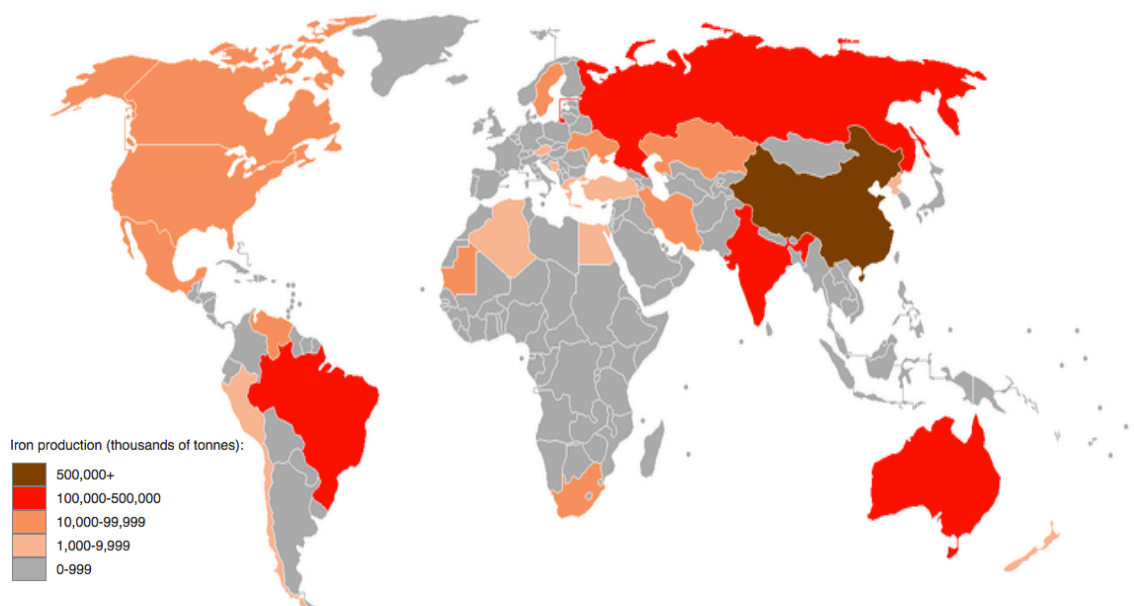


Figure 2.14 – Global iron ore production 2009 (U.S Geological Survey 2017)

Iron ores in sinter blends

A typical sinter blend, as shown in Table 2.1 consists of 63.8% iron ore (Allerdice 2007). Sinter can consist of up to 70% of the total blast furnace burden (Ghosh and Chatterjee 2008). These two points illustrate the importance of iron ore to the iron-making process. With the sinter blend comprising of a mixture of iron ores it is essential that the correct ores are purchased to give the desired chemical and physical composition of the sinter. Not one iron ore makes the desired sinter characteristics but a selective blend does. In addition, optimising the price of different ores in the blend is an essential business requirement, which is achieved by the balancing of commercial, geographical and sourcing risks.

The iron ores that are used in the sintering process can be categorised as follows:

- **Sinter feeds:** these ores are categorised by their wide size distribution of particles where particle sizes range from microns up to 20mm. Brazil, Australia and South Africa produce several sinter feed ores with differing chemical compositions. Brazilian sinter feeds are more chemically neutral than Australian and South African feeds, as they generally contain lower silica (SiO_2), alumina (Al_2O_3) and alkali proportions. Australian feeds tend to have higher levels of silica and alumina whereas South African feeds have higher alkali levels, which limits their usage due to issues further in the iron and steelmaking chain (Allerdice 2007). An example of a sinter feed is Carajas, which is produced by Vale (CVRD) on the North-East coast of Brazil.
- **Concentrates:** These ores have undergone the beneficiation or flotation process to improve the concentration of iron and remove impurities (Australian Government 2015). Concentrated ores are finer than sinter feed ores with generally 100% particles <1mm. Thus, they have a narrower size distribution of particles than sinter feeds. Because of these characteristics, they are acknowledged to be the least costly type of sintering iron ore. However, issues with processing large proportions of concentrated ores in sinter blends have

limited their use at present. An example of a concentrated ore is Mo-I-rana, which is produced by Rana Gruber in Norway.

- **Pellet feeds:** Like concentrates, pellet feeds have undergone the beneficiation or flotation process to improve the concentration of iron and remove impurities (Australian Government 2015). The particle classification method after the beneficiation process is where these ores differ from concentrates. Pellet feeds are the finest type of iron ore (typically 100% <0.5mm) and thus also have a narrow size distribution of particles. Due to these characteristics pellet feeds are more widely used in the pelletising process, however they can also be utilised in sinter blends. An example of a pellet feed is Sydvaranger, which is produced by Sydvaranger Gruve in Norway.

The main types of iron ore that are mined have mainly hematite (Fe_2O_3) or magnetite (Fe_3O_4) mineralogy. Most hematite ores are mined in Brazil and Australia, which are also large contributors to global magnetite mining, however Russia and Sweden also contribute (Iron Investing News 2016; ITP Mining 2013). The key difference between the two ore types is the iron content (Fe_{Total}). Hematite ores have a higher iron content, which can be up to 64%. Magnetite ores have a lower iron content due to the presence of impurities in the ore when found in the earth (25-40%) (Iron Investing News 2016). Magnetite ores therefore all undergo an additional beneficiation process. Once the ore has been extracted, crushed and screened the magnetic properties of the ore can be used to extract the magnetite and produce a concentrated product.

All iron ores contain impurities. The most noticeable are the slag forming impurities silica (SiO_2), alumina (Al_2O_3), lime (CaO) and magnesia (MgO) (Somasundaran and Moudgil 1987). The liquid slag produced in the blast furnace is measured through its basicity, which is the ratio of bases (CaO and MgO) to acids (SiO_2) ($\frac{\text{CaO}+\text{MgO}}{\text{SiO}_2}$). Alumina (Al_2O_3) is often regarded as a neutral agent (Strauss 1970). As most ores have an excess of silica and with coke used as a fuel in the blast furnace then basic flux is added in the sinter blend to produce sinter that creates the correct chemistry in the blast furnace.

Global iron ore market

Since the start of the 21st century the rapid development of China has altered the world's demand patterns for iron ore. The 'boom' in demand by China was a result of the substantial increase in materials required from the construction of infrastructure and the growth of urban areas. During this 'boom' prices for iron ore substantially increased from an historical average of around \$60 per tonne to peak at around \$190 per tonne in 2011 (Marsden 2014). The progression of the global iron ore prices from 2012 to 2014 are shown in Figure 2.15. Figure 2.15 shows the quarterly average spot prices given by Platts, which is the world's source for iron ore prices.

The higher prices paid for iron ores in 2011 attracted new suppliers to the market and caused established suppliers to increase their capacities. Greater amounts of iron ore were available; however, this was at the same time as China's demand started to reduce (Marsden 2014). Combining the increased production and reduced demand meant the iron ore price decreased. This hit a 5-year low in 2014 to less than \$80 per tonne as stated by Platts in Figure 2.15. This was a substantial drop when compared to more than \$130 at the start of 2014.

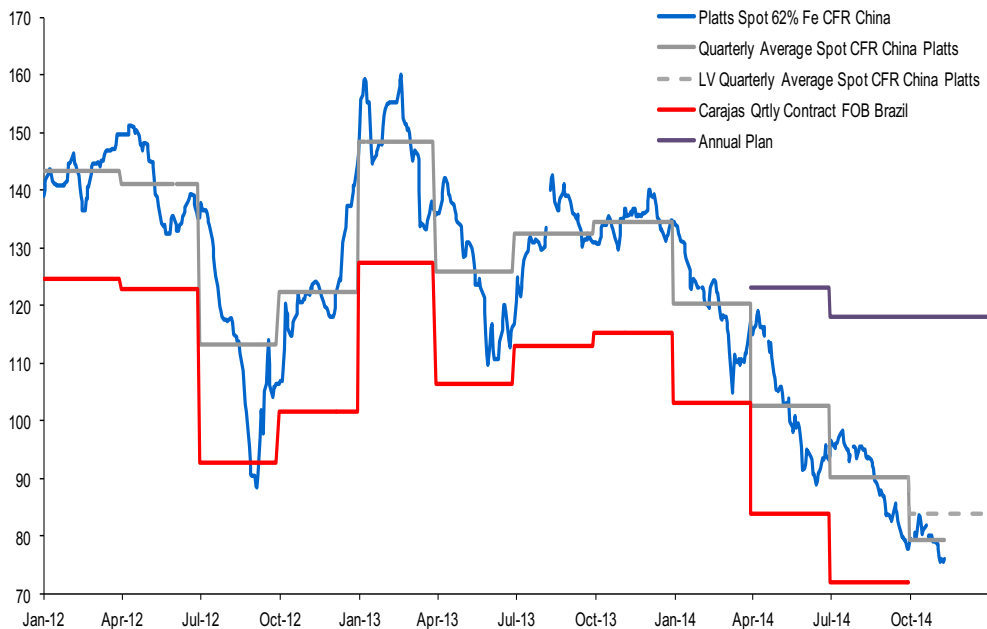


Figure 2.15 – Global iron ore prices for 2012 to 2014 (Marsden 2014)

Looking at the global iron ore market from the perspective of a European iron-making company like Tata Steel, then another aspect to consider has been the ability to secure iron ore as a raw material. Over the years, the financial viability of conventional sinter feeds from countries such as Australia has reduced and is primarily due to the 'boom' in production in China resulting in a large proportion of iron ore being taken there (The Economist 2014). Due to the geographical location of Europe being further from the major iron ore supplying countries the transport cost of the materials places further pressure on the global iron ore sources that are financially viable. European iron-makers have therefore been driven to incorporate greater proportions of cheaper ores (concentrates and pellet feeds) in their sinter blends to minimise raw material costs. As iron ores compose a large percentage of raw material costs then there is the on-going requirement to explore methods to increase the proportion of concentrated and pellet feed ores in their sinter blends.

2.3.2 Coke breeze

Coke breeze is the most widely utilised sintering fuel and provides the heat source for the process (Bhagat 2007). Coke breeze is a finer sized form of coke and is known for having high carbon and heat content and therefore is readily used in sintering (Mohamed et al. 2010). A typical sinter blend contains around 5% coke breeze (Table 2.2) (Allerdice 2007), which is sufficient to raise the temperature in the bed to between 1250-1350°C (Cores et al. 2013). The ability to achieve high sintering temperatures is due to the pre-heating of the combustion gas by the hot sinter above the flame front (Zhou et al. 2015). At the bed surface this cannot be achieved so the coke breeze is ignited through the ignition hood by the burning of combustion gases with the flame front being maintained by suction through the bed.

2.3.3 Flux

Flux is used in the sintering process to enable an energy efficient means to create the correct slag composition in the blast furnace (Allerdice 2007). Fluxes that can be utilised in sintering are limestone, dolomite and olivine with the chemical composition

of each shown in Table 2.3 (Tata Steel Europe 2016a). The flux will be selected mainly based on their silica (SiO_2), alumina (Al_2O_3) and alkali contents to tailor the sinter chemistry for the blast furnace. However, some flux additions such as burnt lime can also increase the rate of sintering. Burnt lime enhances the permeability of the bed by promoting granulation and permeability, thus increases sintering process productivity (Satyendra 2013).

Table 2.3 – Chemical composition of sinter blend flux (Tata Steel Europe 2016a)

Material	Fe	CaO	SiO ₂	MgO	Al ₂ O ₃	Mn	ZnO	Alkalis
wt%								
Limestone	1	52	2	1.3	0.5	0.07	0.003	0.06
Dolomite	1	33	1	18	0.3	0.06	0.002	0.07
Olivine	6	0.6	41	48	0.8	0.07	0.002	0.03
Burnt Lime	0	96	0.3	0.5	0.2	0	0	0

2.3.4 Plant reverts

Revert materials are produced from many different activities at integrated steelworks and the sintering process enables the recycling of these into a blast furnace burden. Reverts are usually in the form of ravellings, mill scale, basic oxygen steelmaking (BOS) slag, sludge and flue dust. It is not effective to evaluate these materials individually but the proportion of reverts used in sinter blends is varied and tends to be designed on the amount of these materials available at plant. Table 2.4 presents the more common revert materials found at integrated steelworks (Tata Steel Europe 2016b).

One limiting factor to the revert proportion in blends is chemical composition. Reverts are composed of a wide range of chemicals but it is the alkalis that can cause downstream process problems if their level is too high in sinter. Once alkalis are charged via the burden into the blast furnace then it is difficult for them to be removed (Besta et al. 2013). These can accumulate in the upper part of the furnace and form scaffolds on the inner walls (Jak and Hayes 2012). It is therefore a requirement to consistently monitor and adjust the blend revert composition to adhere to the specific alkali levels in the sinter as to not adversely affect blast furnace operation.

Table 2.4 – TATA Steel UK revert plant materials (Tata Steel 2016b)

Revert	Plant source
Betsi sludge	Blast furnace scrubbing system
Mill scale	Hot strip mill
Flue dust	Blast furnace flue dust system
BOS slag	Basic oxygen steelmaking (BOS) slag
Ravellings	Across plant

2.3.5 Return sinter fines

Return sinter fines are produced during crushing, cooling and in transportation to the blast furnace due to sinter's brittle nature. Too many fine materials inputted into the blast furnace causes issues with gas flow (Klinger et al. 2010). Therefore, return sinter fines are recycled in the sintering process to be reused as part of the blend. Not only is this a route to reuse otherwise waste materials but the size distribution of the return sinter fines is relatively coarse when compared to the sinter blend materials and offers effective nuclei particles in the granulation phase of the process.

The minimisation of return sinter fines is of importance to process efficiency, as this impacts net process productivity and lowers the cost per tonne of sinter produced (Van den Berg 2008). Return sinter fines are produced in the following ways:

1. The top layer of sinter on the strand is weakened due to the temperature difference when leaving the flame front.
2. Incomplete sintering on the side of the strand due to insufficient heat transfer.
3. Fines produced during sinter crushing and transportation (cold strength).
4. Thermal stresses that lead to the formation of cracks.

2.3.6 Summary

The sintering process was established to transform a wide-range of materials into an effective blast furnace burden. Iron ore is the major contributing factor (approximately 65%), which is focused on in this study. The many differences in iron ores include their PSD, chemical composition and mineralogy. The diversity in the iron ores utilised by iron-makers has increased due to the reduction in the financial viability of utilising conventional iron ore sinter feeds. This was primarily a result of economically 'booming' countries increasing demand. To reduce the impact on sinter raw material costs European iron-makers like Tata Steel have been required to explore other ore options such as concentrated ores rather than the typical sinter feed ores. The characteristics of concentrated ores mean that they are not as high in demand as more common sinter feed ores from Australia and Brazil, thus are generally cheaper with less volatile prices. This is primarily due to their composition and specifically their PSD not being so favourable for use in the sintering process, as they are finer and have a narrower spread of particle sizes.

The other sintering process raw materials have received lesser focus. In summary, coke breeze, flux, reverts and sinter return fines all serve a purpose in the sintering process. Coke breeze is the fuel when combusted and the flux provides an energy efficient means to adjust blast furnace chemistry. Reverts and return sinter fines are incorporated to recycle plant waste materials. The economic drivers for this study encompasses the iron ore proportion of sinter blends, thus iron ore is the only varying material under investigation.

2.4 Granulation process

In general terms granulation is a size enlargement process that converts smaller particles into larger agglomerates often known as granules. Many industries require the narrowing of particle size distributions (PSDs) through granulation including pharmaceuticals, fertilizers and iron ore processing, as granules are known to (Wauters 2001):

1. Prevent segregation.
2. Improve flow properties.
3. Reduce dusting.
4. Improve appearance.
5. Unify the composition.

The mechanism of how granules are produced is illustrated in Figure 2.16. Granulation occurs when a bed of solid particles is agitated by mixing in the presence of a liquid phase where the tumbling motion results in collisions between particles, which stick or coalesce together (Walker 2007). There are a range of granulating devices available, which have their specific applications including high-shear and fluidized bed granulators. However, it is the drum granulation process that is concerned with the production of granules for the sintering process.

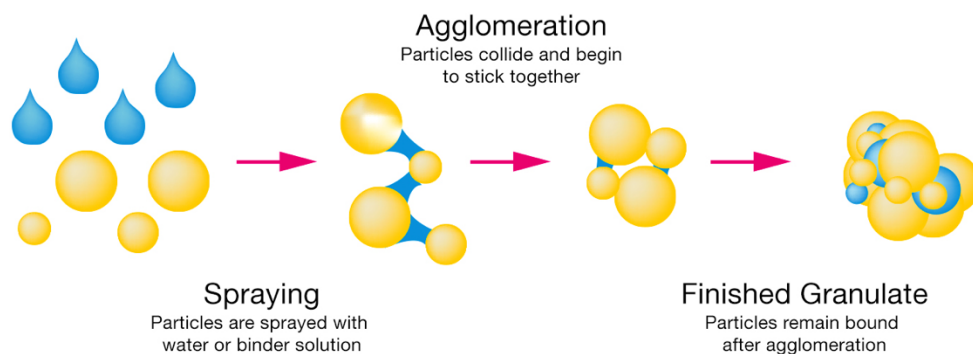


Figure 2.16 – Diagram of granulation process (Fluid Air 2013)

2.4.1 Key early granulation studies

Newitt and Conway-Jones (1958) studied the influence of certain process parameters such as moisture content and particle size distribution (PSD) on the growth behaviour of granules. Initially, they reported that effective granulation only occurred between a minimum and maximum moisture content. Above the maximum moisture content, the growth rate was uncontrollable and produced a 'slurry' of granules. Below a minimum moisture content, only a small amount of weaker larger granules were produced. Increasing moisture between the minimum and maximum resulted in a higher granule growth rate. The effect of PSD on granule growth was related to the ability of the feed particles to deform and bond on impact. Finer particles exhibited less growth at the same moisture contents when compared with larger particles. Growth was therefore inversely related to the mean feed particle size, as finer particles were stated to be less deformable when compared to the larger particles.

Capes and Danckwerts (1965) also targeted the description of growth during granulation. They described a 'nucleation' growth phase as the moisture was added. The rolling action in the drum caused the particles to collide and compact. When enough water was present, the granules became surface wet and had a degree of plasticity, deformed on impact and started to grow. At a certain granule size, the mechanism transferred from random coalescence growth as mentioned to a crushing and layering mechanism. On collision, the smaller granules were crushed and layered onto the other granules, which was proved through using different colour particles and examining the granule structure.

Iveson and Litster (1998) developed growth models. Two growth models were proposed to occur during granulation and are shown in Figure 2.17. Firstly, 'steady' growth, which was said to arise when the system was highly deformable and the granule size increases steadily with time. As moisture content increased the rate of growth increased. Secondly, a growth labelled 'induction' growth, which occurred in systems with low deformability and can be compared to that described by Capes and Danckwerts (1965) as 'nucleation'. No growth behaviour was observed at the start of the process. Growth took place when the particles were surface wet by moisture being

driven to the surface through compaction. Increasing the moisture content was stated to reduce the length of 'induction' growth. A summary of the key granulation studies is shown in Table 2.5.

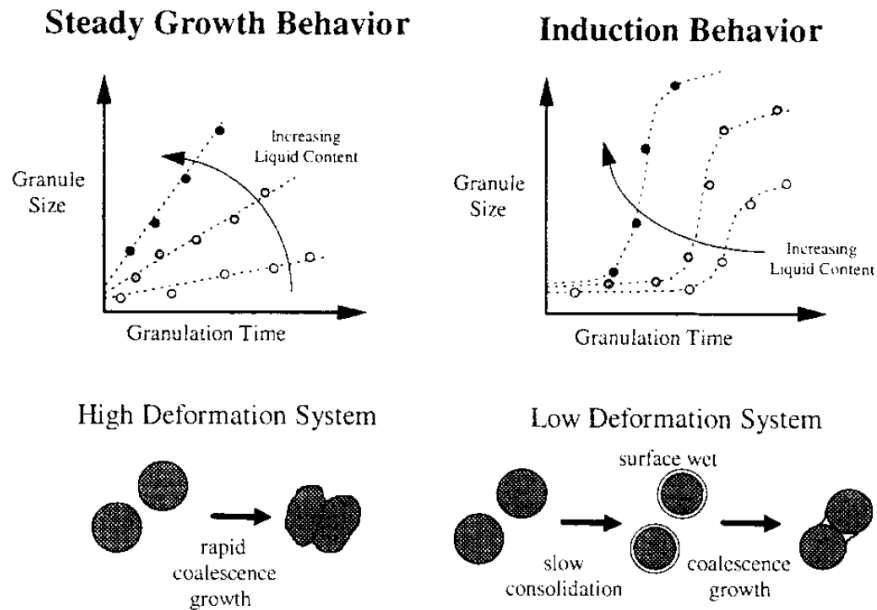


Figure 2.17 – Granulation growth models proposed by Iveson and Litster (1998)

Table 2.5 – Summary of key early granulation studies

Reference	Parameters studied	Comments
Newitt and Conway-Jones	Moisture content, PSD	Growth rate related to the size of the particles and a result of particle deformability.
Capes and Danckwerts	Moisture content	Growth mechanism changes throughout process. 'Nucleation' when moisture was added, where particles compact to become surface wet. Moisture gives degree of plasticity, which allows granule to then deform and grow.
Iveson and Litster	Moisture content	'Steady' growth in deformable systems where granule growth increased with time. 'Induction' growth in less deformable systems with no initial granule growth, as granules need to compact to become surface wet.

2.4.2 Granulation in the sintering process

Drum granulation is one of the most widely utilised granulation processes. The continuous drum granulation process is widely used in the iron ore or sinter blend processing industries. The first commercial continuous drum granulators were established in the USA in the 1930's by Dwight and Lloyd for the agglomeration of iron ore composites (Litster and Ennis 2004). The mixing and granulation phase is located prior to the sintering phase, which can be identified in Figure 2.7.

The initial objective is to mix the sinter blend in the drum without the addition of water. The mixed material is then granulated through the addition of water further into the drum to create granules. A schematic diagram of a typical continuous drum granulator is shown in Figure 2.18. The drum is angled to allow the continuous movement of material through the drum. A rotary scraper bar removes wet material from the drum walls, which would normally affect the rolling action and reduce the active volume of the drum (Litster and Ennis 2004). The granulated material exits the drum through a chute before being charged onto the sinter strand via a roll feeder.

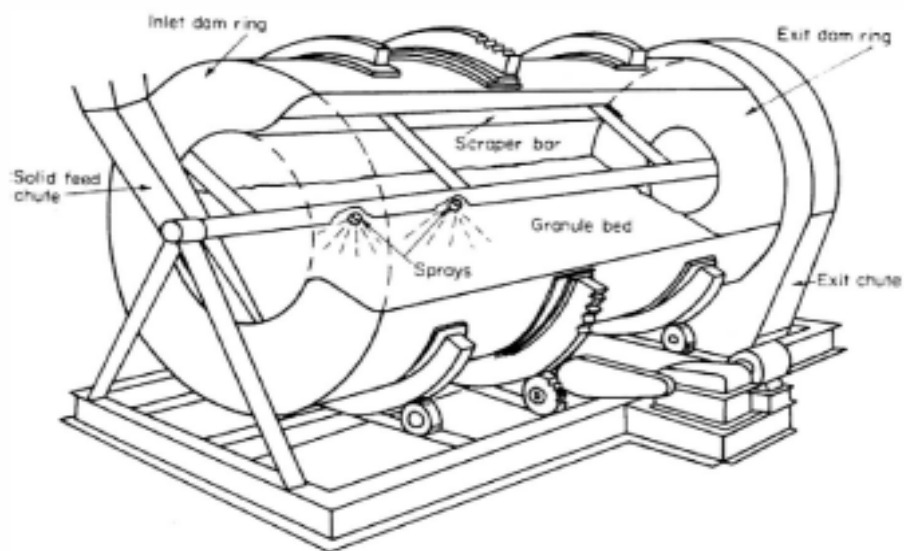


Figure 2.18 – Continuous drum mixer and granulator (Litster and Ennis 2004)

The tumbling or cascading action of the bed enables the layering of finer particles around coarser particles named nuclei. An example of this mechanism, which was presented by Litster and Waters (1988) is illustrated in Figure 2.19. This is similar to the

mechanism presented in the first part of this subsection (Figure 2.16). However, in the granulation of sinter blends the wider PSD of materials (up to 20mm) favours the mechanism of layering finer particles around coarser nuclei particles (Figure 2.19 and 2.20). This is compared to systems that include only a narrow PSD of finer particles such as in the pelletizing of iron ores or pharmaceutical powder processing, as these systems prefer the ‘balling’ granulation mechanism shown in Figure 2.16.

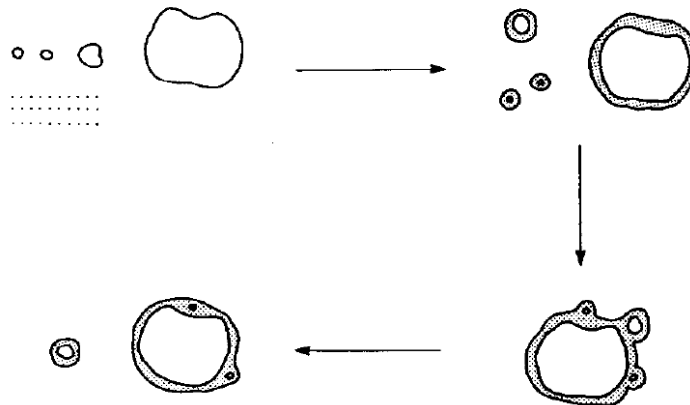


Figure 2.19 – Iron ore sinter blend granulation mechanism presented by Litster and Waters (1988)

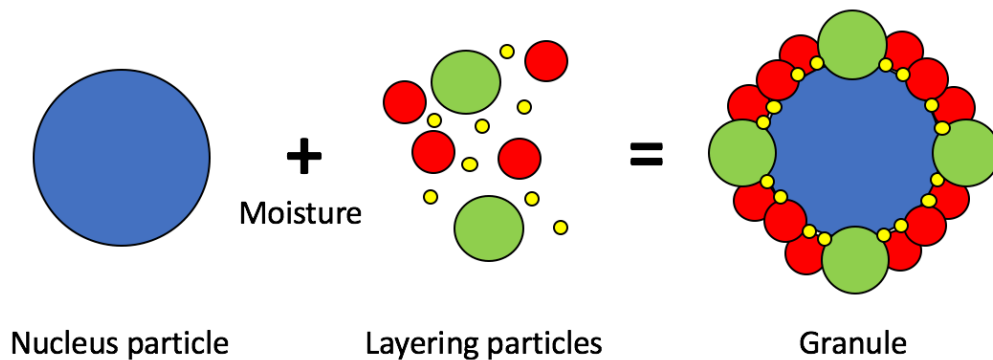


Figure 2.20 – 2D illustration of the creation of granules by the layering of finer particles around a nucleus with moisture

2.4.3 Summary

It can be concluded that there are certain complexities behind the growth mechanisms in the drum granulation process. The earlier drum granulation studies (Section 2.4.1) provided fundamental explanations to the behaviours witnessed, which included

several attempts to classify these behaviours into mechanisms and generated valuable knowledge as the foundation for further work.

Additional studies by Iveson and Litster (1998) combined the knowledge from the earlier studies to model growth behaviours (Figure 2.17). To briefly summarise they proposed that growth depended on the deformability of the particles in the system. 2 growth models are possible, 'steady' growth in systems with particles with high deformability and 'induction' growth in systems with particles which initially have low deformability. In 'steady' growth granules grow linearly with time, whereas 'induction' growth required time for the granules to become surface wet by compaction before growth initiated. From the literature reviewed in this section the explanations offered by Iveson and Litster are thought to be the most comprehensive and are classed as the basis for granule growth in systems.

Granulation in the sintering process involves wider PSDs where particle sizes can range from microns up to 20mm. The granulation mechanism favours the layering of finer particles around coarser nuclei particles (Figure 2.19 and 2.20), which is unlike the more narrowly distributed systems investigated in the studies presented in this section. The drum granulation mechanism converts the wider spread of particle sizes in the sinter blend materials into more narrowly size distributed granules, which increases the bed permeability on the sintering strand. The mixing and granulation of sinter blends is the primary phase under investigation in this study, thus further focus is required on the key parameters that impact this process in the next section.

2.5 Parameters influencing granulation in sintering

2.5.1 Particle size distribution

Particle size distribution (PSD) has a profound impact on the granulation process. Many researchers in the earlier stages of granulation research used materials with narrower PSDs to study the extent of granulation. The PSDs in the mixing and granulation of sinter blends are wider, where the PSD of the blend materials overlaps the granule size distribution (GSD) that is produced. This section introduces the key granulation studies with regards to sinter blends and specifically iron ores.

Litster and Waters (1988) were the founding researchers to tackle the granulation of the wider PSDs in sinter blends. Litster and Waters focused more specifically on the influence of iron ore properties including the type and PSD of nuclei and fine or layering particles. They proposed a measure of granulation effectiveness called $X_{0.5}$, which is based on a partition coefficient (α_i) (Equation 3). During granulation, finer particles are layered around coarser particles, however there will be certain particle sizes which can act as both layering or nuclei particles, referred to as 'intermediate' particles. Thus, the partition coefficient (α_i) was based on the ratio of a specific particle size acting as a nucleus to acting as a layering particle (wt%). Figure 2.21 shows this concept at different moisture contents. If $\alpha_i = 1$ then all particles of that size act as nuclei and if $\alpha_i = 0$ all particles of that size act as layering particles. $X_{0.5}$ was based on the partition coefficient (α_i) when equal to 0.5 and specified the particle size where half of the particles act as nuclei and half as layering particles. If $X_{0.5}$ was larger, then this signified a larger particle size where half of the particles in the blend acted as nuclei and half as layering particles and signified a greater extent of granulation. The key attribute of the partition coefficient (α_i) is that it provides a means to compare the granulation ability of blends with different PSDs and densities.

$$\alpha_i = \frac{m_{ij} + m_{ij+1}}{\sum_{j=i}^n m_{ij}} \quad (3)$$

where: α_i = partition coefficient

m_{ii} = mass of particles of size fraction i in granule size fraction I (kg)

m_{ij} = mass of particles of size fraction i in granule size fraction j (kg)

The influence of PSD alone on $X_{0.5}$ was complicated. Primarily, when increasing the total proportion of layering particles (<0.25mm) but keeping the PSD the same it was found that $X_{0.5}$ decreased at equal moisture contents (Figure 2.22). On the other hand, as the proportion of layering particles increased more moisture was required to achieve a specific $X_{0.5}$ size. This was due to the amount of moisture (W_g) required to achieve the same extent of saturation (S_1) in the feed particles increasing, which was attributed to the volume of layering material (V_{pl}) having an inverse influence on the extent of saturation (S_1) (Equation 4).

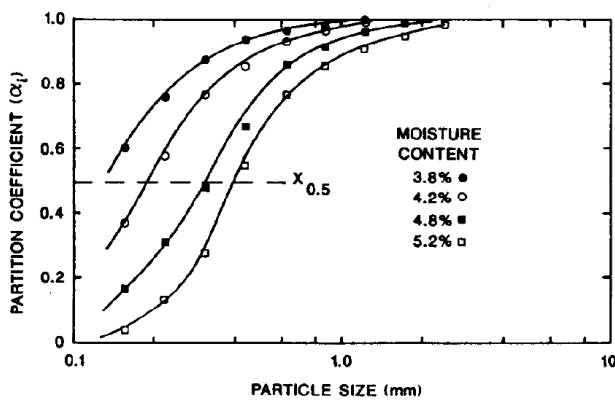


Figure 2.21 – Litster and Waters (1988) partition coefficient (α_i) with particle size

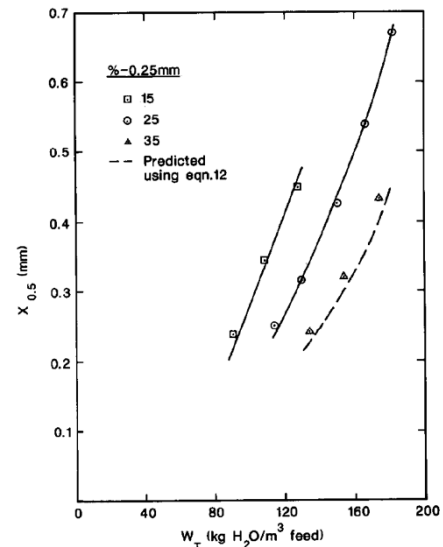


Figure 2.22 – The effect of the proportion of layering particles on $X_{0.5}$ (Litster and Waters 1988)

$$S_1 = \frac{1 - \epsilon_1}{\epsilon_1} \frac{W_g}{\rho_{H_2O} V_{pl}} \quad (4)$$

where: S_1 = saturation of layer

ϵ_1 = layer porosity

W_g = water available for granulation ($\text{kgH}_2\text{O}/\text{m}^3$)

ρ_{H_2O} = density of water (kg/m^3)

V_{pl} = volume fraction of layering particles

When looking further into the influence of layering PSD on $X_{0.5}$ the overall proportion of layering particles was kept constant and the PSD varied. Figure 2.23 identified the effect of adding different proportions of ‘very’ fine particles (mass mean diameter = 0.009mm) to alter the layering PSD. Decreasing the mean particle diameter produced an increased $X_{0.5}$ at equal moisture. This contrasts with increasing the proportion of layering particles (<0.25mm) decreasing $X_{0.5}$ for a given moisture content (Figure 2.22). This proves that to predict $X_{0.5}$ or any extent of granulation an accurate PSD of the fine or layering particles is also essential as well as the layering to nuclei particle proportions. This highlights the impact that blend layering PSD has on granulation.

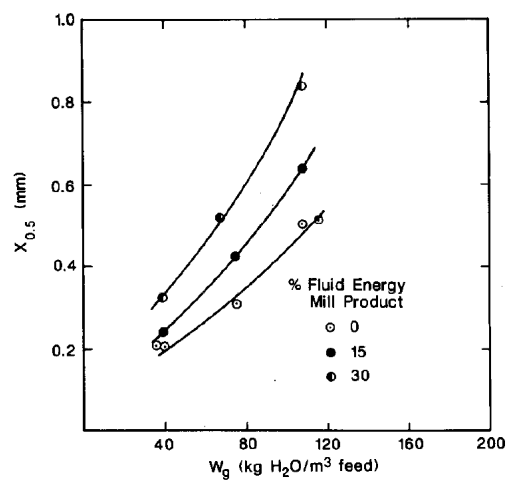


Figure 2.23 – Effect of changing the mass mean size of layering particles on $X_{0.5}$ (Litster and Waters 1988)

Complimentary to Litster and Waters, Khosa and Manuel (2007) aimed to predict granulation behaviour based on iron ore PSD. Using iron ore blends with differing PSDs, they proceeded to establish the effect on ‘cold’ bed permeability, as the measure for granulation effectiveness. In these studies, the size range of particles were created and classified as; layering (<0.075mm), ‘intermediate’ (<1mm >0.1mm) and nuclei (>2.8mm). An area that has received lesser focus is the ‘intermediate’ range of particle sizes because there has been confusion over their behaviour during granulation. Some researchers stated that they act as both layering and nuclei particles whereas others proved that they do not play a role and are detrimental to the extent of granulation. (Litster and Waters 1988; Wu et al. 2015).

Figure 2.24 shows the change in permeability against the increase in the particle size fraction. Permeability was measured as the resistance across the bed at a constant air

flow rate (DP). The resistance across the bed (DP) is the inverse of permeability, thus more negative changes represents that increasing the particles in these size fractions reduces the pressure drop across the bed (DP) or increases bed permeability. Evidently, the largest decrease in permeability was found with the 'intermediate' particle sizes (<1mm >0.1mm) and particularly with an average size of 0.1mm. No explanation of why this was the case was presented by Khosa and Manuel. However, what can be considered was the behaviour of the 'intermediate' sized particles during granulation. If an adverse effect of the 'intermediate' range on permeability was proven in these studies then this suggests that the 'intermediate' particles do not play such a role in granulation i.e. do not layer or act as nuclei and remain 'non-granulated' in the bed. If they did act as both or either of the said roles, then a similar change in permeability would be witnessed as with layering and nuclei particles. The largest increase in permeability in Figure 2.24 was with the layering and nuclei particles implying that an increase in these size fractions promoted granulation.

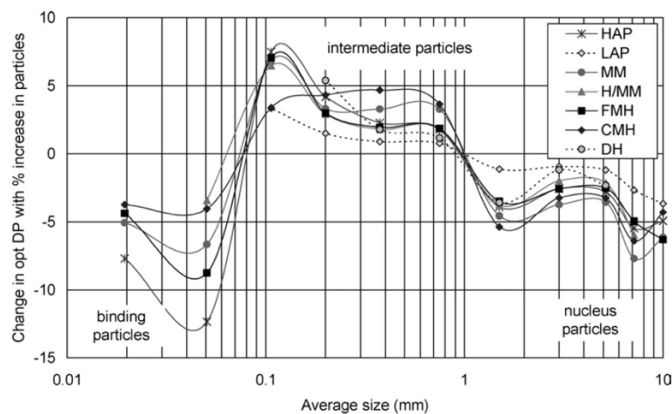


Figure 2.24 – Change in optimum blend bed resistance with particle sizes (Khosa and Manuel 2007)

Khosa and Manuel (2007) produced a comparable graph to Figure 2.24 but with the change in optimum moisture. Optimum moisture was stated as the moisture content at optimum 'cold' bed permeability. Similar behaviour of the particle groups was witnessed with the intermediate size range showing the largest change increase in optimum moisture. Likewise, the layering and nuclei particles gave the largest change decrease in optimum moisture. No explanation was given to the reasons behind these effects. The results on decreasing optimum moisture with increasing layering particles were contradictory to Litster and Waters (1988) as shown in Figure 2.22.

2.5.2 Particle surface properties

Besides PSD the impact of the surface properties of iron ore particles have been studied with regards to the granulation process. Some of the more prominent iron ore particle surface properties are shape, porosity, wettability, and specific surface area and all influence the interaction of particles during the process. Wu et al. (2015) studied factors including circularity with regards to shape, structural compactness with regards to porosity and water contact angle with regards to wettability. Linear regressions were conducted to realise the effect of iron ore surface properties excluding PSD on a granulation index (GI), as a measure of the extent of granulation. Granulation effectiveness was classified as the change in the mean diameter between the original and granulated mixtures. When concerning layering particle (<0.25mm) shape it was found that the less circular the particles the more the particles could embed with each other in the layer (Figure 2.25a and 2.25b). This was attributed to the larger number of contact points between the particles and greater compactness in the layer around the nuclei. The increased compactness also resulted in more moisture being available for granulation when compared to the circular particle case at equal moisture contents. The consequent effect on granulation was positive due to the increase in the attractive forces related to moisture.

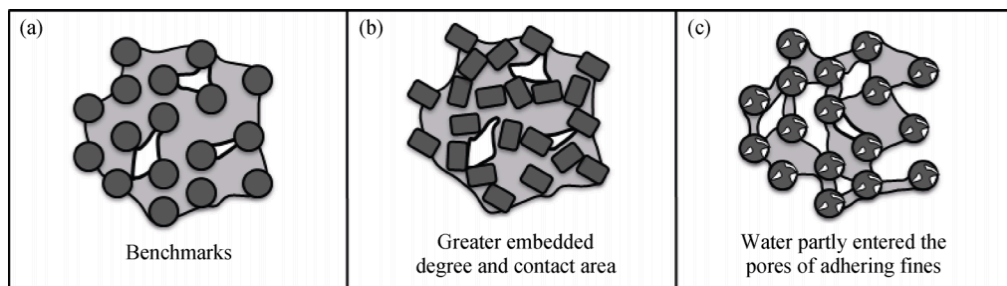


Figure 2.25 – Schematic diagram of impact of layering particle composition (Wu et al. 2015)

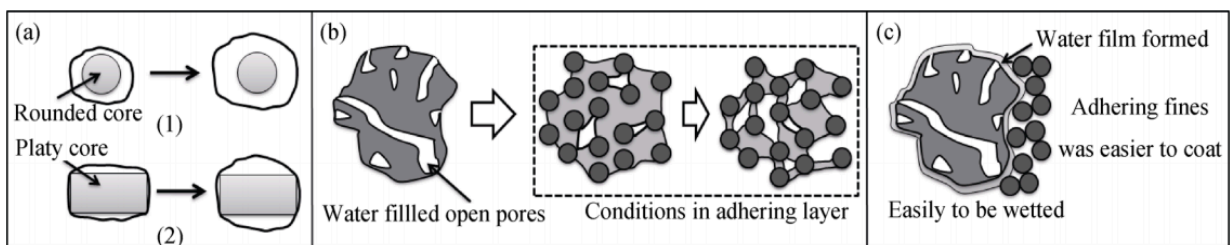


Figure 2.26 – Schematic diagram of impact of nuclei particle composition (Wu et al. 2015)

For nuclei particles, the circularity had the largest effect on the granulation index (GI). The reason suggested was that during the granulation process particles are layered

and rounded off. Thus, less layering particles would be consumed to achieve the same extent of granulation in less circular nuclei particles (Figure 2.26a). It was found that increased nuclei porosity adversely affects granulation. The more porous the nuclei the more water that was consumed by the particle and the less available for granulation (Figure 2.26b). Increased wettability of the nuclei particle showed positive effects on granulation. The easier the extent of wetting the easier it was for the particle to become surface wet and promote granulation (Figure 2.26c).

A further study to compliment the work by Wu et al. (2015) was conducted by Mao et al. (2013) who investigated the granulating ability of iron ores with differing surface properties by using 'cold' bed permeability as a measure of granulation effectiveness. To summarise, it was shown that the permeability-moisture curves, like that shown in Figure 2.9 in Section 2.2.2 differed for the ores. Ores with lower wettability displayed lower optimum 'cold' permeability and increased moisture content at optimum 'cold' permeability. Mao et al. postulated that the wettability of an ore was related to its surface roughness and shape. However, this could not be concluded from their results as there was not a direct relationship between wettability and surface roughness. Instead, Mao et al. related back to previous work which established that the wettability of an ore was mainly dependant on ore chemical composition.

2.5.3 Moisture content

The principal means to achieve granulation is the correct liquid to solid relationship and concerns both the proportion of liquid in the drum but also how it wets solids (Walker 2007). Moisture content in granulation systems is normally classed as the weight or volume percentage of the blend mass. Litster and Waters (1988) proposed some important conclusions in relation to the impact of moisture on the extent of granulation, which were briefly introduced earlier in Section 2.5.1. Granule growth was strongly dependent on the moisture content of the blend. Increased surface moisture was said to lead to a greater probability that the granules would stick together when colliding. It is presented in Equation 5 that the moisture available for granulation (W_g) was a result of the total moisture (W_T) minus the moisture absorbed by the blend (M_{ak}).

$$W_g = W_T - \frac{\sum_{k=1}^m (\delta_k M_{ak})}{\sum_{k=1}^m \left(\frac{\delta_k}{\rho_k}\right)} \quad (5)$$

where: W_g = moisture available for granulation ($\text{kgH}_2\text{O}/\text{m}^3$)

W_T = total moisture ($\text{kgH}_2\text{O}/\text{m}^3$)

M_{ak} = moisture absorbed by component k ($\text{kgH}_2\text{O}/\text{kg}$)

δ_k = mass fraction of component k (kg)

ρ_k = density of component k (kg/m^3)

Granulation effectiveness ($X_{0.5}$), which was introduced previously as a measure for the extent of granulation was evaluated for materials with differing nuclei particles at varying moisture contents (Litster and Waters 1988). Figure 2.27 proved that the nuclei type had a strong influence on the total amount of moisture (W_T) required for a specific extent of granulation. This was stated to be due to the differing amounts of moisture absorbed by the nuclei particles (M_{ak}). In addition, it was evident from Figure 2.27 that there was a clear impact of moisture on $X_{0.5}$. The trend of increasing $X_{0.5}$ with increasing moisture content can be observed for all nuclei types.

To verify the relationship between granulation effectiveness ($X_{0.5}$) and moisture Litster and Waters (1988) produced Figure 2.28. Instead of total moisture (W_T), the moisture available for granulation (W_g) proved to have a positive influence on $X_{0.5}$ and was at a similar rate for all iron ores studied. This was independent of nuclei type and proved that W_g was the dominating factor on $X_{0.5}$. Equation 5 showed that W_g was a result of the W_T minus the moisture absorbed by the blend (M_{ak}). It can be concluded that for granulation to occur the blend constituents must be saturated so any increases in W_T are solely attributed to the W_g to promote granulation.

Matsumura et al. (2009) attempted to create a model to reduce the amount of moisture required for granulation without adversely affecting the extent of granulation or the 'cold' bed permeability in their study. By adjusting the PSD of the ores to be equivalent the effect of moisture on 'cold' permeability could be evaluated. Figure 2.29 shows similar behaviour as shown in Figure 2.9 and 2.10 in Section 2.2.2. An initial increase in the 'cold' permeability with moisture before the

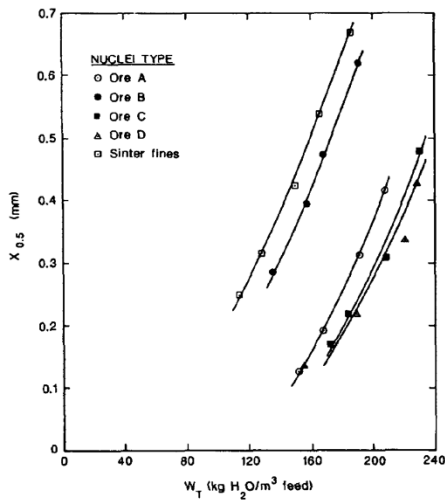


Figure 2.27 – $X_{0.5}$ against total moisture (W_T) for different nuclei types (Litster and Waters 1988)

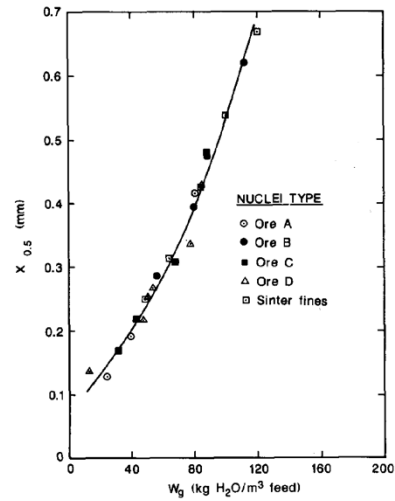


Figure 2.28 – $X_{0.5}$ against available moisture (W_g) for different nuclei types (Litster and Waters 1988)

optimum ‘cold’ permeability and moisture is reached, proceeding to a decrease in the ‘cold’ permeability at higher moisture contents. This differed for the types of ore used. However, it can be observed from Figure 2.29 that the rate of increasing ‘cold’ permeability with moisture was similar for all the materials (except Ore F). This indicates that even though the optimum ‘cold’ permeability and moistures for the ores are different once the moisture to initiate granulation was obtained, all ores display comparable rate increases in ‘cold’ permeability, demonstrating that the moisture available for granulation was the leading factor in the rate of increase in permeability and not the type of ore, as similar to that found by Litster and Waters (1988) in Figure 2.28.

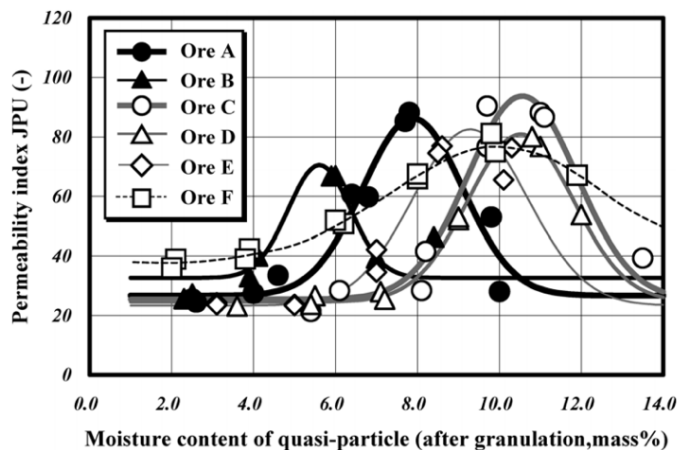


Figure 2.29 – Relationship between moisture content and bed permeability for different ores (Matsumura et al. 2009)

When evaluating the effect of PSD on the moisture at optimum 'cold' permeability Matsumura et al. (2009) varied the proportion of nuclei particles in the ores (>5mm) and proved that an increase in these particles decreased the optimum moisture (Figure 2.30). This was similar to that determined by Khosa and Manuel (2007) in Figure 2.24. This was proposed by Matsumura et al. to be because of the increase in the >5mm fraction widening the PSD of the blend and creating the closer packing and greater contact points between particles during granulation. The closer packing and increasing contact points between the particles meant there were less void spaces for the moisture to fill, thus moisture became available for granulation earlier and lowered the moisture at optimum 'cold' permeability.

However, what also must be considered is the inverse relationship between particle size and total specific surface area based on geometry (Dubois et al. 2010). An increase in the >5mm particles of the ores would decrease the total specific surface area of the blend, suggesting less total surface pores being available for the moisture to infiltrate thus decreasing the moisture required to make the particles surface wet to initiate granulation. This also fits the findings of Matsumura et al. (2009) where moisture content at optimum 'cold' permeability decreased with increasing coarser particles (>5mm), as the moisture became available for granulation at a lower amount compared to a blend with less coarse particles and higher total specific surface area.

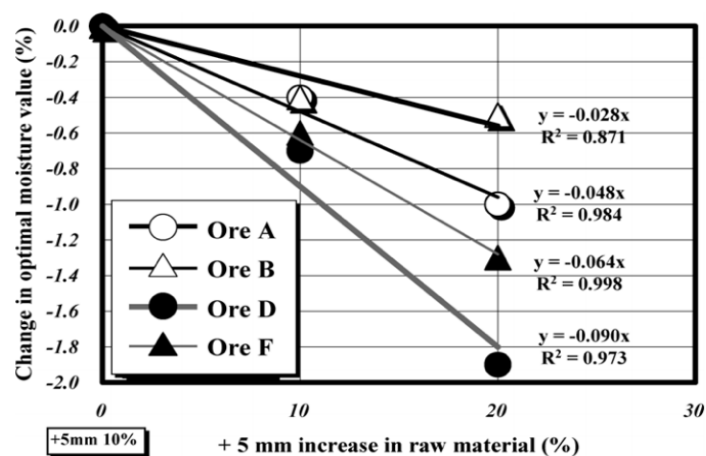


Figure 2.30 – Relationship between optimum moisture and increasing >5mm ore particles (Matsumura et al. 2009)

2.5.4 Summary

A variety of factors can influence the extent of granulation. Most relevant to this study is particle size distribution (PSD) and moisture content and the relationship between the two. In summary, PSD had a similar influence in all studies on the amount of moisture to achieve a certain extent of granulation. Increases in mean particle diameter and coarser fractions reduced the optimum moisture, which was classed as the moisture at optimum granulation or 'cold' bed permeability. Matsumura et al. (2009) suggested that this was due to a wider PSD allowing the closer packing of particles and therefore less void spaces for the moisture to fill. However, it was also suggested that this could be due to the decrease in total specific surface area of the blend when the coarser proportion was increased.

From a different perspective, it was proven that increases in fine or layering particles resulted in a lesser extent of granulation at equal moisture contents. Only at increased moisture was the same extent of granulation achieved. Changes in the PSD of layering particles also had an impact. Decreasing the mean diameter of the layering particles resulted in an increased extent of granulation at equal moisture, which adds emphasis to the impact that the layering PSD of blends has on granulation and moisture. These findings also prove that both theories on the relationship between PSD and moisture content mentioned could apply. This is because increased moisture was required with increasing layering particles and thus increasing total specific area to achieve a certain extent of granulation. However, decreasing the mean layering particle diameter decreased the moisture required for a certain extent of granulation, which could be attributed to the closer particle packing when decreasing the mean layering particle diameter and widening the spread of layering particle sizes.

The permeability of sinter beds has been stressed to be an important process property throughout the background chapter. This section outlined the impact of PSD and moisture content on the 'cold' bed permeability and can be considered as a measure for the extent of granulation. With regards PSD, the intermediate sized particles had the greatest detrimental effect on bed permeability ($<1\text{mm}$ $>0.1\text{mm}$). As mentioned there has been confusion over the behaviour of this particle size range.

Some researchers stated that intermediate particles can act as layering and nuclei particles, however these findings proved that they do not play a role in granulation and reduced the 'cold' bed permeability. Contradictory accounts make an exact conclusion on the behaviour of this particle size range difficult. The studies reviewed highlighted the problematic nature of these particles on optimum 'cold' permeability and moisture.

The optimum 'cold' bed permeability and moisture differed for ore blends even with the same PSD and proves that there are other particle properties influencing permeability. However, once granulation was initiated the 'cold' bed permeability rate increase with moisture was similar for all blends studied by Matsumura et al. (2009) and corresponds with Litster and Waters (1988) theory on the moisture available for granulation being the dominant factor behind rate increases in the extent of granulation or permeability.

Particle surface properties such as wettability, porosity and shape were shown to impact the extent of granulation. Particles that are easily wetted, have low porosity and are less circular were said to promote granulation when acting as either a nucleus or layering particle. Even though iron ore PSD is the key property of interest in this study, particle surface properties cannot be ignored in the discussion of any granulation and permeability results.

Chapter 3 – Materials and Methods

3.1 Materials

The sinter blend materials were introduced in the background chapter (Section 2.3). More definition is required behind the exact materials used in experimental testing. A description of the materials is shown in Table 3.1. The chemical composition of the non-iron ore materials in sinter blends is presented in Table 3.2. More detailed methods for characterising the iron ores are presented in Section 3.2 with the results reported in Section 4.1. As the aims and objectives of this study only entail the variation in the iron ore proportion of sinter blends focus was applied to these materials.

Table 3.1 – Sinter blend raw materials

Material	Description
Ore A	Sinter feed hematite iron ore
Ore B	Magnetite concentrated iron ore
Ore C	Concentrated hematite iron ore
Ore D	Magnetite pellet feed iron ore
Coke breeze	Product of coking process at TATA Steel Europe
Flux A	Flux to tailor chemical composition
Flux B	Flux to tailor chemical composition
Return sinter fines	By-product of sintering process

Table 3.2 – Chemical composition of sinter blend additives

Material	Chemical composition (wt%)						
	Fe _{total}	Al ₂ O ₃	SiO ₂	CaO	MgO	C	P
Coke breeze	1.02	3.37	6.60	0.53	0.14	83.2	0.06
Flux A	0.14	0.22	0.96	54.48	0.62	5.75	0.00
Flux B	0.30	0.25	1.22	31.48	19.90	12.80	0.01
Return sinter fines	68.70	1.33	3.59	12.44	1.21	0.00	0.05

3.2 Methods

To achieve the aims and objectives a range of equipment and methods were required. This section presents these sequentially from iron ore characterisation (Section 3.2.1) to sinter analysis (Section 3.2.9 to 3.2.11). Appendix 9.1 gives a summary of the methods used.

3.2.1 Iron ore characterisation

Particle size distribution

The characterisation of the particle size distribution (PSD) of the iron ores was done using two methods. The rationale is that the finer proportion of the materials (<0.5mm) cannot be accurately analysed in the same method as for the coarser proportion (>0.5mm). This is due to the sieves becoming 'blinded' due to the volume of material. Initially, dry sieve analysis was conducted on the coarser fraction of the ores (>0.5mm). The Haver and Boecker Digital Plus sieve shaker and series used in assessing the PSDs is shown in Figure 3.1 and 3.2. 5kg of the iron ores were dried at $105\pm 2.5^{\circ}\text{C}$ for 12 hours in a fan oven. Once dry the complete samples were split through a riffing box to obtain representative samples. The 400-500g samples were then sieved using the sieve shaker and series shown for 5 minutes at setting 4. The sieve series selected



Figure 3.1 – Haver and Boecker Digital Plus sieve shakers

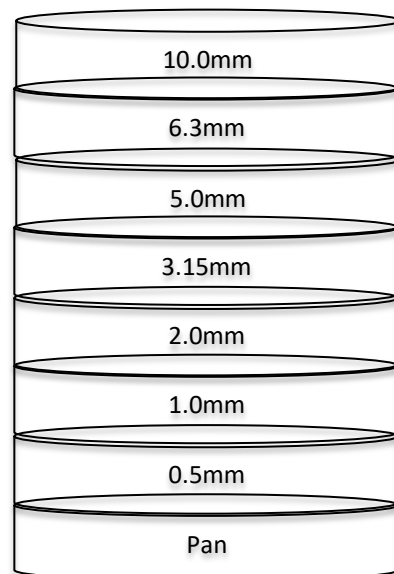


Figure 3.2 – Sieve series for dry size analysis

was the same as that used in RD&T activities at TATA Steel Europe (2016c). Two repetitions of the dry size analysis were conducted. The mass retained in each sieve was weighed using scales with an accuracy of 0.01 ± 0.01 g. The measurements were processed into percentage mass retained in each sieve size based on the total mass. Appendix 9.1 summarises the method used.

When progressing to the finer proportion (<0.5mm) of the ores, which is the primary component under analysis another method was required. Malvern Mastersizer laser diffraction equipment was employed as this allows a rapid and accurate PSD measurement for both wet and dry particles between only a few nanometers to millimetres in diameter (Malvern 2017). To utilise the Malvern Mastersizer equipment standard operating procedures (SOP) were created for each ore. This requires information on the particle density, which was established by the method described later in Section 3.2.1 and the refractive index, which can be found from Malvern Instruments Reference Manual (Malvern 2007). The samples for analysis were approximately 3g but must be large enough to raise the obscuration range, which is the amount of light scattered by the particles to be between 8-20%. This was to create the correct volume of material circulating in the equipment. The Malvern Mastersizer is an automated apparatus, which once the SOP has been created can conduct the particle size analysis. Once analysis was completed the volume and mass of particles in each size range is determined. Appendix 9.1 summarises the method used and the complete PSDs of the iron ores are presented in Section 4.1.1.

Rosin-Rammler distribution

One of the more common equations used to describe the shape of the curve for measured cumulative PSDs is the Rosin-Rammler equation (Vesilind 1980). The Rosin-Rammler equation is frequently used in defining PSD particularly in mineral processing operations like with iron ores. Equation 6 demonstrates the Rosin-Rammler equation used with cumulative size distributions. This method is applied to the iron ore PSD and granule size distribution (GSD) measurements in this study.

$$P(D) = 1 - \exp \left[- \left(\frac{D}{D_m} \right)^n \right] \quad (6)$$

where: P = percentage less than (%)

D = particle size (mm)

D_m = mean particle diameter (mm)

n = spread of particle sizes

The most effective means to express applying the Rosin-Rammler distribution is through an example. Figure 3.3 provides example data determined through the PSD methods described previously. Figure 3.4 shows the Rosin-Rammler distribution fit to the example data based on Equation 6. To determine the Rosin-Rammler curve shown in Figure 3.4 the two unknown parameters of the equation (D_m and n) need to be established. The approach involves utilising a Microsoft Excel™ solver to vary the parameters to minimise the sum of the square of the residuals between the PSD from the measurements and the Rosin-Rammler distribution. Using this method identifies the mean particle diameter (D_m) and spread of particle sizes in the distribution (n). The Rosin-Rammler equation classes the particle size at 63.2% of the cumulative distribution as the mean particle diameter (D_m). The spread of particle sizes gives a relative measure of the uniformity of particle sizes in the distribution. The spread is calculated by the gradient of the fitted curve in the distribution where a steeper slope signifies a narrower spread of particle sizes (larger n). The spread of particle sizes is the key PSD property that is investigated in this study with the layering PSD of sinter blends.

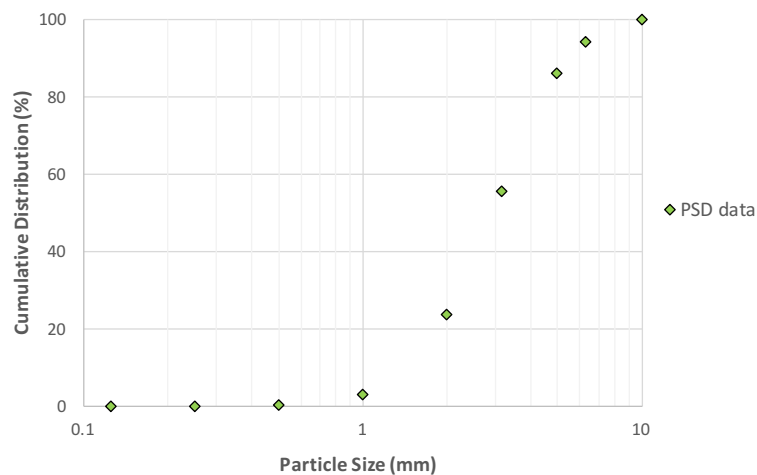


Figure 3.3 – Example cumulative PSD measurements

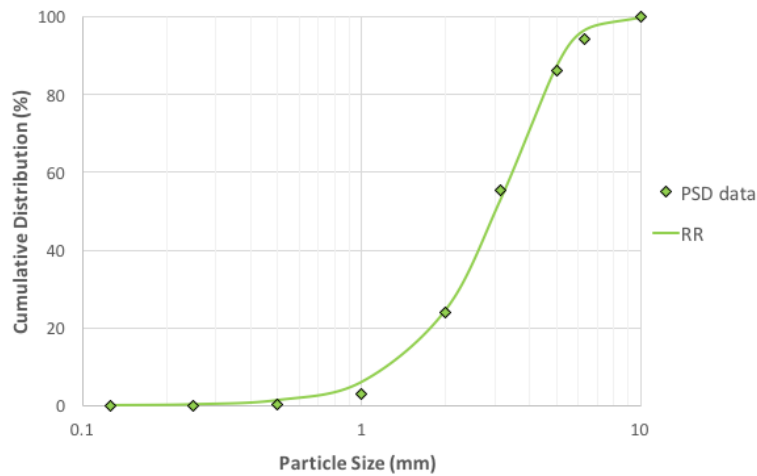


Figure 3.4 – Rosin-Rammler distribution fit to example cumulative PSD measurements

Qualitative description of particle shape

To analyse the particle shape of the iron ores morphological characterisation techniques were applied. Particle shape is a prominent property of materials, which has been shown to impact their granulating ability (Wu et al. 2015). The primary purpose of shape analysis was to provide detailed high-resolution images of the ores. This information was employed to draw qualitative conclusions on the shape of the ores in combination with the shape criteria displayed in Figure 3.5. The ores were sieved at 0.5mm and a representative sample of the finer proportion was mounted in epoxy resin. This could set before a cross-section was cut and polished. The manufacturer and model of microscope employed was Zeiss Axioplan Imager Z1. The acquired images of the shapes of the ores are presented in Section 4.1.2.

Term	Shape
Cylindrical	
Discoidal	
Spherical	
Tabular	
Ellipsoidal	
Equant	
Irregular	

Figure 3.5 – Particle shape analysis criteria (University Saskatchewan 2002)

Chemical composition

Chemical characterisation of the iron ores was determined using X-ray fluorescence (XRF). The ores were prepared by milling before a representative sample was taken and a lithium tetraborate (LiTTB) bead created. The LiTTB acts as a flux in creating the bead but does not show up in the XRF analysis. The bead was inserted into a PANalytical AxioS apparatus for chemical characterisation of the ores. The calibration of the device was conducted with certified materials to the Raad Voor Acreditatie (RVA) 150 standard. The chemical composition of the ores is presented in Section 4.1.3.

Mineralogy

X-ray diffraction (XRD) was utilised to characterise the mineralogy of the iron ores. XRD is primarily used to identify the phases of crystalline materials. The phase proportions of the ores have been determined by XRD and subsequent Rietveld analysis. The XRD radiation source was cobalt (Co). The XRD patterns were recorded in the range of 10-130° in reflection mode using a fully automated Bruker D4 diffractometer equipped with a position sensitive detector. The step size was 0.02° and the time per step was 200 seconds. Quantitative determination of phase proportions was performed by the Rietveld analysis and the refinement was conducted on the assumption of pure phases. Unit cell parameters, background coefficients, preferred orientations, profile parameters and phase proportions were refined using the TOPAS software package for Rietveld refinement. The mineralogical description of the ores is presented in Section 4.1.4.

Density

Helium pycnometry was utilised to determine the 'true' density of the iron ores. This method is a non-destructive technique that uses a gas displacement method to accurately measure volume. The ore samples were ground in a milling machine to open all the internal pores in the sample. The sample was sealed in the primary chamber with known volume. The helium is admitted and then expanded into another chamber

also of known volume. The pressures detected on filling the chamber with the sample and then being released into the second empty chamber allow the calculation of the volume of solid phases in the sample. The benefit of using an inert gas means that all pores are filled with the gas and only the solid phase of the sample will displace the gas. Dividing this volume by the sample weight determines the 'true' density of the ores including all pores, which are presented in Section 4.1.5.

Water pycnometry was utilised to determine the density of the iron ores including only the surface pores. In this method, the ores are not ground but sieved at 0.1mm and a sample of the finer proportion sealed into the primary chamber. Following this step, the same process as described previously with the helium method is used but with water. The solid phase of the sample will displace the water and dividing this volume by the sample weight determines the 'true' density of the ores including only the surface pores. The density of the ores only including surface pores are also presented in Section 4.1.5.

In both density methods, the results will be less dense than the absolute 'true' density of the ores, as there will be pores that both the helium and water could not enter. However, with the equipment available a more accurate density measurement could not be obtained.

Wettability

The characterisation of the wettability of the iron ores is based upon the analyses of particle shape and mineralogy. The qualitative conclusions on the wettability of the ores are presented in Section 4.1.6.

3.2.2 Sinter blend design

Determining Fuller-Thompson equation parameters

The first objective was to determine the parameters of the Fuller-Thompson (FT) equation for the design of the layering proportion of sinter blends. These parameters create the FT particle size distribution (PSD) to fit the blends in a later subsection. The parameters of the FT equation are the maximum particle size in the distribution (D) and exponent (Ψ). The means to obtain these parameters is through experimentation, particularly as the FT equation has not been applied to sinter blend design previously.

Maximum particle size (D)

The maximum particle size of the distribution (D) is the upper particle size where the distribution designed by the FT equation stops i.e. 100% of the cumulative PSD will be at that size. The maximum particle size of the distribution (D) was selected based on microscopy and literature as follows.

From Section 2.5.1 it was shown that particles can be split into layering and nuclei particles. However, the size ranges applied to the layering and nuclei particle categories as presented has had debate. As the application of this method is to design the layering PSD to the FT equation to achieve improved layer properties in granules then the maximum size should relate to the maximum size of layering particles.

To establish the maximum particle size of layering particles (D) microscopic analysis has been applied on granules. The method is explained in greater detail in Section 3.2.6. Microscopic analysis was conducted on the granules from a base blend and the largest layering particles in the granules measured using a Zeiss Axioplan Imager Z1 microscope and Axiovision image analysis software. The base blend is defined as a blend that simulates typically used blends at Tata Steel Europe. The layering particle measurements along with the previous studies that classified the layering particle size category led to conclusions on the maximum particle size in the layer to give the best estimation of this parameter.

Fuller-Thompson exponent (Ψ)

The exponent (Ψ) of the FT equation has had a large amount of research in the past, some of which was introduced in Section 2.1. This parameter plays an important role in determining the FT PSD and thus the behaviour of particles in systems. In the systems that have been reviewed researchers have developed mixtures or blends of materials to give distributions correlating to the PSD with that FT exponent. These mixtures were then tested for the key properties of the materials being designed e.g. strength with concrete. The FT exponent that gave the best properties was selected for the FT equation in further design for that material.

This is the first study to adopt this approach in sinter blend design. The layering PSD can be designed to the FT equation with varying FT exponents. The FT exponents that were examined were 0.3, 0.4, 0.5 and 0.6. To evaluate the influence of the FT exponent on the performance of resulting sinter blends, the blends were processed through the mixing and granulation equipment (Section 3.2.4) at a range of moisture contents and analysed through the 'cold' permeability and 'cold' permeability efficiency equipment detailed later in the methods section (Section 3.2.7). Frozen size analysis was also conducted on the granules to provide granule size distribution (GSD) measurements from each blend (Section 3.2.5).

The layering proportion of the blends determined by the FT equation with differing exponents are shown in Table 3.3. Alumina (Al_2O_3) was incorporated into layer design. The purpose was that the alumina (Al_2O_3) is a very fine material ($D_{50} = 20\mu\text{m}$) and enables a closer fit to the FT PSD than that which could be obtained via solely using the available iron ores (Ore A to Ore D). As these blends are only being tested for the 'cold' bed permeability and 'cold' permeability efficiency then the impact of alumina (Al_2O_3) on sintering does not need consideration.

The layering PSD of the blends designed to each FT exponent are displayed as a cumulative distribution (wt%) in Figure 3.6. There is a notable difference between the PSDs. Some primary properties to consider, which are shown in Table 3.3 are the decrease in mean particle diameter (D_m) and the widening in the spread of particle

sizes in the layer (decreasing n) as the FT exponent decreases. These systems are split into one-part layering and one-part nuclei particles (return sinter fines <3.15mm >1mm) with the total mass percentage of each held constant (50wt%). This was to accentuate any differences in the granulating behaviour of the FT blends with differing FT exponents, as the layering PSD will be the only variable to explain any differences in the measurements obtained. The percentage of layering and nuclei particles was selected based on the similarity with plant operations.

Table 3.3 – Blend layer compositions of FT exponents (Ψ)

Exponent (Ψ)	Ore A	Ore B	Ore C (wt%)	Ore D	Al ₂ O ₃	Mean diameter (mm)	Layering PSD spread (n)
0.6	26.60	0.00	47.70	25.70	0.00	0.19	0.87
0.5	29.02	0.00	37.86	28.99	4.13	0.15	0.76
0.4	19.93	0.00	36.01	29.17	14.89	0.12	0.70
0.3	7.82	0.00	35.83	24.38	31.97	0.08	0.65

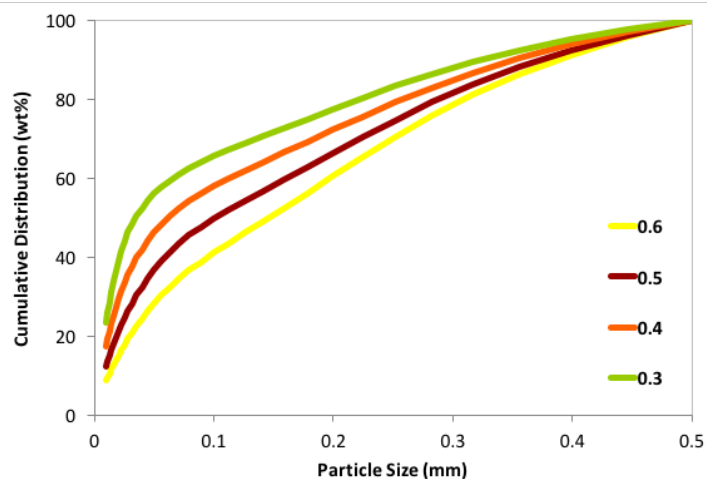


Figure 3.6 – Cumulative PSD of blends with differing FT exponents

Blends designed to study the influence of layering PSD spread (n)

It is postulated that the spread of particle sizes (n) in the layering proportion of sinter blends could be influential on the ‘cold’ permeability, ‘hot’ permeability, ‘hot’ permeability efficiency and sintering times. Layering PSD spread is a relative measure of the uniformity of particle sizes in the distribution and is a parameter determined through applying the Rosin-Rammler distribution to PSDs (Section 3.2.1). Blends were designed with a range of layering PSD spreads, from narrower (larger n) to wider (smaller n) PSDs. The layer compositions designed are presented in Table 3.4.

It is evident when looking at Table 3.4 that the blends have differing layering PSD spreads (n). The PSD created by the FT equation has a fixed layering PSD spread. This is because with a given set of FT equation parameters (D and Ψ) there is only one PSD possible. The FT equation parameters are established in the first part of this study. The layering PSDs of the other blends investigated were designed with wider and narrower layering PSD spreads than the FT blend. The influence on the ‘cold’ permeability, ‘hot’ permeability, ‘hot’ permeability efficiency and sintering time could thus be assessed.

All blends are designed to contain 50wt% layering particles and a 50wt% constant nuclei proportion (Ore A <10mm >1mm), which again was similar to plant operations. The constant nuclei proportion was created by sieving Ore A at 1mm and the coarser proportion processed through a splitter to obtain a representative sample. The reason for creating a constant nuclei proportion in the blends was so that any differences in the granule and sintering process measurements must be attributed to the layering PSD spread (n) of the blend.

Table 3.4 – Layer composition of blends to study the influence of layering PSD spread (n)

Blend	Ore A	Ore B	Ore C	Ore D	Layering Particles	Layering PSD Spread (n)
	(wt%)					
Non-FT0	0	90	0	10	50	1.09
FT	62.5	0	18.75	18.75	50	0.78
Non-FT1	70	0	0	30	50	0.69
Non-FT2	90	0	0	10	50	0.62

Industrial application of Fuller-Thompson blend design

To continue assessing the objectives put forward in this study two differing methods of sinter blend design were incorporated:

1. **Industrial base (BB) blends:** Represent typically used blends at Tata Steel Europe and can be thought of as benchmark blends.
2. **Fuller-Thompson (FT) blends:** Blends designed to the FT equation with the method used explained in greater detail later in this section.

Blends from both methods are designed with varying total layering particle proportions (46wt%, 48wt% and 50wt%). The layering particle proportions are considered representative of those found in plant operations. The primary purpose was to investigate the impact on bed permeability and sintering times of increasing the proportion of layering particles in sinter blends. However, also to evaluate if FT blends can enable an increase in the proportion of layering particles when compared with base (BB) blends. Both the industrial base (BB) and Fuller-Thompson (FT) blends were analysed for granule and sintering process measurements (Section 3.2.4 - 3.2.10).

Industrial base blends

Industrial base (BB) blends are utilised in this research to act as benchmark blends. This category of blend is currently employed in several RD&T sintering projects at TATA Steel Europe. The base blends provide blend compositions that can be tested for all granule and sintering process measurements to give benchmark measurements to which other blends can be compared. This enables the blends designed to methods such as the FT equation to be evaluated against the base blends and any differences whether negative or positive between the two blend design methods assessed. The base (BB) blend compositions are displayed in Table 3.5. The percentage of the blend that is classed as layering particles and the layering PSD spreads (n) are also detailed in Table 3.5. When referring to base blends this only encompasses the iron ore proportion of the blend, as this is the principal component under investigation in this study. Other sinter blend materials do not require to be varied when evaluating the aims and objectives, therefore are not incorporated into blend design. However, the proportions of the other blend materials are given at the end of this section (Table 3.8).

Table 3.5 – Base (BB) blend compositions at different total layering particle proportions

Blend	Ore A	Ore B	Ore C (wt%)	Ore D	Layering Particles	Layering PSD Spread (n)
BB1	80	10	10	0	46	0.94
BB2	70	20	10	0	48	1.01
BB3	60	30	10	0	50	1.11

Fuller-Thompson blends

Particle size distribution (PSD) is the key material property to be able to design to the Fuller-Thompson (FT) equation. A combination of dry sieve analysis and laser diffraction was utilised to obtain the PSD for each ore (Section 3.2.1). Once this information and the FT equation parameters (D and Ψ) were obtained the FT equation can be used to design the layering proportion of the blends.

The FT blend design method developed herein uses a Microsoft Excel™ solver. The Microsoft Excel™ solver is piece of software that finds the optimum solutions for various decision problems (Excel Easy 2017). The solver uses the generalised reduced gradient (GRG) non-linear setting, which is an algorithm within the Microsoft Excel™ solver. This was identical to the setting used in fitting the Rosin-Rammler distribution to PSD measurements in Section 3.2.1. Running the solver in this setting varies the decision variables, which are the iron ores PSD to find the objective function, which is the blend composition that optimally fits the FT PSD. To obtain the objective the sum of the square residuals of mass retained between the blend and FT PSD was minimised. The Microsoft Excel™ solver identifies the iron ore composition that had the minimum difference in the sum of mass retained. An example is the most effective means to demonstrate. Figure 3.7 shows the FT PSD and arbitrary blend (Arb). A difference in the mass retained in each particle size can be identified. The objective is to minimise the sum of these differences by varying the iron ore composition of the blend.

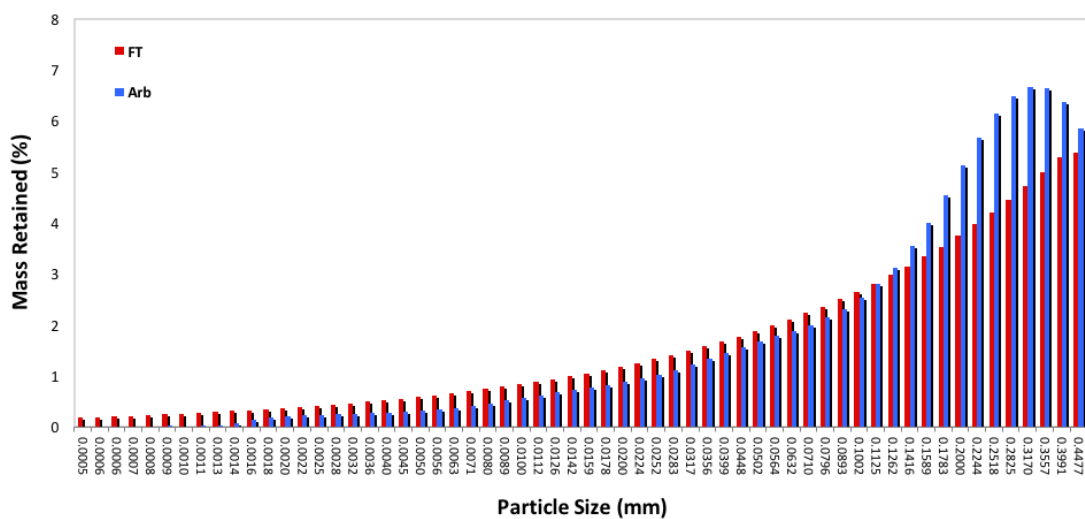


Figure 3.7 – Mass retained (%) for a Fuller-Thompson (FT) and arbitrary (Arb) blend

The Microsoft Excel™ solver parameters and constraints that are employed to achieve the objective are shown in Figure 3.8. The objective is the cell containing the sum of the difference in mass retained between the blend and FT PSD. The objective is set to 'min', to minimise the sum of the differences in mass retained. The variable cells contain the percentage composition of each ore, which were linked to their previously determined PSD. There are only three cells contained in this field whereas there are four iron ores under investigation. The Microsoft Excel™ solver cannot solve the problem if all the iron ores are varied simultaneously. Therefore, one ore must be left out and varied through subtracting the sum of the other three ores from 100%. The constraints were set so that each ore cannot be less than 0wt% or greater than 100wt%. A constraint was set for the proportion of layering particles in the blend, which in Figure 3.8 was 46wt%. This was required to be changed when increasing the layering particle proportions to 48wt% and 50wt%. Once the required parameters and constraints are entered the Microsoft Excel™ solver can be run and the blend that optimally fits the FT PSD determined. An example distribution created by the solver based on Figure 3.8 is shown in Figure 3.9.

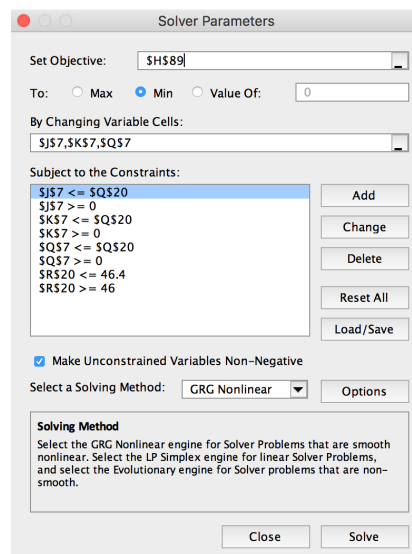


Figure 3.8 – Microsoft Excel™ solver parameters with objectives and constraints to design Fuller-Thompson blends

As can be identified from Figure 3.9 the blend (FTopt) is a much closer fit to the FT PSD (FT) than the arbitrary distribution (Arb) shown in Figure 3.7. However, there is still a discrepancy with the FT PSD. With the constraints that were set no further fit of the FT PSD was possible with the iron ores available. For this reason, the blend compositions

that provide the optimum fit to the FT PSD and are within the constraints are classed as FT blends in this research. The composition of the blends that were designed to the FT equation are detailed in Table 3.6. Appendix 9.1 summarises the FT blend design method.

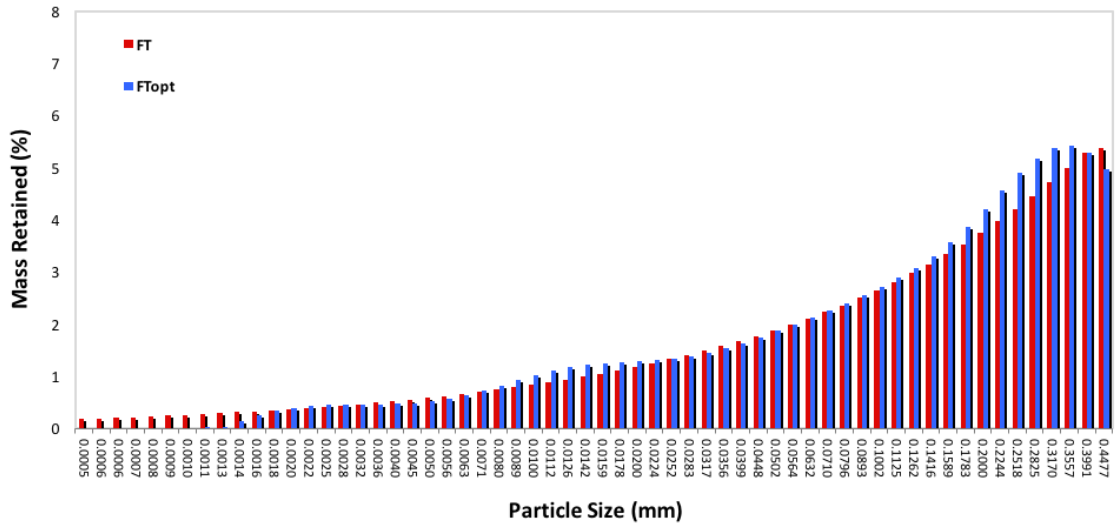


Figure 3.9 – Mass retained PSD of Fuller-Thompson optimised (FTopt) blend and Fuller-Thompson (FT) equation

Table 3.6 – Fuller-Thompson (FT) blend compositions at different total layering particle proportions

Blend	Ore A	Ore B	Ore C (wt%)	Ore D	Layering Particles	Layering PSD Spread (n)
FT1	80.0	11.5	0.0	8.5	46	0.74
FT2	70.0	21.7	0.0	8.3	48	0.75
FT3	60.0	31.8	0.0	8.2	50	0.78

Summary of blends for analysis

Table 3.7 summarises the blends under investigation in this study. As was stated this study is split into two parts: the influence of layering PSD spread (n) in sinter blends and the evaluation of FT blends against those simulating typically used blends at TATA Steel Europe (base (BB) blends). Both categories directly relate back to the aims and objectives and confronting the hypothesis of this research. The complete sinter blend composition including the blend additives is shown in Table 3.8. The composition in Table 3.8 was held constant throughout testing. Three repetitions of each blend were performed at moisture contents of 6-6.5wt%H₂O.

Table 3.7 – Summary of blends for analysis

Blend	Ore A	Ore B	Ore C (wt%)	Ore D	Layering Particles	Layering PSD spread (n)
Investigating the influence of layering PSD spread (layer only)						
Non-FT0	0	0	80	20	50	1.02
FT	85	5	5	5	50	0.78
Non-FT1	17.5	57.5	0	25	50	0.70
Non-FT2	0	57.5	0	42.5	50	0.65
Industrial application: Base vs FT blends (complete blend)						
BB1	80	10	10	0	46	0.94
FT1	80	11.5	0	8.5	46	0.74
BB2	70	20	10	0	48	1.01
FT2	70	21.7	0	8.3	48	0.75
BB3	60	30	10	0	50	1.11
FT3	60	31.8	0	8.2	50	0.78

Table 3.8 – Complete sinter blend composition

Material	Mass (kg)	Mass (wt%)
Iron ore	5.00	62.70
Coke breeze	0.27	3.40
Limestone	1.09	13.60
Dolomite	0.12	1.50
Return sinter fines (<3.15mm >1 mm)	0.75	9.40
Return sinter fines (<5mm >3.15 mm)	0.75	9.40
Total	7.98	100.00

Blend composition sheet

To compose the blends under investigation a blend composition sheet was created with an example illustrated in Table 3.9. This incorporates all sinter blend materials with the mass percentage of each material to be inserted and enables the dry mass of each material to be determined based on the total blend mass required for analysis. The moisture of each blend material is previously determined through the moisture content method described later in Section 3.2.3. Once the moisture content of the blend materials is known this can also be incorporated into the table. This produces the total mass of each material for the blend. The total blend mass is based on the mass of granules to sufficiently analyse the granule and sintering process measurements. This has been established to be 8kg by previous studies at TATA Steel Europe RD&T. Once the composition sheet has been created for all blends the materials can be weighed using a Salter Brecknell scale with a readability of 5g and inserted into the mixer and granulator for processing (Section 3.2.3).

Table 3.9 – Sinter blend composition sheet

Material name	Mass (%)	Dry mass (kg)	H ₂ O (wt%)	Total (kg)
Iron ore	62.7	5.00		5.05
Ore A	47.0	3.75	1.00	3.79
Ore B	3.1	0.25	0.07	0.25
Ore C	7.2	0.58	0.06	0.58
Ore D	5.3	0.42	1.90	0.43
Additives	37.3	2.98		2.99
Limestone	14.1	1.13	0.05	1.13
Dolomite	1.6	0.13	2.13	0.13
Return sinter fines (<5mm >1mm)	19.4	1.55	0.0	1.55
Coke breeze	2.2	0.18	3.52	0.19
Total	57.77	7.98		8.04

3.2.3 Mixing and granulation

The mixing and granulation of the sinter blend is an essential step in the overall sintering process. Various materials are incorporated in blend design, which results in a wide spread of particle sizes (up to 20mm). The primary objective of the mixing and granulation phase is to increase the mean particle size and narrow the spread of particle sizes by creating granules, which enhances sinter bed permeability on the strand. The initial mixing phase consists of the blend materials being dry mixed in the Eirich mixer shown in Figure 3.10 for 120 seconds. Once complete water was added while the device was still mixing to act as the binder for the layering of finer particles around coarser nuclei particles to produce granules. Water addition was conducted under the same settings as the mixing stage by adding through a water injection system to ensure constant flow into the drum. The Eirich mixing equipment ensures that the moisture is uniformly mixed into the blend materials before granulation is conducted.



Figure 3.10 – Eirich mixer (TATA Steel Europe RD&T)

To achieve the correct flow characteristics during the granulation phase it is essential that several parameters are fulfilled. A rolling bench with a granulation drum of internal diameter 300mm and length 500mm was utilised. Figure 3.11 indicates the

possible flows of material inside a granulation drum. For effective granulation, the flow must follow either rolling or cascading (Hage 2015). From Figure 3.12 it can be identified that the appropriate means to control the flow regime is through the Froude number (N_{FR}) and the filling degree of the drum. Froude number (N_{FR}) is defined as the ratio of inertial to gravitational forces, which is in this instance in a rotating drum (Lindeberg 2013). Equation 7 shows that Froude number (N_{FR}) is a function of both drum diameter (D) and the rotational speed (N). As the drum diameter (300mm) and filling degree were constant then the rotational speed was the only means to alter the Froude number in this scenario. In this research, the rotational speed was 24rpm, Froude number (N_{FR}) is 0.0049 and the filling degree 0.38. Appendix 9.1 summarises the method used. Once mixing and granulation was completed the granules were charged into the sintering equipment for analysis (Section 3.2.6 and 3.2.7). The granule size distribution (GSD) was determined through frozen size analysis (Section 3.2.4) and a granule sample was set in epoxy resin for microscopic analysis (Section 3.2.5).

$$N_{FR} = \frac{D N^2}{G} \quad (7)$$

where: D = Inner diameter of the drum mixer (m)

N = rotation speed of the drum mixer (min^{-1})

G = gravity conversion factor (m/min^2)

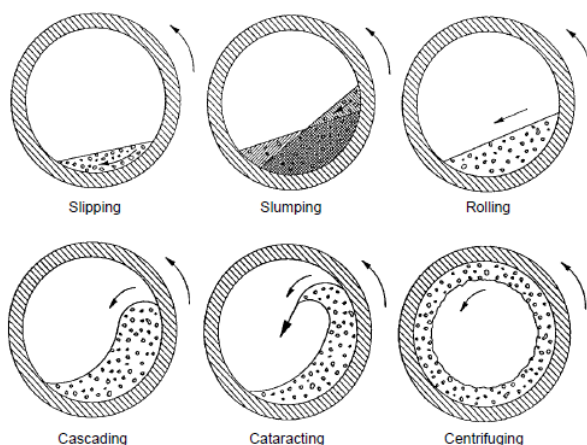


Figure 3.11 – Flows in granulation drum (Hage 2015)

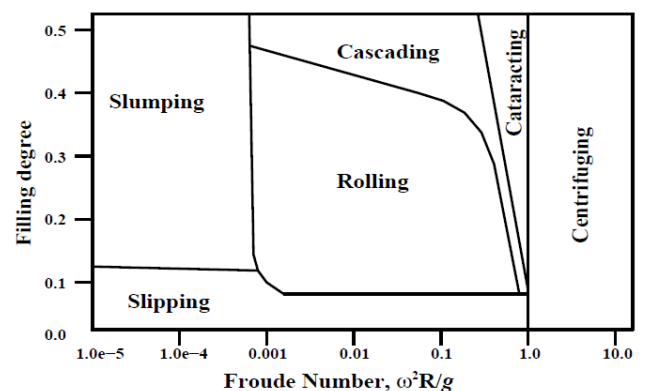


Figure 3.12 – Flows in granulation drum as function of Froude number (N_{FR}) and filling degree (Hage 2015)

Moisture content

Section 2.5.3 emphasised the impact of moisture content on the granulation process and proved it to be a key process parameter. It is essential to accurately monitor the moisture content before and after mixing and granulation. To determine the moisture content of the blend materials and granules a Mettler Toledo moisture balance was utilised.

To compose the blend composition sheet in Table 3.9 the percentage mass of moisture of the blend materials was required. This was to determine the initial moisture content of the blend so the exact amount of moisture to be added during mixing and granulation was known. Total moisture content was measured as a percentage of the blend mass (wt% H_2O). Therefore, a 1wt% addition of moisture would be 80ml of moisture, as the total blend mass was 8kg. Once the required moisture was added and the mixing and granulation process complete the granules were analysed in the balance to establish the exact moisture content of the granules before being charged into the sintering equipment, as a discrepancy could develop. One reason for the difference in the target and actual moisture content is due to some moisture being lost by evaporation from the movement of material during mixing and water addition. If the moisture content is below that required, then the procedure of mixing, water addition and granulation can be repeated with the additional moisture. However, if there is too much moisture then the granules need to be discarded and the whole procedure repeated with new blend materials.

Determining moisture content requires a mass of the blend materials and granules (approximately 40g) being placed onto a foil dish, which is inserted into the Mettler Toledo balance. The balance operates on an automated basis, where the material is heated up by an element. The mass of the material is automatically weighed at regular intervals and the percentage mass of moisture can be calculated based on its original mass. The analysis of moisture content is complete when there is no further change in the granule mass over the measurement interval. The moisture content is then shown on the equipment display as a mass percentage (wt% H_2O). This procedure is repeated

twice for the blend materials and granules with the accuracy of the moisture balance being $0.01 \pm 0.01\%$. Appendix 9.1 summarises the method used.

3.2.4 Granule size distribution

The size distribution of granules can be classed as one of their primary properties. The frozen sieve analysis method is an adaptation of that used by Litster and Waters (1988) and is conducted at TATA Steel Europe (2016c). A granule sample (400-500g) is inserted into a vibrating feeder, which passes the granules into a pot of liquid nitrogen (Figure 3.13). The feeder plays a crucial role in separating the granules so they can be frozen individually and an accurate measurement of the granule size distribution (GSD) taken by sieve analysis. This was conducted through the series shown in Figure 3.14 using the Haver and Boecker Digital Plus sieve shaker at setting 4 for 2 minutes (Figure 3.1). After the sieve analysis was conducted the mass percentages retained in each sieve size could be determined. The Rosin-Rammler distribution was then applied, which is identical to that described previously in iron ore characterisation (Section 3.2.1). The GSD properties; mean diameter (D_m) and spread of granule sizes (n) were therefore characterised. Frozen size analysis is repeated twice for each blend. Appendix 9.1 summarises the method used.



Figure 3.13 – Vibrating feeder and liquid nitrogen pot

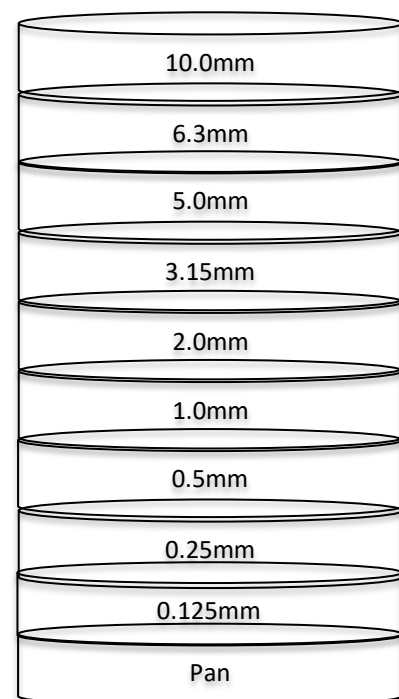


Figure 3.14 – Frozen sieve analysis sieve series

3.2.5 Granule microscopic analysis

To conduct microscopic analysis on the granules a cross-section through the granules was required. The layering of particles around nuclei particles during granulation produces a product that is relatively weak and prone to disintegration with handling. Simply taking a cross-section of the granules in their normal state would result in the break-up of the particles and would not be representative. A sample of granules were dried at $105\pm 2.5^{\circ}\text{C}$ for 12 hours in a fan oven to remove moisture. Once dry, the sample was set in epoxy resin under a vacuum and a cross-section of the granules (diameter = 5cm) taken without any break-up. This was achieved by a cutting device to horizontally dissect the sample. The sample was then polished with an example cross-section shown in Figure 3.15.



Figure 3.15 – Cross-section of granules set in epoxy resin

The primary granule features to be investigated using microscopic techniques and image analysis software were the layers developed around nuclei and the ‘non-layered’ (or ‘non-granulated’) particles. The ‘non-layered’ particles concerns particles that have not acted as a nucleus or been incorporated into a layer and have been referred to as ‘intermediate’ particles in the past. It can be observed in Figure 3.16 that there are several granules incorporated in the cross-section. The mosaic images were created by a Zeiss Axioplan Z1 Imager microscope and camera. Adobe Photoshop™ was utilised to outline the nuclei and layers, as shown in Figure 3.17. Axiovision image analysis software was then employed to determine the required measurements.

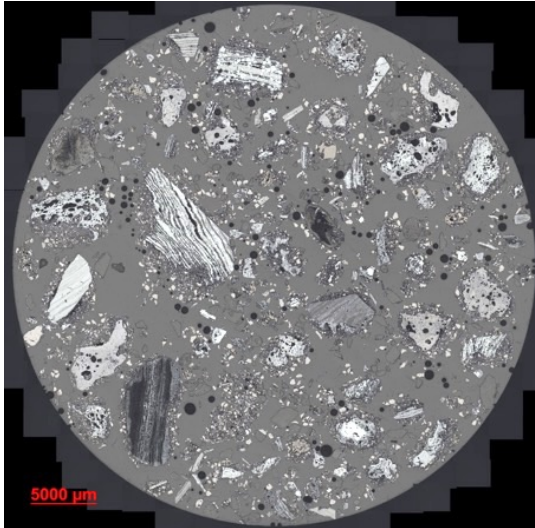


Figure 3.16 – Example microscopic image of granules in cross-section

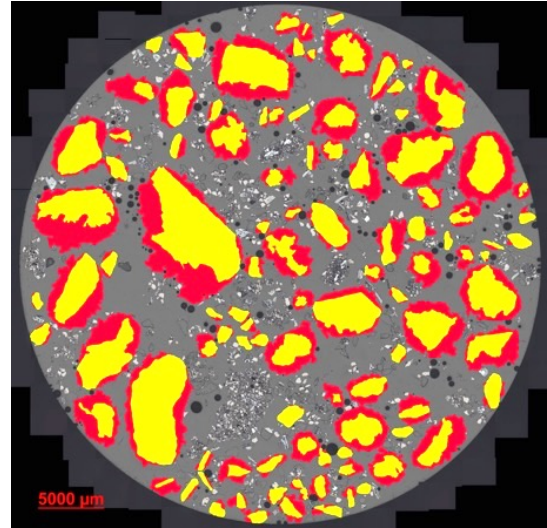


Figure 3.17 – Example microscopic image of granules in cross-section with nuclei and layers outlined

The measurements that were required from image analysis of the granules were the number and area of layering, nuclei and ‘non-layered’ particles. The edited images (Figure 3.17) were segmented using threshold segmentation to separate the layers, nuclei and ‘non-layered’ particles. Binary images were then produced, which only displayed the features of interest. Figure 3.18 to 3.20 show example binary images of these features. Measurements were then taken using the Axiovision image analysis software to determine the number and area of particles in each image.

Average layer thickness was measured as the average layer area per nuclei. This was obtained by dividing the sum of the layering particle areas by the total number of nuclei particles. The sum of the areas of ‘non-layered’ particles was used as a measure for the proportion of ‘non-layered’ particles in the bed. All of these measurements were used in combination with the GSD data generated through the method in Section 3.2.4 to aid result discussion. Appendix 9.1 summarises the method used.

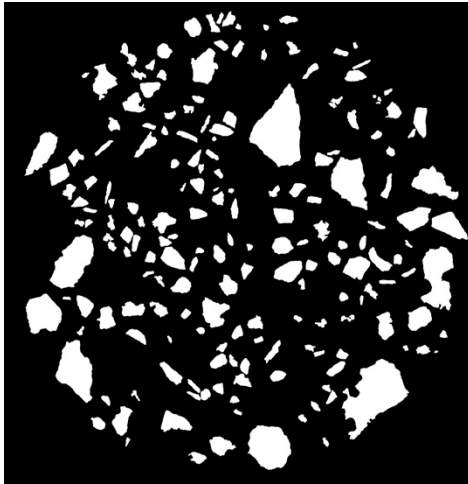


Figure 3.18 – Nuclei particle binary image produced by Axiovision image analysis software

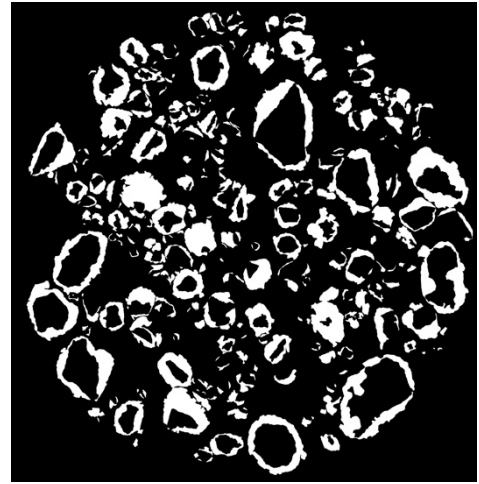


Figure 3.19 – Layering particle binary image produced by Axiovision image analysis software

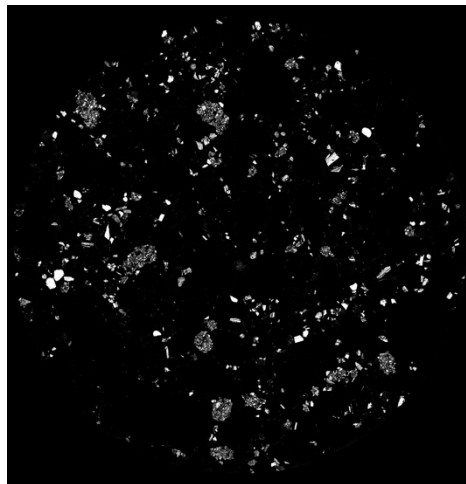


Figure 3.20 – 'Non-layered' particle binary image produced by Axiovision image analysis software

3.2.6 'Cold' permeability and efficiency

The 'cold' permeability of the sinter beds was measured using the apparatus shown in Figure 3.21. 'Cold' permeability efficiency (Equation 8), which relates to how efficient the bed is at maintaining its 'cold' permeability after undergoing movement was also measured in this apparatus. This is a new measurement developed in-house for this research and involves vibrating the bed on a Haver and Boecker Digital Plus sieve shaker (Figure 3.1) on setting 4 for 10 seconds and the 'cold' permeability measurement repeated. The key purpose was to provide indication into the 'cold' permeability changes of beds under movement and can be linked to the movement of

the bed on the sintering strand. This is particularly important as a bed may have 'good' initial 'cold' permeability but as soon as movement is applied shows a significant reduction. Even though this cannot be considered as an exact imitation of the bed movement on the sintering strand this procedure serves to replicate a similar effect in identifying the beds sensitivity to change in the 'cold' permeability under an applied movement.

$$\text{'Cold' Permeability Efficiency (\%)} = \frac{\text{'Cold' permeability after movement}}{\text{'Cold' permeability}} \times 100 \quad (8)$$

The key features of the 'cold' permeability apparatus in Figure 3.21 include a flow meter and pressure gauges to provide the measurements for 'cold' permeability. 'Cold' permeability was determined using the Ergun equation (Equation 2), which was introduced in Section 2.2.2 with the exact method introduced in the next subsection. Further features of the apparatus include the granule bed, which is in a 45cm long cylinder and the vacuum, which provides the suction through the bed to achieve the pressure drops required to calculate a 'cold' permeability measurement. An illustration of the bed and measurement devices is detailed in Figure 3.22. The 'cold' permeability measurement is an automated process. The vacuum is connected to a variable speed drive, which is connected to a programmable logic controller (PLC) and in-house developed software. Once the cylinder is filled with granules, measurement devices attached and the software started the flow rates for the required pressure drops (0, 40, 80, 120, 140mbar) are produced. Appendix 9.1 summarises the method used.

An example of the flow rate and pressure drop measurements before and after movement is shown in Figure 3.23. A reduction in flow rate and thus 'cold' permeability after movement can be observed. This will be the case in any similar system and thus the 'cold' permeability efficiency will never be greater than 100%.

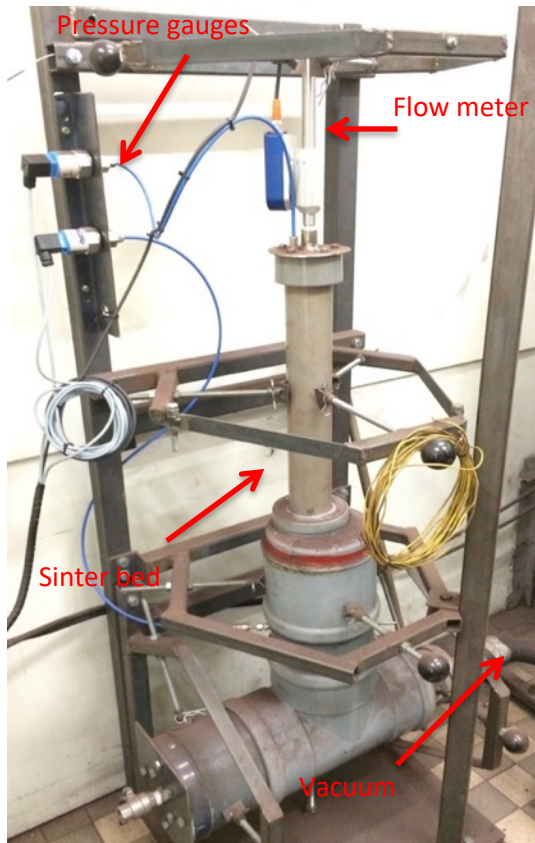


Figure 3.21 – ‘Cold’ permeability and efficiency test equipment (TATA Steel Europe RD&T)

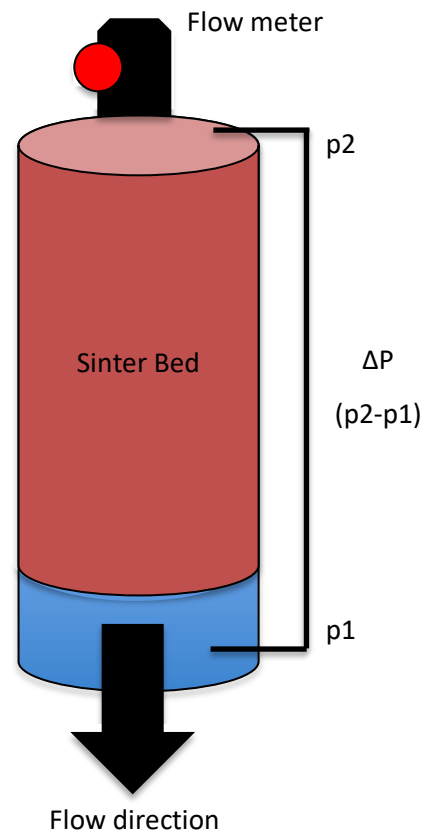


Figure 3.22 – Diagram of sinter bed and measurement devices for ‘cold’ permeability

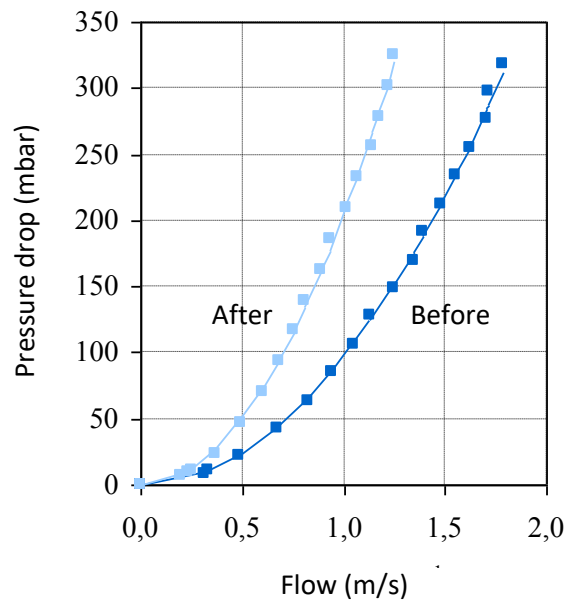


Figure 3.23 – Example ‘cold’ permeability measurements before and after movement (Favre and Kooij 2013)

Ergun equation permeability measurement

An example of the gas flow velocity and pressure drop measurements provided by the 'cold' permeability equipment is shown in Figure 3.23. However, this does not give a single measurement for the 'cold' permeability of sinter beds. For this reason, a method needs to be employed to provide a permeability value of the bed that can allow comparison between blends. The Ergun equation (Equation 2) uses the parameters that are supplied by the 'cold' permeability equipment (gas flow velocity (U) and pressure drop (ΔP)). The mean granule diameter (d_p) can be determined through applying the Rosin-Rammler distribution (Equation 6) to the granule size distribution measurements (Section 3.2.4). The height of the bed (L) is initially measured once in the apparatus and then is measured again after movement on the Haever and Boecker Digital Plus sieve shaker. Other parameters in the equation remain constant throughout testing such as the gas viscosity (μ), gas density (ρ) and shape factor (ϕ). The only unknown parameter left is bed voidage (ϵ). As there is only one variable left in the equation then this parameter can be varied using a similar Microsoft Excel™ solving method as presented with the Rosin-Rammler distribution and design of Fuller-Thompson blends (Section 3.2.1 and 3.2.2). This was to obtain the optimum fit between the curve from the gas flow velocity (U) and pressure drop (ΔP) measurements and that from the Ergun equation (Equation 2). To realise this process example data is provided in Figure 3.24 with the method emphasised as follows.

When evaluating Figure 3.24 we can identify the gas flow velocity (U) and pressure drop (ΔP) measurements provided by the 'cold' permeability equipment. The ΔP -norm column is the pressure drop normalised per meter, which is known by the bed height (L) and allows different bed heights to be analysed in the same method. The gas flow velocity (U) and normalised pressure drop (ΔP -norm) determined from the test can be considered as the measurement data set which we need to fit to the Ergun equation. A plot of this data is shown in Figure 3.25 labelled ΔP -norm. To fit the test data with the Ergun equation some further explanation is required into Figure 3.24. The pressure drop (ΔP -fit) is determined from the Ergun equation and utilises all the relevant parameters to provide each of the values in this column. The sum of the squared errors cell (SSE) is measured as the sum of square residuals between the normalised pressure

drop (ΔP -norm) and that determined by the Ergun equation (ΔP -fit). The SSE cell is to be minimised to optimally fit the Ergun equation to the measurement data. The SSE value is to be minimised by changing the only remaining unknown parameter in the equation, bed voidage (ϵ). Utilising the Microsoft Excel™ solver varies the bed voidage to minimise the SSE and provide the pressure drop values (ΔP -fit) from the equation that best fit the test data (ΔP -norm). The fitted pressure drop curve is labelled in Figure 3.25 as ΔP -fit. In Figure 3.24 the cells labelled C and D simply relate to the total of the two functions of the gas flow velocity (U) in Equation 2 and is also often used in other notations of the Ergun equation.

C	22132.34	dp (m)	0.003
D	62379.16	ϵ	0.20
		SSE	649.03
Height (cm)	32	250	0.48

U m/s	ΔP mbar	ΔP -norm mbar/m	ΔP -fit mbar/m	Error ²
0.00	0.00	0.00	0.00	0.00
0.33	39.79	124.34	139.70	235.94
0.40	60.56	189.25	187.62	2.67
0.49	78.03	243.84	258.22	206.70
0.55	99.20	310.00	308.61	1.93
0.61	120.77	377.41	363.20	201.80

Figure 3.24 – Example of the method to calculate sinter bed ‘cold’ permeability from the Ergun equation

To obtain a single measurement for the ‘cold’ permeability of the bed the gas flow velocity (U) at a certain pressure drop was determined. This was 250mbar/m on the fitted test data curve (ΔP -fit) and is representative of plant operations at TATA Steel Europe. ‘Cold’ permeability was classed as the gas flow velocity through the bed at 250mbar/m and for the example data in Figure 3.24 and 3.25 is 0.48m/s. Appendix 9.1 summarises the method used.

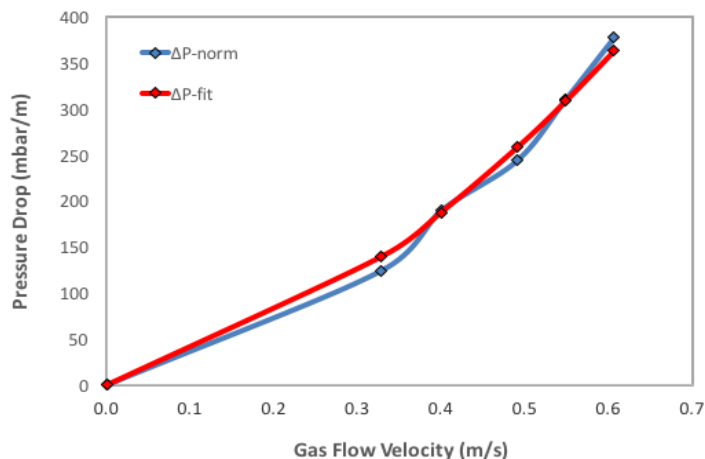


Figure 3.25 – Graph showing test flow rate and pressure drop data (ΔP -norm) fitted to the Ergun equation (ΔP -fit)

3.2.7 Sintering

The RD&T sintering equipment at TATA Steel Europe provides a laboratory scale simulation of the process. The sinter pot is a cylindrical shaped sintering unit of 120mm diameter and 450mm height, which was manufactured in-house and is detailed in Figure 3.26. The equipment is a batch replication of the plant sintering process with various measurement devices attached. Like the 'cold' permeability equipment (Section 3.2.6) these include a flow meter and pressure gauges to obtain gas flow velocity and pressure drop measurements throughout the test. Approximately 6kg of granules were charged into the sintering equipment over a 20mm hearth layer. The top layer was ignited for 3 minutes with compressed air and natural gas at a pressure drop across the bed of 120mbar (266mbar/m). Once ignited the flow meter was reattached so that the gas flow velocities for the 'hot' permeability measurement could be recorded. There are 5 thermocouples that are placed throughout the bed in 7.5cm intervals with a further 3 in the gas extraction system to provide accurate measurements of the off-gas temperatures. The measurement devices all feedback to a central control system with an interface, which displays the data in-situ and records it in a data file. All measurement readings are taken at 5 second intervals. The flow required to create the pressure drops over the bed was provided by suction from an internal fan system, which the equipment has been tapped into. Appendix 9.1 summarises the method used.

An example of the data recorded and displayed on the control system interface is shown in Figure 3.27. The measurements include the temperature profiles of all thermocouples (H1-H5) and gas flow velocity through the bed at a pressure drop of 120mbar (266mbar/m) throughout the test. The 'rookgas' or off-gas temperature profiles are also shown (TI-006 – TI-008). The initial period of the test, where no temperature or gas flow velocity change is witnessed is the ignition period. The control system interface allows in-situ monitoring of the process and manipulates the measurements into one data file for further analysis, which is explained in the remainder of this section.

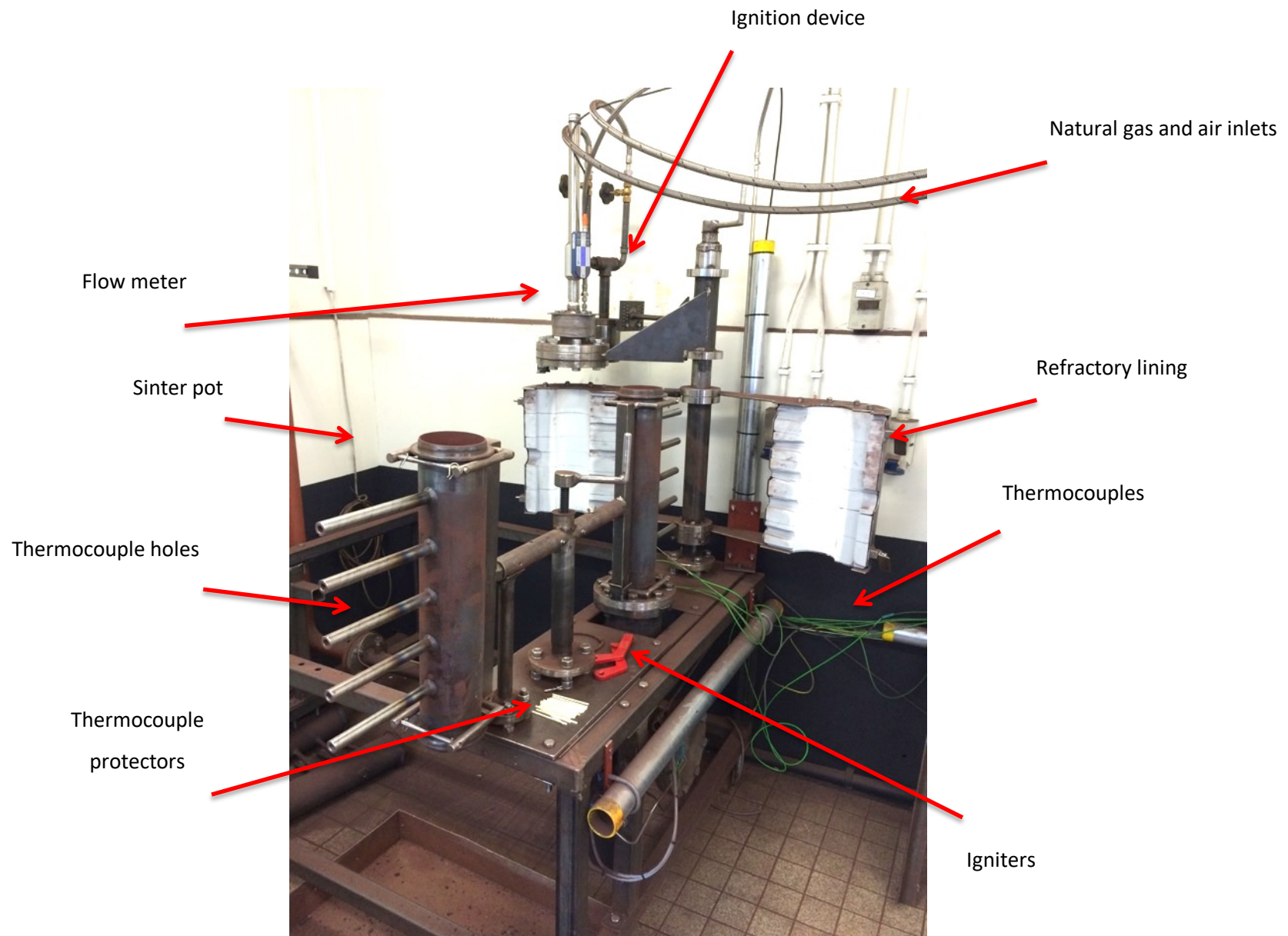


Figure 3.26 – Image of sintering equipment (TATA Steel Europe RD&T)

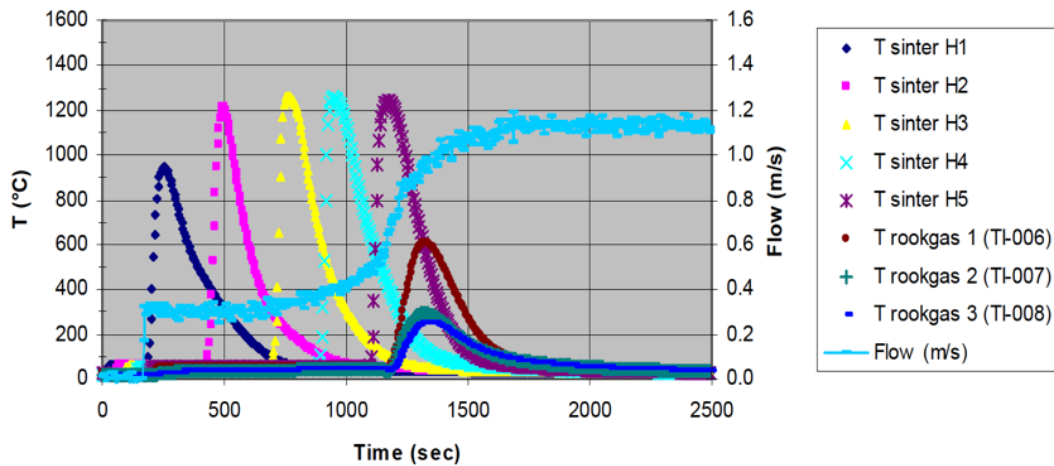


Figure 3.27 – Example results on sintering equipment interface

‘Hot’ permeability and efficiency

Further handling of the data from the sintering equipment is required to determine the ‘hot’ permeability and ‘hot’ permeability efficiency. Primarily, the ‘hot’ permeability is like the ‘cold’ permeability introduced in Section 3.2.6 but concerns the permeability of the bed when sintering has initiated. ‘Hot’ permeability was measured in a similar method as with ‘cold’ permeability. However, where the method differs is that the gas flow velocities at only one pressure drop across the bed are measured (120mbar). During the sintering process the pressure drop across the bed is held constant and is representative of that in plant operations. To obtain a measure of ‘hot’ permeability the flow rate is averaged when the flow rates are at their most stable. Throughout the process the ‘hot’ permeability of the bed is changing due to the less permeable granule bed being converted into more permeable sinter. From Figure 3.27 the stable gas flow velocity period can be observed and usually occurs between the peak temperatures of thermocouples H1 and H3. The gas flow velocities measured between these thermocouples are used to calculate the average gas flow velocity. The pressure drop across the bed is constant (120mbar), therefore abiding by the same method as described in Section 3.2.6 the pressure drop and average gas flow velocity are fitted to the Ergun equation to obtain a measure for the ‘hot’ permeability of the bed.

'Hot' permeability efficiency is a new property of sinter beds that is proposed and has been developed in this study. Its purpose is to provide a measure for how efficient sinter beds are at transferring the initial 'cold' bed permeability through to 'hot' permeability during sintering. This is similar to the 'cold' permeability efficiency, which was introduced in Section 3.2.6. The rationale behind developing this measurement is because beds may exhibit different permeability performance when moving from a 'cold' bed to a 'hot' bed where sintering has initiated. For example, a bed may have high 'cold' permeability but consists of weaker granules that lead to bed collapse during the process creating low 'hot' permeability, thus, providing a means to compare this bed property from the blends under investigation. From Equation 9 it can be observed that the only measurements required to calculate 'hot' permeability efficiency are 'cold' and 'hot' permeability. The methods behind these measurements have already been detailed, thus no further explanation of the hot permeability efficiency calculation is required.

$$\text{'Hot' Permeability Efficiency (\%)} = \frac{\text{'Hot' permeability}}{\text{'Cold' permeability}} \times 100 \quad (9)$$

Production rate

The production rate from the sintering equipment relates to the time taken for the bed to be completely sintered. As this is a batch imitation of the process then this would occur once the flame front has passed through the bed (burn through point). The most appropriate means to determine this time is when the first off-gas thermocouple (TI-006) reaches its peak temperature. The first off-gas thermocouple is positioned close to the bottom of the bed thus the peak temperature of this thermocouple must be when the flame front is in closest proximity and has passed through the bed. From Figure 3.27 the peak temperature of thermocouple TI-006 can be distinguished, which can then be related to the time in the test where this occurs. This time is classed as the time required for the sintering process to complete and therefore production rate for the sintering equipment in this study.

3.2.8 Sinter cold strength

The cold strength of sinter has been emphasised in sinter properties to be part of sinter quality evaluation (Section 2.2.6). It is an important property of sinter, as when the sinter degrades during handling this produces sinter return fines. Consequently, as the sinter cold strength decreases this increases the amount of return fines for the process and decreases the net process productivity. A method has been developed to replicate the handling that sinter endures at laboratory scale. The sinter is tumbled in a drum with internal lifting flights for 50 revolutions (Figure 3.28). The motion impacts the sinter against itself and the drum walls breaking it into smaller sized fractions. To allow the comparison of the sinters sieve analysis was conducted on the tumbled product through the following series using a large-scale sieve shaker; >40mm, <40mm >20mm, <20mm >15mm, <15mm >10mm, <10mm >5mm, <5mm >3.15mm, <3.15mm >1mm and <1mm. From the sieve analysis sinter size distribution properties, such as mean and median sinter diameters can be determined. Also of interest with return sinter fines is the amount of material under a certain size fraction. In this research sinter that is <5mm is classed as return sinter fines. Appendix 9.1 summarises the method used.



Figure 3.28 – Sinter cold strength drum (TATA Steel Europe RD&T)

3.2.9 Sinter chemical composition

Sinter chemical composition was determined by the same XRF method as detailed in iron ore chemical composition (Section 3.2.2). Sample preparation was conducted by

milling a representative sinter sample, which was created by using a riffing box. 5g of milled sinter was required for XRF analysis.

3.2.10 Sinter mineralogy

Sinter mineralogy was determined by the same XRD method as detailed with iron ore mineralogy (Section 3.2.2). Sample preparation was conducted by milling a representative sinter sample, which was created by using a riffing box. 5g of milled sinter was required for XRD analysis.

Chapter 4 – Pilot Plant Testing

4.1 Iron ore characterisation

The materials required for this study were introduced in Section 3.1 with the methods used for characterisation later presented in Section 3.2.1. Attention was applied to the iron ores, as this was the only varying component in the blends. The proportions of the other blend materials; coke breeze, flux and return sinter fines were held constant and therefore excluded from the characterisation process. Their description and chemical composition however was presented in Table 3.1 and 3.2.

4.1.1 Particle size distribution

The cumulative particle size distribution (PSD) of the iron ores fitted with the Rosin-Rammler distribution are displayed in Figure 4.1. Figure 4.1 provides the ores PSD, where various size categories can be identified. Table 4.1 shows the mean diameter (D_m) and spread of particle sizes in the distribution (n) of the ores. Ore D is the finest ore ($D_m = 0.03\text{mm}$) and is classed as a pellet feed as indicated in Section 3.1. Ore B and Ore C are classed as concentrated ores, which have narrower PSD spreads ($n = 1.99$ and 2.34 respectively) and are in an intermediate size range when compared to Ore A and Ore D. Ore A is a conventional sinter feed ore, which has the largest mean diameter ($D_m = 1.55\text{mm}$) and widest spread of particle sizes in the distribution ($n = 0.58$).

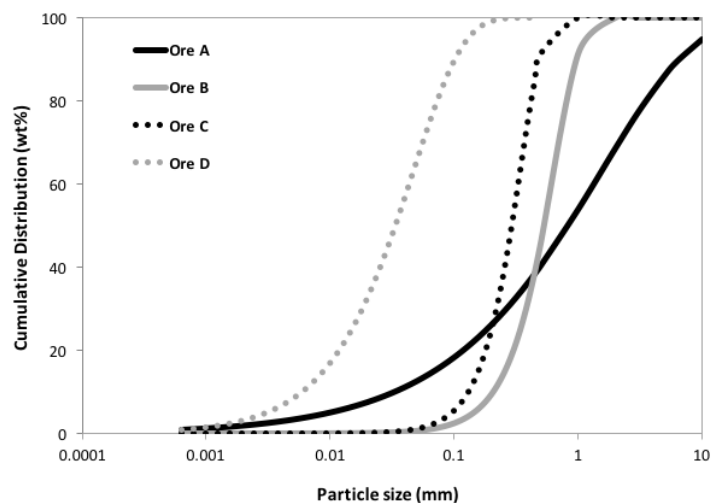


Figure 4.1 – Cumulative particle size distribution of iron ores fitted with the Rosin-Rammler equation

Table 4.1 – Iron ore PSD properties

Material	Ore A	Ore B	Ore C	Ore D
Mean diameter (D_m) (mm)	1.55	0.64	0.34	0.03
Spread of particle sizes (n)	0.58	1.99	2.34	1.27

The PSD properties of the ores (<0.5mm) are shown in Table 4.2. Ore A provided the widest layering PSD spread (n = 0.76). Ore D had the finest layering particles (D_m = 0.03mm) and a narrower PSD spread (larger n) than Ore A. Ore B and Ore C layering particles were the coarsest (D_m = 0.37mm and 0.31mm respectively) and had the narrowest layering PSD spread (n = 3.21 and 2.57 respectively). The differing layering PSD spreads of the ores allowed the construction of the blends presented in Section 3.2.2 to evaluate the influence of layering PSD spread in blends on the key granule and sintering process measurements.

Table 4.2 – Iron ore PSD properties of layering particles

Material	Ore A	Ore B	Ore C	Ore D
Mean diameter (D_m) (mm)	0.16	0.37	0.31	0.03
Spread of particle sizes (n)	0.76	3.21	2.57	1.27

4.1.2 Qualitative description of particle shape

Microscopic images of the iron ores were produced and qualitative shape characterisation conducted based on the categories shown in Figure 3.5. The objective was to realise any differences in ore particle shape to aid discussions in results analysis.

The microscopic images of the ores are presented in Figure 4.2 to 4.5. Qualitative analysis on the particle shape of the ores was conducted individually with an evaluation on the impact that the differing shapes may have on granulation later.

- **Ore A:** This ores shape is classed as irregular. These particles exhibit a more spherical shape with convex and concave features, which are unlike the straighter edges of the other ores.
- **Ore B:** This ores shape is classed as a combination of tabular and equant. These particles are angular and show less roundness but do display some convex and concave features.
- **Ore C:** This ores shape is classed as tabular. These particles have the highest angularity, are least spherical and have the straightest edges. These particles have the least convex or concave features.
- **Ore D:** This ores shape is classed as tabular. These particles are similar in shape to Ore C, however display less angularity.

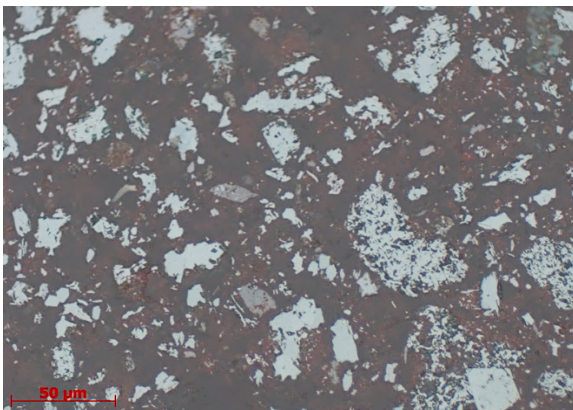


Figure 4.2 – Microscopic image of Ore A

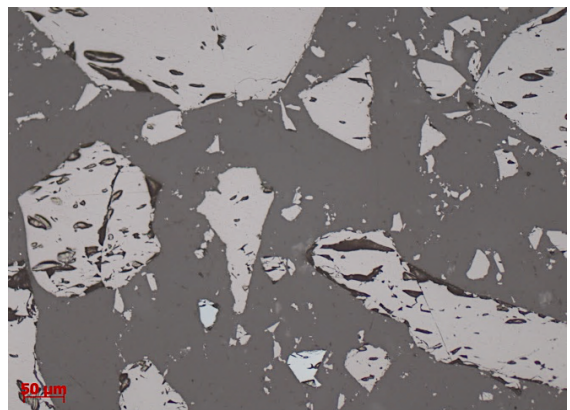


Figure 4.3 – Microscopic image of Ore B

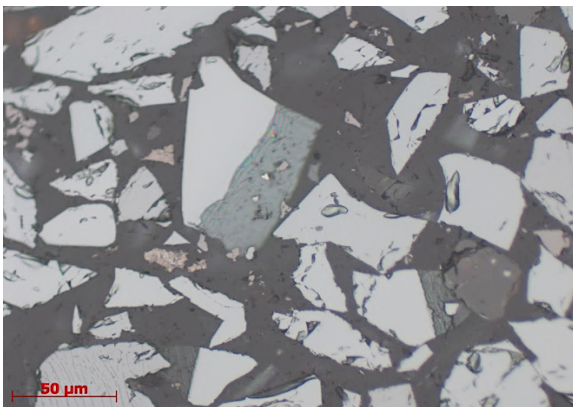


Figure 4.4 – Microscopic image of Ore C

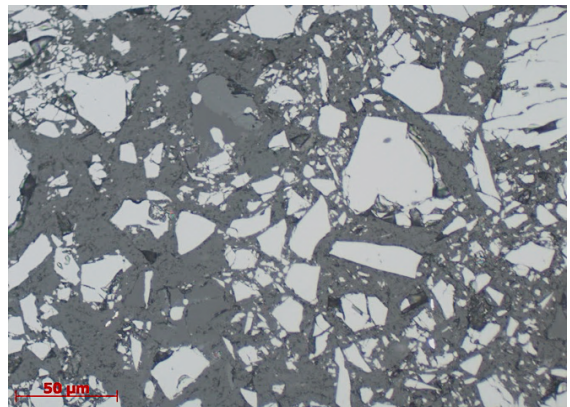


Figure 4.5 – Microscopic image of Ore D

The layering PSD of the blends is the main area of focus in this study. Particle shape has been shown to impact the layering of particles around nuclei during granulation. From Wu et al. (2015) it was presented that less spherical particles embed better with each other within the layer, which was attributed to the greater number of particle contact points (Figure 2.24). This suggests that particles of Ore C and Ore D would be beneficial layering, as they are more tabular than Ore B and not as spherical as Ore A. It is difficult to draw any further conclusions on the how the differing ore shapes presented may impact their layering ability, as minimal further research has been conducted into how this particle property impacts granulation in the past.

4.1.3 Chemical composition

The chemical composition of the iron ores determined by XRF are displayed in Table 4.3. Most notably from Table 4.3 was the differences in FeO and SiO₂. With regards to FeO it will become apparent in mineralogical characterisation (Section 4.1.4) that Ore B and D are magnetite ores, whereas Ore A and Ore C are hematite. The chemical notation of hematite is Fe₂O₃ whereas magnetite is Fe₃O₄, which can also be symbolised as FeO.Fe₂O₃. Naturally magnetite ores have a higher FeO (Fe²⁺) concentration than hematite ores. Thus, a higher FeO concentration is found in magnetite ores like Ore B and Ore D. The small amounts of FeO found within the hematite ores arise from the fact that these ores are not completely pure hematite and therefore will contain a proportion of magnetite and therefore FeO in their chemical composition.

Table 4.3 – Chemical composition of iron ores

Material	Chemical composition (wt%)								
	Fe _{total}	FeO	Al ₂ O ₃	SiO ₂	CaO	MgO	C	P	LOI
Ore A	65.71	0.05	1.48	1.58	0.02	0.05	0.04	0.06	-2.14
Ore B	70.55	29.27	0.27	0.73	0.21	0.36	0.01	0.02	+3.13
Ore C	62.56	0.67	1.37	5.13	1.32	0.52	0.32	0.03	-1.15
Ore D	63.28	27.30	0.43	10.70	0.51	0.51	0.06	0.01	+2.70

It can also be observed from Table 4.3 that the SiO₂ contents of the ores differ. This is a result of the ores global origin. Ore D has 10.7wt% SiO₂, which was significantly higher

than the other ores. The amount of SiO₂ in ores is a characteristic that needs constant monitoring during plant operations. This is because the SiO₂ level in the blend has a direct impact on sinter basicity ($\frac{\text{CaO}+\text{MgO}}{\text{SiO}_2}$).

This study solely focuses on the design of blends from a PSD rather than chemical perspective, thus no specific FeO or basicity ($\frac{\text{CaO}+\text{MgO}}{\text{SiO}_2}$) values of the sinter were aimed for when designing the blends for investigation. However, it is acknowledged that designing blends for plant operations would have chemical constraints that would need adhering to.

4.1.4 Mineralogy

The mineralogy of the iron ores was analysed by the XRD. The XRD data and subsequent Reitveld analysis was utilised to describe the mineralogy of the iron ores. Mineralogical characterisation was also used in Section 4.1.6 to aid characterisation of ore wettability.

- **Ore A:** Nearly pure hematite ore (Fe₂O₃) with only small amounts of magnetite (0.7wt%). Large proportions of fine-grained recrystallized hematite bands and contains 3.1wt% gangue minerals. The gangue minerals are majority gibbsite (Al(OH)₃) but with a small proportion of quartz (SiO₂).
- **Ore B:** Pure coarse grained crystalline magnetite ore (Fe₃O₄) with no primary hematite. This ore contains 3.6wt% of various gangue silicate minerals.
- **Ore C:** Specular coarse grain crystalline hematite ore (Fe₂O₃) with magnetite (Fe₃O₄) present (5wt%). Contains 9wt% silicate gangue minerals.
- **Ore D:** Nearly pure fine grained crystalline magnetite ore (Fe₃O₄) with small amounts of hematite (0.01wt%). Composed of 10.43wt% silicate gangue minerals.

4.1.5 Density

The density of the iron ores is presented in Table 4.4. Initially, it can be observed that the ‘true’ density of the ores including all pores (helium method) were similar. These values range between 4890-5088kg/m³. When comparing the helium and water methods for Ore A, Ore B and Ore C then there was minimal difference. This suggests that the majority of the pores in these ores were found on the particle surface, as the water method filled more of the pores that the helium method could. The exception is Ore D, which showed a greater difference in densities when measuring only surface pores (water method) and all pores (helium method). The lower density of Ore D when only measuring surface pores shows that this ore contained more pores that are not accessible to water when compared to the other ores.

Table 4.4 – Density of iron ores

Method	Ore A (kg/m ³)	Ore B (kg/m ³)	Ore C (kg/m ³)	Ore D (kg/m ³)
Helium pycnometry	4890	5088	4962	4949
Water pycnometry	4857	5061	4966	4132

4.1.6 Wettability

The characterisation on the wettability of the iron ores was based on particle shape and mineralogy in combination with previous studies. Qualitative conclusions have been drawn on the ores individually.

- **Ore A:** Analysing the images of particle shape (Figure 4.2 to 4.5) it can be identified that Ore A had the least straight and roughest edges of the ores. This stemmed from the weathering of this ore during the transformation from magnetite (Fe₃O₄) to hematite (Fe₂O₃) in the earth. Rougher particle surfaces have higher wettability than smooth glossy crystalline surfaces (Maeda et al. 2005), suggesting that Ore A was the most hydrophilic of the ores. The greater proportion of goethite (FeOOH) in Ore A also implied that this ore was more easily wetted than the other ores, as studies have proven that increasing goethite reduces the contact angle (Melzer and Zinngrebe 2005).

- **Ore B:** The nearly pure magnetite (Fe_3O_4) mineralogy suggests that this ore has lower wettability than Ore A and Ore C, which are hematite (Fe_2O_3). Ore B has no goethite (FeOOH) present, which is reported to increase the contact angle and lower the wettability of the ore (Melzer and Zinngrebe 2005).
- **Ore C:** The specular nature of this hematite ore (Fe_2O_3) suggests that it has reduced wettability compared to Ore A. Smooth glossy crystalline surfaces have been reported to reduce the wettability when compared to rougher surfaces (Maeda et al. 2005). No goethite (FeOOH) was identified in the mineralogy, which again indicates an increase in the contact angle and lower wettability of this ore when compared to Ore A (Melzer and Zinngrebe 2005).
- **Ore D:** The nearly pure magnetite (Fe_3O_4) mineralogy suggests that this ore has lower wettability than Ore A and Ore C (Melzer and Zinngrebe 2005). No goethite (FeOOH) was found in the mineralogy thus increasing the contact angle and lowering wettability. The combination of these properties suggests that Ore D had a similar wettability as Ore B.

It can be concluded that Ore B and Ore D would have similar wettability and be the most hydrophobic of the iron ores used. Ore B and Ore D are magnetite (Fe_3O_4) and contain no goethite (FeOOH). All these properties have been documented to lower particle wettability (Melzer and Zinngrebe 2005). It is thought that Ore C would be the next hydrophobic of the ores. Ore C is a hematite ore but is also specular in nature, which indicates smooth glossy crystalline surfaces and were reported to reduce particle wettability (Maeda et al. 2005). Ore A is considered as the most hydrophilic of the ores, predominantly due to its hematite nature and increased goethite proportions.

4.2 Determining the Fuller-Thompson equation parameters

4.2.1 Maximum layering particle size (D)

The choice of the maximum layering particle size (D) used in the Fuller-Thompson (FT) equation for sinter blend design was based on microscopy and literature. Microscopic images on the granules from the base (BB) blend were produced in accordance with the method in Section 3.2.5. The largest layering particles were measured using image analysis software. Figure 4.6 shows a sample image with a granule composed of nucleus and layering particles. It was identified that the largest layering particles were approximately 500 μm (0.5mm). Particles significantly larger than this were not present in the layers in the granule cross-section. Previous studies have classified the behaviour of particles based on size and a commonly utilised value for the maximum layering particles size was 0.5mm (Bergstrand et al. 2005; Gan et al. 2015). With verification through granule image analysis, 0.5mm was the value selected as the best estimation for the largest layering particle size (D) in the FT equation for blend design (Equation 10).

$$P = \left(\frac{d}{0.5} \right)^{\Psi} \times 100 \quad (10)$$

where: P = percentage mass less than d (%)

d = particle size (mm)

Ψ = exponent

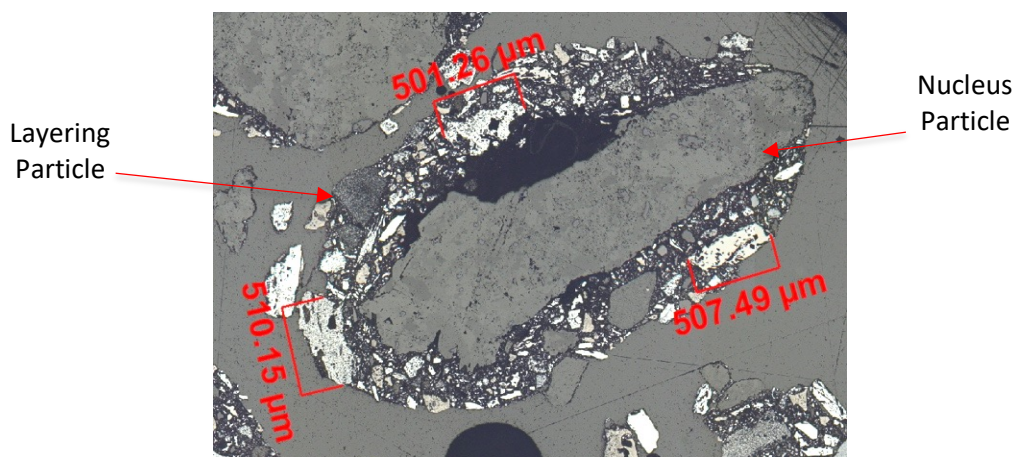


Figure 4.6 – Microscopic image of granule from the base (BB) blend

4.2.2 Fuller-Thompson exponent (Ψ)

Many previous studies in Section 2.1 were directed towards investigating the exponent (Ψ) of the FT equation that provided the optimum material performance. Due to the new application of the FT equation in sinter blend design several FT exponents were investigated (0.3, 0.4, 0.5 and 0.6). The layering proportion of the blends (<0.5mm) designed for the FT exponents were presented in Table 3.3. Evaluating the performance of the FT exponents used bimodal blends of a one-part nuclei (return fines <3.15mm >1mm) and one-part layering (<0.5mm) particles. The layering PSD of the blend was the only variable, thus could be the only factor leading to different granule properties. The blends were mixed and granulated at a range of moisture contents before assessing 'cold' permeability and 'cold' permeability efficiency.

'Cold' Permeability

The results in Figure 4.7 of 'cold' permeability with moisture for the blends designed with differing FT exponents (Ψ) fitted a parabolic trend line. The relationship between 'cold' permeability and moisture was similar to that shown in previous studies (Ellis et al. 2007), which also reported a parabolic trend. The results show an initial increase in 'cold' permeability with moisture before an optimum was reached in all cases. Further increases in moisture decreased the 'cold' permeability for all blends. From Figure 4.7 the differing 'cold' permeability behaviour of the FT exponents can be observed. Trends between the FT exponents and 'cold' permeability were identified. As the FT exponent decreased the optimum 'cold' permeability increased. The optimum 'cold' permeability ranged from 1.1m/s ($\Psi = 0.6$) to 1.75m/s ($\Psi = 0.3$). Based on the parabolic trend lines and except for $\Psi = 0.3$ the moisture at optimum 'cold' permeability increased as the FT exponent decreased. An increase in the sensitivity of 'cold' permeability to moisture was also observed with decreasing FT exponent. The results prove that the FT exponent and layering PSD had a significant impact on the granulating behaviour and 'cold' permeability of the blends.

It was appropriate to obtain further understanding of the driving factors behind the differing 'cold' permeability behaviour of the blends with differing FT exponents. A key

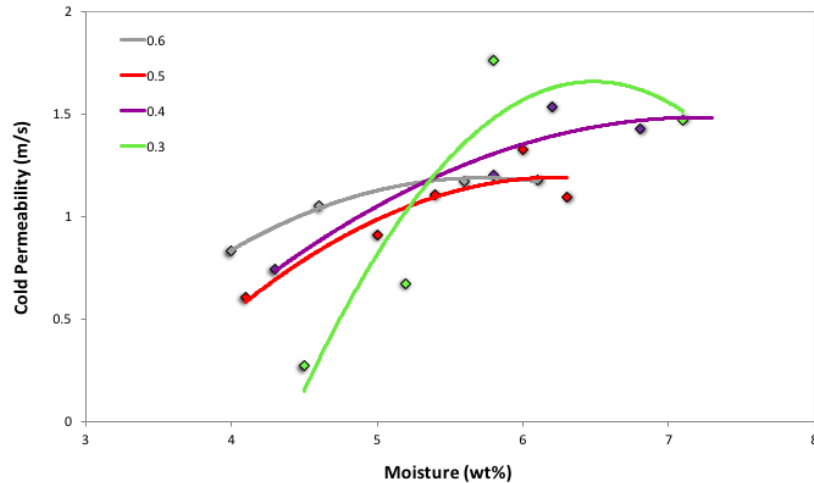


Figure 4.7 – ‘Cold’ permeability of blends with differing FT exponents (Ψ)

granule property is size distribution. Figure 4.8 shows a strong relationship between granule size distribution (GSD) spread (n) and ‘cold’ permeability. The three points for each FT exponent in Figure 4.8 represent the three moisture contents of the blends as shown in Figure 4.7 up to and including the optimum ‘cold’ permeability or moisture. The GSD spread was determined by applying the Rosin-Rammler distribution to the GSD measurements. Narrowing the GSD spread (increasing n) correlated with increasing ‘cold’ permeability for all FT exponents. The optimum ‘cold’ permeability was produced at the narrowest GSD spreads (largest n) and verifies the influence. It would be expected from Figure 4.8 that the lower the FT exponent the narrower the GSD spread (larger n) due to increased optimum ‘cold’ permeability. This was shown in Figure 4.8 except for the results of $\Psi = 0.3$ and 0.4 . The $\Psi = 0.4$ had the narrowest GSD spread (largest n) but lower optimum ‘cold’ permeability compared to $\Psi = 0.3$. This was attributed to the error in the GSD measurement and determining the GSD spread.

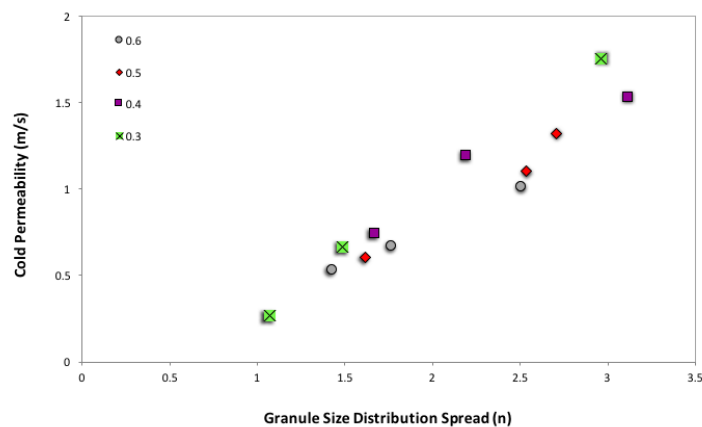


Figure 4.8 – Relationship between ‘cold’ permeability and granule size distribution spread (n) for blends with differing FT exponents (Ψ)

Blends with differing FT exponents achieve narrower GSD spreads due to their layering PSD. As stated these are bimodal systems with a constant nuclei proportion, which enables distinction between the mass of particles that are (>1mm) and have not layered (<1mm) around nuclei. The GSD measurements at optimum 'cold' permeability for each FT exponent were utilised to produce Figure 4.9. It can be observed from Figure 4.9 that the mass of particles passing the 1mm sieve size ('non-layered') decreased as the FT exponent decreased. The consequence was an increase in the mean granule diameter (D_m), which can also be seen in Figure 4.9.

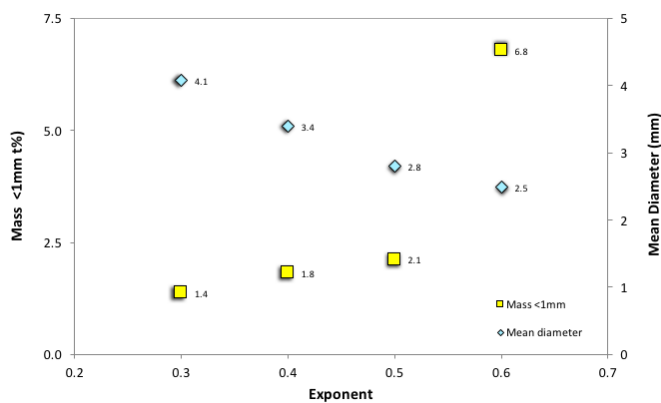


Table 4.5 – Layering PSD properties for FT exponents (Ψ)

	0.3	0.4	0.5	0.6
Spread (n)	0.65	0.70	0.76	0.87
Mean Diameter (D_m) (mm)	0.08	0.12	0.15	0.19

Figure 4.9 – Mass of particles <1mm and mean granule diameter (D_m) for differing FT exponents (Ψ) at optimum 'cold' permeability

Highlighted in Table 4.5 are the layering PSD characteristics of the blends with differing FT exponents. The layering PSD spread (n) is a measure of the uniformity of particle sizes in the distribution. This is determined by applying the Rosin-Rammler distribution, again the larger the n value the narrower the spread of particle sizes within the distribution. Table 4.5 shows that decreasing the FT exponent widened the layering

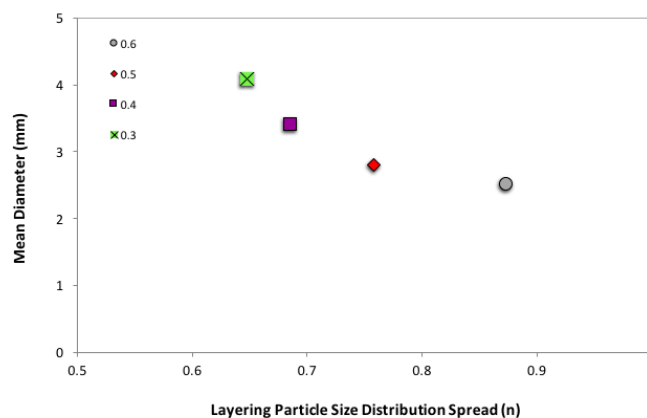


Figure 4.10 – Relationship between layering particle size distribution spread (n) and mean granule diameter (D_m) for the FT exponents (Ψ) at optimum 'cold' permeability

PSD spread (decreased n). The relationship between layer PSD spread and mean granule diameter (D_m) is presented in Figure 4.10. As the layer PSD spread widened (decreasing n) a larger mean granule diameter was created. The results in Figure 4.8 to 4.10 prove that widening the layering PSD spread increased the mean granule diameter and narrowed the GSD spread thus increasing optimum 'cold' permeability.

'Cold' permeability efficiency

Even though 'cold' permeability is considered as the principle property of a granule bed, the bed also needs to provide sufficient resistance to losses in permeability when on the sintering strand. If the bed were to collapse during movement on the strand and lose permeability, then this would be detrimental to the process. The 'cold' permeability efficiency of the blends designed with differing FT exponents at a range of moisture contents are shown in Figure 4.11. From Figure 4.11 the 'cold' permeability efficiency with moisture results again fitted a parabolic trend line, as similar to that seen with the 'cold' permeability (Figure 4.7). The parabolic trend showed an initial increase in 'cold' permeability efficiency with moisture before an optimum was observed, further increases in moisture caused a sharp decrease in the 'cold' permeability efficiency of the bed in all cases.

An interesting trait to consider in Figure 4.11 was that based on the parabolic trend lines a minor reduction in the optimum 'cold' permeability efficiency was observed when the FT exponent decreased. This was the opposite of the trend in 'cold' permeability shown in Figure 4.7. However, the similar relationship of increasing moisture at optimum 'cold' permeability efficiency as the exponent decreased was witnessed, which is explored in the next subsection. The reason for the optimum 'cold' permeability efficiency decrease with decreasing FT exponent was related to a factor introduced previously. Figure 4.10 showed an increase in the mean granule diameter (D_m) at optimum 'cold' permeability with decreasing FT exponent. The increase in mean granule diameter was attributed to a greater mass of particles layering around nuclei and less particles left 'non-layered' in the bed (Figure 4.9). In combination with the 'cold' permeability efficiency results in Figure 4.11 this proves that larger mean granule diameters lost more of their permeability under the applied movement.

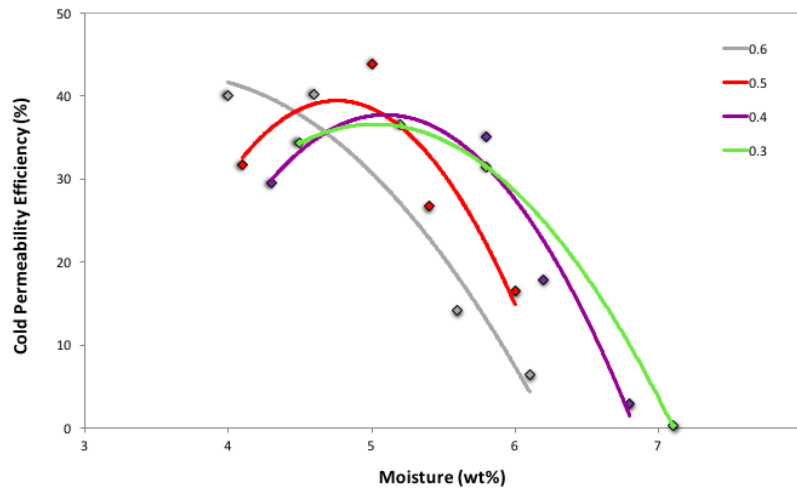


Figure 4.11 – ‘Cold’ permeability efficiency of blends with differing FT exponents (Ψ)

To emphasise this concept Figure 4.12 was produced and shows the relationship between mean granule diameter and optimum ‘cold’ permeability efficiency. It can be distinguished that an increase in mean granule diameter (D_m) decreased the optimum ‘cold’ permeability efficiency. Larger mean granule diameters showed less resistance to permeability losses, which was proposed to be due to the larger layers created displaying greater deformation and losing a larger proportion of their ‘cold’ permeability under movement. Previous studies suggested that layers in granules were relatively weak compared to the nuclei particles (Khosa and Manuel 2007) and this concept is proven from another study as shown in Figure 4.13 (Favre and Kooij 2013). Figure 4.13 shows similar behaviour to the ‘cold’ permeability efficiency results in Figure 4.11. It can be deduced from Figure 4.13 that as the fines or layering particle amount increased the ‘cold’ permeability before compaction did not change significantly. This suggests that the fines must have layered around the nuclei and

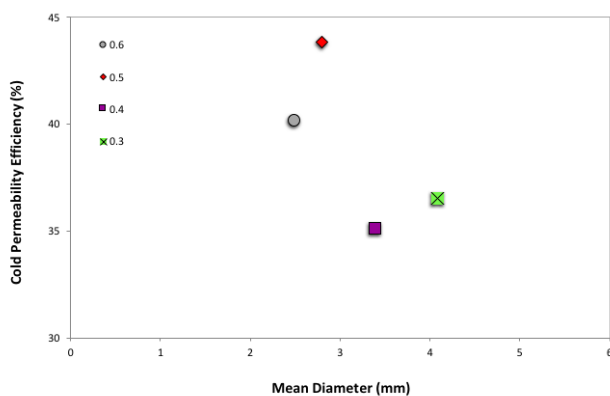


Figure 4.12 – Relationship between optimum ‘cold’ permeability efficiency and mean granule diameter (D_m)

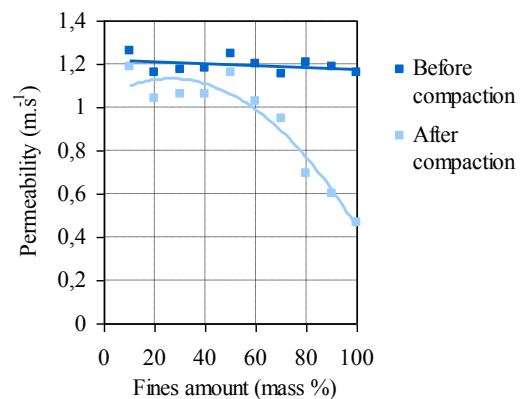


Figure 4.13 – ‘Cold’ permeability before and after compaction (Favre and Kooij 2013)

increased mean granule diameter to maintain 'cold' permeability. If the fines did not layer, then the GSD spread would have widened (decreased n) and reduced 'cold' permeability. It can then be identified that there was a significant decrease in 'cold' permeability after compaction with increasing fines or layering particles thus larger mean granule diameters. Thus, verifying the proposed concept that larger mean granule diameters created by larger layers of particles around nuclei lose more of their 'cold' permeability under the applied movement.

Optimum moisture

Optimum moisture relates to moisture content at which optimum 'cold' permeability and 'cold' permeability efficiency was reached. The optimum moisture for 'cold' permeability and 'cold' permeability efficiency of the blends with differing FT exponents (Ψ) are shown in Figure 4.14 and 4.15 and a similar trend can be realised in both. Optimum moisture was determined from the parabolic trend lines in Figure 4.7 and 4.11, which in some cases had to be estimated due to being outside the range of moisture contents used. A decrease in the FT exponent produced an increase in the optimum moisture for 'cold' permeability and 'cold' permeability efficiency (except $\Psi = 0.3$). The characteristics of the layering PSD of the blends with differing FT exponents shown in Table 4.5 identified the decrease in mean particle diameter (D_m) with decreasing FT exponent. It was previously determined that based on geometry there was an inverse relationship between particle diameter and total specific surface area (Equation 11) (Dubois et al. 2010). This equation proves that a decrease in the diameter of the particles correlates to a larger specific surface area. An increase in the total specific surface area of the particles can indicate more total surface pores available for the moisture to infiltrate. Thus, increasing the optimum moisture for 'cold' permeability and 'cold' permeability efficiency, as more moisture is required to make the particle surface wet, which was previously proven as the key parameter to initiate granulation (Litster and Waters 1988). The decreased mean particle diameter of the blends layering particles with decreasing FT exponent resulted in an increased blend total specific surface area. In conjunction with Figure 4.14 and 4.15 thus proving that more moisture was required to reach optimum 'cold' permeability and 'cold' permeability efficiency in blends with increasing total specific surface area.

$$\text{Specific surface area} = \frac{6}{(D \times \rho)} \quad (11)$$

where: D = diameter (m)

ρ = density (kg/m³)

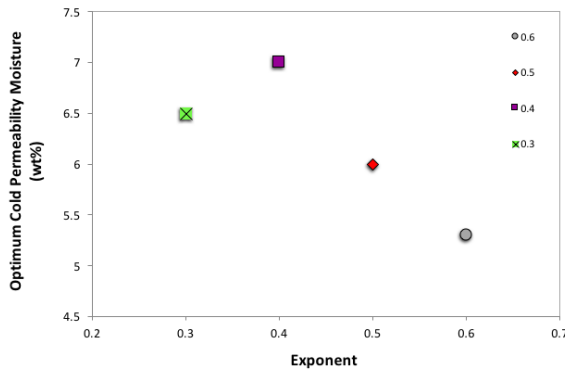


Figure 4.14 – FT exponent (Ψ) optimum moisture for ‘cold’ permeability

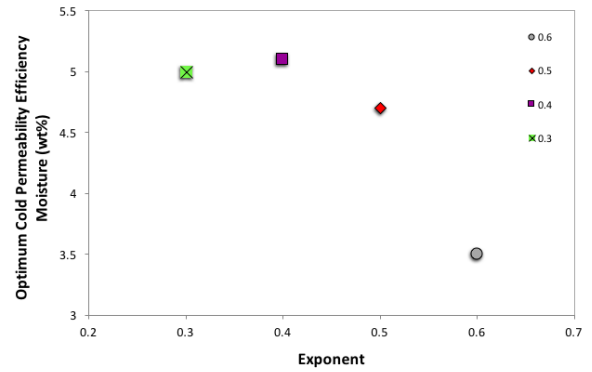


Figure 4.15 – FT exponent (Ψ) optimum moisture for ‘cold’ permeability efficiency

4.2.3 Fuller-Thompson exponent (Ψ) conclusion

To conclude on the exponent (Ψ) to be incorporated into the FT equation for sinter blend design several properties were considered:

- Optimum ‘cold’ permeability.
- Optimum ‘cold’ permeability efficiency.
- Moisture at optimum ‘cold’ permeability and ‘cold’ permeability efficiency.
- Sensitivity of ‘cold’ permeability and ‘cold’ permeability efficiency to moisture.

Even though a lot of attention has been focused on ‘cold’ permeability in previous studies this study investigated other factors that are sometimes disregarded. Analysing the complete performance of the blends with differing FT exponents with the criteria introduced it was concluded that an $\Psi = 0.4$ or 0.5 was the most suited to blend design. Both FT exponents provide increased optimum ‘cold’ permeability when compared to $\Psi = 0.6$ (Figure 4.7). Even though $\Psi = 0.3$ displayed increased optimum ‘cold’ permeability this FT exponent exhibited greater sensitivity of ‘cold’ permeability

with moisture (Figure 4.7) and a lower optimum 'cold' permeability efficiency (Figure 4.11).

The final stage in concluding on the FT exponent to be used in sinter blend design utilised Ore A as a constant nuclei proportion (<10mm >1mm) in the blends. These blend compositions had a more representative PSD of the sinter blends that are created in plant operations when compared with the blends investigated earlier, which composed of return sinter fines (<3.15mm >1mm). The layering proportion of the blends (<0.5mm) were designed with $\Psi = 0.4$ and 0.5 (Table 3.3). The blends were mixed and granulated at a range of moisture contents and analysed for 'cold' permeability and 'cold' permeability efficiency.

Figure 4.16 and 4.17 shows the 'cold' permeability and 'cold' permeability efficiency results of the blends with differing FT exponents. Again, the results fitted a parabolic trend line, as similar to seen previously in this section (Figure 4.7 and 4.11), where there was an initial increase in 'cold' permeability and 'cold' permeability efficiency before an optimum was reached and followed by a decrease at higher moisture contents. $\Psi = 0.5$ showed a small increase in optimum 'cold' permeability based on the parabolic trend lines. It is difficult to draw any conclusions on the optimum 'cold' permeability efficiency results in Figure 4.17, as the parabolic trend line fit in one of the cases did not reach an optimum because it was outside the range of moisture contents used. However, when analysing the data points in Figure 4.17 and not the trend lines then a minimum difference in the 'cold' permeability efficiency results can be seen with the $\Psi = 0.5$ and $\Psi = 0.4$.

The key difference was that $\Psi = 0.5$ had lower moisture content at optimum 'cold' permeability. Based on the parabolic trend line fit in Figure 4.16 the $\Psi = 0.5$ had a moisture content at optimum 'cold' permeability of 7.5%, whereas the $\Psi = 0.4$ had 8.25%. It is proposed that this was the influence of the increased total specific surface area of the blend due to the decreased mean particle diameter of layering particles with the $\Psi = 0.4$, as proved from Table 4.5 and Equation 11. Minimisation of moisture in the sintering process is desired to negate permeability reductions due to excess moisture lower in the bed, thus it was fitting to select $\Psi = 0.5$ for the FT equation in the

design of the layering proportion of blends. The FT equation with both the exponent (Ψ) and maximum layering particle size (D) to be used in sinter blend design in the further testing is presented in Equation 12.

$$P = \left(\frac{d}{0.5} \right)^{0.5} \times 100 \quad (12)$$

where: P = percentage mass less than d (%)

d = particle size (mm)

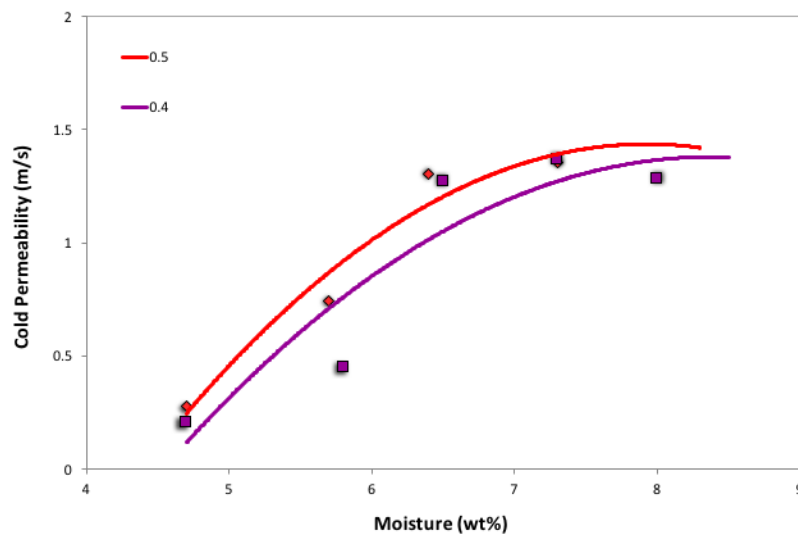


Figure 4.16 – ‘Cold’ permeability of blends with FT exponent (Ψ) of 0.4 and 0.5 in complete sinter blends

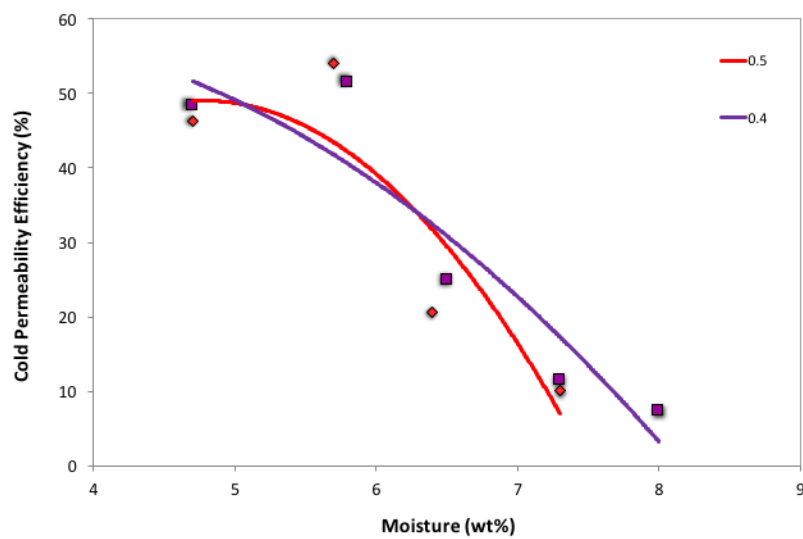


Figure 4.17 – ‘Cold’ permeability efficiency of blends with FT exponent (Ψ) of 0.4 and 0.5 in complete sinter blends

4.3 Influence of layering particle spread (n) in bimodal blends

Blends were introduced in Table 3.4 to study the impact of layering particle size distribution (PSD) spread (n) in sinter blends on key granule and sintering process measurements. To reemphasise, the layering PSD spread is a relative measure for the uniformity of particle sizes in the distribution. It is a parameter determined by applying the Rosin-Rammler distribution to the PSD measurements. Larger spread values represent narrower distributions. Blends were divided into nuclei (Ore A <10mm >1mm) and layering (<0.5mm) proportions with differing layering PSD spreads.

The layering PSD spreads (n) of the blends are shown in Table 4.6. The Fuller-Thompson (FT) equation with the parameters determined in Section 4.2 determines the layering PSD spread of the FT blend. Blends were designed with layering PSD spreads that were narrower (Non-FT0) and wider (NonFT1 and Non-FT2) than the FT blend to focus on this PSD property throughout the granulation and sintering process.

Table 4.6 – Layering PSD spread (n) of blends to study the influence of layering PSD spread (n)

	Non-FT0	FT	Non FT1	Non FT2
Spread (n)	1.09	0.78	0.69	0.62

4.3.1 ‘Cold’ permeability

Figure 4.18 shows changes in ‘cold’ permeability were strongly related to the granule size distribution (GSD) spread (n) and were similar to that seen in Figure 4.8. The GSD measurements are presented in Table 4.7. As the GSD spread narrowed (increasing n) an increased ‘cold’ permeability was observed. The Ergun equation (Equation 2) indicated that the gas flow velocity (thus permeability) was a function of bed voidage (ϵ). Maximum bed voidage is achieved in a bed of equal sized spheres (Suzuki et al. 1999). The less uniform the size of spheres i.e. widening GSD spread the lower the bed voidage.

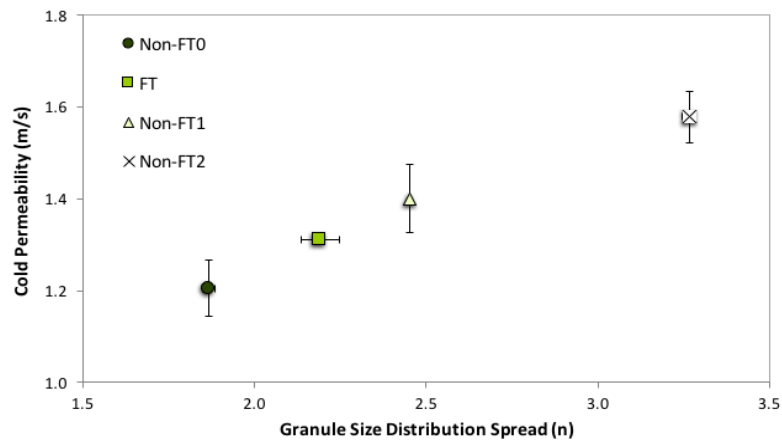


Figure 4.18 – ‘Cold’ permeability as a function of GSD spread (n)

Figure 4.19 shows the relationship between layering PSD spread (n) with GSD spread (n) and mass of particles <1mm. It can be identified in Figure 4.19 that there was an inverse relationship between layering PSD and GSD spread. As the layering PSD spread widened (decreasing n) a narrowing in the GSD spread (increasing n) was found. There are no error bars in the x-axis, as the layering PSD spread does not change in the three repetitions of the blend. The y-axis error bars cannot be seen in all measurements and is due to the small measurement error with the respective blends. The mass of particles that can be considered as ‘non-layered’ (or ‘non-granulated’) were defined as those that were <1mm. Figure 4.19 also shows the mass (%) of ‘non-layered’ particles plotted against the layer PSD spread for all blends. As the layer PSD spread widened (decreasing n) the mass of ‘non-layered’ particles (those passing 1mm sieve) decreased and indicated that a greater mass layered when the layer PSD spread was wider. This explains the narrower GSD spread (larger n) with widening layer PSD spread (decreasing n) also in Figure 4.19. The interpretation of these data is that a wider range of particle sizes within the distribution of layering particles means that more particles (and hence more mass) can become entrained within the layer around the nucleus.

Table 4.7 – GSD measurements for blends designed to study the influence of layering PSD spread (n)

Blend	Size distributions of granules (mm)/wt% mass passing								Spread (n)	Mean diameter (mm)
	>10	>6.3	>5	>3.15	>2	>1	>0.5	>0.25		
Non-FT0	99.3	95.2	88.1	58.9	31.8	9.7	1.9	0.3	1.9	3.4
FT	99.1	93.2	81.2	49.5	19.2	3.1	0.5	0.1	2.2	3.9
Non-FT1	98.7	87.7	67.5	32.0	11.2	1.4	0.2	0.0	2.5	4.7
Non-FT2	97.1	81.2	54.9	15.9	4.0	0.4	0.0	0.0	3.3	5.4

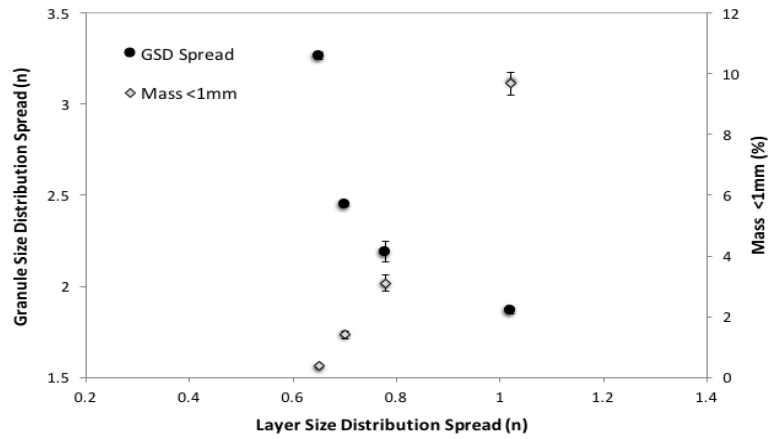


Figure 4.19 – Relationship between layer PSD spread (n) and GSD spread (n) and mass passing 1mm sieve for all blends

Further evidence for this concept is demonstrated in Figure 4.20, which presents the relationship between mean granule diameter (D_m) and both layering PSD and GSD spread (n) for all blends. Widening the layering PSD spread (decreasing n) created a larger mean granule diameter. From Figure 4.20 the direct relationship between mean granule diameter and GSD spread can also be seen, where increasing mean granule diameter was correlated with a narrowing in GSD spread (increasing n).

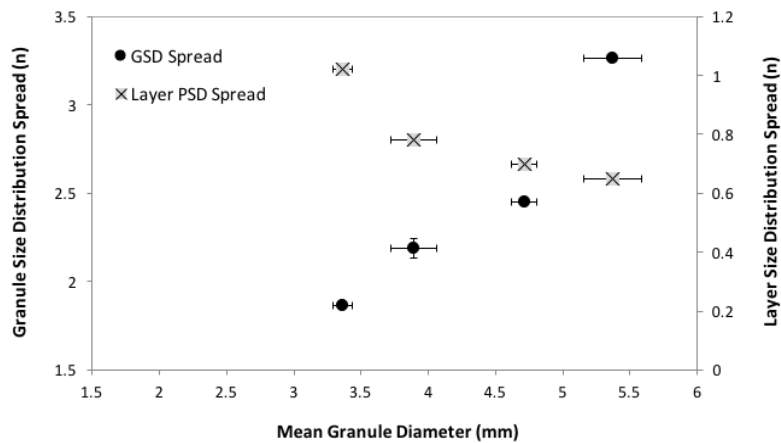


Figure 4.20 – Relationship between mean granule diameter (D_m) and layer PSD and GSD spread (n) for all blends

Binary microscopic images of the layers formed around granule nuclei are shown in Figure 4.21 to 4.24. The measurements obtained from image analysis of the granules are presented in Table 4.8. The data in Table 4.8 support the observations in Figure 4.20 that widening the layering PSD spread (decreasing n) increased the mean granule diameter (D_m). As the layering PSD spread widened (decreasing n) there was a corresponding increase in the average layer area per nuclei in the granules (Table 4.8). Figure 4.25 to 4.28 show the ‘non-layered’ particles highlighted in the granule cross-sections. The areas of ‘non-layered’ particles are presented in Table 4.8. These data

confirm the trends highlighted in Figure 4.19, as the layering PSD spread widened there was a smaller mass of ‘non-layered’ particles as more particles report to the layers around the nuclei. This was verified with the reduced ‘non-layered’ particle area in Table 4.8. In summary of Figure 4.18 to 4.28 and Table 4.7 and 4.8 when the PSD of layering materials was wider, larger layers around nuclei and thus larger granules were formed along with less ‘non-layered’ particles in the bed. The result was a narrower GSD spread and increased ‘cold’ permeability. For the blends used, widening the spread of particle sizes meant a reduction in the coarser layering particles and an increase in the finer layering particles. It is thought that systems with a larger spread of particle sizes allows particles to more closely pack with each other in the layers, which allows more particles to be incorporated and retained within the layers when compared to a narrower spread of layering particle sizes with more coarser layering particles. The result is larger layers and less particles left ‘non-layered’ in the bed after granulation, which increases bed permeability due to the narrower spread of granule sizes. Figure 4.29a and Figure 4.29b were produced to emphasise this concept. Figure 4.29a shows an illustration of the concept of granule and sinter bed formation with a wider layering PSD spread and Figure 4.29b with a narrower layering PSD spread.

Table 4.8 – Granule image analysis measurements of blends to study the influence of layering PSD spread (n)

Blend	Number of nuclei	Layer area (mm ²)	Average layer area/nuclei (mm ²)	‘Non-layered’ particle area (mm ²)
Non-FT0	186	224.3	1.2	29.0
FT	190	249.4	1.3	21.1
Non-FT1	187	283.4	1.5	16.3
Non-FT2	162	343.1	2.1	7.4



Figure 4.21 – Microscopic image of layers in Non-FT0

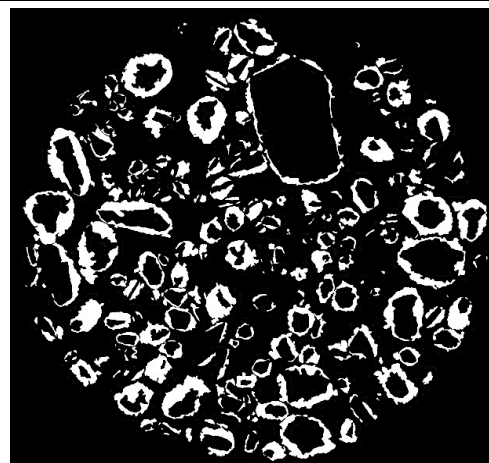


Figure 4.22 – Microscopic image of layers in FT

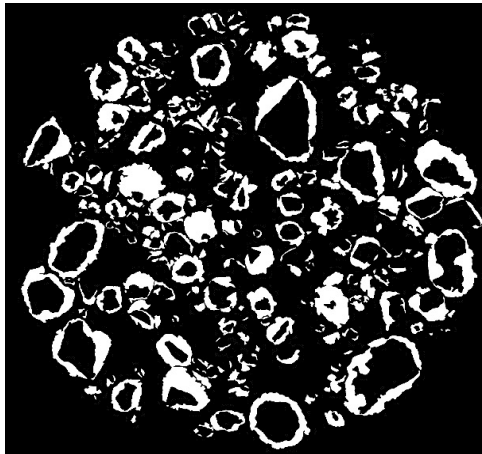


Figure 4.23 – Microscopic image of layers in Non-FT1

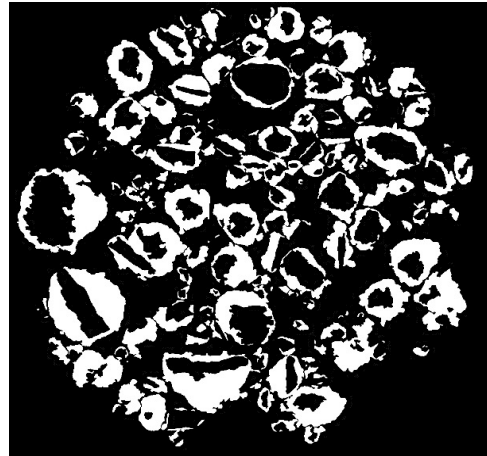


Figure 4.24 – Microscopic image of layers in Non-FT2

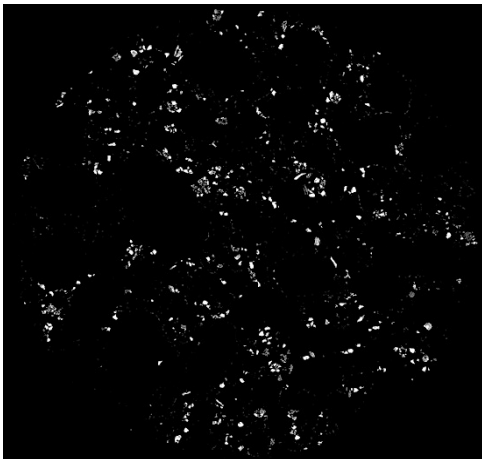


Figure 4.25 – Microscopic image of non-layered particles in Non-FT0

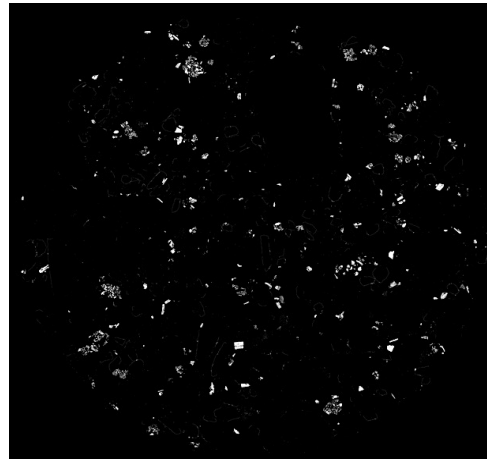


Figure 4.26 – Microscopic image of non-layered particles in FT

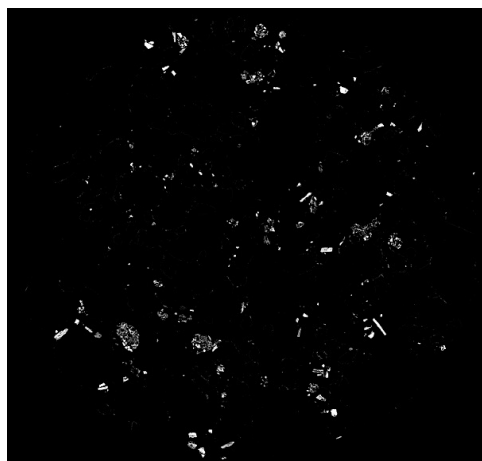


Figure 4.27 – Microscopic image of 'non-layered' particles in Non-FT1

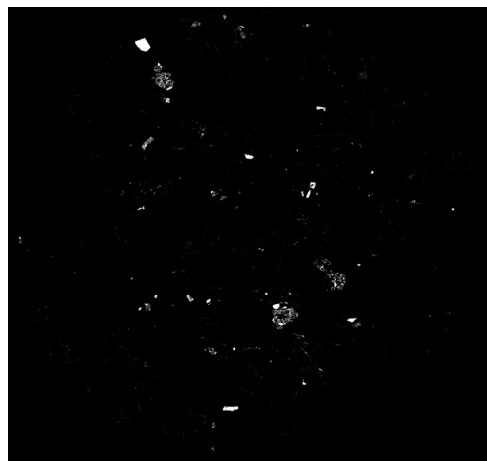


Figure 4.28 – Microscopic image of 'non-layered' particles in Non-FT2

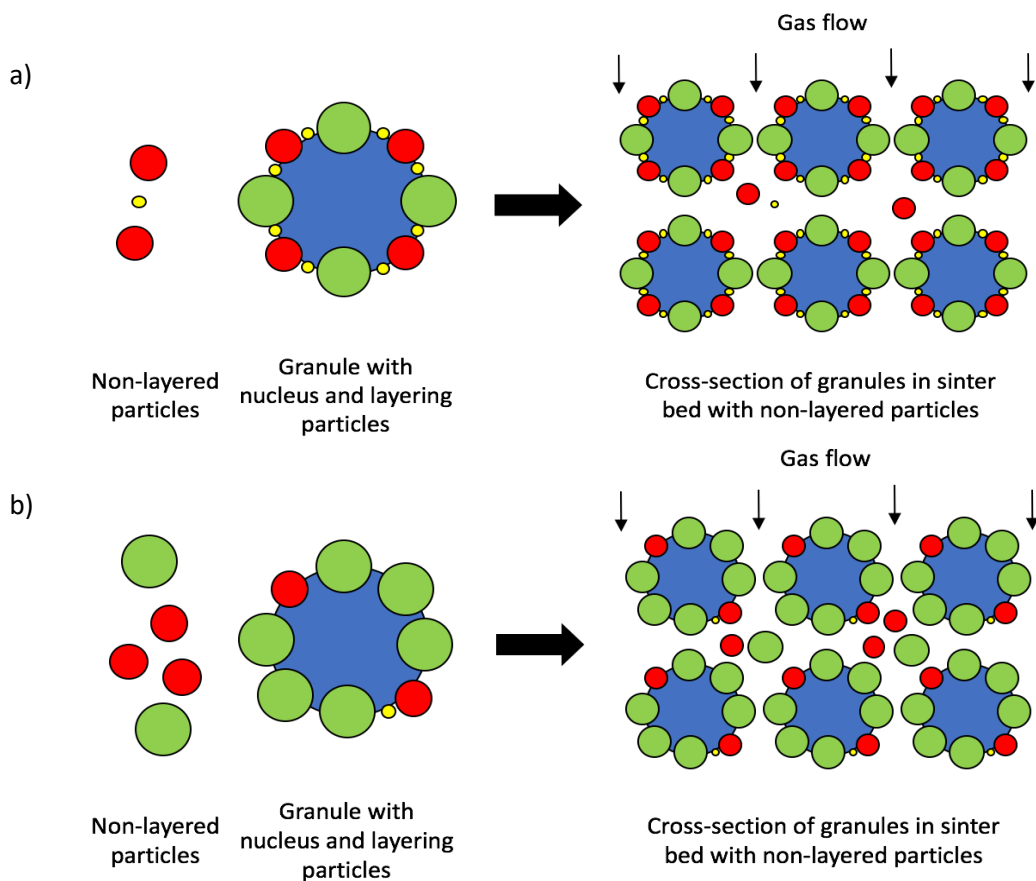


Figure 4.29 – 2D illustration of the impact of layering PSD spread (n) on granule and sinter bed formation a) Wider spread b) Narrower spread

4.3.2 ‘Hot’ permeability, efficiency and production rate

Whilst the ‘cold’ permeability and ‘cold’ permeability efficiency are important parameters to ensure good gas flow in the initiation of sintering, the permeability of the bed during sintering referred to as the ‘hot’ bed permeability is also critical. A bed will have a relatively high permeability prior to sintering (‘cold’ permeability) but once a flame front is created this leads to a permeability reduction due to bed collapse and the pressure drop regions caused by the flame front reactions. The ‘hot’ permeability strongly influences sintering time (Figure 4.30) and the sinter strand production rate will be impacted by longer sintering times. The Fuller-Thompson (FT) blend produced the greatest ‘hot’ permeability and shortest sintering time out of all the blends.

It was required to represent the decrease in permeability experienced by the sinter bed during transition from ‘cold’ to ‘hot’ conditions during sintering. This was introduced in Section 3.2.7 defined as the ‘hot’ permeability efficiency and indicates the relative size of the decrease in (%) permeability between ‘cold’ and ‘hot’ conditions.

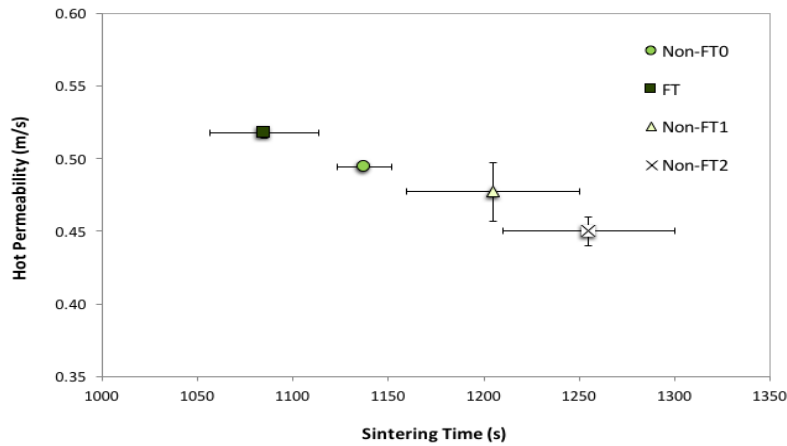


Figure 4.30 – Relationship between ‘hot’ permeability and sintering time

Widening the PSD spread of layering particles (decreasing n) was shown to increase the mean granule diameter (D_m) and narrow the GSD spread (increasing n) and led to an increased ‘cold’ permeability (Figure 4.18 and 4.20). However, an increase in mean granule diameter was also correlated with a decrease in the ‘hot’ permeability efficiency as can be seen in Figure 4.31 i.e. larger mean granule diameters, which was the result of the development of larger layers created around nuclei, lost more of their ‘cold’ permeability when transferring to ‘hot’ permeability during the process. It has been previously proposed that layers of fine particles more readily deform than the nuclei particles (Khosa and Manuel 2007). It is thus thought that larger layers created around nuclei display more deformation and collapse when the bed makes the transfer from ‘cold’ to ‘hot’ permeability during the process.

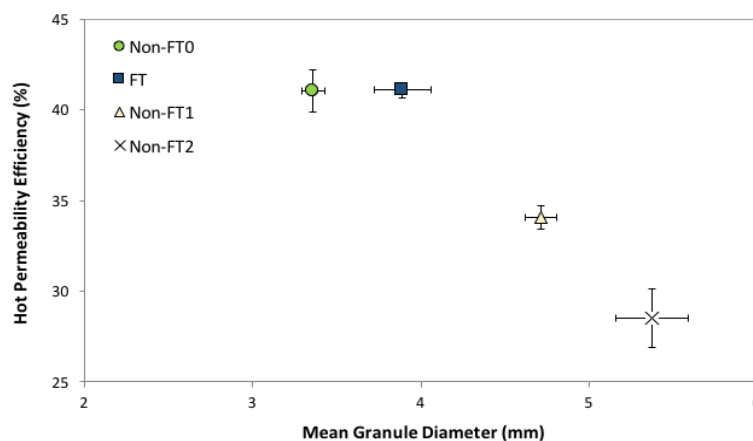


Figure 4.31 – Relationship between ‘hot’ permeability efficiency and mean granule diameter (D_m)

The trend in Figure 4.31 shows that decreasing mean granule diameter (D_m) correlated with increasing ‘hot’ permeability efficiency. However, it can be seen that the mean

granule diameter of the FT blend was greater than for Non-FT0 and still provided increased 'hot' permeability efficiency. This proves that the FT blend created greater resistance to permeability losses when transferring from a 'cold' to 'hot' bed when compared to Non-FT0 even though the mean granule diameter was larger.

Of the blends investigated in the study of the impact of layering PSD spread (n) on sintering process measurements the FT blend provided greatest 'hot' permeability and shortest sintering times (Figure 4.30). The greater 'hot' permeability produced by the FT blend must be a result of the layering PSD, as this is the varying factor in the blends. The layering PSD spread of the FT blend did not create the largest mean granule diameter or narrowest granule size distribution (GSD) spread (n) and thus not the greatest 'cold' permeability (Figure 4.18). This was because the FT blend did not have the widest layering PSD spread which correlated with increasing mean granule diameter (D_m) and narrowing GSD spread (Figure 4.20). However, the increased 'hot' permeability efficiency of the FT blend based on the trend line shown in Figure 4.31 with mean granule diameter enabled a greater proportion of the 'cold' permeability to be transferred to 'hot' permeability than anticipated. The other blends investigated provided either only 'cold' permeability (Non-FT1 and Non-FT2) or 'hot' permeability efficiency (Non-FT0). Therefore, with the blends investigated in this study it is thought that the layering PSD of the FT blend gave the best compromise between mean granule diameter for 'cold' permeability and resistance to permeability losses for 'hot' permeability efficiency, which created the greatest 'hot' permeability and shortest sintering times.

4.4 Industrial application of Fuller-Thompson blend design

The evaluation of blends designed to the Fuller-Thompson (FT) equation against industrial base (BB) blends was highlighted as a key objective. These blends have increasing masses of layering particles (<0.5mm wt%), which are similar to those of sinter plant operations to also assess the impact of increasing the layering proportion of particles in blends on sinter bed permeability and process productivity (Table 3.7).

4.4.1 'Cold' permeability

Figure 4.32 presents the comparison of the 'cold' permeability of the base (BB) and FT blends at varying layering particle proportions (1=46wt%, 2=48wt% and 3=50wt%). Table 4.9 presents the granule size distribution (GSD) measurements of the blends. Again, 'cold' permeability was directly related to granule size distribution (GSD) spread (n). Narrowing the GSD spread (increasing n) increased the 'cold' permeability of the bed. Figure 4.32 showed that increasing the layering particles from 46-48wt% did not reduce the 'cold' permeability significantly enough to be outside the 95% confidence intervals (BB1–BB2 and FT1–FT2). This was the same for increasing the layering particles from 48-50wt% (BB2–BB3 and FT2–FT3). However, the blends could not incorporate 4wt% more layering particles without reducing 'cold' permeability as the 95% confidence intervals then did not overlap (BB1–BB3 and FT1–FT3).

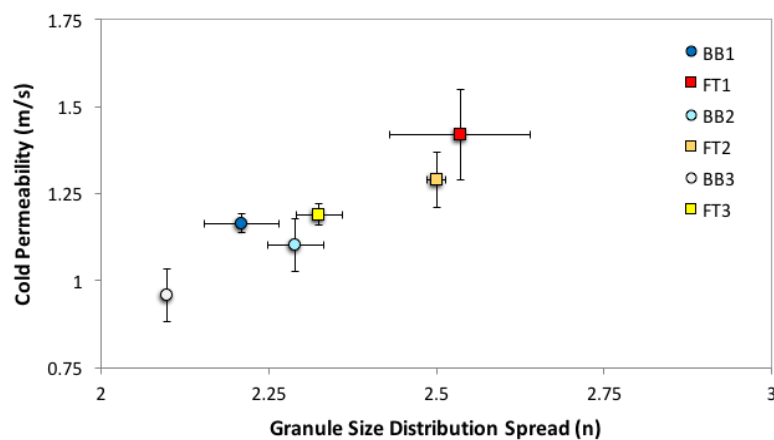


Figure 4.32 – 'Cold' permeability and GSD spread (n) for base (BB) and Fuller-Thompson (FT) blends

When comparing the base (BB) and FT blends in Figure 4.32, the FT blends provided enhanced ‘cold’ permeability at equal layering particle proportions. To emphasise the increase in ‘cold’ permeability with FT blends, the percentage increase in ‘cold’ permeability with FT blends at equal layering particle proportions is shown in Figure 4.33. The ‘cold’ permeability increase ranged from 13-20%. Further, it was realised that the FT blends could incorporate 4wt% more layering particles and exhibited ‘cold’ permeability results that were the same inside the 95% confidence interval of the base (BB) blend (BB1-FT3). This was attributed to the narrower GSD spread (n) created due to the wider layering PSD spread (n) of the FT blends (Table 3.5 and 3.6).

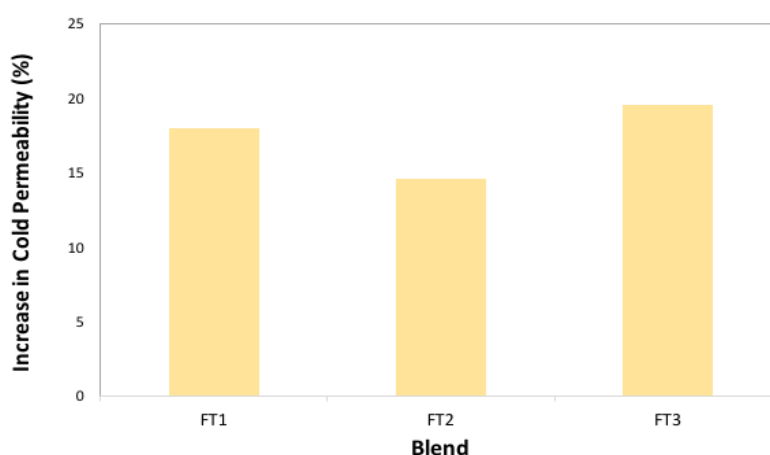


Figure 4.33 – Increase in ‘cold’ permeability with Fuller-Thompson (FT) blends compared to base (BB) blends at equal layering particle proportions

Table 4.9 – GSD measurements of base (BB) and Fuller-Thompson (FT) blends

Blend	Granule size distribution (mm)/wt% mass passing								GSD spread (n)	Mean diameter (mm)
	>10	>6.3	>5	>3.15	>2	>1	>0.5	>0.25		
BB1	100.0	94.9	86.2	54.9	23.2	2.8	0.2	0.0	2.2	3.6
FT1	99.1	93.6	82.6	42.5	14.4	1.6	0.1	0.0	2.5	4.0
BB2	100.0	95.1	84.0	48.2	20.4	2.7	0.4	0.1	2.3	3.8
FT2	98.0	88.2	71.0	33.3	10.4	1.0	0.1	0.0	2.5	4.6
BB3	96.8	92.2	82.3	48.2	22.5	3.4	0.5	0.1	2.1	3.9
FT3	98.2	93.5	76.7	40.3	17.2	1.9	0.1	0.0	2.3	4.2

The narrower GSD spread (n) and increased ‘cold’ permeability of the FT blends was a result of their layering PSD. It was shown in Figure 4.18 and 4.20 in the study on layering PSD spread that wider layer PSD spreads produced increased ‘cold’ permeability due to narrowing GSD spread (increasing n) and increasing mean granule diameter (D_m). In this phase of the study the FT blends created narrower GSD spreads than the base (BB) blends as they had a wider layer PSD spread (smaller n) (Table 4.10) and could layer a greater mass of particles, consequently increasing mean granule diameter and narrowing the GSD spread (increasing n). In the case of BB1, FT1, BB3 and FT3 this was verified by granule image analysis with the results shown in Table 4.11. It can be observed from Table 4.9 and 4.11 and from Figure 4.34 to 4.41 that the FT blends had larger layer area per nuclei and smaller mass and area of ‘non-layered’ particles compared to the base (BB) blends at equal layering particle proportions.

Table 4.10 – Layering PSD spread (n) of base (BB) and Fuller-Thompson (FT) blends

	BB1	FT1	BB2	FT2	BB3	FT3
Spread (n)	0.94	0.74	1.01	0.75	1.11	0.78

Table 4.11 – Granule image analysis measurements for base (BB) and Fuller-Thompson (FT) blends

Blend	Number of nuclei	Layer area (mm ²)	Average layer area/nuclei (mm ²)	‘Non-layered’ particle area (mm ²)
BB1	241	271.2	1.13	33.289
FT1	231	284.7	1.23	27.135
BB3	205	280.7	1.37	36.629
FT3	208	293.9	1.41	32.733

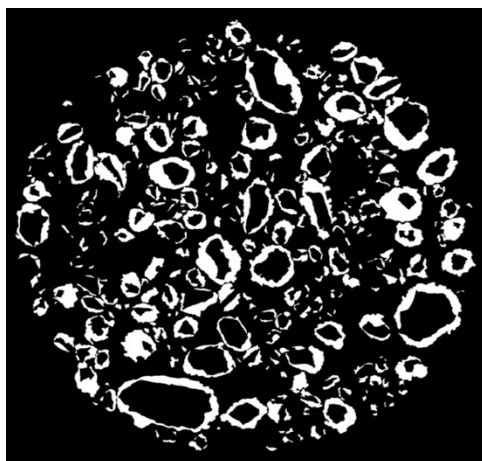


Figure 4.34 – Microscopic image of layers in BB1

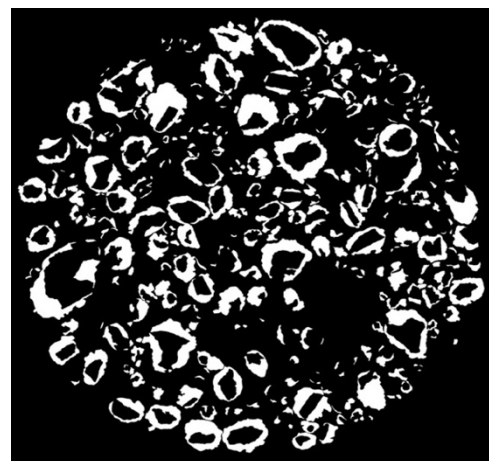


Figure 4.35 – Microscopic image of layers in FT1

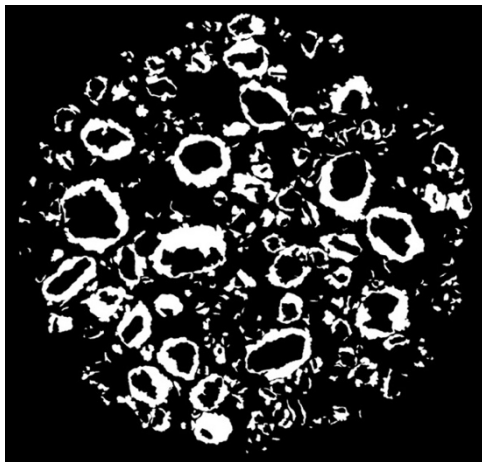


Figure 4.36 – Microscopic image of layers in BB3

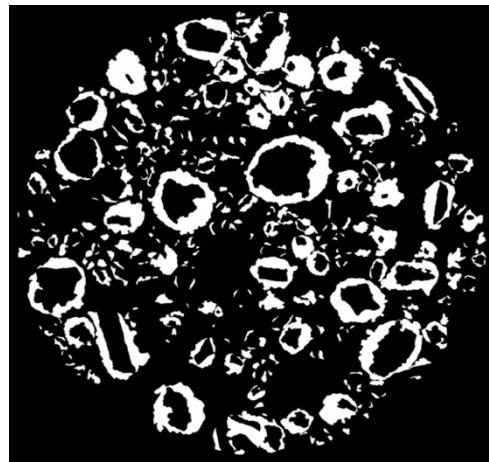


Figure 4.37 – Microscopic image of layers in FT3

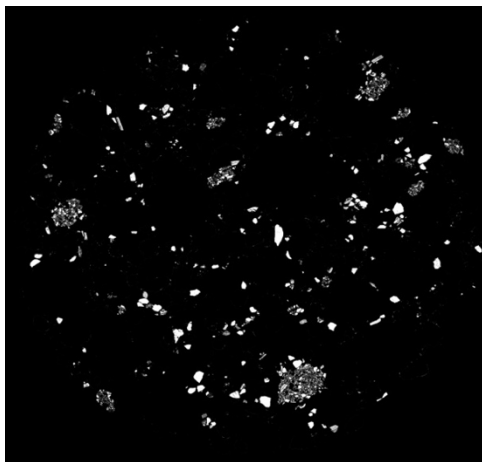


Figure 4.38 – Microscopic image of 'non-layered' particles in BB1

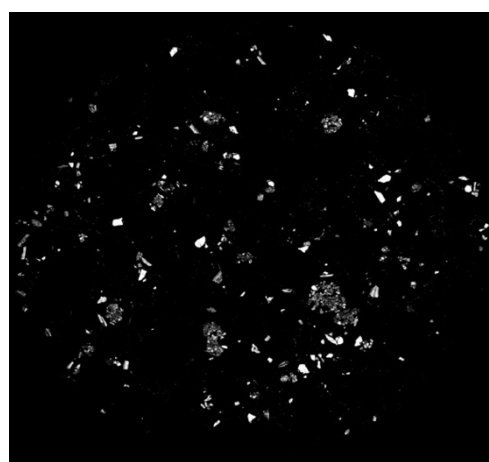


Figure 4.39 – Microscopic image of 'non-layered' particles in FT1

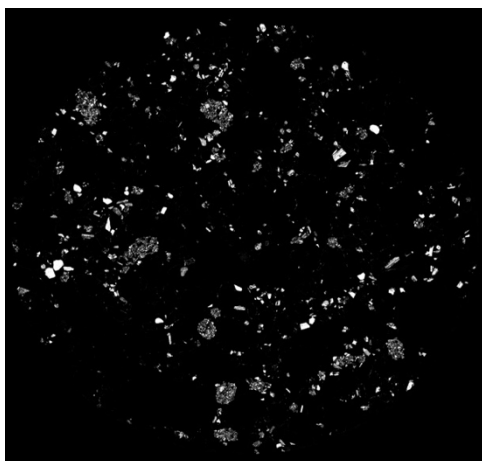


Figure 4.40 – Microscopic image of 'non-layered' particles in BB3

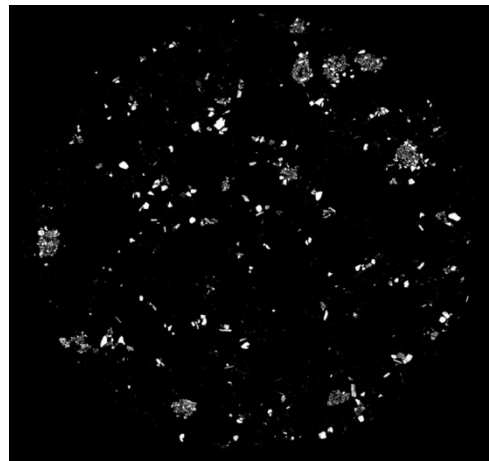


Figure 4.41 – Microscopic image of 'non-layered' particles in FT3

4.4.2 'Hot' permeability, efficiency and production rate

Figure 4.42 shows the 'hot' permeability and sintering time results for the base (BB) and Fuller-Thompson (FT) blends at varying layering particle proportions (1=46wt%, 2=48wt% and 3=50wt%). Similar to Figure 4.30 there was a direct relationship between 'hot' permeability and sintering time. Increasing 'hot' permeability correlated with decreasing sintering times. Increasing the layering particle proportion by 2wt% for both the FT and base (BB) blends did not show any difference in the sintering times as the 95% confidence intervals overlapped (BB1-BB2 and FT1-FT2). This was similarly the case when increasing the layering particle proportion by 4wt% (BB1-BB3 and FT1-FT3).

The FT blends provided shorter sintering times than the base (BB) blends at the equal layering particle proportions. The decrease in sintering times are shown in Figure 4.43. The largest decrease in sintering time at equal layering particle proportions was 9.5% (BB1-FT1). The FT blend incorporated 4wt% more layering particles and the sintering times were the same within the 95% confidence interval of the base blend (BB1-FT3). The results indicated that designing the layering proportion of sinter blends (<0.5mm) to the FT equation provided a layering PSD that gave improved sintering times when compared to the base (BB) blends at equal layering particle proportions. Further, the FT blend could incorporate 4wt% more layering particles and have similar sintering times, suggesting the potential to increase the proportion of layering particles (<0.5mm) in sinter blends when designing blends to the FT equation without jeopardising sintering times.

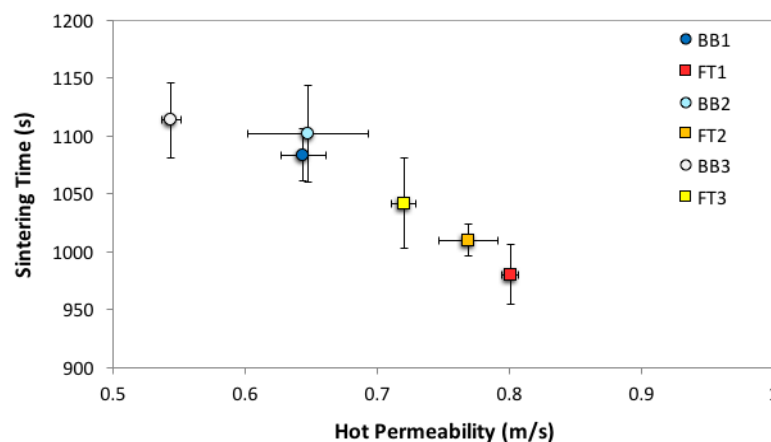


Figure 4.42 – 'Hot' permeability and sintering time for base (BB) and Fuller-Thompson (FT) blends

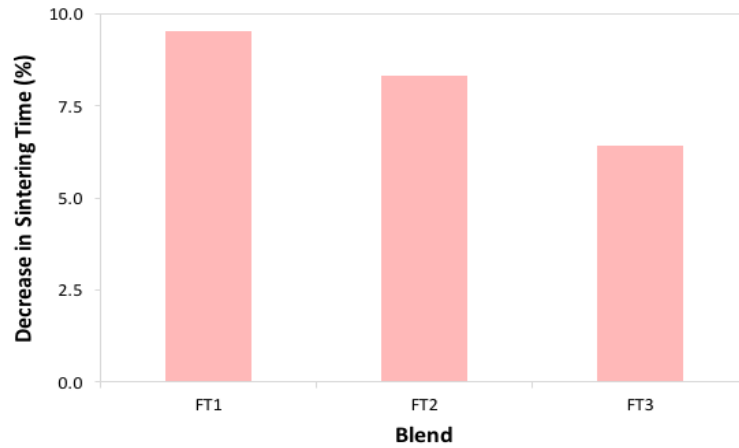


Figure 4.43 – Decrease in sintering time with Fuller-Thompson (FT) compared to base (BB) blends at equal layering particle proportions

The reason behind the increased ‘hot’ permeability and shorter sintering times of the FT blends relates to the ‘hot’ permeability efficiency. From Figure 4.44 the ‘hot’ permeability efficiency results for the blends are the same within the 95% confidence intervals. As the FT blends were shown to provide increased ‘cold’ permeability (Figure 4.32) this was transferred through to increased ‘hot’ permeability and thus shorter sintering times. It was shown previously that the increase in mean granule diameter (D_m) due to the creation of larger layers around nuclei resulted in the narrowing of the GSD spread (increasing n), which increased ‘cold’ permeability and decreased ‘hot’ permeability efficiency (Figure 4.18 and 4.31). The FT blends did not follow this trend, as no difference between the ‘hot’ permeability efficiency could be distinguished between the base (BB) and FT blends, even with the increased mean granule diameter of the FT blends (Table 4.9).

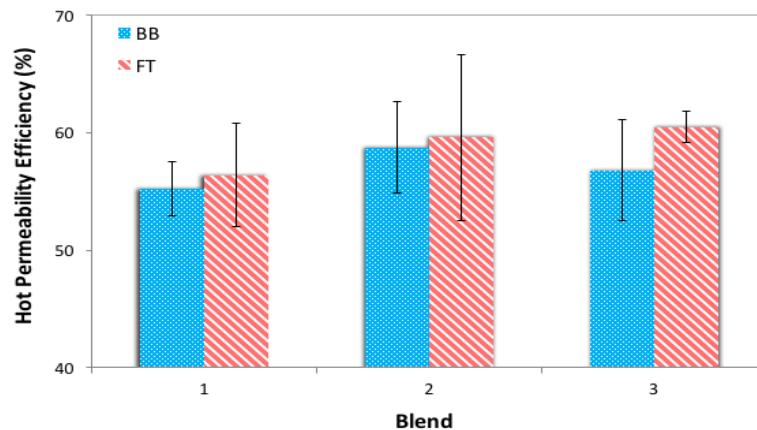


Figure 4.44 – ‘Hot’ permeability efficiency of base (BB) and Fuller-Thompson (FT) blends

4.4.3 Sinter cold strength

Sinter cold strength was introduced in Section 2.2 as measure for the degradation of sinter under transportation. Reducing sinter cold strength is detrimental to the process as this creates a smaller net productivity through increased sinter return fines. Sinter cold strength was used to emphasise differences between the strength of the sinters produced from the base (BB) and FT blends. This was particularly important, as it has been determined that FT blends can provide faster sintering times when compared to the base (BB) blends at equal layering particle proportions. It is essential that sinter quality is maintained with faster sintering times, as it is counterproductive to increase the sinter production rate but also increase the proportion of return sinter fines produced.

Sieve analysis on sinter provided a numerical measure for sinter quality. Two measures for sinter cold strength were used. Figure 4.45 shows the median sinter diameter (d50) at the varying layering particle proportions (1=46wt%, 2=48wt% and 3=50wt%). The median diameter is the sinter diameter, where half of the mass is greater and half the mass is less than. From Figure 4.45 the median sinter diameter for the base (BB) and FT blends are the same within the 95% confidence intervals shown. The differences in cold strength were not significant enough to show a distinction between the sinters. The results from Figure 4.45 propose that the sinter cold strength was not impacted by the quicker sintering time of the FT blends.

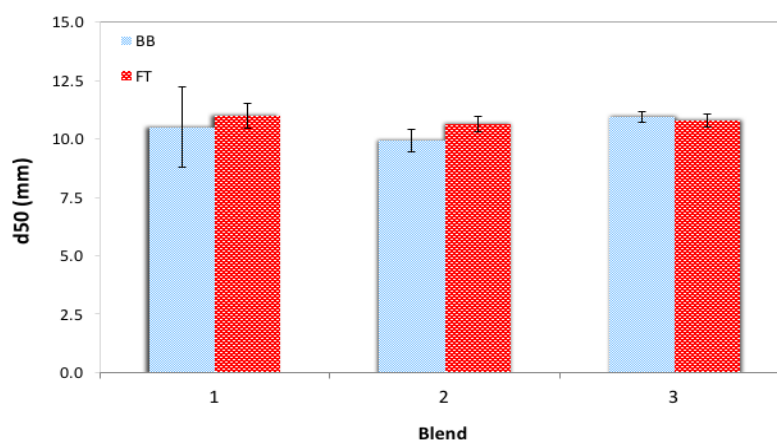


Figure 4.45 – Median sinter diameter (d50) after cold strength testing for base (BB) and Fuller-Thompson (FT) blends

To validate, a second measure for sinter cold strength was the mass of sinter <5mm. This is similar to the measure used in sinter plants to calculate the mass proportion of sinter return fines. It can be identified from Figure 4.46 that the FT blends did not increase the mass of sinter <5mm, thus again proved that the cold strength of the sinter was not negatively impacted when designing FT blends

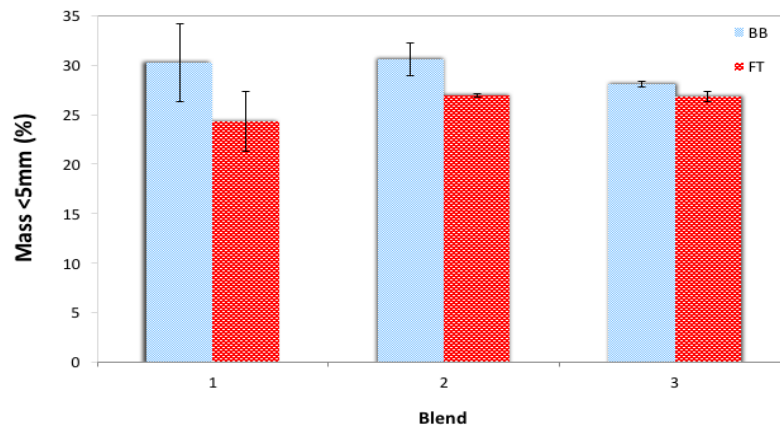


Figure 4.46 – Mass passing 5mm sieve after cold strength testing for base (BB) and Fuller-Thompson (FT) blends

To summarise the cold strength results it was proven that FT blends did not exhibit decreased sinter cold strength. Due to the minimal differences shown in Figure 4.45 and 4.46 it is possible to state that the quicker sintering times produced by the FT blends did not lead to a reduction in the cold strength of the sinters. The reason is related to the complete blend composition including the additives (Table 3.8). The composition of the iron ore proportion of the blends was the only varying parameter. Coke breeze, flux and return sinter fine proportions were held constant. It is proposed that differences in sinter cold strength found during plant operations are a greater impact of the changes in these blend additives rather than iron ore composition.

To aid this proposition Figure 4.47 is shown. Figure 4.47 presents the cold strength measurements for a series of tests with increasing coke breeze proportions (Small 2017). A significant increase in the median sinter diameter (d50) and thus cold strength can be identified as the coke breeze proportion increased. This reached an optimum before reducing at higher coke breeze proportions. It can be observed that there was a much larger change in sinter median diameter (d50) with coke breeze when compared to the results shown in Figure 4.45. The median sinter diameter varied between 6-

14mm and proved a much more dominant effect of this blend additive on the cold strength of sinter when compared to the changes in the iron ore composition of the blends conducted in this study.

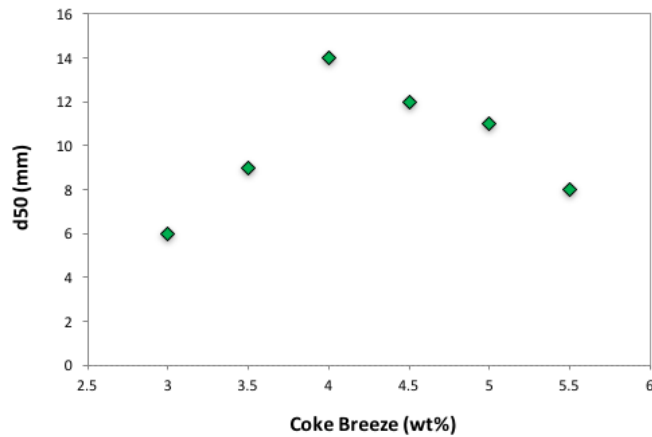


Figure 4.47 – Median sinter diameter (d50) after cold strength testing for a coke breeze series

4.4.4 Sinter chemical composition

Sinter chemical composition was detailed as one of the key properties that must be closely monitored and controlled to be an effective blast furnace burden. Some of the more prominent chemical elements and compounds introduced were Fe, FeO, SiO₂, CaO and gangue materials. The impact of these chemicals was discussed in Section 2.2. The XRF measurements for the base (BB) and Fuller-Thompson (FT) blends at 46wt% layering particle proportion are presented in Table 4.12 and Figure 4.48. It was assumed that any differences in chemistry would be the same in the blends at greater layering particle proportions due to the similar differences in blend compositions.

The key result in Table 4.12 and Figure 4.48 are the minimal differences in the chemical compositions of the base (BB) and FT blends. The chemistry of the sinters produced did not change significantly when designing FT blends. It is thought that the reason again stems back to the complete sinter blend composition. The only varying factor between the blends was the iron ore composition. The additives (coke breeze, flux and return fines) remained constant throughout (Table 3.8). What can be postulated, as similar to the sinter cold strength was that the changes to the iron ore composition of the blend

did not significantly alter the chemical composition of the sinters. However, when designing blends with the FT equation this only considers the particle size distribution (PSD) and not the iron ore and blend chemistry. It is recommended that when designing FT blends at plant scale that the blend chemistry is monitored so as to not create blends that produce sinter with a non-desirable chemical composition. This is particularly the case when aiming for a certain sinter basicity ($\frac{\text{CaO}+\text{MgO}}{\text{SiO}_2}$), FeO and adhering to gangue material limits.

Table 4.12 – XRF results of base (BB) and Fuller-Thompson (FT) blends at 46wt% layering particle proportion

Blend	Chemical composition (wt%)											
	Fe	FeO	SiO ₂	Al ₂ O ₃	CaO	MgO	MnO	Zn	TiO ₂	P ₂ O ₅	Pb	Ni
BB1	58.65	4.15	3.16	1.39	10	1.19	0.45	0.008	0.16	0.061	0.0024	0.0071
FT1	58.42	6.63	3.50	1.37	10.2	1.28	0.44	0.009	0.12	0.069	0.0027	0.0073

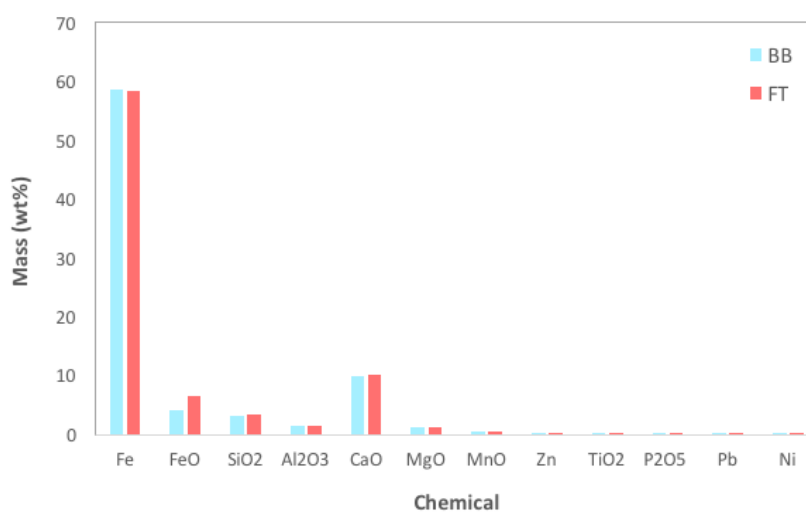


Figure 4.48 – Chemical composition of base (BB) and Fuller-Thompson (FT) blends at 46wt% layering particle proportion

The only significant chemical difference shown in Figure 4.48 between the base (BB) and FT blend was FeO. When referring to the chemical characterisation of the iron ores in Table 4.3 it was reported that magnetite ores (Fe_3O_4 or $\text{FeO}\cdot\text{Fe}_2\text{O}_3$) have a larger mass of FeO contained. The FT blends were composed of more magnetite ores (Ore B and Ore D) and therefore contained more FeO than the base (BB) blend. Utilising this information in combination with the XRF results it can be realised that this was

translated through to the chemistry of the sinter. The impact of increased FeO on sinter quality also depends on the other materials in the blend; coke breeze and flux, which were held constant during testing (Table 3.8). The sinter quality results indicated that there were no differences in sinter cold strength (Figure 4.45 and 4.46), therefore the differing FeO contents of the blends were not significant enough to impact this sinter quality parameter.

4.4.5 Sinter mineralogy

Section 2.2 introduced some of the key aspects with regards sinter mineralogy. The more common phases included hematite (Fe_2O_3), magnetite (Fe_3O_4) and the silica ferrites of calcium and alumina (SFCAs). XRD analysis was conducted on the sinters from the base (BB) and FT blend at 46wt% layering particle proportion. The results are presented in Figure 4.49 and Table 4.13. It was assumed that any differences in mineralogy would be the same in the blends at greater layering particle proportions due to the similar differences in blend compositions.

The key disparity in mineralogy identified in Figure 4.49 and Table 4.13 was the total mass of hematite (Fe_2O_3) and magnetite (Fe_3O_4) in the sinters. The total mass of hematite in the base (BB) blend sinter was 7.1wt% greater than the FT blend. In contrast, the FT blend has 4.8wt% more magnetite in the sinter. Relating back to the mineralogy of the iron ores that were used in FT blends, then it is apparent that they contained a larger proportion of magnetite ores (Ore B and Ore D). This transferred to a larger proportion of magnetite phases in the sinter mineralogy.

In Figure 4.49 apart from the hematite (Fe_2O_3) and magnetite (Fe_3O_4) phases the error bars from the XRD measurements for every phase overlapped. This signified that no further differences in sinter mineralogy could be differentiated between the base (BB) and FT blends. The results prove that designing FT blends in this case did not alter the sinter mineralogy substantially. However, as the design of FT blends is based solely on particle size distribution (PSD) this does not consider the mineralogy of the iron ores and the blend. For this reason, it is recommended that the hematite and magnetite

proportions in blends are monitored when utilising FT blend design so as to not change the FeO in the sinter beyond any limits set for the sinter plant.

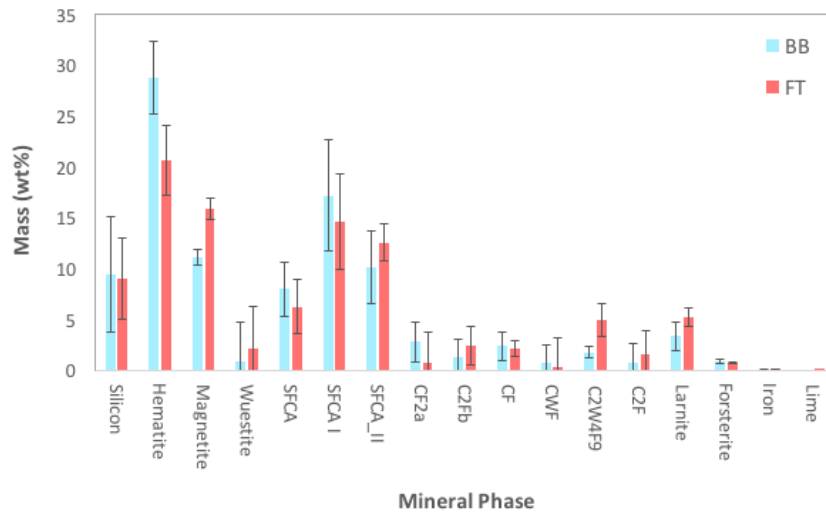


Figure 4.49 – Sinter mineralogy of base (BB) and Fuller-Thompson (FT) blends at 46wt% layering particle proportion

Table 4.13 – XRD results for base (BB) and Fuller-Thompson (FT) blends at 46wt% layering particle proportion

Mineral Phase	BB1		FT1	
	Comp wt%	2 σ wt%	Comp wt%	2 σ wt%
Silicon (reference)	9.5	1.2	9.0	1.1
Hematite	28.8	5.7	20.7	4.0
Magnetite	11.1	3.6	15.9	3.4
Wuestite	0.9	0.8	2.1	1.0
SFCA	8.0	3.8	6.3	4.2
SFCA I	17.2	2.7	14.7	2.6
SFCA_II	10.2	5.5	12.6	4.7
CF2a	2.8	3.6	0.7	1.8
C2Fb	1.3	2.0	2.5	3.1
CF	2.4	1.8	2.2	1.9
CWF	0.8	1.4	0.3	0.8
C2W4F9	1.8	1.7	5.0	2.9
C2F	0.8	0.6	1.6	1.6
Larnite	3.4	1.9	5.3	2.3
Forsterite	0.9	1.4	0.8	0.9
Iron	0.0	0.2	0.1	0.1
Lime	0.0	0.1	0.2	0.1

Chapter 5 – TATA Steel Europe Trials

5.1 Introduction

The results generated in the pilot plant testing (Chapter 4) led to Fuller-Thompson (FT) sinter blend design being trialled at full plant-scale at TATA Steel Europe. In the same method, as in the pilot plant methodology (Section 3.2.2), blends were designed to the FT equation and evaluated against blends that were in current plan. The process key performance indicators (KPIs) used in evaluation were ignition permeability, flame front speed (FFS) and specific net production rate. Cold strength, reduction-disintegration index (RDI) and dust production were used as the measures for sinter quality. 5 trials were conducted throughout July and August 2016. The data used for analysis was hourly data on the 3 sinter machines, which was averaged for the time that the blends were in plant (5-6 days).

Initially, this chapter focuses on the development of the FT blends to fulfil this objective. Since this was now full-scale operations there were several constraints that needed to be adhered to. Iron ore stock levels were the main determining constraints to the proximity that the blends could be designed to the FT equation. Not all the ores shown in Table 5.1 were available simultaneously. Blend chemistry also had an impact, where a certain blend basicity ($\frac{\text{CaO}+\text{MgO}}{\text{SiO}_2}$) was targeted to achieve the desired sinter chemistry. However, as will be identified, the layering particle size distribution (PSD) of the blends designed to the FT equation are noticeably different to those that were in the current plan (TS). The remainder of the chapter evaluates the sintering process KPIs of the blends (Section 5.3-5.6). To exclude any data sensitivity issues in some instances no units and the relative changes were used in result presentation.

5.2 FT trial design

5 trials were conducted with blends designed using the FT equation (Equation 12). Iron ores that were currently stocked at TATA Steel Europe were incorporated into blend design. The methodology was an exact replica of that described in Section 3.2.2. Table

5.1 shows the composition of the FT blends, which were evaluated against blends that were in current plan (TS). For a fair evaluation, the burnt lime additions to the blends during mixing and granulation were equal. Burnt lime enhances the mixing and granulation process by acting as a binder to aid granulation and increase sinter bed permeability. Further, blend basicity ($\frac{\text{CaO}+\text{MgO}}{\text{SiO}_2}$) was also kept relatively constant to negate any impact on the KPIs from this change in blend chemistry. The differing total fine iron ore proportions, which is classed as the total amount of concentrated and pellet feed ores (Ore E to Ore I) in the trials will be explained during analysis.

The mass retained PSD of layering particles (<0.5mm) for FT trial 1 are shown in Figure 5.1 and 5.2. These blends are compared to the PSD determined by the FT equation (FT). The PSDs of the blends in the other trials also showed similar PSD differences between the planned and FT blends as shown in Figure 5.1 and 5.2.

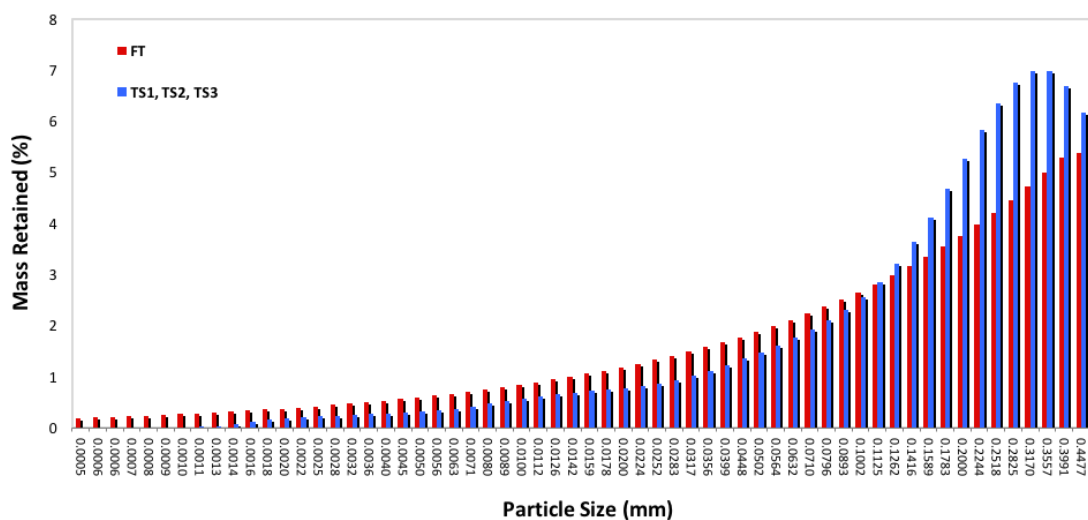


Figure 5.1 – Mass retained layering PSD of TS1, TS2, TS3

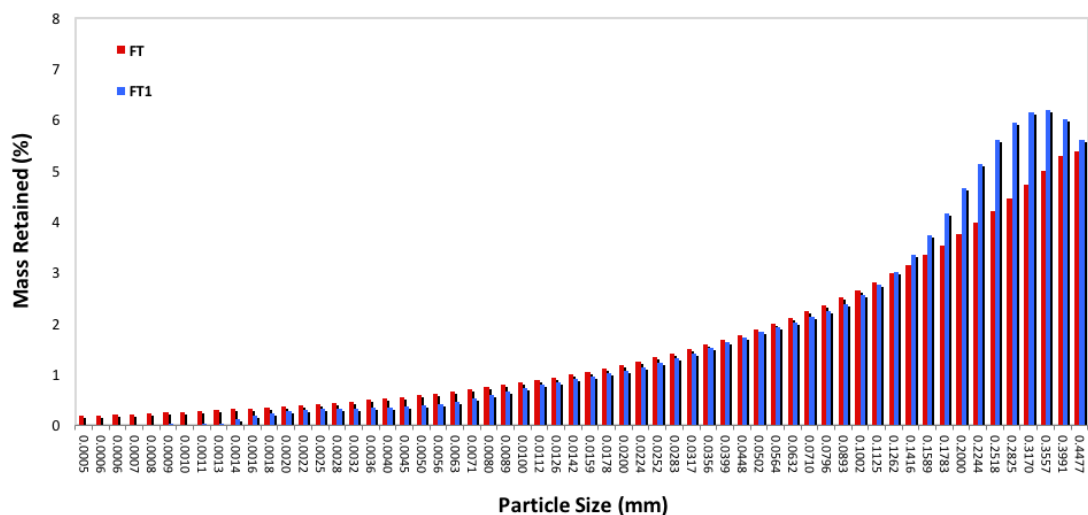


Figure 5.2 – Mass retained layering PSD of FT1

Table 5.1 – Blend compositions for FT trials

Blend	Ore A	Ore B	Ore C	Ore D	Ore E	Ore F	Ore G	Ore H	Ore I	Total Fine Ores
(wt%)										
FT TRIAL 1										
TS1, TS2, TS3	45.4	16.3	13.8		19.5	5.0				24.5
FT1	65	15			8.9	2.1		9		20.0
FT TRIAL 2 & 3										
TS4, TS5	53.5		21.5		25.0					25.0
FT2	65		5		9.4		10	10.6		30.0
FT3	52.9	27.4	4.7		4.5		5.0		5.5	15.0
FT TRIAL 4 & 5										
TS6	58.2	22.6			19.2					19.2
TS7	57.0	22.6			20.4					20.4
FT4	65.0	18.0		2.0	5.0		5.0		5.0	15.0
FT5	64.6			20.3	4.6		4.9		5.5	15.0

5.3 Ignition permeability

Ignition permeability is the bed permeability in the ignition zone of the process. Throughout the background and pilot plant chapters (Chapter 2 and 4) bed permeability was extensively investigated and stressed as the key process parameter in determining sinter strand productivity. It was proven in pilot plant testing that differing blend compositions can impact both the ‘cold’ and ‘hot’ permeability through their behaviour in the mixing and granulation phase of the process. Therefore, the ignition permeability KPI was the most effective parameter to examine the granules created from the mixing and granulation of the blends. The ignition permeability results of all FT trials are shown in Figure 5.3.

5.3.1 FT trial 1

From Figure 5.3 it can be observed that FT1 showed a positive impact on ignition permeability in all 3 sinter machines (SM) when compared to the other blends in

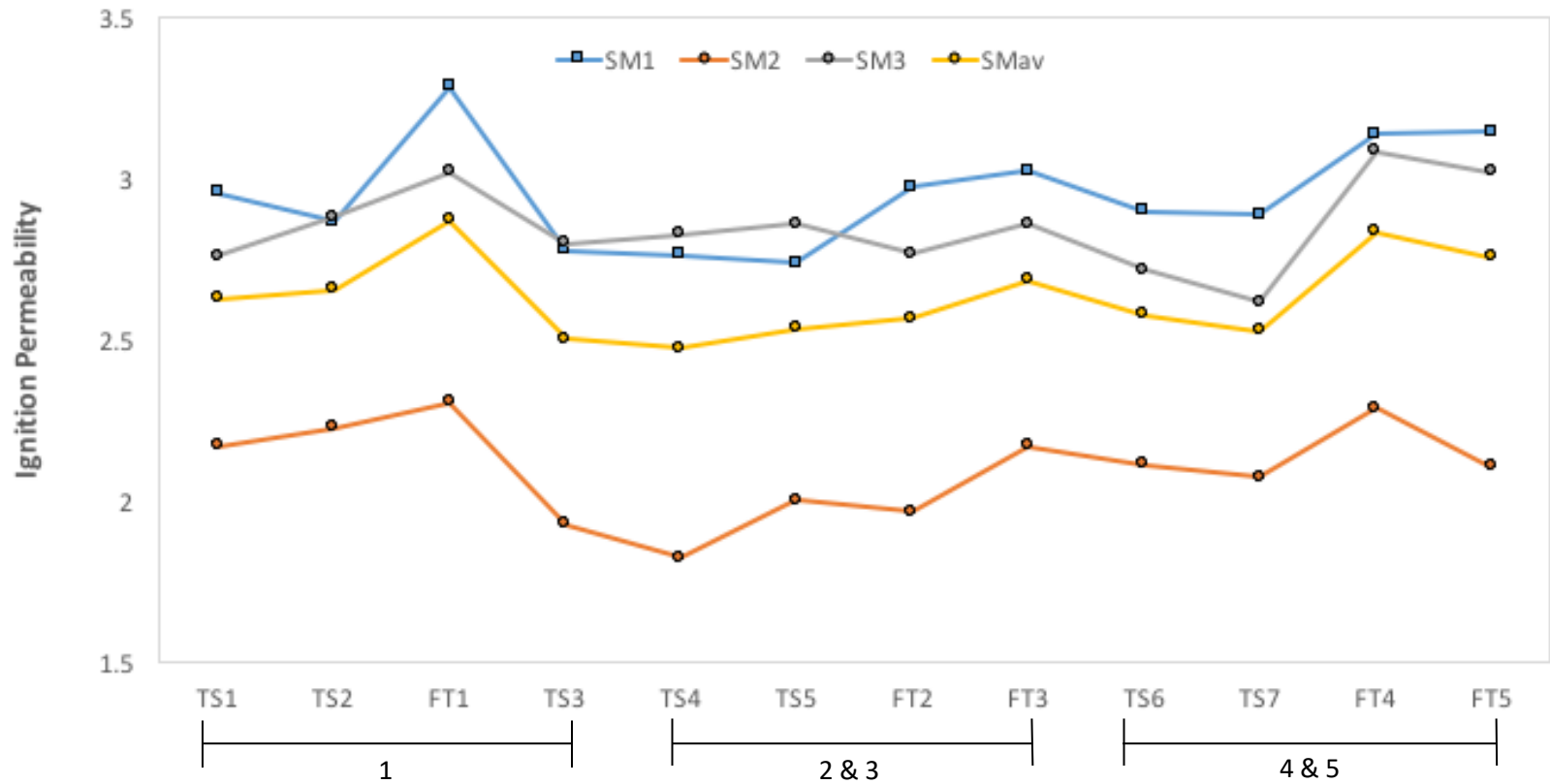


Figure 5.3 – Sinter machine ignition permeability (relative units) for FT trials

the trial (TS1, TS2 and TS3). Considering the average sinter machine (SMav) ignition permeability then the increase compared to the best performing planned blend in the trial was 7.4% (Figure 5.7). The total fine ore proportion (concentrated and pellet feed ores) of FT1 was 5% lower than the planned blends, which was designed due to the new application of FT blend design (Table 5.1). Past plant measurement data was utilised to draw a correlation with total fine ore proportions and ignition permeability (Figure 5.8). As can be seen in Figure 5.8 there is not a significantly strong correlation between increasing total fine ore proportions and reducing average sinter machine (SMav) ignition permeability. Thus, it is thought that the increase in average sinter machine (SMav) ignition permeability with FT1 was substantially greater than the impact of decreasing the total fine ore proportion by 5wt% in the blend.

During the FT trial 1 granule samples were taken for blends TS2, FT1 and TS3. Frozen sieve analysis was conducted twice on the samples with the same methodology as in Section 3.2.4. Like the pilot plant testing the aim was to evaluate differences in the granule size distributions (GSDs) produced from the mixing and granulation phase and validate the previous concepts discussed about the driving factors behind sinter bed permeability (Chapter 4). The GSD of the blends are shown in Figure 5.4. The GSDs were utilised to calculate the mean diameter (D_m) (Figure 5.5) and spread of granule sizes (n) (Figure 5.6) by applying the Rosin-Rammler distribution as described in Section 3.2.1.

Figure 5.5 and 5.6 show that the FT1 blend created the largest mean granule diameter (D_m) and the narrowest spread of granule sizes (largest n). Relating back to the pilot plant testing it was proven that both mean granule diameter (D_m) and GSD spread (n) were interconnected. Increasing mean granule diameter resulted in a narrowing of the GSD spread (increasing n) (Figure 4.20). The narrowing in GSD spread was demonstrated to increase the 'cold' permeability of the bed (Figure 4.18 and 4.32). The GSD and ignition permeability results in FT trial 1 abided by the same principles. The FT1 blend had the greatest ignition permeability, which was a consequence of the larger mean granule diameter and narrower GSD spread (larger n) created by the granulation of the FT blend when compared to the other blends in the trial.

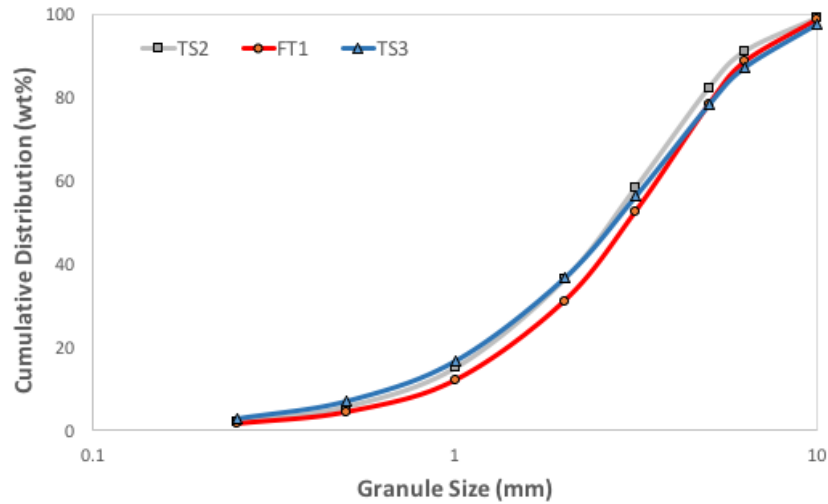


Figure 5.4 – GSD fitted with the Rosin-Rammler distribution for blends in TS2, FT1 and TS3

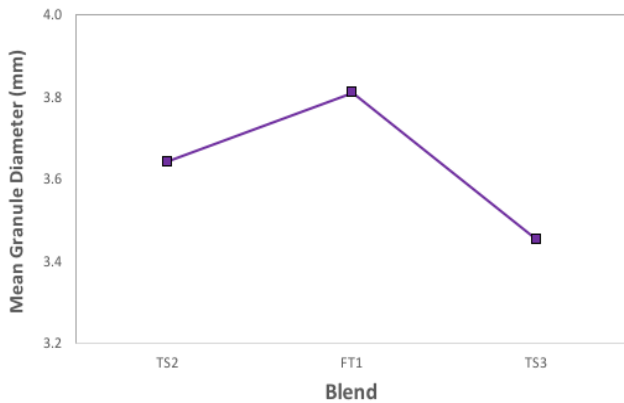


Figure 5.5 – Mean granule diameter (D_m) for TS2, FT1 and TS3

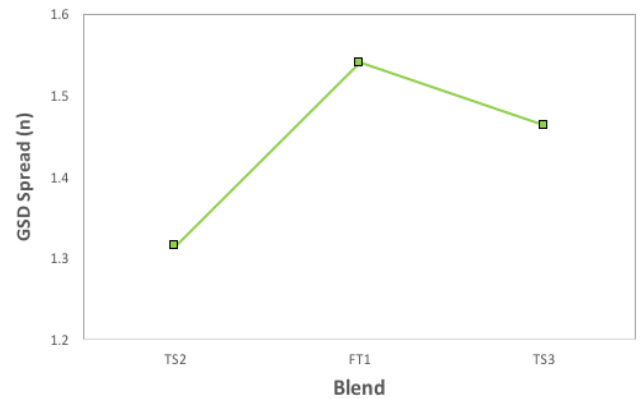


Figure 5.6 – GSD spread (n) for TS2, FT1 and TS3

5.3.2 FT trial 2 and 3

From Figure 5.3 the blends FT2 and FT3 created increased average sinter machine (SMav) ignition permeability when compared to the planned blends (TS4 and TS5). Interestingly during the FT2 trial, the ignition permeability of the 3 sinter machines did not change uniformly, as with FT1 and FT3. In fact, for sinter machines 2 and 3 (SM2 and SM3) the ignition permeability decreased. Referring to Table 5.1 the FT2 blend had 5wt% more total fine ores in the blend and was at the largest total fine ore proportion out of any of the blends in the trials. Even though as stated there has been a weak correlation between total fine ore proportions and ignition permeability in the past (Figure 5.8) this does suggest that improvements in ignition permeability when

designing FT blends were not so consistent as in the lower total fine ore proportions in FT1 and FT3. This could also be seen in the ignition permeability results summary where FT2 showed the smallest increase in average sinter machine (SMav) ignition permeability compared to the best planned blend in the trial (1.3%) (Figure 5.7). This result contradicts the pilot plant studies as it was shown in Figure 4.33 that the 'cold' bed permeability increase was greatest with the FT blends at the largest layering particle proportion (50wt%). SM1 showed similar behaviour to this effect with a significant increase in ignition permeability, which makes the results from FT trial 2 difficult to completely conclude on.

The ignition permeability of the sinter machines for FT3 all displayed comparable increases compared to the planned blends (TS4 and TS5). FT3 was designed at a lower total fine ore proportion to determine whether the ignition permeability would reach that during FT1. As can be identified from Figure 5.3 this was not the case. Even though there were 5wt% less total fine ores when compared to FT1 the average sinter machine (SMav) ignition permeability was lower, proving that decreasing the total fine ore proportion in blends does not necessarily mean the ignition permeability of the bed increases. FT3 did still show enhanced average sinter machine (SMav) ignition permeability compared to the next best planned blend in the trial, which was 4.0% (Figure 5.7).

5.3.3 FT trial 4 and 5

FT4 and FT5 exhibited increased average sinter machine (SMav) ignition permeability when compared to the planned blends in the trial (TS6 and TS7). Figure 5.7 shows that this increase when compared to the best performing planned blend in the trial was 9.2% and 6.6% respectively. The differing average sinter machine (SMav) ignition permeability's of FT4 and FT5 imply that there are other process factors that impact blend ignition permeability. FT4 and FT5 were similarly composed (Table 5.1), therefore the blend composition cannot be responsible for the differing results. At present reasons can only be postulated to why this occurred, however this information did highlight other process parameters such as moisture content that could require greater monitoring and control to consistently optimise blend ignition permeability.

5.3.4 Ignition permeability results summary

The FT trials proved that FT blends created enhanced ignition permeability compared to the planned blends. The increases in average sinter machine (SMav) ignition permeability compared to the best planned blends in the trials were 1.3-9.2% (Figure 5.7). Ignition permeability is a key bed property, as it is the beds starting permeability and therefore the first process KPI showing the capacity available through the blend.

Ignition permeability provided a measure for the granules created by the blends during granulation. The 'cold' bed permeability was previously proven to be related to increasing mean granule diameter (D_m) and narrowing GSD spread (n). Granule sampling during FT trial 1 similarly showed that ignition permeability was also related to these factors. FT1 produced a larger mean granule diameter and narrower GSD spread (larger n) than the planned blends (TS2 and TS3), thus increased ignition permeability. The reason for the increased ignition permeability is the layering PSD of the FT blends compared to the planned blends. The FT blends had a wider layering PSD spread (smaller n), as like in the pilot plant testing (Section 4.4). Wider layering PSD spreads were proven in Section 4.3.1 to increase the 'cold' bed permeability through narrowing the GSD spread and increasing mean granule diameter due to a greater mass of particles layering in granulation (Figure 4.18 to 4.20). The same concept can be applied to the FT trials, which was verified during granule sampling in FT trial 1.

The differing total fine ore proportions (concentrated and pellet feed ores), which were in some cases purposely designed and in others an impact of ore stock levels could have impacted the ignition permeability results. However, Figure 5.8 shows the correlation between total fine ore proportions and ignition permeability for blends over a recent period. As can be identified from Figure 5.8 blends at similar total fine ore proportions had very different average sinter machine (SMav) ignition permeability. This again shows that differing blend compositions significantly impact the beds ignition permeability. The FT blends in each trial proved to have greater ignition permeability's than any of the typically planned blends used for comparison (Figure 5.7). Further, despite the fact that there were differing total fine ore proportions in the blends during the FT trials, the FT blends created average sinter

machine (SMav) ignition permeability's that were greater than any other planned blends (TS) at similar total fine ore proportions over a recent period (Figure 5.8). This was except for FT3 but none the less emphasises the positive impact that designing FT blends has on the ignition permeability of the bed.

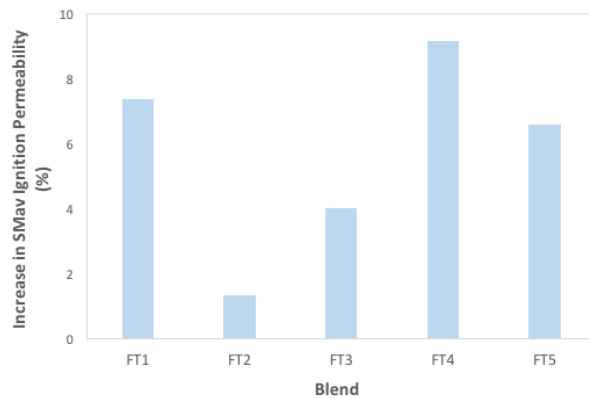


Figure 5.7 – Increases in average sinter machine (SMav) ignition permeability compared to the best planned blend for FT trials

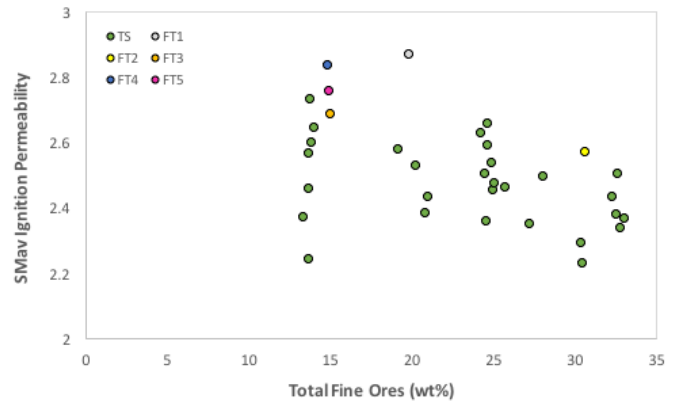


Figure 5.8 – Relationship between total fine ore proportion and average sinter machine (SMav) ignition permeability (relative units)

5.4 Flame front speed

Flame front speed (FFS) is a measure of the rate the flame front passes through the bed. FFS is based on strand length, end sinter point, strand speed and bed height (Equation 13 and 14). FFS has a direct impact on production rate, the faster the flame front passes through the bed the greater the production rate (Figure 5.12), thus stresses the importance of this KPI. The FFS results for the FT trials are shown in Figure 5.9.

$$ESPT = \frac{(L-ESPD)}{SS} \quad (13)$$

$$FFS = \frac{H}{ESPT} \quad (14)$$

where: ESPT = End sinter point time (min)

SS = Strand speed (m/min)

L = Strand length (m)

FFS = Flame front speed (cm/min)

ESPD = End sinter point distance (m)

H = Bed height (cm)

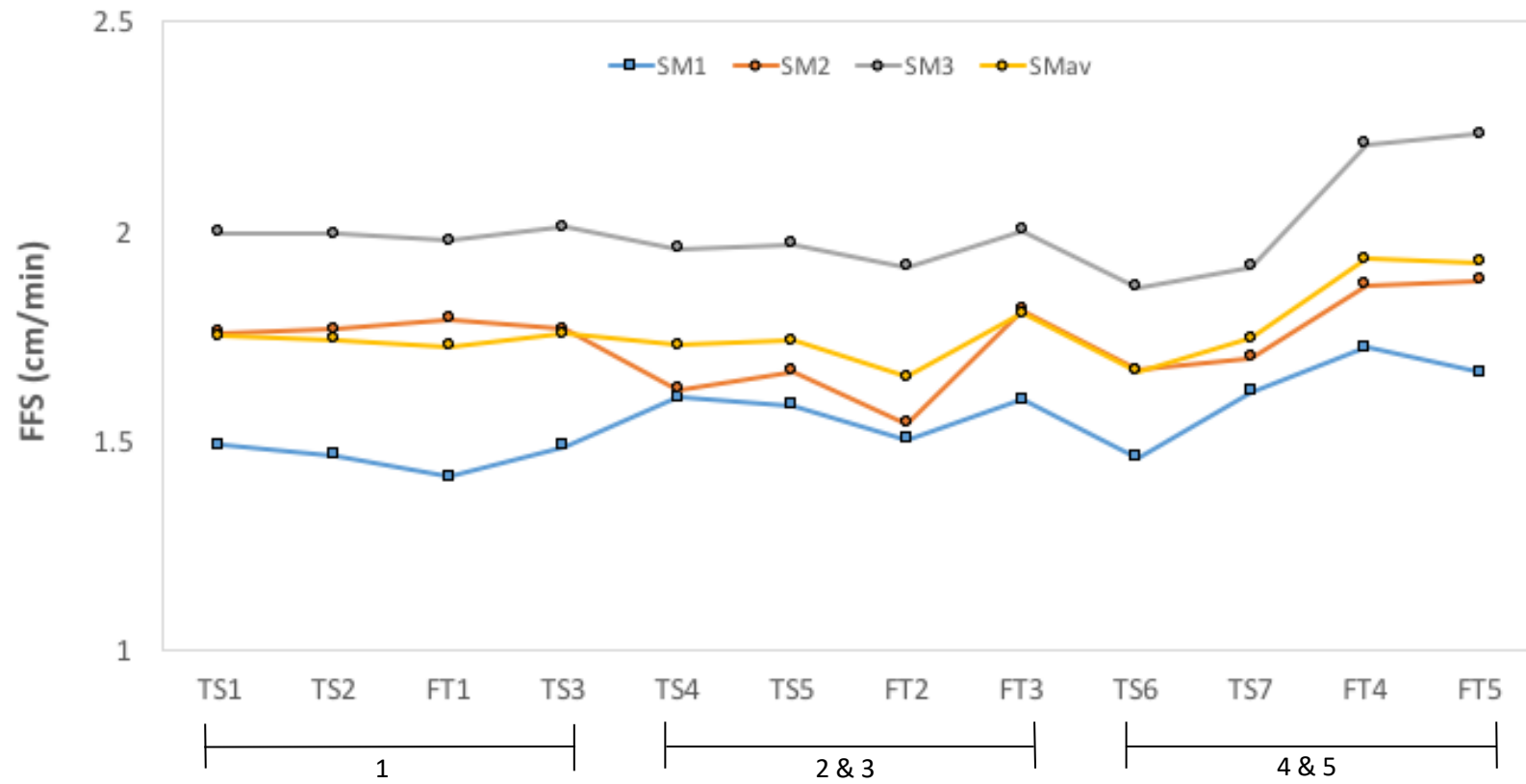


Figure 5.9 – Flame front speed (FFS) for FT trials

5.4.1 FT trial 1

Figure 5.9 indicates that there was no increase in average sinter machine (SMav) FFS for FT1. Even though ignition permeability increased by 7.2% (Figure 5.7) this was not utilised to increase the FFS. The reason was due to plant issues with sinter cooling, which meant that the sinter could not leave the strand too hot as this would burn the conveyor belts. Thus, the strand speed could not be maximised.

Even though there were process issues in FT1 only a small decrease in average FFS was observed. In combination with the 7.2% increase in ignition permeability this implied that there was greater process capacity available with the FT1 blend when compared to the other blends in the trial (TS1, TS2 and TS3). It can confidently be stated that if there were no process issues with sinter cooling then the average sinter machine (SMav) FFS of FT1 would have been faster than the other blends in the trial.

5.4.2 FT trial 2 and 3

The FFS of FT2 decreased in comparison with the other blends in the trial (TS4 and TS5) (Figure 5.9). Referring to Figure 5.7 FT2 had the smallest average sinter machine (SMav) increase in ignition permeability (1.3%) when compared to the other FT trials. The increased ignition permeability did not translate through to increased FFS. This was an unexpected result, especially after analysing the results in FT1.

Moving to FT3 a sharp increase in average sinter machine (SMav) FFS can be observed in Figure 5.9. Compared to FT2 this blend had a smaller total fine ore proportion, which was designed to identify if the capacity in FT1 could again be reached but this time utilised with no process issues to increase FFS and production rate. This blend reached average sinter machine (SMav) FFS that was greater than any blends in the trials before with an increase of 3.3% compared to the best planned blend in the trial.

5.4.3 FT trial 4 and 5

FT4 and FT5 showed significant further increases in average sinter machine (SMav) FFS when compared to all the other blends and particularly those planned blends in the trial. Even though FT4 and FT5 had a 5wt% less total fine ore proportion the magnitude of the increase in average FFS outweighed any increases in FFS seen with previous similar changes in total fine ore proportions. This proved the positive impact of designing FT blends on FFS with the improvements in production rate shown later.

5.4.4 FFS results summary

The FFS KPI was not only dependent on blend design. Other factors, including process issues can impact the results, which was particularly the case in FT trial 1. Blends can be designed to maximise process capacity, however if process issues arise then the FFS during the blend is impacted. This stresses the importance of maintaining operational efficiency to gain benefit from a FT blend design to increase FFS.

FT trial 4 and 5 provided the grounds for more effective conclusions on FFS. These trials were at similar total fine ore proportions and there were no process issues to impact the results. The increase in average sinter machine (SMav) FFS in the trials compared to the best planned blend was 9.8% and 9.5% respectively. This was considerably more than any other changes in the trials and shows the potential improvement in the FFS KPI when designing FT blends.

FT4 and FT5 showed the largest increase in average sinter machine (SMav) ignition permeability, which was translated through to increased average sinter machine (SMav) FFS. By correlating average sinter machine (SMav) ignition permeability and FFS for all trials in Figure 5.10, a strong correlation can be observed and proves that maximising ignition permeability is key to increase the FFS of the process. However, process issues did impact this correlation, as was the case with FT1. From Figure 5.10 the ignition permeability of FT1 was the greatest out of any of the trials, however did not translate to the greatest FFS. FT1 showed the potential to reach an average sinter machine (SMav) FFS of approximately 2cm/min based on the trend with the other

results. This did not transpire, as the flame front could not pass through the bed at the maximum potential speed because the sinter temperature would be too high when leaving the strand due to the cooler issues during this trial.

FT2 contradicted the results from the other FT trials by showing reduced average sinter machine (SMav) FFS than that anticipated based on the other blend results (Figure 5.10). FT2 was at the highest total fine ore proportion out of all the blends, which may suggest that FFS increases with FT blend design are reduced at higher total fine ore proportions. Process issues were not a factor during this trial, thus did not impact the average sinter machine FFS. No further conclusions can be drawn on why FT2 did not reach the greater FFSs like the other FT blends during the trials.

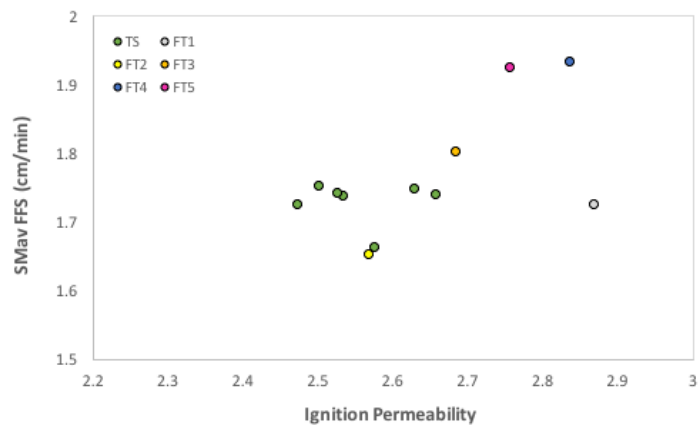


Figure 5.10 – Average sinter machine (SMav) ignition permeability (relative units) and flame front speed (FFS) for FT trials

5.5 Production rate

Production rate measurements for the FT trials were presented as specific net production rate (tonnes/m²/day). Due to sensitivity issues the production rate figures presented are calculated based on the difference from the first blend in the trial. The changes in specific net production rate of the FT trials are shown in Figure 5.11.

5.5.1 FT trial 1

A reduction in average sinter machine (SMav) specific net production rate for FT trial 1 can be observed in Figure 5.11. As stated previously process issues with the cooling of

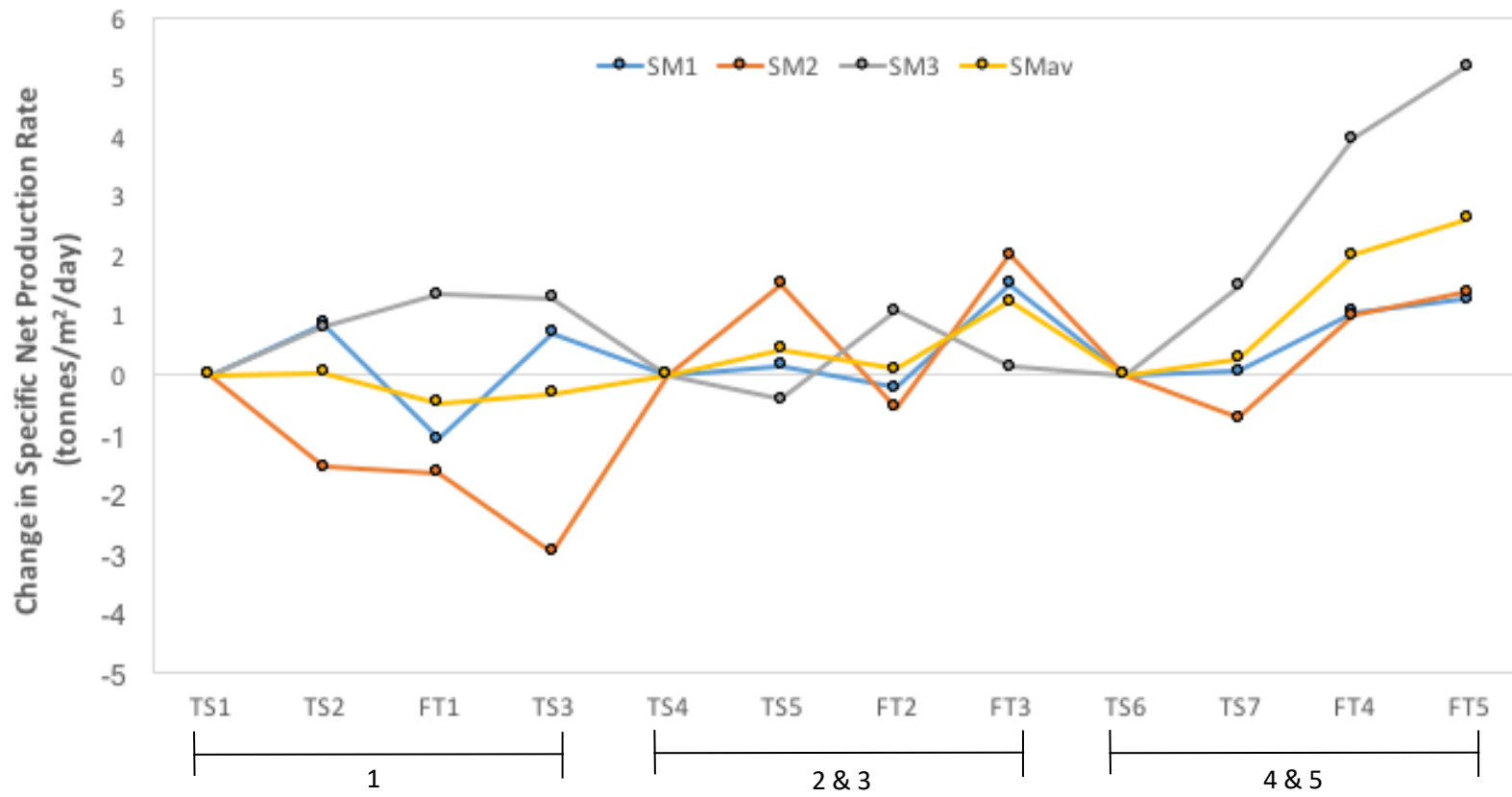


Figure 5.11 – Change in specific net production rate for FT trials

the sinter during FT trial 1 reduced the FFS and thus impacted the specific net production rate. This was verified in Figure 5.10 with the relationship between average sinter machine (SMav) ignition permeability and flame front speed (FFS). FT1 was the largest anomaly to the trend with a significantly smaller average sinter machine (SMav) FFS than expected for the ignition permeability. If the FFS predicted for the ignition permeability was utilised during the process, then it can be confidently stated that there would have been an increase in specific net production rate during FT trial 1.

5.5.2 FT trial 2 and 3

It was earlier shown that FT2 gave the smallest increase in average sinter machine (SMav) ignition permeability (Figure 5.7) and unexpectedly led to a reduction in FFS (Figure 5.9). Due to the strong relationship between average sinter machine (SMav) FFS and changes in specific net production rate (Figure 5.12) this meant a reduction in average sinter machine (SMav) specific net production rate compared to the best planned blend in the trial (Figure 5.11).

FT3 increased the average sinter machine (SMav) specific net production rate (Figure 5.11). Using the actual specific net production figures, as shown in Figure 5.12 this was an increase of 2.5% compared to the best planned blend in the trial and was attributed to the increased FFS (Figure 5.9). However, from Table 5.1 a reduction in the total fine ore proportion occurred during this trial. This could have impacted the specific net production result shown for FT3 in Figure 5.11 but was purposely designed to try and obtain the specific net production rates that could have been obtained by FT1 without the process issues.

5.5.3 FT trial 4 and 5

The final FT trials displayed the largest increases in average sinter machine (SMav) specific net production rate (Figure 5.11). As shown in Figure 5.9 FT4 and FT5 created the greatest FFSs, which translated through to the greatest increases in specific net production rate compared to the other blends in the trials (Figure 5.13). Figure 5.13

shows the increase in average sinter machine (SMav) specific net production rate compared to the best planned blend in the trial based on actual production figures. This was 5.4% and 7.2% respectively. The similar total fine ore proportions shown in Table 5.1 reduces the impact of this factor on the production rate measurements and proved that the effect was an impact of designing blends to the FT equation. The similar compositions of FT4 and FT5 also showed consistency in the average sinter machine (SMav) specific net production rate increases observed.

5.5.4 FT trial production rate summary

FFS was the driving factor behind production rate. Figure 5.12 emphasises the relationship by showing the positive influence of average sinter machine (SMav) FFS on specific net production rate. Figure 5.13 shows the increases in average sinter machine (SMav) specific net production rate based on actual production figures. The increases compared to the best blends in each trial were 2.5-7.1%.

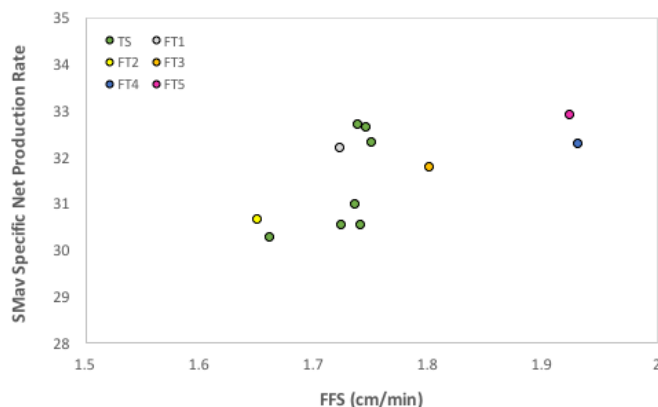


Figure 5.12 – Relationship between average sinter machine (SMav) flame front speed (FFS) and specific net production rate (relative units)

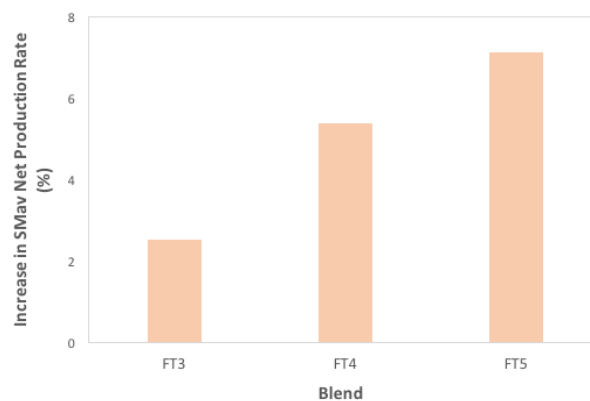


Figure 5.13 – Increases in average sinter machine (SMav) specific net production rate compared to the best planned blend for FT trials

The remaining FT trials (FT1 and FT2) did not exhibit increased specific net production rates, which was a result of their decreased FFS (Figure 5.9). In FT1 this was attributed to process issues with the cooling of the sinter. The additional process capacity created in the ignition permeability of FT1 (Figure 5.7) could not be utilised to increase FFS and thus specific net production rate. However, it can confidently be assumed that without the process issues that this blend would have increased both process KPIs.

FT2 proved to be an anomaly as the increased average sinter machine (SMav) ignition permeability did not translate through to FFS and specific net production rate even though there were no process issues. The increase in average sinter machine (SMav) ignition permeability however was the lowest out of the trials at 1.3% (Figure 5.7). It is postulated that as FT2 was at the largest total fine ore proportion it impacted the ignition permeability increase. Previously during pilot plant testing it was shown that larger layers in granules were created at increased layering particle proportions (Table 4.9 and 4.11). The larger layers developed reduced the 'cold' and 'hot' permeability of the beds and thus reduced sintering times (Figure 4.32 and 4.42). Even though ignition permeability is not the 'cold' or 'hot' permeability but an intermediate this suggests that during the trials a reduction in permeability occurred between ignition and 'hot' bed permeability. This would not be visible in the ignition permeability KPI, however would impact the FFS and specific net production rate of the blend as 'hot' permeability was proven to be the driving factor behind sintering time and production rate (Figure 4.30 and 4.42). This stresses the requirement for the development of an on-line 'hot' bed permeability measurement at Tata Steel Europe to enable continual permeability optimisation for the diverse sinter blend compositions used in operations.

5.6 Quality

Cold strength, as introduced in the background chapter (Section 2.2) and pilot plant testing (Section 4.4.3) is a measure for the degradation of sinter on transport and directly impacts the net production rate through the return sinter fines rate. Cold strength was measured by the Japanese Tumble test, where a sinter sample is tumbled for a period and <5mm and >10mm proportions determined by sieve analysis. Sinter

samples are regularly taken and analysed as part of normal practice. Increased sinter cold strength would signify smaller proportions <5mm and larger proportions >10mm.

Reduction-disintegration index (RDI) was another key sinter property introduced in Section 2.2. RDI is a measure for sinter break-up from the stresses created by reduction in the blast furnace. The production of finer fragments of sinter in the furnace is undesirable as it affects gas flow (Geerdes 2009). RDI is determined by processing a sinter sample through an in-house developed blast furnace simulation apparatus before tumbling and sieve analysis to determine <3.15mm proportion of sinter. Smaller sinter proportions <3.15mm signify greater resistance to reduction-disintegration.

A different factor that was incorporated in sinter quality was the amount of dust produced from the bed throughout the blend. Increased dust production has the consequent impact of reducing net production rate and can provide indications to how effectively the bed sintered. Dust was collected through filters and deposited into bins for recycling through the process. The mass of dust produced per blend was recorded.

5.6.1 Cold strength

No trend in the cold strength results could be distinguished during the FT trials (Figure 5.14). It was not hypothesised that designing FT blends would increase the cold strength and there was no difference between the cold strengths during the pilot plant testing (Section 4.4.3). The changes in cold strength shown in Figure 5.14 were not significant enough to cause issues down the process chain. This was particularly important in the FT trials where increased flame front speed (FFS) and production rate was produced, as creating a faster production rate but with an increased return fines rate would be counterproductive.

5.6.2 Reduction-disintegration index (RDI)

The reduction-disintegration index (RDI) results from the sinters are shown in Figure 5.15. Similar to cold strength no consistent trend was observed with RDI during the

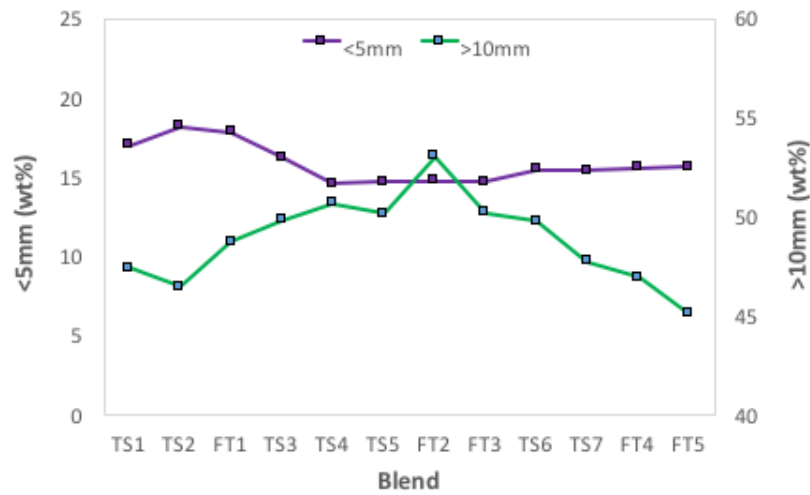


Figure 5.14 – Japanese tumble test results for FT trials

trials. In none of the FT blends were the RDI values above the non-tolerable limit of 30% of the sinter sample <3.15mm. There were no reported issues concerning RDI further down the process chain. RDI results could not be obtained for FT4 due to maintenance of the RDI analysis equipment.

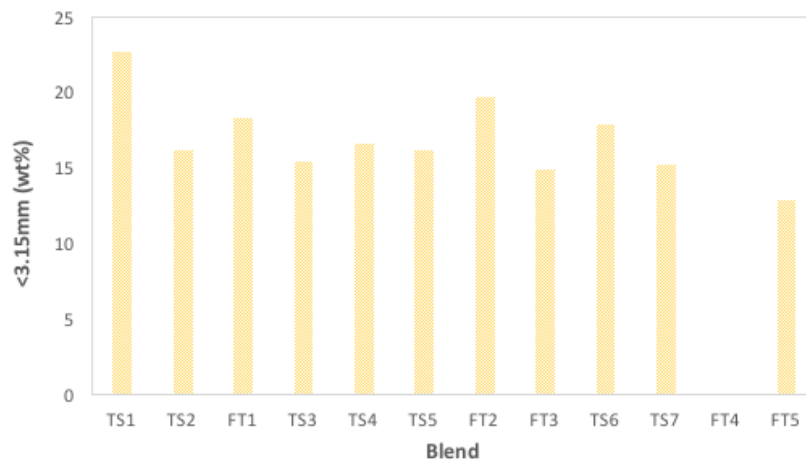


Figure 5.15 – Reduction-disintegration (RDI) results for FT trials

5.6.3 Dust production

The dust production from the trials is presented in Figure 5.16. For the FT4 and FT5 dust production was not recorded because of issues with the measurement system in the bins. However, the remaining FT blends proved to have a strong impact by reducing the amount of dust produced during the trials.

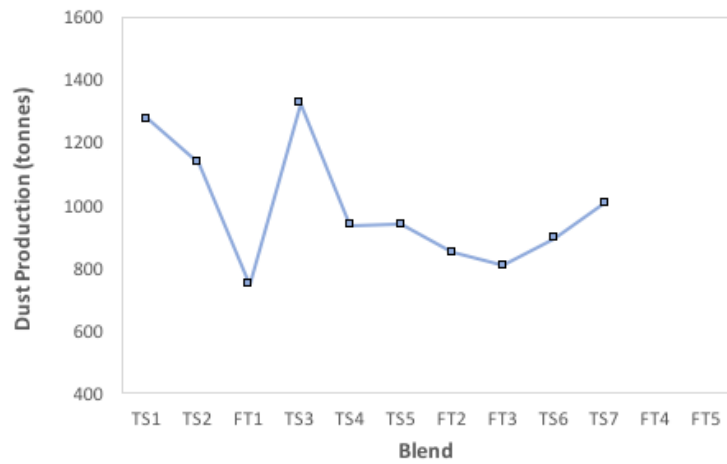


Figure 5.16 – Dust production for FT trials

Correlating dust production with ignition permeability in Figure 5.17 identified that increased average sinter machine (SMav) ignition permeability reduced dust production. Most of the dust produced from the bed is a result of remaining ‘non-sintered’ material. ‘Non-sintered’ material is relatively weak when compared to sinter, thus increased dust production is linked to larger amounts of ‘non-sintered’ material. It is thought that increased ignition permeability creates a more uniform and effective ignition across the bed. The increased ignition permeability created fewer areas in the bed where the flame front did not reach to create the temperatures required for sintering leaving less ‘non-sintered’ material in the bed.

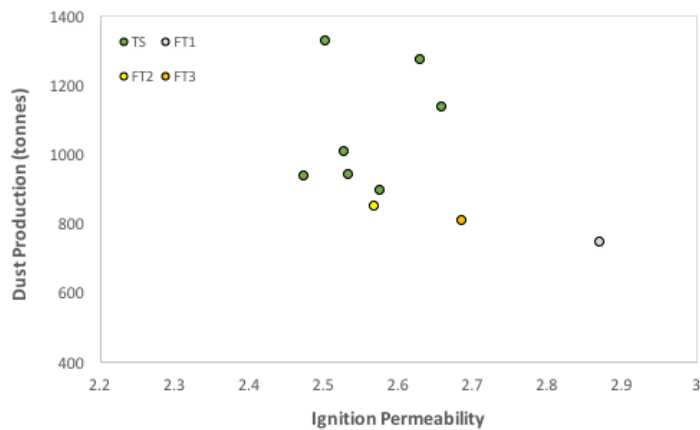


Figure 5.17 – Relationship between average sinter machine (SMav) ignition permeability (relative units) and dust production for FT trials

5.7 FT trial summary

To summarise the FT trials, it was initially clear that the FT blends had a positive impact on ignition permeability. Increases in average sinter machine (SMav) ignition

permeability between 1.3-9.2% were observed against the best planned blends (TS) in the trials (Figure 5.7). The results validated the increased 'cold' permeability during pilot plant testing, however not at the same magnitude. Further, all but one of the FT trials (FT3) increased ignition permeability compared to planned blends over a recent period at similar total fine ore proportions (Figure 5.8). The reason refers to the pilot plant studies where wider layering PSD spreads (smaller n) increased the 'cold' bed permeability (Section 4.3 and 4.4). The FT blends similarly had a wider layer PSD spread compared to the planned blends and thus exhibited increased ignition permeability.

Flame front speed (FFS) was shown to be impacted by operational issues in plant. This was the situation during FT trial 1, as the increased average sinter machine (SMav) ignition permeability could not be utilised to increase FFS. No increase in FFS was observed during FT trial 2. It is still not clear why this occurred, as there was an increase in average sinter machine (SMav) ignition permeability of 1.3%. Reasons were postulated as to why within this section. The remaining FT trials showed increases in FFS of up to 9.8%.

Due to the strong relationship shown between FFS and specific net production rate (Figure 5.12) the three FT trials with increased average sinter machine (SMav) FFS had a positive impact on average sinter machine (SMav) specific net production rate. Increases between up to 7.1% were produced. The more conclusive results can be taken from FT trials 4 and 5 where a consistent increase in average sinter machine (SMav) specific net production rate was observed (5.4% and 7.1% respectively). The similar total fine ore proportions compared to the planned blends in the trial diminished the impact of this factor. It is predicted that FT trial 1 would have created similar increases in average sinter machine (SMav) specific net production rate if not for the process issues encountered.

The major impact on sinter quality during the trials was related to dust production. Ignition permeability strongly impacted dust, thus decreased dust production occurred with the FT blends. No trend in the other sinter quality parameters; cold strength and RDI were seen during the trials. At no point were there reports of the sinter qualities below the non-tolerable limits that could impact processes further down the chain.

It is difficult to compare the results from the FT trials to other similar and available literature or data. In terms of the available literature on investigating the impact sinter blend PSD at full-scale plant operation then to our knowledge none could be found. This highlights the originality of the work conducted and builds on the lack of currently available literature by investigating and openly reporting the impact that sinter blend PSD has on the sintering process parameters at full plant scale. In addition, the FT blend design method provides an example of a means to optimise blend PSD to gain benefits in terms of permeability and productivity. Ideas such as this can be further developed or stand as an example to create other spin-off projects with optimising sinter blend PSD. With regards the available data from other sinter plants in Europe or globally then the sensitivity of this information means that it is not freely shared, thus making it very difficult to compare the results from the FT trials with other similar trials. Again, it is hoped that this research serves as an example to the sharing of full-scale plant trial results between sinter plants and in particular sinter blend PSD to increase the overall knowledge on this topic with the objective to increase sinter plant efficiency worldwide.

Chapter 6 – Conclusions

The pilot plant testing and TATA Steel Europe plant trials enabled several conclusions to be drawn:

1. The particle size distribution (PSD) of the iron ore component of sinter blends has a significant impact on granule properties, sinter bed permeability and production rate.
2. The FT equation exponent (Ψ) that gave the optimum performing granules in terms of the 'cold' permeability and 'cold' permeability efficiency was 0.5. A maximum particle size of layering particles was estimated as 0.5mm in this study.
3. The investigation on the layering PSD spread (n) in sinter blends showed that 'cold' permeability was directly related to granule size distribution (GSD) spread (n). Narrowing GSD spread led to increases in 'cold' permeability. GSD spread was impacted by the spread of particle sizes in the layering material. Widening the layer PSD spread in blends narrowed the GSD spread and increased mean granule diameter (D_m), which were proven to be interconnected. This was a result of more particles layering and less 'non-layered' (or 'non-granulated') particles in the bed.
4. The measured 'hot' permeability was lower than the 'cold' permeability in all blends investigated. A new term was introduced, the 'hot permeability efficiency' defined as the ratio of 'hot' permeability to 'cold' permeability (%) as a useful measure of the beds ability to maintain permeability during the process.
5. The investigation on the layering PSD spread (n) showed that increasing mean granule diameter (D_m) reduced the 'hot' permeability efficiency. However, for the blends analysed in this study the FT blend produced increased 'hot' permeability efficiency than that expected from the other blends based on the

trend with mean granule diameter. The FT blend thus had the greatest 'hot' permeability and shortest sintering times out of the blends used in the study.

6. When comparing base (BB) and Fuller-Thompson (FT) blends at pilot plant scale the FT blends showed enhanced 'cold' permeability at equal layering particle proportions of between 15-25%.
7. Blends designed to the FT equation showed reductions in sintering times of up to 9.5% when compared to the base (BB) blends at equal layering particle proportions. This was a consequence of the increased 'hot' permeability.
8. Designing blends to the FT equation enabled the incorporation of 4wt% more layering particles but which still exhibited the same 'cold' permeability and sintering times as the base (BB) blends. This identifies the potential to increase the proportion of layering particles in FT blends.
9. TATA Steel Europe trials identified that blends designed to the FT equation can increase ignition permeability when compared to typically planned blends by up to 9.2%. Granule sampling proved that this was attributed to the narrower GSD spreads (larger n) and increased mean granule diameters (D_m) created by the FT blends.
10. TATA Steel Europe plant trials proved the potential to increase sintering process specific net production rate by up to 7.1% when designing blends to the FT equation. This was attributed to the faster flame front speeds (FFS).
11. Designing the layering proportion of sinter blends to the FT equation provides a rationale and methodology to increase sinter bed permeability and process production rate without affecting sinter quality.

Chapter 7 – Recommendations

Based on the results from the pilot plant testing and TATA Steel Europe trials several recommendations can be made.

7.1 Sinter blend particle size distribution

This study emphasised the impact that the particle size distribution (PSD) of sinter blends has on key granule and sintering process measurements. It is recommended that PSD receives more consideration during the planning of sinter blends. Even though chemical composition and stock levels are the main controlling factors, the optimisation of the blend PSD should also be considered in blend design practice. The FT blend design method provides an effective means to achieve this. Thus, it is essential that the potential is recognised and utilised to obtain greater value from raw materials and sinter blends. In addition, PSD should play more of a role in iron ore purchasing decisions. If there are certain ores available with more favourable sizes, then these should be considered as valuable for sintering process productivity and receive the necessary priority in the planning and purchasing of iron ores in the future.

7.2 TATA Steel Europe implementation

The FT blend design method should be utilised as an additional tool in current blend design practice. Alongside fulfilling the other blend design criteria such as chemical composition and stock levels the method can be utilised to determine the optimum blend composition with respect to the FT equation. However, being the first study to apply this concept to sinter blend design it is recommended that parallel research, development and further plant trials are conducted alongside implementation.

7.2.1 Development of FT blend design tool

To utilise the FT equation for blend design a tool should be built which can fit in alongside current practice. The FT tool should incorporate the particle size distribution

(PSD) of all sinter blend materials and the FT equation with the optimisation method using the Microsoft Excel™ solver as in Section 3.2.2. The input in the tool would be the planned blend composition. Iron ores that are currently stocked would be varied using the optimisation method along with constraints regarding chemical composition and stock levels. The outcome of running the tool would be the blend composition that has the PSD that optimally fits the FT equation and is within the blend constraints set.

7.2.2 Continued R&D

- **Maximum particle size of the FT equation (D):** Investigating the impact of changing the maximum particle size of layering particles in the FT equation on key granule and sintering process measurements. 0.5mm was selected as the maximum layering particle size (D) during this study, which was determined by microscopy and literature. However, further investigations with varying the maximum particle size (D) would only add to the knowledge and rigour of the FT blend design, particularly as this is a new concept.
- **Layering particle proportions:** Extending the proportions of layering particles used in this study to continue the investigation on the impact on key granule and sintering process measurements with FT and base blends. Focusing on greater layering particle proportions than used in this study to identify the ability of FT blends to incorporate more layering particles in blends and identify if there are layering particle proportion limits with FT blend design.

7.2.3 Plant trials 2

It is recommended that further full-plant trials are carried out at TATA Steel Europe. During the FT trials in this study the FT blends showed the potential to increase the sintering process production rate. However, a longer campaign of FT designed blends (10+) would be required to assess the consistency in process productivity. Financial evaluation of the blend costs and production rates would be required to realise the value in consistently incorporating FT blend design into standard blend design practice. A proposal has been created and FT trials 2 are planned for Q4 Financial Year 2016/17.

Chapter 8 – References

Allerdice, B. 2007. *Module 3: Ore preparation and sintering*. Unpublished internal document, Corus Strip Products UK.

Australian Government. 2015. *Iron Fact Sheet*. Available at: http://www.australianminesatlas.gov.au/education/fact_sheets/iron.html [Accessed: 28 May 2015].

Bergstrand, R. et al. 2005. The Effect of Marra Mamba Ore Addition on the Granulation Characteristics of Pisolite Based and Hematite Based Sinter Blends. *ISIJ International* 45(4), pp492-499.

Besta, P. et al. 2013. The cycle and effect of zinc in the blast furnace process. *Metalurgja* 52(2), pp197-200.

Bhagat, R.P. 2007. *Fundamentals of Iron Ore Sintering*. Available at: <http://eprints.nmlindia.org/5910/1/132-149.PDF> [Accessed: 26 May 2016].

Capes, C.E. and Danckwerts, P.V. 1965. Granule formation by the agglomeration of damp powders. Part 1: The mechanism of granule growth. *Transactions Institution Chemical Engineers* 43, pp116-124.

Cores, A. et al. 2013. Iron ore sintering: Part 1. Theory and practice of the sintering process. *Dyna* 80(180), pp153-171.

Dawson, P.R. 1992. *Recent developments in sintering technology*.

Di Giorgio, N. et al. 2011. Reengineering Bluescope Steel's Port Kembla sinter plant for high productivity and reduced steel works greenhouse emissions. *Proceedings of the 2011 Chemeca, Engineering a Better World*. Sydney; Australia, 18-21 September, 2011.

Dubois, I. et al. 2010. S. Correlation between particle size and surface area for chlorite and K-feldspar. *Proceedings of the Water Rock Interaction*. Guanajuato; Mexico, January, 2010.

Ellis, B. G. et al. 2007. Effect of ore properties on sinter bed permeability and strength. *Ironmaking & Steelmaking* 34(2), pp99-108.

Ergun, S. 1952. Fluid flow through packed columns. *Chemical Engineering Progress* 48, pp89-94.

Excel Easy. 2017. *Solver*. Available at: <http://www.excel-easy.com/data-analysis/solver.html> [Accessed: 17 October 2015].

Favre, S. and Kooij, C. 2013. *A roadmap to optimal sinter feed granules*. Unpublished internal document, Tata Steel Europe.

- Fennis, S. A. A. M. and Walraven, J. C. 2012. Using particle packing technology for sustainable concrete mixture design. *Heron* 57(2), pp73-101.
- Fluid Air. 2013. *High-Shear Granulation*. Available at: http://www.fluidairinc.com/high-shear_granulation.html [Accessed: 24 October 2016].
- Fuller, W. B. and Thompson, S. E. 1907. *The laws of proportioning concrete Transactions of American Society of Civil Engineers*.
- Fwa, T. F. 2005. *The handbook of highway engineering*. CRC Press.
- Gan, M. et al. 2015. Optimising method for improving granulation effectiveness of iron ore sintering mixture. *Ironmaking & Steelmaking* 42(5), pp351-357.
- Geerdes, M. et al. 2009. *Modern Blast Furnace Ironmaking: An Introduction*. 2nd ed. Amsterdam: IOS Press.
- Ghosh, A. and Chatterjee, A. 2008. *Ironmaking and Steelmaking: Theory and Practice*. New Dehli: PHI Learning Private Limited.
- Glavind, M. and Pedersen, E. J. 2012. Packing calculations applied for concrete mix design. *Proceedings Creating with Concrete*. University of Dundee, May, 1999. Available at https://www.dti.dk/_/media/Pack-calc-Dundee_May_1999.pdf [Accessed: 10 January 2015].
- Hage, J. L. T. 2015. *IMSIMI – Improved sinter mix preparation while using challenging input materials*. Unpublished internal document, Tata Steel Europe.
- Harsha Nistala, S. et al. 2015. Study of generation of sinter return fines during transportation. *Ironmaking & Steelmaking* 42(3), pp226-232.
- Iron Investing News. 2016. *Types of Iron Ore: Hematite vs Magnetite*. Available at: <http://investingnews.com/daily/resource-investing/base-metals-investing/iron-investing/types-of-iron-ore-hematite-vs-magnetite/> [Accessed: 29 May 2015].
- ITP Mining. 2013. *Iron*. Available at: <https://energy.gov/sites/prod/files/2013/11/f4/iron.pdf> [Accessed: 25 May 2015].
- Iveson, S.M. and Litster, J.D. 1998. Growth regime map for liquid-bound granules. *AIChE Journal* 44(7), pp1510-1518.
- Jak, E. and Hayes, P. 2012. The use of thermodynamic modeling to examine alkali recirculation in the iron blast furnace. *High Temperature Material Processes* 31(4-5), pp657-665.
- Khosa, J. and Manuel, J. 2007. Predicting granulating behavior of iron ores based on size distribution and composition. *ISIJ International* 47, pp965-972.

Klinger, A. et al. 2010. *Expert systems controlling the iron making process in closed loop operation*. Available at: <https://www.intechopen.com/books/expert-systems/expert-systems-controlling-the-iron-making-process-in-closed-loop-operation> [Accessed: 13 August 2016].

Lindeberg, M.R. 2013. *Mechanical Engineering Reference Manual for the PE exam*. 13th ed. California: The Power to Pass.

Litster, J. D. and Waters, A. G. 1988. Influence of material properties of iron ore sinter feed on granulation effectiveness. *Powder Technology* 55, pp141-151.

Litster, J. and Ennis, B. 2004. *The Science and Engineering of Granulation Processes*. The Netherlands: Kluwer Academic Publishers.

Maeda, T. 2005. Effect of adding moisture and wettability on granulation of iron ore. *ISIJ International* 45(4), pp477-484.

Malvern. 2007. *Sample dispersion and refractive guide*. Available at: https://www2.warwick.ac.uk/fac/cross_fac/sciencecity/programmes/internal/themes/am2/booking/particlesize/sample_dispersion__refractive_index_guide.pdf [Accessed: 20 October 2015].

Malvern. 2017. *Mastersizer 3000*. Available at: <http://www.malvern.com/en/products/product-range/mastersizer-range/mastersizer-3000/> [Accessed: 20 November 2015].

Mao, H. et al. 2013. Effect of surface properties of iron ores on their granulation behaviour. *ISIJ International* 53(9), pp1491-1496.

Marsden, M. 2014. *SteelFirst the shifting face of the iron ore derivatives market*.

Matsumura, T. et al. 2009. Effect of moisture absorption behaviour on optimal granulation moisture value of sinter raw material. *ISIJ International* 49(5), pp618-624.

Melzer, S. and Zingrebe, E. 2005. *Characterisation of ores used as sinter feed*. Unpublished internal document, Corus Research, Development and Technology.

Minerals Council of Australia. 2015. *The World's Biggest Iron Ore Producers*. Available at: <http://www.ironorefacts.com/the-facts/iron-ore-global-markets/> [Accessed: 28 May 2015].

Miranda, B.L. 2012. *Gradation-based framework for asphalt mixtures*. Available at: www.diva-portal.org/smash/.../FULLTEXT02.pdf Gradation-Based [Accessed: 16 Jan 2015].

Mohamed, F.M. et al. 2010. Granulation of coke breeze fines for use in the sintering process. *Science of Sintering* 42, pp193-202.

- Mong, L. E. and Adelman, D. M. 1958. Control of factors affecting reproducibility of mechanical properties of refractory semidry press specimens. *Journal of the American Ceramic Society* 41(7), pp267-272.
- Newitt, D.M. and Conway-Jones, J.M. 1958. A contribution to the theory and practice of granulation. *Transactions Institution Chemical Engineers* 36, pp422-442.
- Ouyang, S. and Daemen, J.J.K. 1991. Design of bentonite/crushed rock seals. *Geotechnical and Geological Engineering* 9(1), pp63-72.
- Polat, R. et al. 2013. The correlation between aggregate shape and compressive strength of concrete: Digital image processing approach. *International Journal of Structural and Civil Engineering Research* 2(3), pp62-80.
- Quiroga, P.N. and Fowler, D.W. 2003. *The effects of aggregates characteristics on the performance of Portland cement concrete, Research Report ICAR – 104-1F*. Available at: https://repositories.lib.utexas.edu/bitstream/handle/2152/35333/104_1F_completed.pdf?sequence=2 [Accessed: 10 January 2015].
- Richardson, D.N. 2005. *Aggregate gradation optimization – literature search*. Available at: <https://library.modot.mo.gov/rdt/reports/ri98035/rdt05001.pdf> [Accessed: 6 February 2015].
- Satyendra. 2013. *Technologies for improvements in sintering process*. Available at: <http://ispatguru.com/technologies-for-improvement-in-sintering-process/> [Accessed: 10 August 2015].
- Sen, R. et al. 2010. Effect of grading of chromite ores on the quality of briquettes. *ISIJ International* 50(2), pp200-206.
- Small, J. 2017. *Results and learnings from first campaign of IJTC small sinter pot setup: varying limestone and breeze input with constant blend and moisture*. Unpublished internal document, Tata Steel Europe.
- Sobolev, K. and Amirjanov, A. 2007. The simulation of particulate materials packing using a particle suspension model. *Advanced Powder Technology* 18(3), pp261-271.
- Somasundaran, P. and Moudgil, B. 1987. Reagents in iron ore processing. *Reagents in Mineral Technology* 27, p583.
- Strauss, K. 1970. *Applied Science in the Casting of Metals*. Oxford: Pergamon Press.
- Suresh, V. et al. 2015. Influence of iron ore micro-fines on sinter structure. *Proceedings of the 2015 International Conference on Processing of Lean Grade Urban Ores*. Jamshedpur; India, January, 2015.
- Suzuki, M. et al. 1999. Effect of the size distribution on the relation between coordination number and void fraction of spheres in a randomly packed bed. *Advanced Powder Technology* 10(4), pp353-365.

Tata Steel Europe. 2016a. *Flux chemical compositions*. Unpublished internal document.

Tata Steel Europe. 2016b. *Revert materials*. Unpublished internal document.

Tata Steel Europe. 2016c. *Particle and granule size distribution analysis procedure*. Unpublished internal document.

The Economist. 2014. *Iron ore mining, down but not out*. Available at: <http://www.economist.com/news/business-and-finance/21616294-iron-ore> [Accessed: 25 May 2015].

Umadevi, T. et al. 2011. Influence of iron ore fines feed size on microstructure, productivity and quality of iron ore sinter. *ISIJ International* 51(6), pp922-929.
University of Saskatchewan. 2002. *Particle Shape*. Available at: <http://homepage.usask.ca/~mjr347/prog/geoe118/geoe118.017.html> [Accessed: 21 October 2016].

U.S Geological Survey. 2003. *Mineral Commodity Summaries*. Available at: <https://minerals.usgs.gov/minerals/pubs/mcs/2016/mcs2016.pdf> [Accessed: 22 May 2015].

U.S Geological Survey. 2017. *List of countries by iron ore production*. Available at: https://en.wikipedia.org/wiki/List_of_countries_by_iron_ore_production [Accessed: 29 May 2015].

Van den Berg, T. 2008. *An assessment of the production of fine material in iron ore sinter*. MSc Dissertation, University of Pretoria.

Vazquez C.G. et al. 2010. *Laboratory evaluation of influence of operational tolerance (Acceptance Criterion) on performance of hot-mix asphalt concrete*. Available at: https://ctr.utexas.edu/wp-content/uploads/pubs/O_6045_1.pdf [Accessed: 11 January 2015].

Vesilind, P.A. 1980. The Rosin-Rammler particle size distribution. *Resource Recovery and Conservation* 5, pp275-277.

Walker, G.M. 2007. *Drum Granulation Process*. In: Salman et al. eds. *Handbook of Powder Technology Granulation*. Elsevier, pp.220-254.

Wang, Z. et al. 2014. Effect of sintering conditions on the formation of mineral phases during iron ore sintering with New Zealand ironsand. *Proceedings of the 2014 High Temperature Processing Symposium*. Swinburne University of Technology; Australia, February, 2014.

Wauters, P.A.L. 2001. *Modelling and mechanisms of granulation*. PhD Thesis, University of Delft.

Weeks, R.E. 1965. *The prediction of mix design properties dense graded bituminous moistures*. MSc Dissertation, Missouri University of Science and Technology.

World Steel Association. 2017. *Fact sheet steel and raw materials*. Available at: www.worldsteel.org [Accessed: 25 May 2015].

Wu, S. et al. 2015. Effects of particle characteristics on the granulation ability of iron ores during the sintering process. *International Journal of Minerals, Metallurgy and Materials* 22(9), p907.

Yu, Q.L. and Brouwers, H.J.H. 2012. Development of a self-compacting gypsum-based lightweight composite, *Cement & Concrete Composites* 34, pp1033-1043.

Zheng, J. et al. 1990. Improved equation of the particle size distribution for dense packing. *Journal of the American Ceramic Society* 73(5), pp1392-1398.

Zhou, H. et al. 2015. Influence of coke combustion on NO_x emission during iron ore sintering. *Energy Fuels* 29(2), pp974-984.

Chapter 9 – Appendices

9.1 Summary of methods

Particle size distribution (>0.5mm)

1. 5kg batches of the iron ores dried in a fan oven for 12 hours at $105\pm 2.5^{\circ}\text{C}$.
2. Batches split into 400-500g samples using a riffing box to obtain representative samples.
3. Two repetitions of sieve analysis conducted through the sieve shaker and series shown in Figure 3.1 and 3.2 for 5 minutes at setting 4.
4. Mass retained in each sieve size weighed using scales with $0.01\pm 0.01\text{g}$ accuracy.
5. Masses in each sieve are processed into percentage mass retained. Data is further processed into cumulative size distributions.

Particle size distribution (<0.5mm)

1. Create standard operating procedure (SOP) for each iron ore.
2. Add the ore into an ultrasonic bath containing de-ionised water until the obscuration range is within the limits (8-20%).
3. Start the Malvern Mastersizer software and allow measurement to complete.
4. Masses in each sieve are processed into percentage mass retained. Data is further processed into cumulative size distributions.

FT blend design

1. PSD analysis of iron ores (Section 3.2.1).
2. Calculate the Fuller-Thompson PSD based on Equation 1 and the determined equation parameters (D and Ψ).
3. Microsoft ExcelTM solver: set the objective as the sum of square residuals of mass retained between the FT PSD and the blend.

4. Microsoft Excel™ solver: set the function to 'min' to minimise the sum of the differences in mass retained.
5. Microsoft Excel™ solver: create the required constraints for the blend.
6. Microsoft Excel™ solver: select GRG nonlinear solving method and solve.

Mixing and granulation

1. Create the blend composition sheet as shown in Table 3.9.
2. Determine the water content of the blend by using a moisture balance.
3. Calculate the water addition required.
4. Weigh and add the blend materials to the Eirich mixer.
5. Mixing for 120 seconds at -2000rpm for paddle (+83rpm for drum).
6. Water addition until complete at -2000rpm for paddle (+83rpm for drum).
7. Water mixing for 60 seconds at -2000rpm for paddle (+83rpm for drum).
8. Granulation – Drum on rolling bench for 180 seconds at 24rpm.
9. Determine the exact water content of the granules by using a moisture balance.

Moisture content

1. Measure moisture content of all blend materials (two repetitions).
2. Calculate the moisture to be added to achieve target blend moisture content.
3. Add the required amount of moisture during the mixing process through a moisture injection system.
4. Measure the moisture content of granules after mixing and granulation for exact moisture content (two repetitions). Adjust moisture content if necessary.

Granule size distribution

1. A bulk sample of granules (approximately 2kg) was split into two samples (400-500g) using a riffing box.

2. Each sample is fed through the vibrating feeder into a pot of liquid nitrogen for freezing (Figure 3.13).
3. Excess liquid nitrogen drained away from the pot.
4. The frozen granules are quickly put into the sieve series (Figure 3.14) and vibrated at setting 4 for 2 minutes in the Haver and Boecker Digital Plus sieve shaker (Figure 3.1).
5. The frozen granules in the sieve size ranges are then weighed on scales with an accuracy of $0.01 \pm 0.001\text{g}$.
6. Masses in each sieve are processed into percentage mass retained. Data is further processed into cumulative size distributions and the Rosin-Rammler distribution applied.

Granule microscopic analysis

1. A sample of granules dried at $105 \pm 2.5^\circ\text{C}$ for 12 hours in a fan oven.
2. Set granule sample in epoxy resin under a vacuum.
3. Horizontally dissect the sample to produce a cross-section and polish.
4. Microscopic imaging using Zeiss Axioplan Z1 Imager microscope and camera to produce the mosaic image (Figure 3.16).
5. Microscopic image edited in Adobe Photoshop™ to outline nuclei and layers (Figure 3.17).
6. Threshold segmentation of layering, nuclei and 'non-layered' particles in Axiovision image analysis software.
7. Binary images of layering, nuclei and 'non-layered' particles produced in Axiovision image analysis software (Figure 3.18 to 3.20).
8. Measurements taken by Axiovision image analysis software on number and area of particles in binary images.

'Cold' permeability and efficiency

1. Attach flow meter.
2. Start software.

3. Select pressure differential values – 0, 40, 80, 120, 140mbar.
4. Input bed height (cm).
5. Start measurement.
6. Stop measurement once complete.
7. Save data file.
8. Remove bed in cylinder from device and vibrate on Haver and Boecker Digital Plus sieve shaker on setting 4 for 10 seconds (Figure 3.1).
9. Measure new bed height (cm).
10. Reattach flow meter.
11. Input new bed height (cm).
12. Start measurement.
13. Stop measurement once complete.
14. Save data file.

Ergun equation

1. Input the gas flow velocity (U) and pressure drop (ΔP) measurements provided by the 'cold' permeability equipment into Figure 3.24.
2. Input the bed height (L) and mean granule diameter (d_p) determined by frozen sieve analysis and Rosin-Rammler distribution (Section 3.2.4) into Figure 3.24.
3. Set the Microsoft Excel™ solver to minimise the sum of square residuals (SSE) between the measured and fitted pressure drops by varying bed voidage (ϵ).
4. Run the solver in GRG non-linear setting.
5. Gas flow velocity (m/s) at 250mbar/m is determined from the fitted pressure drop (ΔP -fit) as the measure for the 'cold' permeability.

Sintering

1. Hearth layer inserted into sinter pot – 500g.
2. Charge granules into sinter pot.
3. Ceramic sleeves around all thermocouples – Insert into bed.
4. Close refractory insulation device.

5. Place ignition device over pot.
6. Name and start new test.
7. Turn natural gas and air on and ignite with ignitors and start measurement.
8. Allow burner to ignite the bed for 180 seconds.
9. Turn natural gas and air off.
10. Roll out the O-ring seal and insert on top of pot.
11. Connect the flow meter.
12. Allow sintering to complete then stop test.
13. Save data file.
14. Allow sinter to cool before tapping into bucket for further analysis.

Cold strength

1. Cooled sinter is removed from the sintering equipment, approximately 6kg.
2. Sinter placed in the drum (Figure 3.28).
3. Rotate the drum for 50 revolutions.
4. Once complete empty the sinter out of drum.
5. Sieve the sinter through the series using a large-scale shaker.
6. Masses in the sieves measured on scales with an accuracy of 0.1 ± 0.1 kg. Data processed into mass percentage retained and cumulative distributions.

9.2 Pending publications

Application of the Fuller-Thompson equation in sinter blend design to increase sinter plant productivity

A. Purnell*¹, D. Sapsford¹, C. Kooij² and P. Wauters³

1. School of Engineering, Cardiff University, CF24 3AA, UK.
2. STRIP Products MLE, TATA Steel, IJmuiden, 1970 CA, Netherlands.
3. STRIP Products UK, TATA Steel, Port Talbot, SA13 2NG, UK.

* Corresponding author, email Alex.J.Purnell@tatasteel.com

Abstract

Sinter blend design is one of the key parameters that affects sinter plant productivity and sinter quality. In this study, various iron ore blends were used to elucidate the effect that the particle size distribution (PSD) of layering material (-0.5mm) has on granulation and subsequent sintering process parameters during laboratory-scale sintering. Cold bed permeability was correlated to the spread of the PSD within the layers around granule nuclei. Widening the PSD spread within the layer increased cold bed permeability due to a narrowing in the spread of the granule size distribution (GSD) and increase in mean granule diameter. The Fuller-Thompson (FT) blend exhibited increased permeability during sintering (hot permeability) which led to a shorter sintering times. This was a result of enhanced hot permeability efficiency, which is a measure for the proportion of cold permeability maintained to hot permeability than anticipated based on the trend with mean granule diameter. Complete industrial (IS) blends were compared with blends designed to the FT equation with varying proportions of layering particles. At the same layering particle proportions, the FT blends exhibited increased cold and hot permeability by up to 20% and 25% respectively and led to a maximum 10% decrease in sintering time.

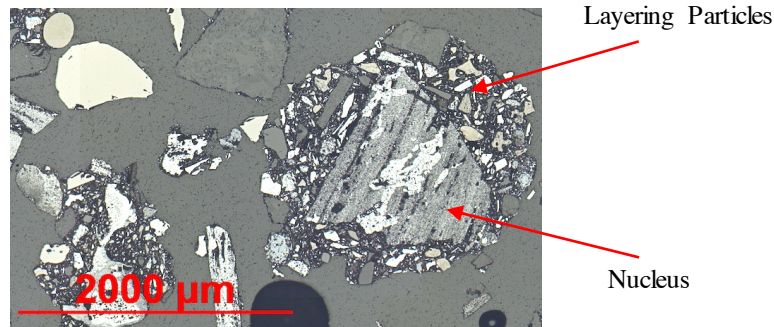
Keywords: iron ore, particle size distribution, granulation, permeability, Fuller-Thompson

Introduction

The mixing and granulation phase of the sintering process converts a wide-range of raw materials into a granulated feed that can be sintered. Sinter blends consist of iron ore, coke breeze, fluxes, plant reverts and return sinter fines, which are mixed before water is added for granulation in a continuous drum. The key mechanism operating during granulation is the layering of finer materials around larger nuclei particles to create granules.¹ A microscopic image of a granule composing of a nucleus with layering particles is shown in Figure 1. Granulation enhances sinter bed permeability, which controls the rate the flame front can pass through the bed.² Thus, is the limiting factor in sintering process productivity and is the key process parameter targeted in this study. In this paper, the authors use the terms (i) cold permeability; the permeability of the granulated mixture before sintering (ii) hot permeability; the permeability during sintering and we introduce a new term (iii) hot permeability efficiency defined as the proportion of hot permeability to cold permeability (expressed as %).

Earlier granulation studies have focused on the influence of parameters including moisture, drum speed and residence time.^{3 4} The major constituent of sinter blends is iron ore, Litster and Waters¹ conducted the initial studies on the impact of particle size distribution (PSD) on mixing and granulation of iron ores. Litster and Waters proposed a measure for granulation effectiveness ($X_{0.5}$), which could compare granule growth in blends with different PSDs. One of the key findings was that increasing the proportion of layering particles reduced the extent

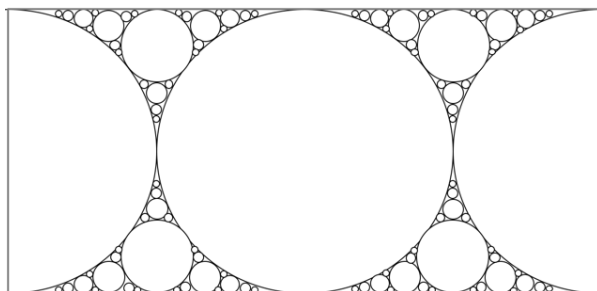
of granulation at a specific moisture content, however decreasing the mean layering particle size increased it. Other studies have taken this further to investigate the impact of iron ore PSD on sintering process parameters; bed permeability and strength.⁵⁻⁷ Preceding to further attempts to model these parameters based on iron ore properties such as particle size categories and the SiO₂ and Al₂O₃ content.⁵⁻⁸⁻⁹ However, to date this is the first study that applies an approach based solely on optimising the iron ore PSD to create enhancements in sinter bed permeability and process productivity.



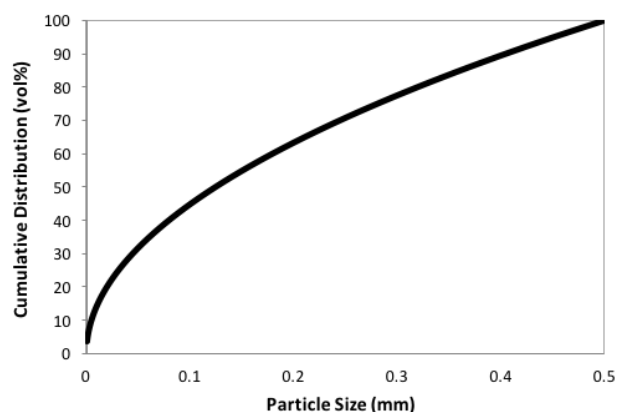
1 Microscopic image of granule

The Fuller-Thompson (FT) equation (1) was developed for designing the aggregate blends used in concrete, where blends with PSDs that fit the FT distribution provided increases in material properties such as strength and durability.¹⁰⁻¹³ P_i is the percentage less than the particle size d_i , D is the maximum particle size of the distribution and Ψ is the exponent of the equation. The equation has also been applied in other industries including pavement and briquette design.¹⁴⁻¹⁶ The equation produces the PSD to give the optimum particle packing density. A 2D visual representation of the concept, which is based on spheres is shown in Figure 2, where smaller particles are packed between larger particles. The PSD determined by the FT equation for a set of parameters is shown Figure 3 ($D=0.5$ mm and $\Psi=0.5$). This study examines the application of the FT particle design method to the design of sinter blends. It was hypothesised that designing the layering proportion of the blend (<0.5 mm)¹⁷⁻¹⁸ to the FT equation would provide enhancements in the density and coherence of the layers created during granulation and that this would translate to increases in sinter bed permeability and sintering process productivity.

$$P_i = 100 \left(\frac{d_i}{D} \right)^\Psi \quad (1)$$



2 Arrangement of Fuller-Thompson distribution of particles (2D representation)



3 Fuller-Thompson PSD with $D=0.5$ mm and $\Psi=0.5$

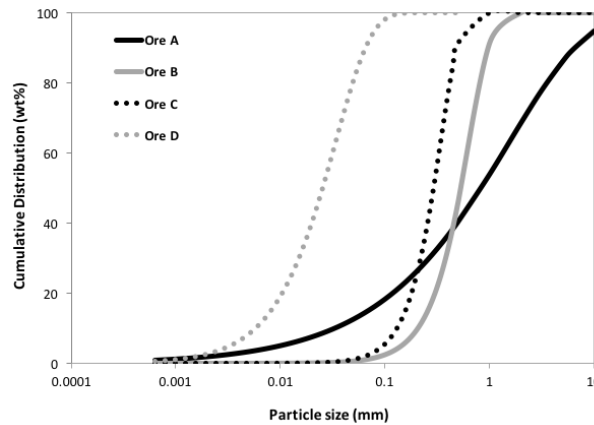
Materials and Methods

Materials

Four commercial grade iron ores, which originate from various locations worldwide were investigated in the experimental testing (Ore A to Ore D). Figure 4 shows the iron ore PSD, which was determined by dry sieve analysis through the following sieve series: +10 mm, -10+6.3 mm, -6.3+5 mm, -5+3.15 mm, -3.15+2 mm, -2+1 mm, -1+0.5 mm.¹⁹ A representative sample of the particles -0.5 mm were laser diffracted with a Malvern Mastersizer 2000. The complete iron ore PSD was fitted with the Rosin-Rammler distribution (2).²⁰ Where P(D) is the percentage less than the particle size D, D_m is the mean particle diameter and n is the spread of particle sizes within the distribution. The Rosin-Rammler distribution is utilised in describing the PSDs created during mineral processing operations and allows the determination of the mean particle diameter (D_m) and spread of particle sizes (n).

$$P(D) = 1 - \exp \left[- \left(\frac{D}{D_m} \right)^n \right] \quad (2)$$

The mean particle diameter (D_m) and spread of particle sizes (n) of the ores were determined by using the Microsoft Excel™ solver. These parameters were iteratively varied to minimise the sum of square residuals between the measured iron ore PSD and the distribution created by the Rosin-Rammler equation (2). Table 1 gives the mean particle diameter (D_m) and spread of particle sizes (n) for the iron ores. Table 2 gives the mean particle diameter (D_m) and spread of particle sizes (n) of -0.5 mm particles of the iron ores, which are considered as layering particles in this study. The primary difference in PSD under investigation is layer PSD spread (n), which is a relative measure for the uniformity of particle sizes in the distribution of the layer. Spreads can range from narrower to wider distributions (larger to smaller n). Combining these ores in different proportions enabled specific blend layer PSD spreads (n) to be created.



4 Iron ores cumulative PSD with Rosin–Rammler approximation

Table 1 Iron ore PSD properties

Material	Ore A	Ore B	Ore C	Ore D
Mean (D_m) (mm)	1.55	0.64	0.34	0.03
Spread of particle sizes (n)	0.58	1.99	2.34	1.27

Table 2 Iron ore layer PSD properties (-0.5mm)

Material	Ore A	Ore B	Ore C	Ore D
Mean (D_m) (mm)	0.16	0.37	0.31	0.03
Spread of particle sizes (n)	0.76	3.21	2.57	1.27

Table 3 - Sinter blend composition

Material	Mass (kg)	Mass (wt%)
Iron ore	5.00	62.70
Coke breeze	0.27	3.40
Flux A	1.09	13.60
Flux B	0.12	1.50
Return sinter fines (-3.15+1 mm)	0.75	9.40
Return sinter fines (-5+3.15 mm)	0.75	9.40
Total	7.98	100.00

Other sinter blend materials; coke breeze, limestone, dolomite and return sinter fines were utilised in conducting the laboratory sintering experiments. The ores and additional materials were held in constant proportions throughout experimentation with Table 3 presenting the mass of each on a dry basis.

Sinter blend design

The Microsoft ExcelTM solver was used to design the PSD of the layering proportion of the blends (-0.5 mm) by best-fitting the PSD to the FT equation (1). The solver was used to iteratively vary the proportions of the four iron ores, which displayed different PSDs (Figure 4). The objective was to minimise the sum of square residuals between the FT equation and the blend PSD to determine the blend composition with optimum fit. The solver is an in built ExcelTM algorithm that varies the decision variables to achieve the objective. Constraints set for the solver included ores being $\geq 0\text{wt}\%$ and $\leq 100\text{wt}\%$. Also, in the evaluation of industrial (IS) blends with FT blends the proportion of layering particles were set as a constraint (46wt%, 48wt% and 50wt%). This enabled a constant proportion of layering particles in the blends, so that the layer PSD was the only variable in the investigation.

Bimodal blends comprising a layering fraction of particles mixed with a constant mass of nuclei (Ore A +1-10 mm) were utilised to examine the influence of layer PSD spread (n) on sinter bed permeability. The blends composed of 50wt% layering and 50wt% nuclei particles. The layering fraction of one of the blends was designed to the FT equation (FT). A blend was designed with layer PSD spread that was narrower (smaller n) than the FT blend, termed 'Non-FT0'. Additional blends 'Non-FT1' and 'Non-FT2' were designed with a wider PSD spread (larger n) than the FT blend. The blend compositions and layering PSD spreads (n) of the blends are shown in Table 4.

The bed permeability and sintering process productivity of FT blends were also compared with industrial (IS) blends containing a fraction of layering particles similar to those typical in sinter plant operations (46wt%, 48wt% and 50wt% -0.5 mm). These blends are complete sinter blends containing all the particles from the iron ores and not the manipulated nuclei proportion in the blends introduced in the first part of the study. The composition of the blends used in the industrial evaluation are shown in Table 5. Each experimental blend in Table 4 and 5 were repeated in triplo at a moisture content of 6-6.5wt%.

Table 4 Composition of layering proportion (-0.5mm) of bimodal blends

Blend	Ore A	Ore B	Ore C (wt%)	Ore D	-0.5 mm	Layer PSD spread (n)
Non-FT0	0	0	80	20	50	1.02
FT	85	5	5	5	50	0.78
Non-FT1	17.5	57.5	0	25	50	0.70
Non-FT2	0	57.5	0	42.5	50	0.65

Table 5 Composition of industrial (IS) and Fuller-Thompson (FT) blends

Blend	Ore A	Ore B	Ore C (wt%)	Ore D	-0.5 mm	Layer PSD spread (n)
IS1	80	10	10	0	46	0.94
FT1	80	11.5	0	8.5	46	0.74
IS2	70	20	10	0	48	1.01
FT2	70	21.7	0	8.3	48	0.75
IS3	60	30	10	0	50	1.11
FT3	60	31.8	0	8.2	50	0.78

Mixing and Granulation

Dry mixing was conducted for 2 minutes in an Eirich mixer before being granulated in a plastic drum of internal diameter 300mm and length 500mm. Granulation was achieved by adding 6-6.5wt% water for 3 minutes at 24 rpm. The Froude number (N_{Fr}) was 0.0049 and the filling degree of the drum was 0.38. Two approximately 400g samples were taken for granule size distribution (GSD) analysis. This was measured by freezing the granules in liquid nitrogen before sieving through the following sieve series: +10 mm, -10+6.3 mm, -6.3+5 mm, -5+3.15 mm, -3.15+2 mm, -2+1 mm, -1+0.5 mm, -0.5+0.25 mm and -0.25 mm.¹⁹ The mass (+/- 0.01g) retained in each sieve fraction was measured. This allowed the GSD, mean granule diameter (D_m) and the spread of granule sizes (n) to be determined through applying the Rosin-Rammler distribution (2). A further two 50g granule samples were taken to determine the moisture content (wt%) using an automated moisture balance with an accuracy of 0.1 ± 0.1 wt%.

Granule microscopic analysis

Representative samples of granules produced by the blends in Table 4 and 5 were set in epoxy resin and horizontal cross-sections cut and polished. Mosaic images of the granules in the cross-sections were taken under a Zeiss Axioplan Imager Z1 microscope and Axiovision image analysis software. The images were processed through Adobe Photoshop™ to outline the layers and nuclei particles in the cross-sections before further image analysis was conducted. The measurements obtained from analysis were the number and areas of nuclei, layering and ‘non-layered’ (or ‘non-granulated’) particles.

Sintering

Laboratory sintering tests were carried out in a cylindrical shaped sintering unit of 120 mm diameter and 450 mm height, which was manufactured in-house. Approximately 6kg of sinter granules were charged into the sintering equipment over a 20 mm hearth layer. The flow rates through the bed (m/s) at pressure drops of 40, 80, 100 and 120 mbar were recorded for 2

minutes to provide the measurements for cold permeability. The top layer was ignited for 2 minutes with compressed air and natural gas at a pressure drop of 120 mbar. Once ignited the flow meter was reattached so that the flow rates to obtain a measure for hot permeability could be recorded. The measurements used for hot permeability was the average of the flow rates (m/s) when at their most stable, which was when the flame front was between 0-22.5 cm along the height of the sintering bed.

The pressure drop (ΔP) through a sinter bed can be described by the Ergun equation (3).²¹ This equation defines pressure drop in terms of bed height (L), superficial gas flow velocity or flow rate (U), gas viscosity (μ), gas density (ρ), mean granule diameter (D_p), shape factor (Φ), and porosity (ϵ). The pressure drop, flow rate and mean granule diameter are determined by the methods discussed previously. The shape factor and gas properties are constant. The Ergun equation (3) was fitted to the measurement data by minimising the sum of square residuals by iteratively varying the bed porosity (ϵ) using the Microsoft ExcelTM solver. Sinter bed permeability (cold and hot) was then classed as the flow rate through the bed at a pressure drop of 120mbar, which is similar to that found in plant operations.

$$\frac{\Delta P}{L} = \frac{150 \mu v(1-\epsilon)^2}{(\Phi D_p)^2 \epsilon^3} U - \frac{1.75 \rho v^2(1-\epsilon)}{\Phi D_p \epsilon^3} U^2 \quad (3)$$

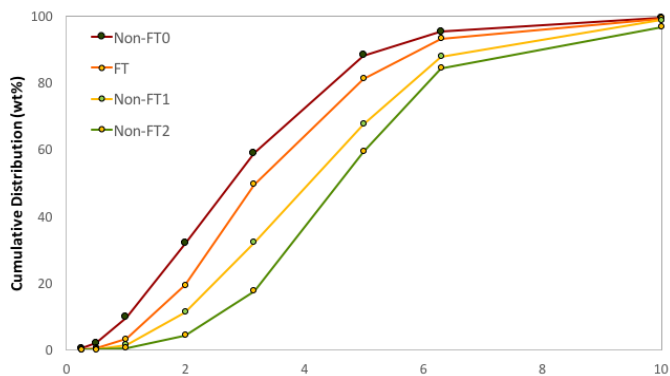
Sintering continued until the flame front had passed through the entire bed. The time taken to reach the burn-through point defines the sintering time (seconds) and is classed as a measure for sintering process productivity in this study. There were 5 thermocouples placed throughout the bed at 7.5cm intervals with a further 3 in the gas extraction system. The timing of the burn through point was determined when the first thermocouple in the gas extraction systems reached its peak temperature. All measurements were taken at 1-second intervals and recorded automatically via a programme logic controller (PLC) into a data file.

Results and Discussion

Influence of layer particle size distribution spread (n) in bimodal blends

Cold permeability

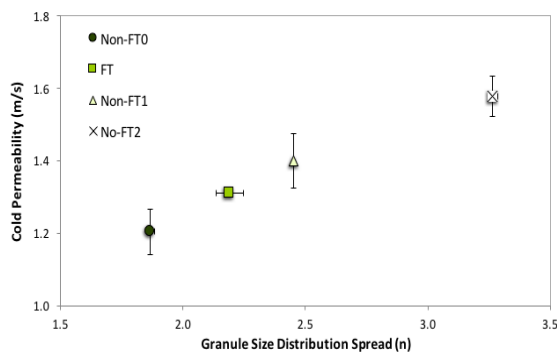
To understand the impact of layer PSD spread (n) on cold permeability it was important to first understand which factors have primary influence. The granule size distributions (GSDs) for the blends in Table 4 are shown in Figure 5 with the mean granule diameters (D_m) and GSD spreads (n) shown in Table 6. Figure 6 shows changes in cold permeability were strongly related to the GSD spread (n). As the GSD spread became narrower (increasing n) an increased cold permeability was observed. Note that the Fuller-Thompson (FT) blend did not create the narrowest GSD spread or greatest cold permeability. The Ergun equation (3) indicates that the flow rate (and hence permeability) is a function of bed voidage (ϵ). Maximum bed voidage is achieved in a bed of equal sized spheres.²² The less uniform the size of spheres i.e. widening GSD spread (decreasing n) the lower the bed voidage.



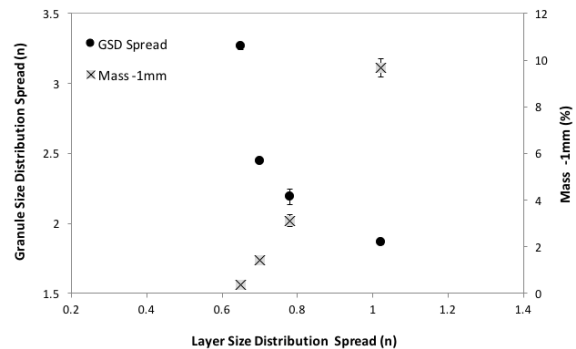
5 GSD measurements for bimodal blends in Table 4

Table 6 GSD spread and mean granule diameter for bimodal blends in Table 4

Blend	GSD spread (n)	Mean granule diameter (mm)
Non-FT0	1.9	3.4
FT	2.2	3.9
Non-FT1	2.5	4.7
Non-FT2	3.3	5.2



6 Relationship between cold permeability and GSD spread for bimodal blends in Table 4



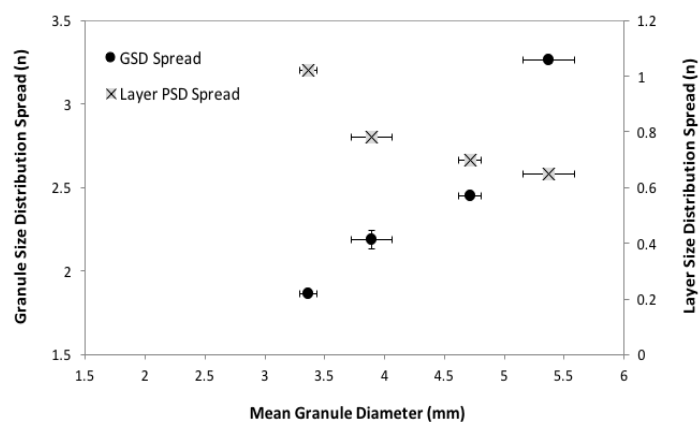
7 Relationship between GSD spread and mass passing 1mm sieve with layer PSD spread for bimodal blends in Table 4

Figure 7 shows the relationship between layer PSD spread (n) with GSD spread (n) and mass of particles -1 mm. It can be identified in Figure 7 that there is an inverse relationship between layer PSD and GSD spread (n). As the layer PSD spread widened (decreasing n) a narrowing

in the GSD spread (increasing n value) was found. There are no error bars in the x-axis, as the layer PSD spread (n) does not change in the three repetitions of blend. The y-axis error bars cannot be seen in all measurements, which is due to the small measurement error with those blends. The mass of particles that can be considered as ‘non-layered’ (or ‘non-granulated’) at the end of a granulation experiment were defined as those that were less than 1 mm. Figure 7 also shows the mass (%) of ‘non-layered’ particles at the end of granulation, plotted against the layer PSD spread (n). As the layer PSD spread widened (decreasing n) the mass of non-granulated particles (those passing 1 mm sieve) after granulation decreased and indicates that a greater mass of material layered when the layer PSD spread (n) was wider. This explains the narrower GSD spread (n) with increased layer PSD spread (n), as shown in Figure 7. The interpretation of these data is that a wider range of particle sizes within the distribution (lower n) for layering particles means that more particles (and hence more mass) can become entrained within the layer around the nucleus during granulation.

Further evidence for this phenomenon is demonstrated in Figure 8 which presents the relationship between GSD and layer PSD spread (n) with mean granule diameter (D_m). Widening the layer PSD spread (decreasing n) created a larger mean granule diameter. From Figure 8 the direct relationship between mean granule diameter and GSD spread can also be seen, where increasing mean granule diameter is correlated with a narrowing in GSD spread (increasing n).

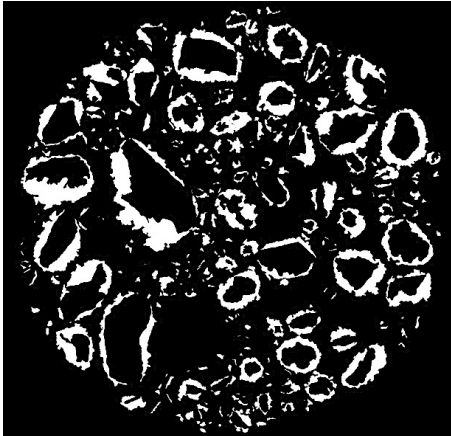
Microscopic cross-section images of the layers formed around nuclei are shown in Figure 9 to 12. The measurements obtained from image analysis of these cross-sections are presented in Table 7. The data in Table 7 support the observations in Figure 8 that widening layer PSD spread (decreasing n) increased the mean granule diameter (D_m). As the layer PSD spread widened from Non-FT0 to Non-FT2 (decreasing n in Table 4) there was a corresponding increase in the average layer area per nuclei in the cross-sections. Further evidence can be seen from Figure 13 to 16 which show the ‘non-layered’ (or ‘non-granulated’) particles highlighted in the cross-sections after granulation. The areas of ‘non-layered’ particles are presented in Table 7. These data confirm the trends highlighted in Figure 7 and 8, as the layer PSD spread widened (decreasing n) there was a smaller area of ‘non-layered’ particles as more particles report to the layers around the nuclei. In summary of Figure 6 to 16 and Table 6 and 7 when the PSD of layering materials is wider (smaller n), larger granules are formed which have a narrower GSD (larger n) and increased cold permeability.



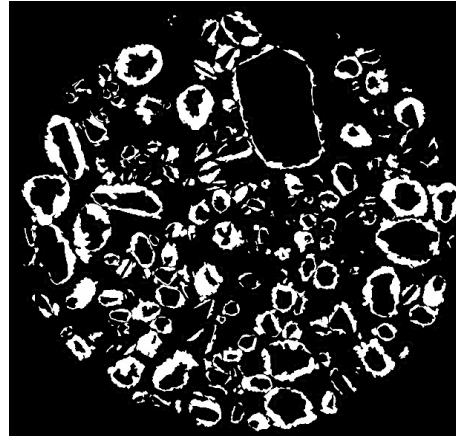
8 Relationship between GSD and layer PSD spread with mean granule diameter for bimodal blends in Table 4

Table 7 Granule image analysis measurements of bimodal blends in Table 4

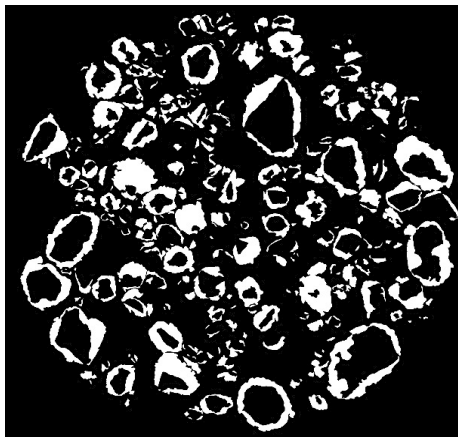
Blend	Number of Nuclei	Layer Area (mm ²)	Average Layer Area/Nuclei (mm ²)	Non-Layered Particle Area (mm ²)
Non-FT0	186	224.3	1.2	29.0
FT	190	249.4	1.3	21.1
Non-FT1	187	283.4	1.5	16.3
Non-FT2	162	343.1	2.1	7.4



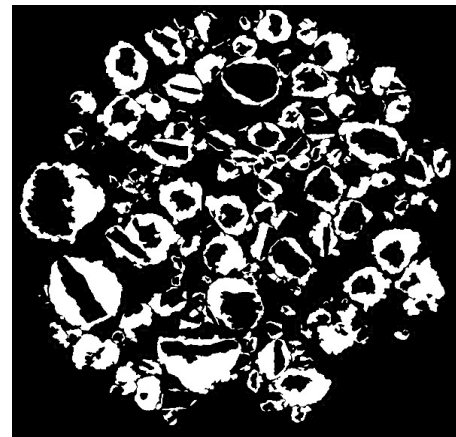
9 Microscopic image of layers in Non-FT0



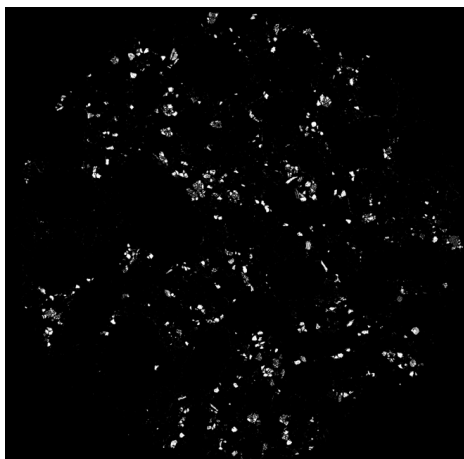
10 Microscopic image of layers in FT



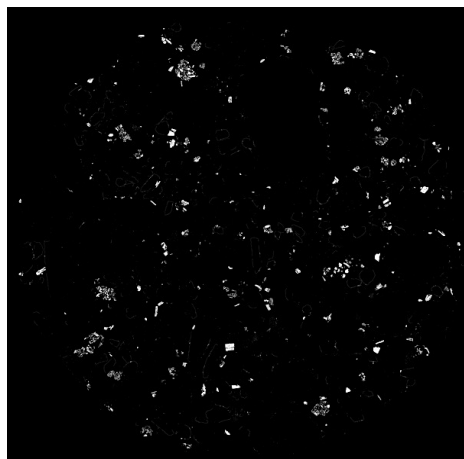
11 Microscopic image of layers in Non-FT1



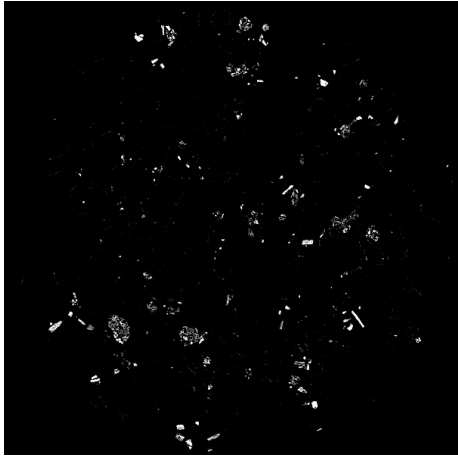
12 Microscopic image of layers in Non-FT2



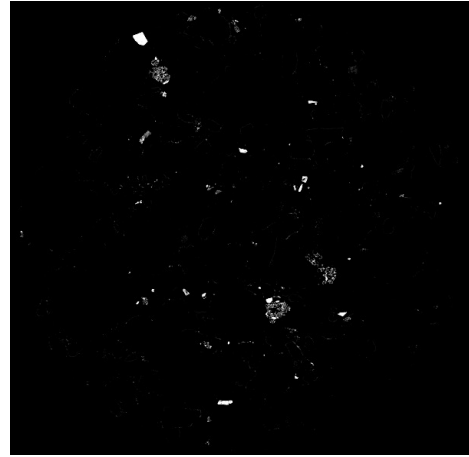
13 Microscopic image of non-layered particles in Non-FT0



14 Microscopic image of non-layered particles in FT



15 Microscopic image of non-layered particles in Non-FT1



16 Microscopic image of non-layered particles in Non-FT2

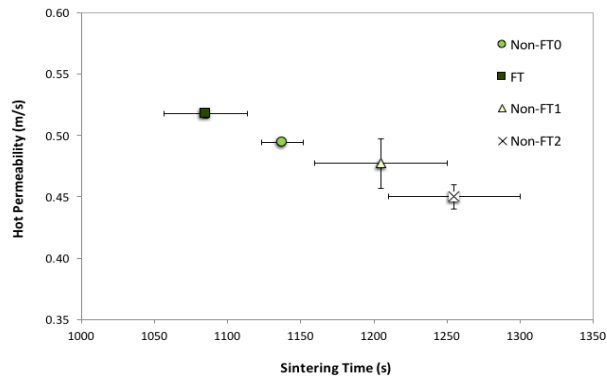
Hot permeability and sintering time

Whilst the cold permeability is an important parameter to ensure good gas flow during the initiation of sintering, the permeability of the bed during sintering (referred to as the ‘hot permeability’) is also critical. A bed will have a relatively high permeability prior to sintering (cold permeability) but once a flame front is created will lead to a permeability reduction. This is primarily due to a sharp increase in pressure drop caused by the reactions in the flame front and bed deformation. The hot permeability strongly influences sintering time (Figure 17) and the sinter strand productivity will be impacted by longer sintering times. Note that the Fuller-Thompson (FT) blend produced the greatest hot permeability and shortest sintering time.

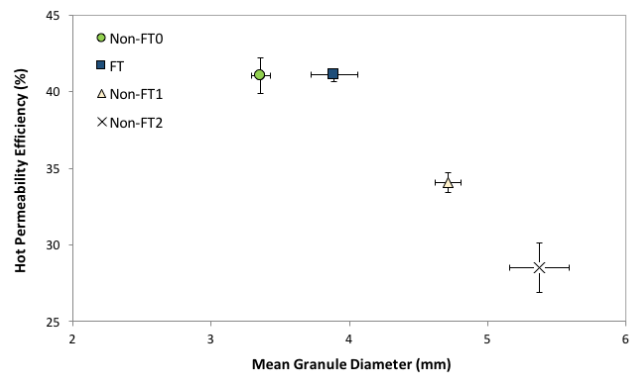
It is thus essential to represent the decrease in permeability experienced by the sinter bed during transition from cold to hot conditions during sintering. The authors introduce a measure – the “hot permeability efficiency” defined as $\text{hot permeability}/\text{cold permeability} \times 100$, to indicate the relative size of the decrease in permeability between cold and hot conditions.

Widening the PSD spread of layering material (decreasing n) has been shown to increase the mean granule diameter and narrow the GSD spread (increasing n) which leads to an increased cold permeability. However, an increase in mean granule diameter is correlated with a decrease in hot permeability efficiency (Figure 18). i.e. larger mean granule diameters lost more of their cold permeability when transferring to hot permeability during the process. Layers of fine particles more readily deform than nuclei particles.⁶ Thus, it is thought that larger layers display more deformation and bed collapse when transferring from cold to hot permeability.

However, there was an anomaly to this trend, which was the FT blend. The FT blend showed enhanced hot permeability efficiency compared to the other blends (Figure 18). The trend in Figure 18 showed that decreasing mean granule diameter correlated with increasing hot permeability efficiency, however it can be seen that the mean granule diameter of FT was greater than for Non-FT0. The result suggested that the FT blend provided greater resistance to permeability losses when transferring from a cold to a hot bed. With the blends investigated the FT blend created the layer PSD spread (n) that gave the best compromise between mean granule diameter for cold permeability and layer coherence to maintain to hot permeability. This was unlike the other blends studied, which provided only cold permeability (Non-FT1 and Non-FT2) or hot permeability efficiency (Non-FT0).



17 Relationship between hot permeability and sintering time for bimodal blends in Table 4



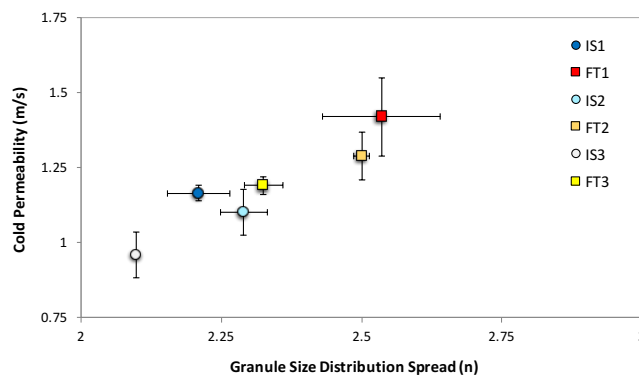
18 Relationship between hot permeability efficiency and mean granule diameter for bimodal blends in Table 4

Industrial application of Fuller-Thompson design

Industrial (IS) blends were evaluated against blends designed to the FT equation (Table 5 IS1-IS3 and FT1-FT3). These blends have increasing masses of layering particles (-0.5 mm wt%), which are similar to those of sinter plant operations to assess the impact of increasing the layering proportion of blends on sinter bed permeability and productivity.

Cold permeability

Figure 19 shows the comparison of the cold permeability of the industrial (IS) and FT blends at the layering particle proportions shown in Table 5 (1=46wt%, 2=48wt% and 3=50wt%). The cumulative GSD of the blends is shown in Figure 20 and Table 8 identifies the mean granule diameters (D_m) and GSD spreads (n). Figure 19 showed that increasing the layering material from 46-48wt% did not reduce the cold permeability significantly enough to be outside the 95% confidence intervals (IS1-IS2 and FT1-FT2). However, when increasing the layering material from 48-50wt% a decrease in cold permeability was observed (IS2-IS3 and FT2-FT3). The blends could also not incorporate 4wt% more layering particles without reducing cold permeability (IS1-IS3 and FT1-FT3).



19 Cold permeability and GSD spread for industrial (IS) and Fuller-Thompson (FT) blends in Table 5

When comparing the IS and FT blends in Figure 19, the FT blends provided enhanced cold permeability at equal layering particle proportions. It was realised from Figure 19 that the FT

blends could incorporate 4wt% more layering particles and exhibited cold permeability results that were inside the 95% confidence intervals of the IS blend (IS1-FT3).

Where increased cold permeability was exhibited in Figure 19 the blends created a narrower GSD spread (larger n). It was shown in Figure 7 and 8 that wider layer PSD spreads (smaller n) produced increased cold permeability due to narrowing GSD spread (increasing n) and increasing mean granule diameter (D_m). The FT blends created narrower GSD spreads (larger n) than the IS blends as they had a wider layer PSD ($n = 0.8$ for FT and $n = 1-1.2$ for IS), thus increasing cold permeability. In the case of IS1 and FT1 this was verified by image analysis. It can be observed from Table 8-9 and Figure 21-24 that FT1 had larger mean granule diameter and layer area per nuclei and smaller mass and area of ‘non-layered’ particles compared to IS1. This corresponds with Figure 7 and 8 where wider layer PSD spreads (smaller n) were able to layer more a greater mass of particles, consequently increasing mean granule diameter and narrowing the GSD spread.

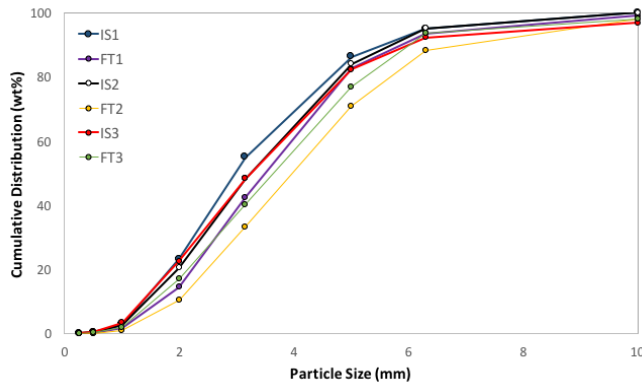


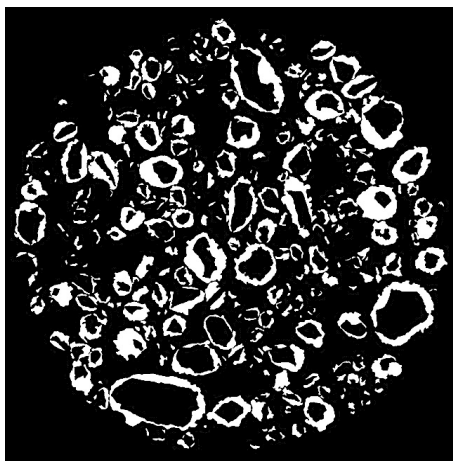
Table 8 GSD spread and mean granule size of industrial and Fuller-Thompson blends in Table 5

Blend	GSD spread (n)	Mean granule diameter (mm)
IS1	2.2	3.6
FT1	2.5	4.0
IS2	2.3	3.8
FT2	2.5	4.6
IS3	2.1	3.9
FT3	2.3	4.2

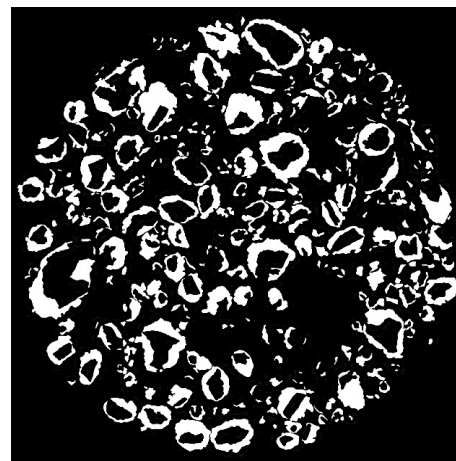
20 GSD measurements for industrial and Fuller-Thompson blends in Table 5

Table 9 Granule image analysis measurements for IS1 and FT1

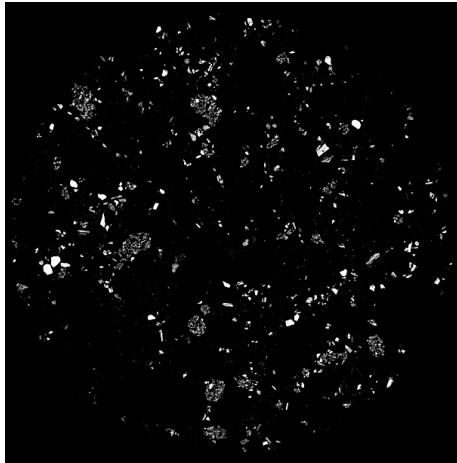
Blend	Number of Nuclei	Layer Area (mm ²)	Average Layer Area/Nuclei (mm ²)	Non-Layered Particle Area (mm ²)
IS1	241	271.2	1.13	33.3
FT1	231	284.7	1.23	27.1



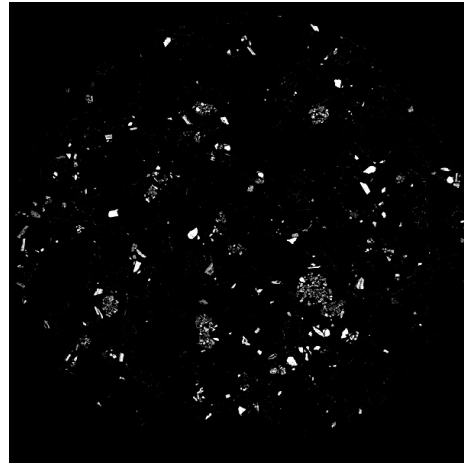
21 Microscopic image of layers in IS1



22 Microscopic image of layers in FT1



23 Microscopic image of non-layered particles in IS1

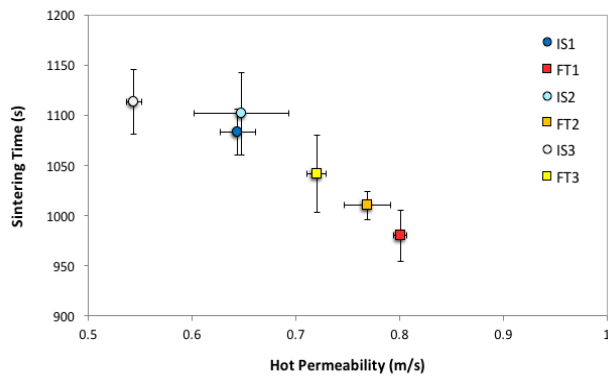


24 Microscopic image of non-layered particles in FT1

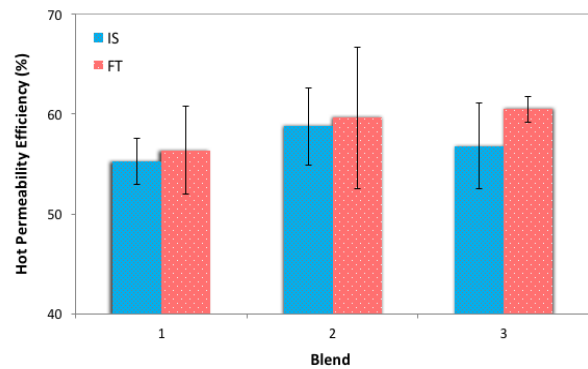
Hot permeability and sintering time

Figure 25 shows the hot permeability and sintering time results for the industrial (IS) and FT blends at the layering particle proportions presented in Table 5 (1=46wt%, 2=48wt% and 3=50wt%). Similar to Figure 17 there was a direct relationship between hot permeability and sintering time. Increasing hot permeability correlated with decreasing sintering time. The FT blends provided shorter sintering times than the IS blends at the same layering particle proportion. The largest decrease in sintering time at equal layering particle proportions was 9.5% (IS1-FT1). The results in Figure 25 indicated that designing the layering proportion of sinter blends (-0.5mm) to the FT equation provided a layering PSD that gave improved hot permeability and sintering times when compared to the IS blends at equal layering particle proportions. Further, the FT blend incorporated 4wt% more layering particles and still exhibit sintering times that were inside the 95% confidence intervals of the IS blend (IS1-FT3) demonstrating a means to increase the layering particle proportions in FT blends when compared to IS blends.

The reason behind the increased hot permeability relates back to hot permeability efficiency. From Figure 26 the hot permeability efficiency results for the blends are the same within the 95% confidence intervals. As the FT blends were shown to provide increased cold permeability (Figure 19) this was therefore transferred through to increased hot permeability and shorter sintering times. It was shown previously that the increase in mean granule diameter (D_m) due to larger layers created around nuclei resulted in the narrowing of the GSD spread (increasing n), which increased cold permeability and decreased hot permeability efficiency. The FT blends did not follow this trend, as no difference between the hot permeability efficiency could be distinguished between the IS and FT blends, even with the increased mean granule diameters of the FT blends (Table 8). This was the same as the trend seen in Figure 18 with the Non-FT0 and FT blends.



25 Hot permeability and sintering times for industrial and Fuller-Thompson blends in Table 5



26 Hot permeability efficiency of industrial and Fuller-Thompson blends in Table 5

Conclusions

This study focused on the influence of layer particle size distribution (PSD) spread (n) of sinter blends on sinter bed permeability. Several concepts were presented and discussed, which led to several important conclusions to be drawn. Due to the novel application of the FT equation in sinter blend design the evaluation of FT blends against industrial (IS) blends was conducted to emphasise potential enhancements in bed permeability and process productivity for plant operations.

1. Widening the layer PSD spread in blends increased mean granule diameter and narrowed the granule size distribution (GSD) spread, which was a result of a greater mass of particles layering and less ‘non-layered’ (or ‘non-granulated’) particles in the bed. This led to increases in cold permeability.
2. The measured hot permeability was lower than the cold permeability in all cases. The authors introduce a new term, the ‘hot permeability efficiency’ defined as the ratio of hot permeability to cold permeability (%) as a useful measure of the beds ability to maintain permeability during the process.
3. An increase in mean granule diameter correlated with a reduction in the hot permeability efficiency. Beds with larger mean granule diameter lost more of their permeability during the process.
4. With the blends investigated the blends designed to the FT equation had a greater hot permeability efficiency than anticipated based on the results from the other blends. The FT blend thus had the greatest hot permeability and shortest sintering times.
5. The industrial application of designing blends to the FT equation showed reductions in sintering times of up to 9.5% at equal layering particle proportions. This was attributed to an increased hot permeability, which was a result of increased cold permeability and enhanced hot permeability efficiency than expected with mean granule diameter. This suggests improved layer properties when designing to the FT equation, as they were able to maintain the same proportion of the permeability with larger mean granule diameters.

6. Designing blends to the FT equation enabled the incorporation of 4wt% more layering particles and still exhibit the same cold bed permeability and sintering times as industrially simulated blends.
7. Designing the layering proportion of sinter blends (-0.5mm) to the FT equation provides a rationale and methodology to not only increase bed permeability and reduce sintering times but also incorporate a larger proportion of layering particles in blends.

References

1. J. D. Litster and A. G. Waters: 'Influence of material properties of iron ore sinter feed on granulation effectiveness', *Powder Technology*, 1988, **55**, 141-151.
2. H. Zhou, Z. Liu, M. Cheng and K. Cen: 'Effect of flame-front speed on the pisolite-ore sintering process', *Applied Thermal Engineering*, 2015, **75**, 307-314.
3. M. Butensky and D. Hyman: 'Rotary drum granulation. An experimental study of factors affecting granule size', *Industrial and Engineering Chemistry Fundamentals*, 1971, **10** (2), 212-219.
4. P. A. L. Wauters: 'Modelling and mechanisms of granulation', PhD thesis, Delft University of Technology, Netherlands, 2001.
5. J. Khosa and J. Manuel: 'Predicting granulating behavior of iron ores based on size distribution and composition', *ISIJ International*, 2007, **47**, 965-972.
6. B. G. Ellis, C. E. Loo and D. Witchard: 'Effect of ore properties on sinter bed permeability and strength', *Ironmaking & Steelmaking*, 2007, **34** (2), 99-108.
7. E. Kasai, W. J. Rankin and J. F. Gannon: 'The effect of raw mixture properties on bed permeability during sintering', *ISIJ International*, 1988, **29**, (1), 33-42.
8. J. D. Litster, A. G. Waters and S. K. Nicol: 'A model for predicting the size distribution of product from a granulation drum', *ISIJ International*, 1986, **26**, 1036-1044.
9. X. Lv, C. Bai, X. Huang and G. Qui: 'Prediction of size distribution of iron ore granules and permeability of its bed', *Journal of mining and metallurgy*, 2011, **47**, (2), 113-123.
10. W. B. Fuller and S. E. Thompson: 'The laws of proportioning concrete', *Transactions of American Society of Civil Engineers*, 1907, **59**, 67-143.
11. Q. L. Yu and H. J. H Brouwers: 'Development of a self-compacting gypsum-based lightweight composite', *Cement & Concrete Composites*, 2012, **34**, 1033-1043.
12. M. Glavind and E. J. Pedersen: 'Packing calculations applied for concrete mix design', *Creating with Concrete*, University of Dundee, 1999.
13. S. A. A. M. Fennis and J. C. Walraven: 'Using particle packing technology for sustainable concrete mixture design', *Heron*, 2012, **57** (2), 73-101.
14. B. L. Miranda: 'Gradation-based framework for asphalt mixtures', *School of Architecture and Built Environment, Division of Highway and Railway Engineering, Stockholm*, 2012.
15. T. F. Fwa: 'The handbook of highway engineering', *CRC Press*, 2005, 7-8.
16. R. Sen, M.K. Mitra, S. Mukherjee and R. Dey: 'Effect of grading of chromite ores on the quality of briquettes', *ISIJ International*, **50** (2), 2010, p200-206.
17. R. Bergstrand, J. Khosa, A. Waters and J. Garden: 'The effect of Marra Mamba ore addition on the granulation characteristics of Pisolite based and Hematite based sinter blends', *ISIJ international*, 2005, **45** (4), 492-499.
18. M. Gan, X. H. Fan, Z. Y. Ji, X. L. Chen, L. Yin, T. Jiang, Z. Y. Yu & Y. S. Huang: 'Optimising method for improving granulation effectiveness of iron ore sintering mixture', *Ironmaking & Steelmaking*, 2014, **42** (5), 351-357.
19. Tata Steel Europe: 'Granule size distribution analysis procedure', *RD&T Ironmaking - Sinter testing*, 2015.

20. P. A. Vesilind: 'The Rosin-Rammler particle size distribution', *Resource Recovery and Conservation*, 1980, **5**, 275-277.
21. S. Ergun: 'Fluid flow through packed columns', *Chemical Engineering Progress*, 1952, **48**, 89-94.
22. M. Suzuki, H. Kada and M. Hirota: 'Effect of the size distribution on the relation between coordination number and void fraction of spheres in a randomly packed bed', *Advanced Powder Technology*, 1999, **10** (4), 353-365.